INHOMOGENEOUS RF FIELDS: A VERSATILE TOOL FOR THE STUDY OF PROCESSES WITH SLOW IONS

DIETER GERLICH

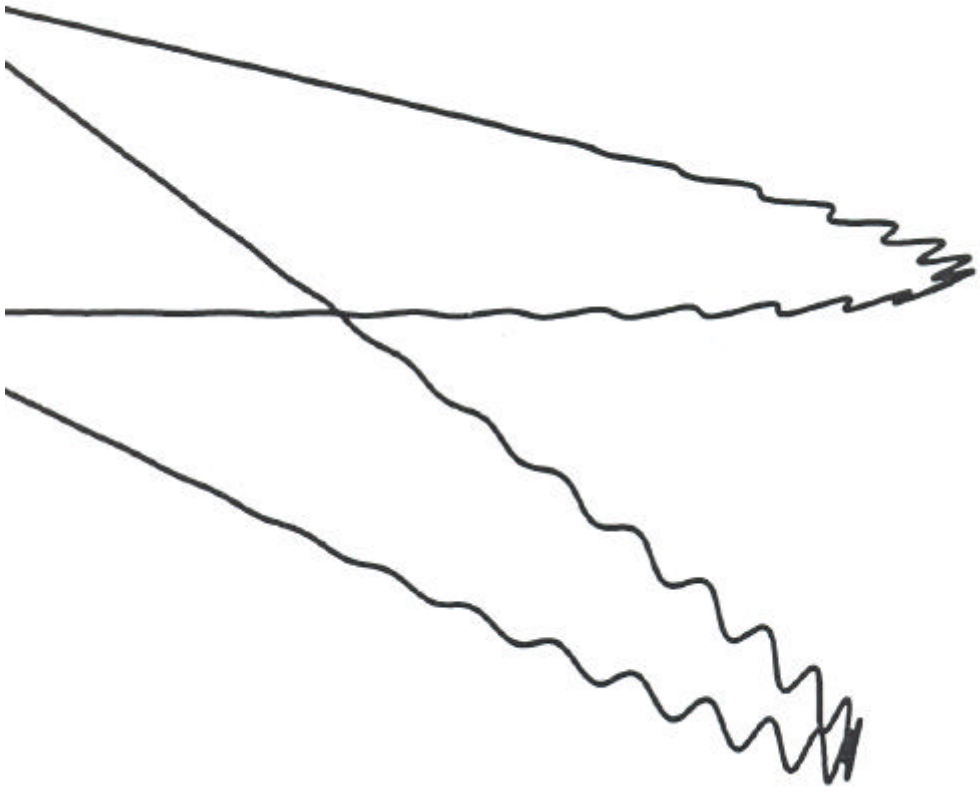

State-Selected and State-to-State Ion-Molecule Reaction Dynamics. Part 1: *Experiment,* Edited by Cheuk- Yiu Ng and Michael Baer. Advances in Chemical Physics Series, Vol. LXXXII.
ISBN 0-471-53258-4 CD 1992 John Wiley & Sons, Inc.

INHOMOGENEOUS RF FIELDS: A VERSATILE TOOL FOR THE STUDY OF PROCESSES WITH SLOW IONS

DIETER GERLICH

Fakultät für Physik, Universität Freiburg, Freiburg, Germany

CONTENTS

I. INTRODUCTION

Over the last four decades, the study of reactions between ions and neutral molecules has grown into a rather large field of research in chemistry and physics. Interest in the experimental investigation of the detailed dynamics

of collision processes has resulted in the construction of a variety of novel devices, and considerable emphasis has been placed on the design and development of specific instrument components for ion generation (e.g., temperature-controlled ion sources, photoionization methods, and production of metal and cluster ions), interaction regions (scattering cells, molecular flows, and molecular beams), and product detection (mass, energy, and state analyzers). These devices have been combined in many different instruments such as flowing afterglow and drift tubes, ion–cyclotron resonance cells, ion traps, as well as ion-beam arrangements (e.g., beam–cell, crossed beam, and merged beam). Each of these instruments has proven useful for solving specific problems, but none is ideally suited for answering all questions of interest. For example, studies at low energies have been dominated by swarm and trapping techniques yielding predominantly thermal reaction-rate coefficients, while beam methods, which provide very detailed information on reaction dynamics, have been restricted to higher energies, typically above 1 eV. Different aspects of the field of gaseous ion chemistry have been reviewed often. A list of the most important reference up to 1979 is found in Franklin (1979), while more recent advances have been described in several extensive collections of reviews (Ausloos, 1979; Ausloos, and Lias, 1987; Bowers, 1979, 1984; Futrell, 1986).

In a recent review (Farrar, 1988) on *the major techniques for the study of ion–molecule reactions*, several authors have summarized advantages and shortcomings of different *bulk* and *beam* methods. Comparison of the variety of available techniques leads to the conclusion that there is still a large technology gap between the idealized experiment and the currently available methods. This is partly because electrostatic potentials, used in most of the apparatuses for handling charged particles, have the disadvantage that the stationary points are always saddle points, that is, there are no real minima, a direct consequence from Laplace's equation in a charge-free domain. Usually the situation becomes worse if space charges and field distortions are involved. Some of the resulting problems and other inherent difficulties encountered by most of the standard electrostatic techniques can be overcome by the use of *effective potentials* created by fast oscillatory electric or electromagnetic fields, since these fields allow one to create two- and three-dimensional potential minima. The principle of guiding or trapping charged particles by time-dependent forces has a longer history than its application in gas-phase ion chemistry and mass spectrometry. The most prominent examples of the use of *radio frequency* (*rf*) fields are the quadrupole mass filter and the Paul trap; however, the 1950s and 1960s have also seen many other related activities such as plasma confinement in rf fields, interaction of electrons with microwaves or light, and other applications, as will be briefly mentioned in Section II.

The first apparatus used to determine integral cross sections became operational 20 years ago (Gerlich, 1971; Teloy and Gerlich, 1974). This early instrument demonstrated several outstanding capabilities including a wide energy range, extreme sensitivity, and high accuracy for the determination of integral cross sections. These advantages (and also some weaknesses) have been discussed by Gentry (1979), who presented a semiquantitative comparison of different ion-beam instruments. In the past decade the *guided ion-beam method* has gained some popularity, but its incorporation into other laboratories has been rather slow. The number of research groups routinely using guided ion beams to determine integral cross sections is still limited to a few. This may, in part, be due to a lack of detailed theoretical information as well as missing technical and practical hints. Therefore, one aim of this chapter is to present a comprehensive overview of the technique and to provide some insight into the theory.

A second aim of this chapter is to demonstrate by several examples that the application of inhomogeneous rf fields is not limited only to precise integral cross-section measurements. Simultaneous recording of longitudinal and transverse velocities of guided product ions allows one to derive differential cross sections and product kinetic energy distributions. The combination of a guided ion beam with a coaxial supersonic beam has opened up the collision energy range down to 1 meV. Other examples, which illustrate the general use of rf fields in ion chemistry and physics, include several applications of the time-of-flight method, employment of lasers for ion preparation and/or product detection, use of coincidence techniques, and various combinations. Finally, we will show that rf storage of ions opens up a wide field of applications. Trapping in a large field-free region allows one to obtain very low ion temperatures and long storage times and to measure extremely small rate coefficients. On the other hand, trapping in quadrupole fields generally causes ion heating; this geometry is, however, better suited for mass analysis and therefore more frequently used in chemical applications (March and Hughes, 1989).

Section II provides information on the interaction between charges and fast oscillatory fields. After a historical overview of the development of related theories (mainly from the 1950s and 1960s), principles of ion motion in rf fields are explained within the adiabatic approximation. Computer simulations are used to illustrate the influence of potential distortions, to explain features of ion motion, and to derive realistic energy distributions.

Section III shows that effective potentials are generally applicable for trapping, storing, and confining ions in space, as well as selecting them according to energy and mass, focusing ion beams, and other purposes. Several instrument devices will be described including rf ion sources, energy and mass filters, and long ion guides for time-of-flight analysis or for studying

ion–laser beam interactions. Technical and practical hints, as well as some design considerations, are also given. In addition, a few important performance tests of several rf devices are presented.

Several complete instruments in which a number of different rf components are assembled for special applications are described in Section IV. Here, we include a short list of applications from research groups besides our own. Some comments on kinematical averaging are included that are necessary for the characterization of the apparatuses and the interpretation of the experimental results.

Finally, Section V presents a series of measurements performed primarily in our laboratory over the past few years using different rf electrode arrangements. Included are some examples from previously unpublished work. The goal in selecting these examples is to demonstrate the technical variety of applications of inhomogeneous rf fields, rather than discuss in detail the dynamics of the chosen collision systems.

The conclusion will show that there remain many detailed improvements in the design of existing devices, and that through combinations with other established techniques the versatility of the apparatuses can be further advanced. A few speculations concerning new rf devices and applications to new problems are included.

II. MOTION OF CHARGED PARTICLES IN FAST OSCILLATORY FIELDS

The motion of a system under the influence of a force varying in time and space is a rather fundamental subject, well studied in theoretical and experimental physics. In general, most differential equations describing such systems are nonlinear and usually cannot be solved exactly. For special purposes, for example, for the characterization of solutions of mechanical and technical problems, analytical approximation procedures have been developed (Arnold, 1988, Hayashi, 1985; Lichtenberg and Lieberman, 1983), such as the perturbation, iteration, and averaging methods, the method of harmonic balance, or the guiding center approach (Littlejohn, 1979). It is beyond the scope of this chapter to discuss the modern mathematical developments of the analysis of nonlinear systems, and since we are more concerned with experimental applications, the principal aim of this section is to impart some basic understanding of the motion of a particle under the influence of a fast oscillatory force.

In the following we restrict the examples to the special case of the interaction between charges and time-dependent electric or electromagnetic fields, although a discussion of work performed in other areas would also contribute to the understanding of the mathematics relevant to our ion

physics applications. The first part of this section briefly reviews a few related physical situations that are treated in the literature. Examples include the interaction of a free electron with a radiation field, applications in plasma and accelerator physics, mass spectrometry, and ion chemistry. Here, we report only the basic ideas and theoretical aspects, while pertinent experimental investigations will be mentioned in Section III. Following this overview we will introduce the adiabatic approximation and derive the effective potential. Particular attention is directed toward the question of stability of the ion motion and several practical and mathematical criteria for stability are discussed. Computer simulations are used both for illustrative purposes and for finding the limitations of approximate solutions.

A second purpose of this section, besides searching for solutions of the equation of motion, is to give support for the determination of electric fields from given boundary conditions or the search for appropriate electrode geometries. Although all related problems are well documented in electrodynamics textbooks, a few formulas are compiled in Section II C for calculating potentials for different geometrical arrangements of electrodes. A separate section is devoted to the special class of multipole fields. The last part of Section II is concerned with the analysis of the kinetic energy distribution of ions in different oscillatory fields. Some related questions can be answered analytically within the adiabatic approximation, while in the presence of collisions, analysis of kinetic energy distributions requires numerical simulations. These simulations will be used to derive realistic energy distributions of ions stored in the presence of a buffer gas.

A. Remarks on the Development of the Theory

One of the earliest treatments of the interaction of electrons with electromagnetic waves was Thomson's (1903) determination of the X-ray scattering cross section. His calculation is based on the classical non-relativistic motion of an electron in the field of a plane wave which is simply described by the equation of motion

$$m\ddot{\mathbf{r}} = q\mathbf{E}_0 \cos(\Omega t). \tag{1}$$

Here q is the charge of the electron, m is the mass, $\mathbf{E}_0$ is the peak electric field vector, and Ω is the angular frequency.

At high light intensities, electron–photon scattering is dominated by stimulated photon interactions known as the ponderomotive effect. This was first recognized by Kapitza and Dirac (1933), who suggested that an optical standing wave could scatter electrons. It was the availability of intense optical radiation, following the development of the laser in the 1960s, which prompted many new theoretical and experimental studies. The problem has

been reexamined in detail in both relativistic and nonrelativistic regimes using classical or quantum-mechanical descriptions, or quantum field theory (Eberly, 1969).

It has been discussed by several authors [see, for example, Motz and Watson (1967)] that in special situations the properties of the field make it possible to obtain analytical solutions of the equation of motion without any approximation. An instructive example is the classical, nonrelativistic motion of an electron in a standing plane electromagnetic wave with circular polarization. In this case, it is an exact result (Motz and Watson, 1967) that the time-averaged energy of the classical wiggling motion of the electron, $q^2E_0^2/4m\Omega^2$, in response to the field $\mathbf{E}_0$, acts as a potential V^*. The resulting average force, $-\nabla V^*$, tends to confine the particle close to the nodes of the wave, where the motion is a harmonic oscillation with a frequency $\omega = qE_0/mc$.

A slightly different example is a standing wave with plane polarization. Here the trajectories close to the nodes obey the Mathieu equation. For the more general case, where $\mathbf{E}_0$ is some arbitrary but smoothly varying function of $\mathbf{r}$, for example, a laser beam with a realistic spatial profile, an approximate solution, called the guiding center theory, has been derived (Motz and Watson, 1967). The main result is that the smooth guiding center motion can be derived from a *quasipotential*, which is identical to the previously mentioned potential V^*. An early derivation of this quasipotential, which is also called the *ponderomotive potential*, the *pseudopotential*, or the *effective potential*, was given by Kapitza (1951) within the framework of classical mechanics. A comprehensive description of his treatment can be found in the textbook by Landau and Lifshitz (1960).

Other interesting contributions to the subject of this chapter were inspired by the goal to contain a nuclear fusion reaction by using rf confinement to isolate the plasma from the material walls of an apparatus. This was first proposed in the 1950s and discussed by several authors (Linhard, 1960; Weibel, 1959), and a comprehensive review has been given by Motz and Watson (1967). An important result from these studies is that one can create *two-* and *three-dimensional potential wells* with oscillatory fields, provided that certain stability conditions (see following discussion) are fulfilled. For the confinement of both electrons and ions in a neutral plasma, it has been recognized that the effective potential is proportional to q^2, that is, V^* is independent of the sign of the charge. It has also been proposed to make use of superimposed fields at different frequencies for simultaneous compression of electrons and ions as well as to cause plasma heating (Gapanov and Miller, 1958).

Orbits of electrons in the field of a cylindrical wave guide have been studied by Weibel (1959) and Weibel and Clark (1961) in the microwave

region. As in the previous examples, the fields were treated as standing electromagnetic fields, and it was shown that particles can be bound to the nodal points, lines, or surfaces of these fields. The problem was again treated in a first-order approximation, taking just the time-averaged influence of the oscillating field. As an important contribution to the development of the theory, several conditions were studied under which the orbits remain bound for all times, and the criteria were tested by numerical integration of the equation of motion. The resulting stability condition [Eq. (3) in Weibel and Clark (1961)] is very similar to that which we are using (Gerlich, 1986; Teloy and Gerlich, 1974) (see Section II B 3).

More theoretical work related to this chapter was inspired by techniques and theories developed for high-energy particle accelerators. It was demonstrated in 1952 (Courant, 1952) that a series of quadrupole fields alternating in space can confine fast beams of protons. This strong-focusing alternating-gradient principle stimulated the invention and development of a new dynamic mass spectrometer by Paul and coworkers (Paul and Raether, 1955; Paul and Steinwedel, 1953; Paul et al. 1958), the well-known quadrupole mass filter. In this instrument, the spatial periodicity is replaced by quasistationary fields, which alternate in time, leading, under suitable conditions, to a focusing force for low-energy ions.

The principle of operation of quadrupoles, including the three-dimensional Paul trap (Fissher, 1959; Wuerker et al., 1959a), is well understood. Many details of the theory have been discussed in the literature, which, in turn, has been reviewed in several comprehensive monographs (Dawson, 1976; Dawson and Whetten, 1971; March and Hughes, 1989). It must, however, be emphasized that oscillating quadrupole fields occupy a very special place among all other field geometries. They are unique because the equation of motion describing the ion trajectory can be reduced to a set of *decoupled, one-dimensional* differential equations of the Mathieu type. Making use of the properties of their solutions, it is easy to see that the stability of a trajectory depends only on two dimensionless parameters and not on the initial conditions of the ion.

Some theoretical aspects that explore possible applications of higher-order multipole fields, for example, hexapoles, octopoles, or other field geometries, have been discussed by several authors. One of the earliest related proposals is due to Gaponov and Miller (Gaponov and Miller, 1958; Miller, 1958a, 1958b), who also investigated the nonrelativistic motion of charged particles in oscillatory electromagnetic fields. Using the high-frequency approximation, they derived the previously-mentioned effective potential and came to the conclusion that, under suitable conditions, such fields can be used to reflect charged particles from potential barriers or to squeeze and confine charges in bounded regions of space. For creating appropriate potential wells they

proposed the use of two- and three-dimensional quasielectrostatic multipole fields.

Related ideas and suggestions were developed independently by Teloy (Bahr et al., 1969, 1970; Teloy and Gerlich, 1974) who also initiated the construction of various rf devices (see Sections III and IV) and gave many impulses to the work presented in this chapter. He has made contributions to the further development of the theory by generalizing the adiabatic approximation. In his treatment (Kohls, 1974; Teloy, 1980) the solutions of the equation of motion are expanded simultaneously in a power series in terms of $1/\Omega$ (the rf frequency) and a Fourier series in time. This theory allows the determination of higher-order correction terms for both the ion trajectories and the effective potential.

Dawson and Whetten (1971) have briefly prospected possible applications of higher-order multipole fields, trying to extend or generalize the quadrupole mass filter principle. They pointed out that, unlike the special case of the Mathieu equation, the equations describing the motion become *nonlinear coupled* differential equations, and that the stability of the ion motion depends strongly on the initial conditions (position, velocity, and rf phase). Fundamentals of ion motion in rf multipole fields have been treated by Friedman et al. (1982), as a "tutorial for mass spectrometrists and ion physicists." A similar textbook level presentation of the equation of motion and the solution of the Laplace equation has been published by Szabo (1986). In a series of papers, Hägg and Szabo (1986a, 1986b, 1986c) have tried to characterize the solutions of these differential equations based exclusively on the analysis of numerical simulations. They concluded that an overall classification of higher-order multipole fields within their proposed generalization of the quadrupole stability diagram is not possible. Unfortunately, these authors did not consider the adiabatic approximation, although those of their conclusions that have some general validity can be explained within this approximation. More details will be discussed in Section III D 3.

There are other theoretical aspects of rf containment of charged particles that have been treated in the literature. One example is the combination of an rf field with a magnetostatic field (Motz and Watson, 1967). A second is the inclusion of space charge, which can cause significant perturbations. This problem has been dealt with using many different theoretical approaches. Other perturbations through collisions or impairment by geometrical distortions have also been discussed. These problems have been treated in detail for the Paul ion trap, and a summary is given in the recent comprehensive review by March and Hughes (1989). Some of the developed analytical methods and conclusions make use of the linearity of the equation of motion and are therefore only valid for quadrupoles, while others could be extended to general rf devices.

Finally, and especially worthwhile mentioning, is a recent treatment of the motion of a particle in a high-frequency time-dependent potential by Cook et al. (1985). They have shown that the high-frequency approximation of the exact Schrödinger equation is identical with a Schrödinger equation that is based on the classically derived effective potential. These solutions are important for the quantum-mechanical description of very slow ions and ion crystals, prepared by laser cooling in rf fields (Diedrich et al., 1989; Neuhauser et al., 1978; Wineland and Dehmelt, 1975).

B. The Adiabatic Approximation

1. *The Equation of Motion*

Consider a particle of charge q and mass m moving in an external electromagnetic field $\mathbf{E}(\mathbf{r}, t)$ and $\mathbf{B}(\mathbf{r}, t)$. In the nonrelativistic regime, the classical equation of motion is (Gapanov and Miller, 1958; Motz and Watson, 1967)

$$m\ddot{\mathbf{r}} = q\mathbf{E}(\mathbf{r}, t) + q\dot{\mathbf{r}} \times \mathbf{B}(\mathbf{r}, t). \tag{2}$$

It has been mentioned in Section II A that this equation can be solved analytically only for special field geometries (Motz and Watson, 1967; Eberly, 1969). Here, we simplify this equation and derive an approximate but general solution. We begin by making use of the fact that most of the applications described in this chapter deal with weak electric fields and heavy particles with low kinetic energies (in contrast to electrons in intense laser fields). This means that the velocity $\dot{\mathbf{r}}$ is very small in comparison to the velocity of light, and, as a result, the weak force exerted by the magnetic field can be disregarded. Quasistationary magnetic fields are not discussed, since they are excluded so far in our experiments.

In addition, we assume that the quasistationary electric field $\mathbf{E}(\mathbf{r}, t)$ is composed of a static field, $\mathbf{E}_s(\mathbf{r})$, and a time-dependent part, $\mathbf{E}_0(\mathbf{r})\cos(\Omega t + \delta)$, where $\mathbf{E}_0(\mathbf{r})$ is the field amplitude, $\Omega = 2\pi f$ is a fixed angular frequency, and δ is a phase. The motion is then described by the differential equation

$$m\ddot{\mathbf{r}} = q\mathbf{E}_0(\mathbf{r})\cos(\Omega t + \delta) + q\mathbf{E}_s(\mathbf{r}). \tag{3}$$

The following derivation is easier to survey if, for the moment, we set the static field $\mathbf{E}_s(\mathbf{r})$ equal to zero and eliminate the phase δ by a shift in the time origin.

For illustrative purposes, we first solve this differential equation for the simple case of a charge q in the rf field of a parallel plate capacitor, as depicted in Fig. 1*a*. In this case, the field $\mathbf{E}_0$ is *homogeneous*, that is, independent of $\mathbf{r}$, and Eq. (3) can be solved directly. The special solution

$$\mathbf{r}(t) = \mathbf{r}(0) - \mathbf{a}\cos(\Omega t) \tag{4}$$

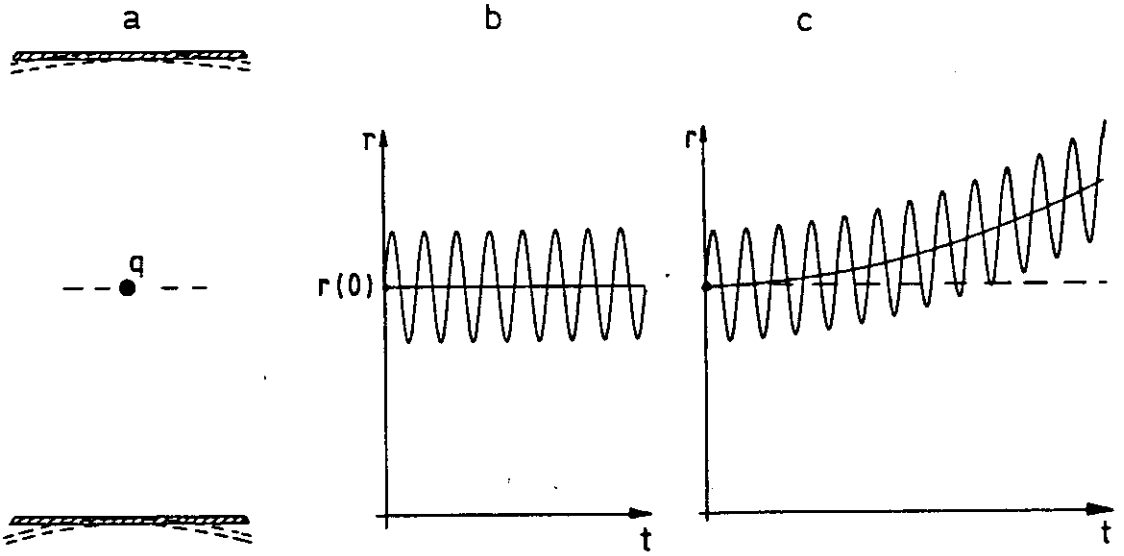

Figure 1. Motion of a charge q in an oscillatory electric field. (*a*) Schematic indication of the electrodes. For the parallel plate capacitor, the field is homogeneous; bending of the electrodes (dashed lines) results in an inhomogeneous field. (*b*) In the homogeneous field, the particle oscillates as a function of time with constant amplitude and without changing its mean position $\mathbf{r}(0)$. (*c*) The inhomogeneity of the field causes as additional slow drift motion toward the weaker field region.

can be verified immediately by inserting it into Eq. (3), and one obtains for the amplitude vector $\mathbf{a}$ the relation

$$\mathbf{a} = q\mathbf{E}_0/m\Omega^2. \tag{5}$$

This solution is plotted in Fig. 1*b* as a function of time. On average, the particle remains stationary at $\mathbf{r}(0)$, but it oscillates with an amplitude that is proportional to the field amplitude and inversely proportional to mass and to the square of the frequency.

The situation changes if the field becomes *inhomogeneous*. This is indicated in Fig. 1*a* by the dashed lines, in which the parallel plates are bent or replaced by a large-radius cylindrical capacitor. In general, the differential equation, Eq. (3), can no longer be solved analytically and the often complicated orbits of the particle can only be determined by numerical integration. However, in the present example, the field is only weakly inhomogeneous and the resulting trajectory, plotted in Fig. 1*c*, deviates only slightly from the homogeneous case. The amplitude is almost the same; however, the charge now experiences a varying field strength during its oscillatory motion, resulting in several modifications, the most important being a seeming force that causes the slow drift toward the outer electrode.

The goal of the following section is to make use of these observations to derive an approximate analytical solution of Eq. (3), and then to determine some general properties of the motion of a charge in an oscillatory field.

Related ideas and theories presented in the literature have already been reviewed in Section II A. For the purpose of the present chapter, it is sufficient to summarize the first-order results of the *adiabatic approximation* following essentially the derivations given by Dehmelt (1967), Eberly (1969), and Teloy and Gerlich (1974). A more fundamental discussion of the importance of adiabatic invariants and approximate integration methods can be found in the modern literature on the mathematical treatment of nonlinear dynamical systems (Arnold, 1988; Lichtenberg and Lieberman, 1983).

2. *The Effective Potential*

To describe the motion in an inhomogeneous rf field, we assume that the field varies smoothly as a function of the coordinate $\mathbf{r}$, and that the frequency is high enough to keep the amplitude $\mathbf{a}$ in Eq. (5) small. These assumptions will be elaborated in Section II B 3. It can be expected that along the slow drift motion, as visualized in Fig. 1*c*, the amplitude $\mathbf{a}(t)$ and phase of the oscillatory motion vary slowly with time. We therefore seek a solution of Eq. (3) by superimposing a smooth drift term $\mathbf{R}_0(t)$ and a rapidly oscillating motion $\mathbf{R}_1(t)$:

$$\mathbf{r}(t) = \mathbf{R}_0(t) + \mathbf{R}_1(t), \tag{6}$$

with

$$\mathbf{R}_1(t) = -\mathbf{a}(t)\cos\Omega t. \tag{7}$$

We presume that slow spatial variation of $\mathbf{E}_0$ allows us to keep only the first two terms in the expansion

$$\mathbf{E}_0(\mathbf{R}_0 - \mathbf{a}\cos\Omega t) = \mathbf{E}_0(\mathbf{R}_0) - (\mathbf{a}\cdot\nabla)\mathbf{E}_0(\mathbf{R}_0)\cos\Omega t + \cdots, \tag{8}$$

and furthermore, that the slow time variation of $\mathbf{a}$ and $\mathbf{R}_0$ implies $\dot{\mathbf{a}} \ll \Omega\mathbf{a}$ and $\ddot{\mathbf{R}}_0 \ll \Omega\dot{\mathbf{R}}_0$. Substituting Eq. (6) and Eq. (8) into Eq. (3), and neglecting the small time derivatives, leads to an equation of the form

$$m\ddot{\mathbf{R}}_0 + m\Omega^2\mathbf{a}(t)\cos\Omega t = q\mathbf{E}_0(\mathbf{R}_0)\cos\Omega t - q[\mathbf{a}(t)\cdot\nabla]\mathbf{E}_0(\mathbf{R}_0)\cos^2\Omega t. \tag{9}$$

Assuming that the amplitude $\mathbf{a}$ changes in time only due to the motion along $\mathbf{R}_0$, we can replace $\mathbf{a}(t)$ with $\mathbf{a}(\mathbf{R}_0)$ using Eq. (5). In this way the amplitude factors of the two $\cos\Omega t$ terms in Eq. (9) become identical and cancel. To simplify the remaining equation we use the vector analysis relation

$$(\mathbf{E}_0\cdot\nabla)\mathbf{E}_0 = \tfrac{1}{2}\nabla\mathbf{E}_0^2 - \mathbf{E}_0\times(\nabla\times\mathbf{E}_0) = \tfrac{1}{2}\nabla E_0^2, \tag{10}$$

because the rotation of $\mathbf{E}_0$ vanishes ($\nabla\times\mathbf{E}_0 = 0$) for quasistatic field condi-

tions. Finally, replacing $\cos^2 \Omega t$ by its time averaged value $\frac{1}{2}$ leads to a differential equation for the nonoscillating motion $\mathbf{R}_0(t)$:

$$m\ddot{\mathbf{R}}_0 = -\frac{q^2}{4m\Omega^2}\nabla E_0^2. \tag{11}$$

This equation of motion shows the time-averaged effect of the oscillatory field. The charged particle experiences a force caused by the inhomogeneity of the field, the so-called *field gradient force.* This force is proportional to the square of the charge q, that is, independent of the sign, is mass dependent, and is inversely proportional to the square of the frequency Ω. The direction and the strength is determined by the gradient of E_0^2. Charged particles are always pushed into regions of weaker fields, as we have already seen in Fig. 1.

Now, if we account anew for the electrostatic force $q\mathbf{E}_s(\mathbf{r})$ in Eq. (3) and write the electrostatic field $\mathbf{E}_s$ as the negative gradient of the electrostatic potential Φ_s, that is,

$$\mathbf{E}_s = -\nabla\Phi_s, \tag{12}$$

the total average force acting on the ion can be derived from a time-independent *mechanical potential* V^*

$$V^*(\mathbf{R}_0) = q^2E_0^2/4m\Omega^2 + q\Phi_s. \tag{13}$$

With this definition the equation of motion describing the smooth trajectory becomes simply

$$m\ddot{\mathbf{R}}_0 = -\nabla V^*(\mathbf{R}_0). \tag{14}$$

We shall subsequently refer to V^* as the *effective potential* (Eberly, 1969; Landau and Lifschitz, 1960). Other authors have designated V^* as the high-frequency potential (Gapanov and Miller, 1958; Miller, 1958a, 1958b), the quasipotential (Motz and Watson, 1967), or the pseudopotential (Dehmelt, 1967).

For most of our applications, this approximation allows a satisfying characterization of the properties of arbitrary field geometries based on the effective potential given in Eq. (13). Also, the important features of the resulting motion can be predicted easily. According to Eq. (6), $\mathbf{r}(t)$ is composed of only two terms, the smooth motion $\mathbf{R}_0(t)$ (also called the guiding center or secular motion) and the fast oscillating term $\mathbf{R}_1(t)$ (wiggling motion).

In order to determine the trajectory $\mathbf{R}_0(t)$ from Eq. (14), it is indeed necessary to solve a differential equation. However, this equation is much

easier to discuss and to solve than the original one given in Eq. (3), since it does not contain time explicitly. The slowly varying amplitude of the superimposed sinusoidal oscillation is directly determined from Eq. (7) and Eq. (5) by inserting $\mathbf{E}_0(\mathbf{R}_0)$,

$$\mathbf{R}_1(t) = -q\mathbf{E}_0(\mathbf{R}_0)/m\Omega^2 \cos \Omega t. \tag{15}$$

Additional microoscillations and higher-frequency components, which can be seen in a Fourier analysis of the numerically exact trajectories, are corrections in higher order and are therefore neglected here. The resulting smooth motion is independent of the starting phase [see, for example, Fig. 4 of Teloy and Gerlich (1974)], provided that the trajectory starts in a sufficiently weak field region. Otherwise, the initial phase may influence the kinetic energy, as will be discussed in further detail in Sections II D and III C.

It has also been shown [see, for example, Motz and Watson (1967)] that the effective potential can be derived directly from Eq. (2) under inclusion of the magnetic part of an electromagnetic field, leading essentially to the same result given in Eq. (13). However, comparison of the velocity amplitude, $q\mathbf{E}_0/m\Omega$, obtained from Eq. (15), with the speed of light, shows quantitatively that the influence of the magnetic field and relativistic corrections can usually be disregarded, except for electrons in very strong fields.

The first integral of Eq. (14),

$$\tfrac{1}{2}m\dot{\mathbf{R}}_0^2 + q^2E_0^2/4m\Omega^2 + q\Phi_s = E_m, \tag{16}$$

demonstrates that the total energy E_m is a constant of the ion motion, or more precisely, an adiabatic constant of the motion. This equation expresses that kinetic energy of the smooth motion can be transferred into effective potential energy or electrostatic potential energy. It is easy to prove, using the time derivative of $\mathbf{R}_1(t)$ given in Eq. (15), that the second term of Eq. (16) is identical to the time-averaged kinetic energy of the oscillatory motion

$$\langle \tfrac{1}{2}m\dot{\mathbf{R}}_1^2 \rangle = q^2E_0^2/4m\Omega^2. \tag{17}$$

This proves that the so-called effective potential energy V^* is actually stored as kinetic energy in the fast oscillatory motion. Therefore, motion through an inhomogeneous field leads to a permanent exchange between three different forms of energy, the kinetic energies, $\frac{1}{2}m\dot{\mathbf{R}}_0^2$ and $\frac{1}{2}m\dot{\mathbf{R}}_1^2$, and the electrostatic potential energy $q\Phi_s$. For some calculations it is useful to express the momentary kinetic energy of the oscillatory motion using the effective potential V^*

$$\tfrac{1}{2}m\dot{\mathbf{R}}_1^2 = 2V^* \sin^2 \Omega t. \tag{18}$$

More details on the different forms of energy will be discussed in Section II E 1.

Some of the results obtained thus far are illustrated in Fig. 2, which depicts the motion of a charge in a cylindrical capacitor. The electrodes are sketched in the upper panel, where the applied voltage is $U_0 - V_0 \cos \Omega t$. The effective potential, defined in Eq. (13), can be calculated from the well-known electrostatic potential [see Eq. (33)]. Three results of $V^*(r)$ are plotted in the middle panel, each obtained for a different value of the dc voltage U_0, and all normalized to $V^*(r_0) = 0$. These potentials have minima, since the field gradient force always pushes the charge toward larger radii, independent of the sign of the charge, but it is counterbalanced by the electrostatic force, provided the sign of the dc voltage has been properly chosen in accordance with the sign of the charge. If an ion starts at the marked position (+), for simplicity with zero initial velocity and with phase $\delta = 0$ (e.g., created by photoionization), the trajectory depends on the applied dc voltage U_0, as can be seen in the lowest panel. The three resulting trajectories are easy to understand within the effective potential approximation. Different dc voltages correspond to different potential energies at the starting point (+) and therefore to different total energies E_m. These energies are indicated by the three dashed lines in the middle panel, and they determine the amplitudes of the pertinent secular motion. The amplitude of the wiggling motion is unaffected, since it depends only on the rf field, which is the same for all three cases.

A second example that illustrates the results of this section is the ion motion in an rf quadrupole. It is well known from earlier theoretical treatments (Dehmelt, 1967; Fischer, 1959) as well from an early experiment (Wuerker et al., 1959a) that, under certain conditions, the effective potential approximation can be used to clarify some of the features and working principles of quadrupoles. Although the motion of ions is fully described by the theory of the Mathieu equation and the well-known (a_2, q_2) stability diagram (Dawson and Whetten, 1971; March and Hughes, 1989), significant simplifications can be obtained for $q_2 \leqslant 0.4$ (to avoid confusion with the charge q, and to extend to higher-order multipoles, we use q_n to signify a $2n$-pole). Figure 3*a* depicts several ion trajectories for $q_2 = 0.1$. If a_2 is chosen such that $a_2 = \frac{1}{2}q_2^2$, that is, just on the border of the stability diagram, the smooth trajectory is a straight-lined steady motion. As will be demonstrated in Section II D, the effective potential V^* is equal to $\frac{1}{2}q_2^2 - a_2$, and therefore zero in this case. It can be seen from the growth of the amplitude of the wiggling motion that the electrostatic potential energy is completely converted into oscillatory motion. Increasing a_2 above $\frac{1}{2}q_2^2$ results in a net acceleration of the secular motion ($\frac{1}{2}m\dot{\mathbf{R}}_0^2$ increases), leading to the curved trajectories. Nonetheless, in this case, the total energy $\mathbf{E}_m$, as defined in

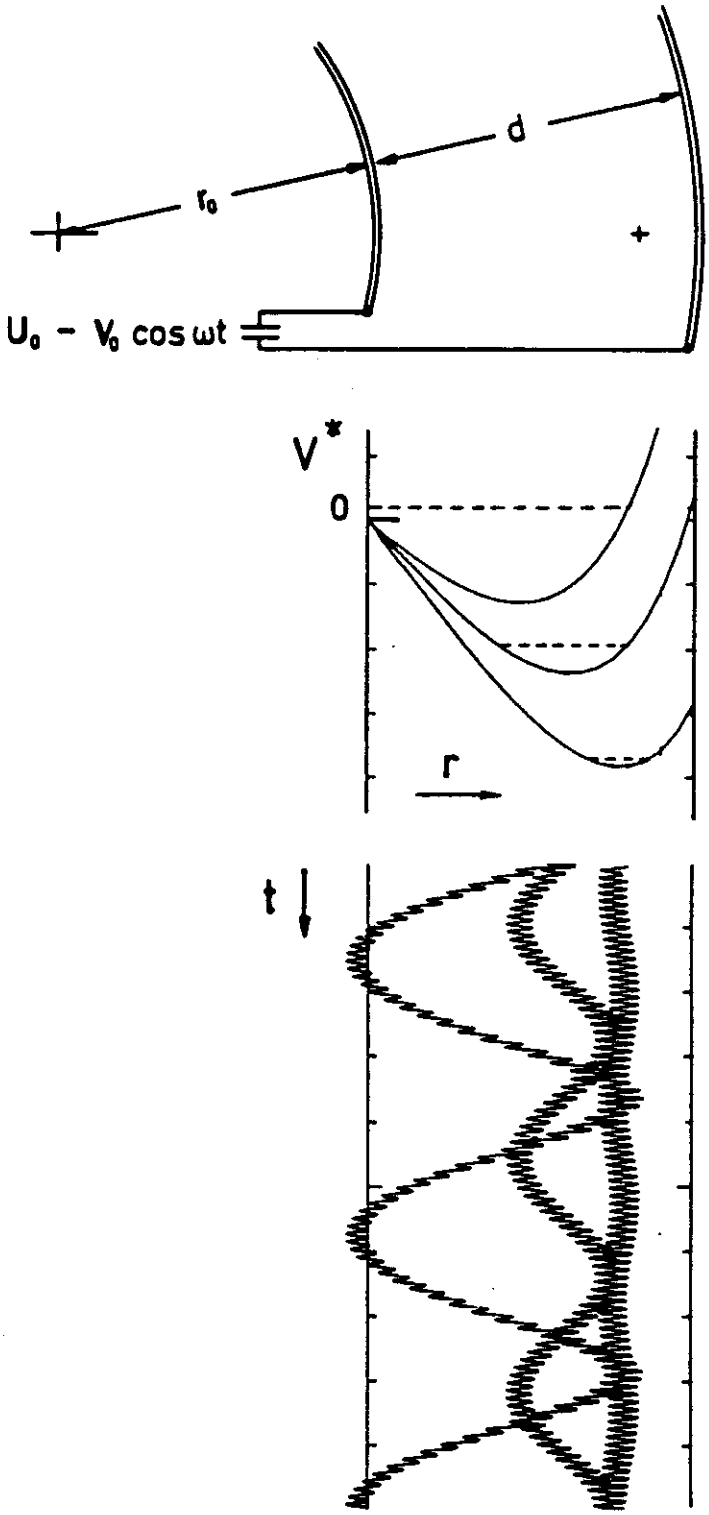

Figure 2. Motion of a charge in the oscillatory electric field of a cylindrical capacitor with different superimposed dc voltages. The upper panel sketches the geometry and the (+) marks the position where the ion is started with zero initial energy. The middle panel shows effective potentials V^* for three different dc voltages U_0, each leading to a different trajectory, plotted in the lower panel as a function of time. The dashed lines in the potential curves mark the respective total energies.

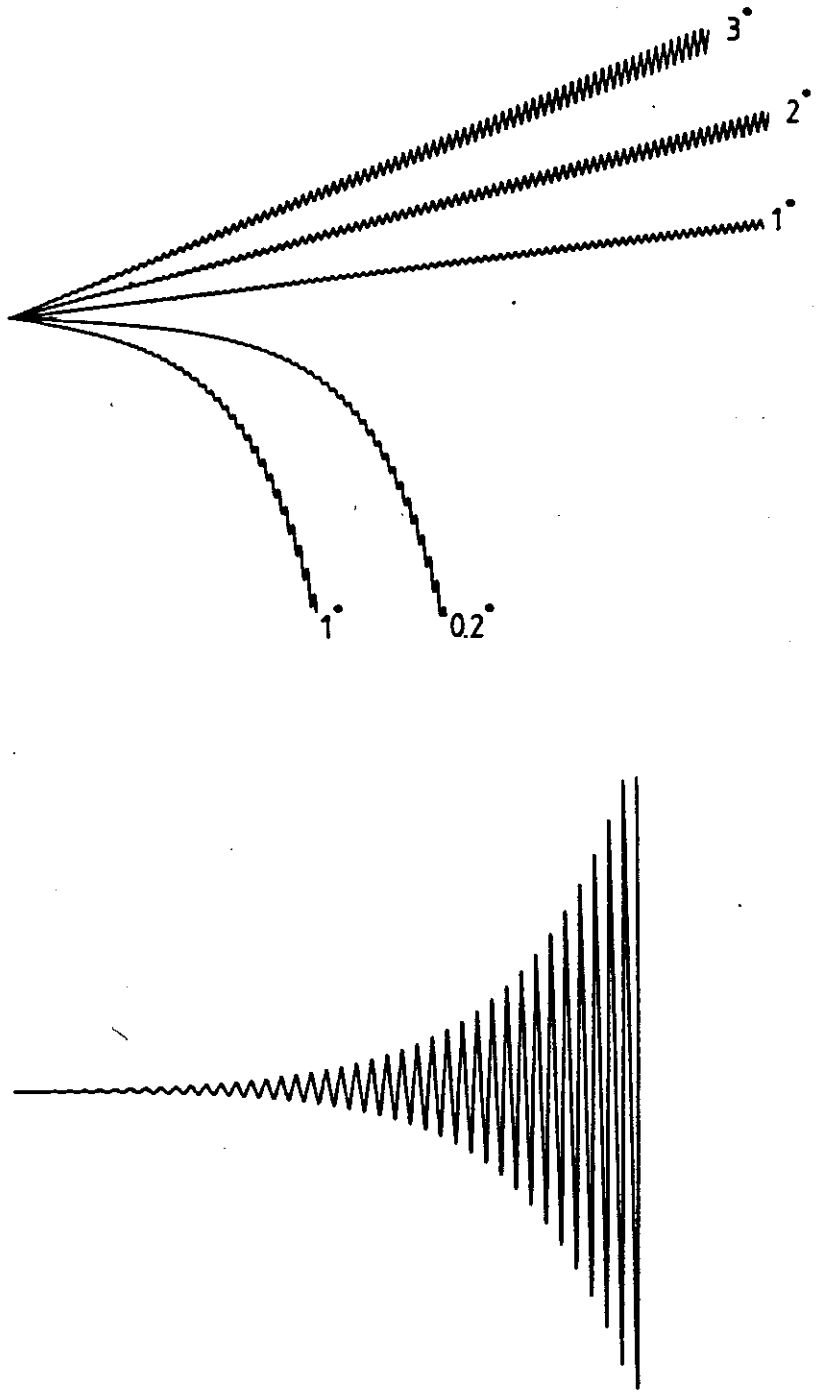

Figure 3. Illustration of unstable trajectories with different starting angles in a quadrupole for several (a_z, q_z) values (see text). In the upper panel the adiabatic approximation is valid ($q_z = 0.1$); however, the effective potential is too weak to confine the ions. In the lower panel, the operating point $(a_z, q_z) = (0.2, 0.739)$ is outside of the stability triangle leading to an instability due to resonant energy build up.

Eq. (16), is an adiabatic constant of the motion and the loss of the ion is only due to the acceleration in the electrostatic field. Bound trajectories in a quadrupole will be discussed in Section III B (see Fig. 25). The situation in Fig. 3*b* is completely different, as will be seen subsequently.

3. *Adiabaticity*

The derivation presented in the preceding section leads to the important result that the average total energy is an adiabatic constant of the ion motion. This result is based on assumptions that allow one to separate the trajectories into fast and slowly varying terms. The range of validity of these assumptions will be further discussed and specified in this section. In general, a mechanical system, as described by Eq. (3), is not conservative, and it is conceivable that under certain conditions the oscillating force can continuously augment the energy of the particle and cause nonadiabatic behavior or instability.

Such a situation is illustrated in the lower part of Fig. 3, which depicts an unstable ion trajectory in a quadrupole mass filter. Here, the point of operation is $(a_2, q_2) = (0.2, 0.739)$, and therefore outside of the previously cited condition $q_2 < 0.4$. The effective potential approximation is no longer applicable. Indeed, this point is already past the right border of the lowest range of the stability diagram (for details see Section III B and Fig. 24). The result is a continuous augmentation of the kinetic energy, as indicated in the figure by the increase in the amplitude of the secular motion.

This example illustrates the well-known fact that for an ideal quadrupole (infinite length, etc.), the mathematical definition of stability can become equivalent to practical prescriptions of stability, which must be based on ion transmission or similar experimental requirements. Unfortunately, the simple (a_2, q_2) stability criterion *cannot be extended* or generalized to field geometries where the differential equations describing the motion are nonlinear and coupled. Related attempts (Dawson and Whetten, 1971; Friedman et al., 1982; Szabo, 1986) (see also Section II D3) to characterize the complete family of multipole fields were therefore unsuccessful. Also, according to our knowledge, no general mathematical criterion has been applied so far to rigorously characterize stable and unstable solutions from Eq. (3). Therefore, we have divided the following discussion into two parts. We search first for conditions for *adiabaticity*, and, in the following section, we discuss *stability*, briefly from a mathematical point of view but as motivated primarily from practical applications.

The range of validity of the effective potential approximation has been discussed in several publications, as indicated in Section II A. Typically, these approximations require a high frequency and other changes in time to be slow, that is, behave adiabatically. To quantify comparisons of *slow* and *fast*, such as $\dot{\mathbf{a}} \ll \Omega \mathbf{a}$ and $\ddot{\mathbf{R}}_0 \ll \Omega \dot{\mathbf{R}}_0$, it is common to introduce a dimensionless ratio that compares two characteristic features. For quasiperiodic motions, such as shown in Fig. 2, the frequency of the secular motion ω must be slow relative to the rf frequency, that is, ω/Ω must be small. Another possibility is to compare the maximum velocity acquired during one cycle with the unperturbed velocity. More complicated constructions have also been

mentioned, for example $L|\nabla E|/E$, where L was designated as a characteristic length (Gapanov and Miller, 1958).

Our definition of such a characteristic parameter is motivated from Eq. (8). There, in deriving the adiabatic approximation, we assumed a smooth spatial variation of the electric field to justify keeping only the first two terms in the Taylor expansion of $\mathbf{E}_0$. We therefore demand that over the full distance of the oscillation, that is, over $2\mathbf{a}$, the change of the field be much smaller than the field itself

$$|2(\mathbf{a}\nabla)\mathbf{E}_0| < |\mathbf{E}_0|. \tag{19}$$

This basic requirement has already been imposed by Weibel and Clark (1961) for predicting safe confinement of charged particles in effective potential wells. Using this relation, we define (Teloy and Gerlich, 1974) our characteristic parameter η as

$$\eta = |2(\mathbf{a}\nabla)\mathbf{E}_0|/|\mathbf{E}_0|. \tag{20}$$

Inserting $\mathbf{a}$ from Eq. (5) and making use of the vector analytical identities given in Eq. (10), we obtain the definition of the *adiabaticity parameter* η in its final form

$$\eta = 2q|\nabla E_0|/m\Omega^2. \tag{21}$$

For a given mass, frequency, and charge, the parameter η depends only on the inhomogeneity of the field $\mathbf{E}_0$. For $|\nabla E_0| = 0$, we obtain the homogeneous field treated in Section II B, and the exact solution given in Eq. (4). The condition $\nabla E_0 = \text{const}$ leads to quadrupole fields, and, as will be seen in Section II D, in this case η is identical with the conventional stability parameter q_2. In general, $|\nabla E_0|$ is a function of the space coordinate $\mathbf{r}$, and as such the scalar field $\eta(\mathbf{r})$ must be known, at least along each individual ion trajectory, in order to check whether the adiabaticity parameter remains sufficiently small.

Before pursuing this idea further, it is necessary to find a generally applicable procedure to specify the maximum tolerable limit of the adiabaticity parameter, designated as η_m. Although the mathematical treatment of nonlinear mechanics is a rapidly growing field (Arnold, 1988; Lichtenberg and Lieberman, 1983), we have not yet found a general analytical means of determining η_m within the framework of the adiabatic theory. Based on the previous derivation of η and Eq. (19), we can only conclude that η_m must be smaller than 1. Therefore, we describe briefly in the following a few heuristic criteria and numerical methods for testing adiabaticity, and provide a few illustrative examples that support the already reported empirical result

(Gerlich, 1986; Teloy and Gerlich, 1974), that $\eta_m = 0.3$ guarantees adiabaticity for most practical applications. This limit has proven to be *sufficient* according to all of our numerical simulations and experimental observations. It is also in agreement with the restriction $\eta = q_2 < 0.4$, generally accepted for describing quadrupole fields using the effective potential (Dehmelt, 1967; Fischer, 1959; Wuerker et al., 1959a and b).

For lack of a rigorous mathematical characterization of the solutions from Eq. (3), we have determined η_m, the limiting value for safe application of the first-order adiabatic approximation, by computer simulation, that is, by numerically integrating Eq. (3). Of course it is not surprising that the fine details of limits determined this way are conditional on the specific criterion used to test the quality of the adiabatic approximation, and that the results depend as well on the field geometry and even on the initial conditions of individual trajectories. One of the simplest operational criteria to characterize adiabaticity in an arbitrary field geometry is to calculate the adiabaticity parameter $\eta(r)$ along a set of representative trajectories. This set of data is reduced by defining for each trajectory a series of numbers, η_{m_i}, using

$$\eta_{m_i} = \max_{t \in T_i} [\eta(\mathbf{r}(t))]. \tag{22}$$

The η_{m_i} values must be determined during consecutive time intervals T_i, which should be large enough that several local maxima of $\eta(r)$ are included. Since we are usually interested in stable confinement of ions in two- or three-dimensional effective potential wells, these maxima occur at the turning points of the trajectories. We have performed such calculations for different multipole fields and the ring electrode arrangement, and have found an empirical rule, that all values of η_{m_i} agree with each other within less than 1% if they are below 0.3. Therefore, such trajectories can be terminated if the first few values of η_{m_i} are below 0.3, leading to a significant saving of computer time. If the sequence of η_{m_i} lies between 0.3 and 0.5, the values fluctuate, typically by several percent. Above 0.5, a fast increase of η_{m_i} is often observed, which can be used as a typical indication of nonadiabaticity. Based on such observations, we can define η_m and formulate our rule for *safe operation* within the *validity of the adiabatic approximation* as

$$\eta_m = \max [\eta_{m_i}] = 0.3. \tag{23}$$

Another criterion for testing the quality of the adiabatic approximation is to check whether the mean kinetic energy of the ion is conserved within a given limit. This criterion is the most important for our experimental applications. However, as we have already seen in the last section, the momentary kinetic energy fluctuates, and it is not straightforward to define

a numerical procedure for determing the adiabatic total energy E_m, as defined in Eq. (16). Related details will be discussed in Section II E. The problem is significantly simplified if one studies special trajectories, that is, those that pass periodically through a field-free region, since in this region their kinetic energy is well defined. Such a case is the oscillation of an ion along a symmetry axis of an octopole. We have performed one-dimentional trajectory calculations along such a line [$\varphi = 0$, that is, crossing a pole; see Eq. (39)]. The ions were started in the middle along the symmetry axis, the phase δ [Eq. (3)] was held fixed at zero, and the only remaining free initial condition was the starting velocity. Variation of the phase leads to insignificant changes in the results. Each trajectory was followed over 5000 rf periods, and each time it crossed the center its velocity was interrogated. The maximum of the relative changes, $\Delta v/v$, is plotted in Fig. 4 as a function of the nominal

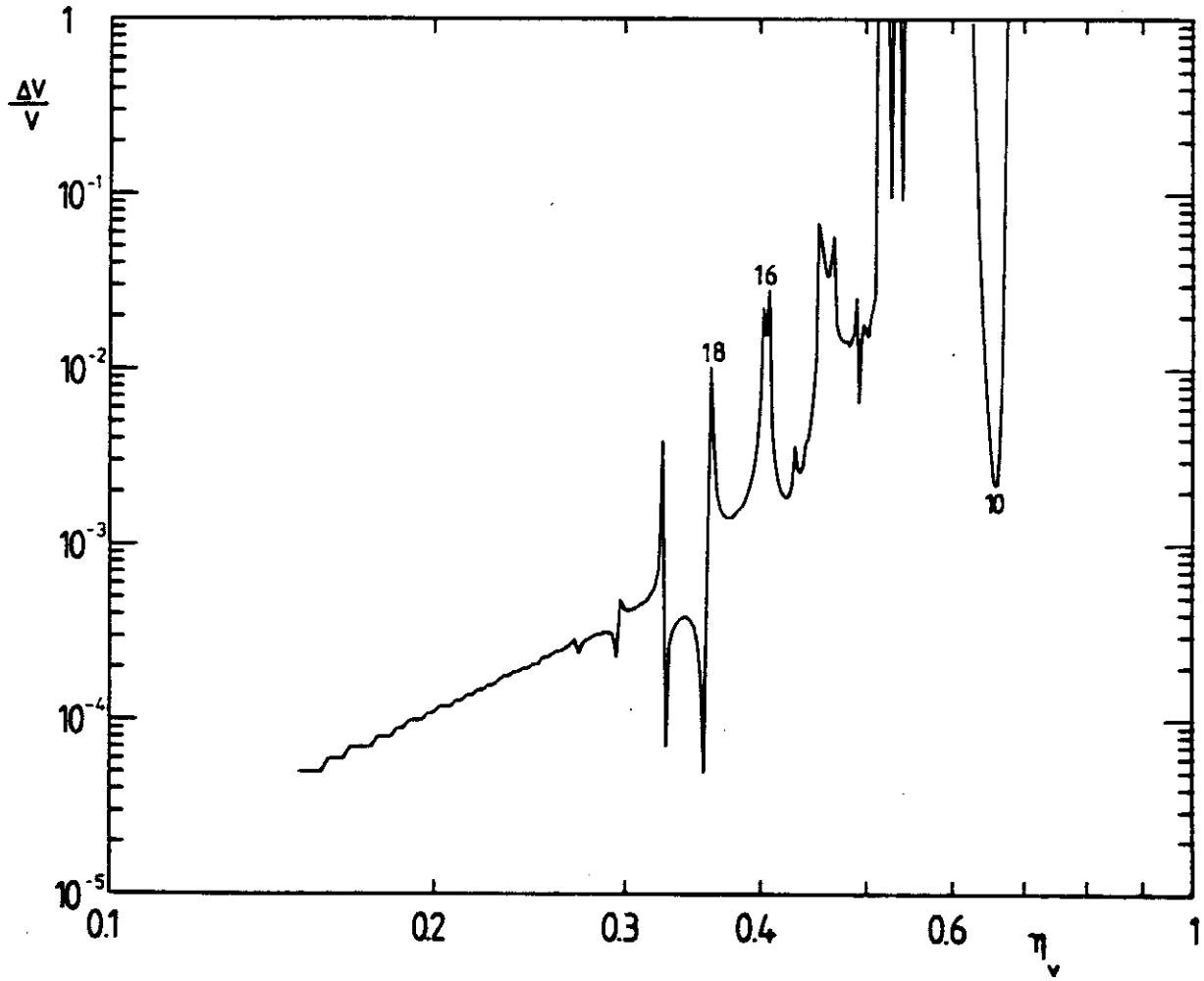

Figure 4. Maximum relative velocity change $\Delta v/v$ as a function of the nominal stability parameter η_v determined over 5000 rf periods. The difinition of η_v is given in Eq. (24). Details of the underlying one-dimensional motion along a symmetry line of an octopole are described in the text. The numbers on the peaks refer to the ratio of the rf frequency to the frequency of the secular motion. The stable region around $\eta_v = 0.65$ is in the vicinity of the special periodic orbit with $\Omega/\omega = 10$.

v-dependent adiabaticity parameter η_v in the turning point given by

$$\eta_v = 8^{1/2}(n-1)v/\Omega r_0. \tag{24}$$

This can be derived from Eq. (52) and Eq. (54), see Section II D, by setting $E_m = \frac{1}{2}mv^2$, $L = 0$, $\hat{r}_m = 1$, and eliminating V_0.

Although only a special class of trajectories has been selected in this example, the results demonstrate some interesting features. Below $\eta_v = 0.3$, $\Delta v/v$ is smaller than 10^{-3} and varies as a smooth function of η_v. Between 0.3 and 0.5, the change in ion velocity remains limited; however, the fluctuations of $\Delta v/v$ become larger. Above $\eta_v = 0.5$ there is a dramatic increase in the velocity, except for a few regions of stability. The connection of these regions with periodic orbits will be discussed subsequently. The most important conclusion to be drawn from Fig. 4 is the almost perfect conservation of energy below $\eta_v = 0.3$, that is, the fluctuations $(\Delta v/v)^2$ are smaller than 10^{-6}. This again supports our requirement of $\eta_m = 0.3$ for safe application of the adiabatic approximation. We wish to anticipate for our discussion in Section II E that the rf impairment of the ion energy is completely negligible in comparison to perturbations caused by collisions.

A very restrictive criterion for testing the quality of the adiabatic approximation can be formulated by measuring the deviation of the first-order approximation, $\mathbf{R}_0(t) + \mathbf{R}_1(t)$, from the exact solution, $\mathbf{r}(t)$, during one reflection from an rf wall. Typically, excellent agreement can be obtained for $\eta < 0.1$. A related comparison, analyzing the approximate and the exact energy, will be discussed in Section II E (Fig. 19). Other tests of the validity of the adiabatic approximation are based, for example, on the analysis of the Fourier components of the motion $\mathbf{r}(t)$, or on the conservation of orbital angular momentum for rotationally symmetric effective potentials, as in the case of multipole fields (see Section II D).

To summarize the discussion on adiabaticity, it is important to repeat that the scalar field $\eta(\mathbf{r})$, as defined by Eq. (21), charaterizes the rf field at each point in space and is independent of individual trajectories. Taking our empirical η restriction $\eta_m < 0.3$, one can mark out those regions in which the influence of the rf field can be described using the adiabatic approximation. However, in order to predict whether ions starting in such a region remain there, it is either necessary to follow their trajectories or to make profit from adiabatic constants of motion that restrict their phase space. For example, the accessible range of a trajectory is limited by the effective potential and the total energy E_m, which can be determined from the initial conditions. This will be further discussed in the next section and, for multipole fields, in Section II D.

4. *Stability*

In the preceding sections, we have applied the expression *stability* in several contexts. For example, the stability of the solutions of Mathieu's equation is characterized by the (a_2, q_2) stability chart, we have called the fast increase of η_{m_i} in Eq. (23) or of $\Delta v/v$ in Fig. 4 unstable behavior, and we have used stability in association with experimental requirements for safe ion transimission or long-time ion trapping. In this section we will make some general remarks about the *mathematical* meaning of stability and discuss briefly an illustrative example. Since, however, the mathematical theorems are not easy to apply to our concrete physical system, we simplify the problem by treating it only within the adiabatic approximation. As a result, we propose a simple definition of stability in a *practical* sense that can be directly applied to many experimental situations.

In general, it is difficult to define exactly what is meant by stability in a nonlinear and nonautonomous dynamical system. Typical mathematical definitions of stability (Arnold, 1988; Hayashi, 1985) either require that a trajectory remains forever in a bounded domain of the phase space (Lagrange stability) or are concerned with the question of what happens if the system is disturbed slightly near a stable stationary or oscillatory equilibrium (Liapunov stability). It has been discussed in Lichtenberg and Lieberman (1983) that the motion of a charged particle in a time-dependent electromagnetic field cannot be easily analyzed using standard methods of nonlinear mechanics. The main difficulty in this so-called guiding-center problem is to split the system into an unperturbed part and the perturbation. Several methods for obtaining such a separation using adequate coordinate transformations or multiple-scale averaging methods have been discussed in the literature (Kruskal, 1962; Lichtenberg and Lieberman, 1983; Littlejohn, 1979).

It is beyond the scope of this chapter to go into further details concerning the fundamental theory; however, we want to make a few illustrative remarks related to Fig. 4. On the one hand, we cannot exclude the possibility that there are unstable regions below $\eta_v < 0.3$, since the numerically determined limitation of $\Delta v/v$ is not a strict mathematical proof. More detailed numerical studies would have to search more carefully for regions of instability, which are expected (Lichtenberg and Lieberman, 1983) to become exponentially small with decreasing η_v [to order $\exp(-\text{const}/\eta_v)$]. On the other hand, it is evident from Fig. 4 that there are also regions of stability located significantly above our limit $\eta_v = 0.3$.

The stable region around $\eta_v = 0.65$ can be used to illustrate the definition of stability in the Liapunov sense. For this purpose one has to find a periodic orbit and to prove that this orbit is a stable oscillatory equilibrium. The

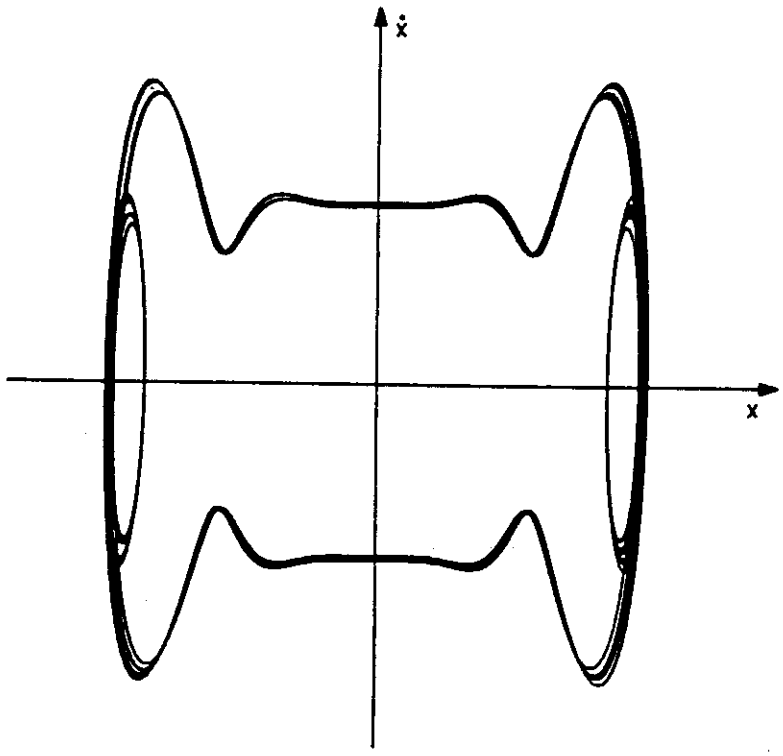

Figure 5. Phase space $(x, \dot{x})$ representation of a stable one-dimensional trajectory started with $\eta_v = 0.65$ in the vicinity of the periodic orbit $\Omega/\omega = 10$ ($\eta_v = 0.6454...$).

required periodic orbit, where the ratio of the rf frequency and the frequency of the secular motion is an integer, $\Omega/\omega = 10$, is obtained for $\eta_v = 0.64546355...$, as determined by a Fourth-order Runge-Kutta integration of Eq. (3). Instead of going into the details of stability investigations, we simply show in Fig. 5 a single trajectory that has been started in the neighborhood of this periodic orbit. The phase-space representation shows many cycles, and the fact that the slight change of initial conditions results in a quasiperiodic trajectory can be taken as a sign for stability.

The discussed examples are very special cases of one-dimensional trajectories in an octopole. This dynamical system, which is equivalent to an autonomous system of two degrees of freedom due to its explicit time dependence, could be studied in further detail using standard methods of nonlinear mechanics. However, a full characterization of ion confinement or transmission functions of rf devices requires treatment of the motion in two or three spatial dimensions. From the symmetry of a multipole arrangement, it can be concluded that there are many more periodic orbits, and one can expect that there are also many islands of stability that are localized in the unsafe η range. The question whether they are of some practical importance will be raised in Section II D 3.

Since we have no rigorous mathematical means to fully characterize stable solutions of Eq. (3), we restrict ourselves in the rest of this section to derive

a simple condition for *stability* in a *practical* sense. For this purpose we make use of the effective potential and apply the experimentally necessary condition that the excursion of the ion does not exceed the internal dimensions of the electrodes. Adiabatic conservation of energy ensures that the accessible spatial range of an ion with a total energy E_m can be determined from Eq. (16) by setting $\dot{\mathbf{R}}_0 = 0$. To avoid ion loss by collision with the electrodes, the effective potential V^* close to the surfaces must be larger than E_m. Safe operating conditions must provide sufficient space for the small oscillatory motions $\mathbf{R}_1(t)$, Eq. (6). Therefore, an experimental condition for stability based on Eq. (16) can be formulated as

$$q^2 E_0(\mathbf{r}_m)^2/4m\Omega^2 + q\Phi_s(\mathbf{r}_m) > E_m, \tag{25}$$

where the vector $\mathbf{r}_m$ designates the closest allowed approach to the electrode surfaces. Note also that $\eta(\mathbf{r}_m) < 0.3$ is required for adiabatic behavior. An illustrative example is the periodic, large-amplitude oscillation in Fig. 2. Here the motion of the ion is unstable, since it exceeds the limitations imposed by the center cylinder. The total energy, marked by the dashed line, is too large to satisfy Eq. (25).

In order to predict whether certain initial conditions lead to stable trajectories as defined by Eq. (25), it is necessary to determine the energy E_m. If an electrode arrangement has a region where the field is zero, or sufficiently weak, E_m is simply equal to the kinetic energy, $\frac{1}{2}m\dot{\mathbf{r}}^2 = \frac{1}{2}m\dot{\mathbf{R}}_0^2$, of the ion in that region. If the ion starts somewhere in the rf field, the determination of the total energy E_m has to account for the local field strength $\mathbf{E}_0$ and the start phase δ. The condition given in Eq. (25) also allows one to determine experimentally the kinetic energy of stored ions. A detailed discussion of such critical operation modes for multipoles follows in Section III C 3.

We want to repeat that our practical criterion for stability, that is, adiabatic conservation of energy and stable confinement in a given geometrical region, is primarily motivated from experimental applications. The derived stability condition is a sufficient condition assuming the validity of the adiabatic approximation. The actual range of stable solutions of the dynamical system is larger and extends into regions $\eta > 0.3$.

Finally, from an experimental point of view, it seems to be necessary to draw attention to instabilities caused by sources other than the ideal rf field. For example, space-charge effects due to high ion densities can lead to plasma oscillations. An interesting study of chaos and order of Coulomb-interacting laser-cooled ions in a Paul trap has been reported recently (Blümel et al., 1989). Instabilities can also be induced through a superimposed low-frequency field or resonant modulation of the rf amplitude, as is well known from different applications of quadrupoles (Busch and Paul, 1961a, 1961b; March and

Hughes, 1989). Time-dependent effective potentials, for example, fast or slow variation of the amplitude, have been proposed for plasma acceleration (Miller, 1959) or can also be used for adiabatic cooling.

C. Special Field Geometries

1. *Laplace's Equation*

This section provides some explicit formulas for calculating the effective potential V^* and the adiabaticity parameter η for different boundary conditions. In addition, several formulas for practical applications are derived. In general, one has to determine the electromagnetic field from Maxwell's equations using appropriate boundary conditions. A thorough discussion of this subject is presented in many textbooks (Jackson, 1962; Magid, 1972; Simonyi, 1963; Sommerfeld, 1964). Related references can be found in the paper by Friedman et al. (1982), where several fundamental aspects of rf multipole fields are discussed. One typical example, which includes both the electric and the magnetic field components, has been given by Weibel (1959) who calculated the effective potential for a TE_{01} field in a circular waveguide. A more complete analysis of electromagnetic fields set up by arbitrary modes of excitation of square and circular section waveguides has been reported by Miller (1958a, 1958b). In both publications, it was shown that effective potential wells can be created in one, two, or three dimensions simply by choosing a suitable frequency and mode type, or by a linear combination of quasipotentials.

Since in most of our applications the charged particles are slow ions, the frequency of the oscillating field can usually be chosen low enough (<30 MHz) that the wavelength (>10 m) is much greater than typical geometrical dimensions (<1 m). As such, not only the static part of the field, $\mathbf{E}_s(\mathbf{r})$, but also the time-varying part of the field, $\mathbf{E}_{rf} = \mathbf{E}_0(\mathbf{r})\cos\Omega t$, can be derived from the simpler quasistatic solution. Furthermore, the electric field can be determined completely independently from the magnetic field. As has already been justified, the interaction of the magnetic field with the slow charged particles can be disregarded. In this *quasielectrostatic* limit, both fields $\mathbf{E}_s$ and $\mathbf{E}_{rf}$ are derived from the potentials Φ_s and Φ_{rf}, respectively. Because of the superposition principle, it is sufficient to search for a potential $\Phi = \Phi_s + \Phi_{rf}$, and the problem is therefore reduced to the solution of Laplace's equation under the inclusion of the appropriate boundary conditions, and possibly the space charge $\rho(\mathbf{r})$

$$\Delta\Phi(\mathbf{r}) = -4\pi\rho(\mathbf{r}). \tag{26}$$

For most of our applications, the problem can be treated in the limit of low ion densities. In the space-charge-free limit, Laplace's equation becomes

simply

$$\Delta\Phi(\mathbf{r}) = 0. \tag{27}$$

Boundary conditions are imposed by the geometrical structure of a manifold of electrodes, which are assumed to be equipotential surfaces, and by the static and rf voltages applied to each of them.

There are several methods to find functions $\Phi(\mathbf{r})$ including the method of images, complex-variable theory, and infinite series expansion. This problem is well treated in the previously mentioned textbooks and in Friedman et al. (1982). For convenient future reference, some particular Laplacian solutions in different coordinate systems are listed here. Also, some hints for obtaining numerical solutions of Eq. (27) are given.

For certain symmetries it is convenient to write Laplace's equation in terms of spherical polar coordinates (r, ϑ, φ). Typical solutions are superpositions of functions such as

$$\Phi(r, \vartheta, \varphi) = (Ar^n + Br^{-n-1})P_n^m(\cos\vartheta)(C\sin m\varphi + D\cos m\varphi), \tag{28}$$

where A, B, C, and D are constants, P_n^m are the associated Legendre functions, and n and m are positive integers.

The problem of infinitely long cylindrical conductors, where the boundary conditions impose no z dependence, can be described in plane polar coordinates (r, φ). In this case, one obtains general solutions of Laplace's equation of the following type for $n > 0$:

$$\Phi(\mathbf{r}, \varphi) = (Ar^n + Br^{-n})(C\sin n\varphi + D\cos n\varphi), \tag{29}$$

and for $n = 0$:

$$\Phi(\mathbf{r}, \varphi) = (A + B\ln r)(C + D\varphi). \tag{30}$$

If the situation is adequately described in cylindrical coordinates (r, φ, z) and has azimuthal symmetry, general solutions containing the modified Bessel functions of the first kind, I_n and K_n, are obtained in the form

$$\Phi(r, z) = (A\cos kz + B\sin kz)(CI_n(r) + DK_n(r)). \tag{31}$$

2. *Special Solutions*

To achieve a simple mathematical solution represented by one of the exact potentials above, precisely machined and arranged electrodes are needed. Under such ideal conditions, the geometrical electrode surfaces follow the

equipotential surfaces given by the selected solution, and the potential has a known and constant value at every surface, as given by the applied voltage. A very simple example of such a boundary value problem is the field of two line charges q and $-q$ and a cylindrical shield S, arranged according to Fig. 6. If in this special geometry the boundary condition $\Phi(\hat{r} = \alpha, \varphi) = \Phi_0$ is fulfilled, the potential at an arbitrary point in space is determined by

$$\Phi(\hat{r}, \varphi) = \Phi_0 / \ln(\alpha^2) \ln \frac{\hat{r}^2 + 1 - 2\hat{r}\cos\varphi}{\hat{r}^2 + \alpha^4 - 2\alpha^2\hat{r}\cos\varphi}, \tag{32}$$

where α is a constant >1, r_0 is a characteristic length, and $\hat{r} = r/r_0$ is a reduced variable. This problem and the quadrupole potential of four line charges have already been discussed in detail in Sommerfeld (1964). The lower panel of Fig. 6 shows an arrangement of eight line charges that we have used to describe a wire octopole with shield S (Müller, 1983).

Another textbook example is the cylinder capacitor, shown schematically in Fig. 2. Two concentric conductions with potentials Φ_0 and 0 impose the boundary conditions $\Phi(r_0) = \Phi_0$ and $\Phi(r_0 + d) = 0$, and one obtains from

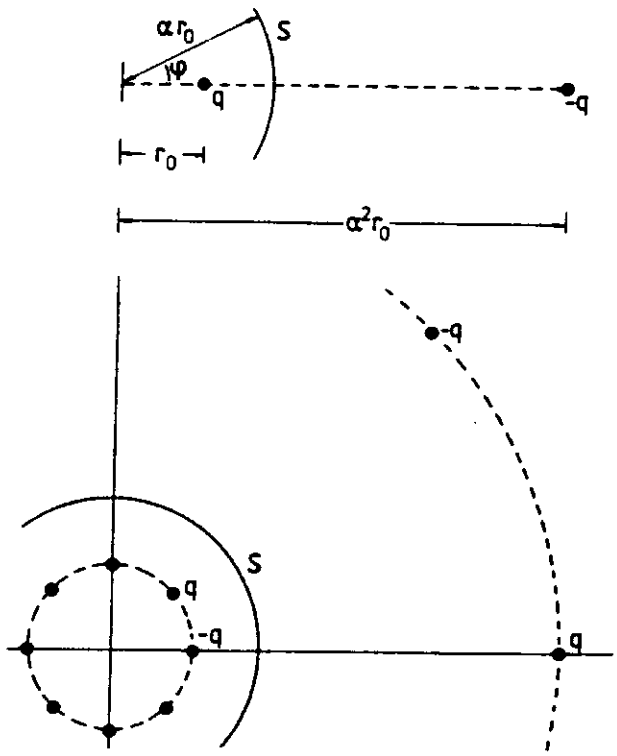

Figure 6. To obtain a cylindrical equipotential surface S with radius αr_0, the two line charges q and $-q$ must be situated at r_0 and $\alpha^2 r_0$, respectively. The potential is given in Eq. (32). The lower panel illustrates that superposition of eight cylindrical dipoles with line charges alternating in sign allows one to calculate the potential of an octopole made of eight thin wires surrounded by the cylindrical shield S.

Eq. (30) the r-dependent potential

$$\Phi(r) = \Phi_0 \ln(r/(r_0 + d))/\ln(r_0/(r_0 + d)). \tag{33}$$

A somewhat more complicated arrangement is a stack of ring electrodes, depicted in Fig. 7. In this case, it is appropriate to measure all distances in the unit z_0 and the reduced variables are $\hat{r} = r/z_0$, $\hat{r}_0 = r_0/z_0$, and $\hat{z} = z/z_0$. With the boundary conditions $\Phi(\hat{r}_0, \hat{z}) = \Phi_0 \cos \hat{z}$, which are shown as the parabolic shaped lines in Fig. 7, the following potential is obtained from Eq. (31).

$$\Phi(r, z) = \Phi_0 I_0(\hat{r})/I_0(\hat{r}_0) \cos \hat{z}. \tag{34}$$

Such an arrangement of similarly shaped electrodes is used as an ion trap, as discussed in Section III E.

Another simple potential that describes an rf grid and that can be assembled from a series of parallel rods has been used by Teloy (Kohls, 1974; Teloy, 1980) for many tests of his adiabatic theory

$$\Phi(\hat{x}, \hat{y}) = \Phi_0 \exp(-\hat{x}) \cos \hat{y}. \tag{35}$$

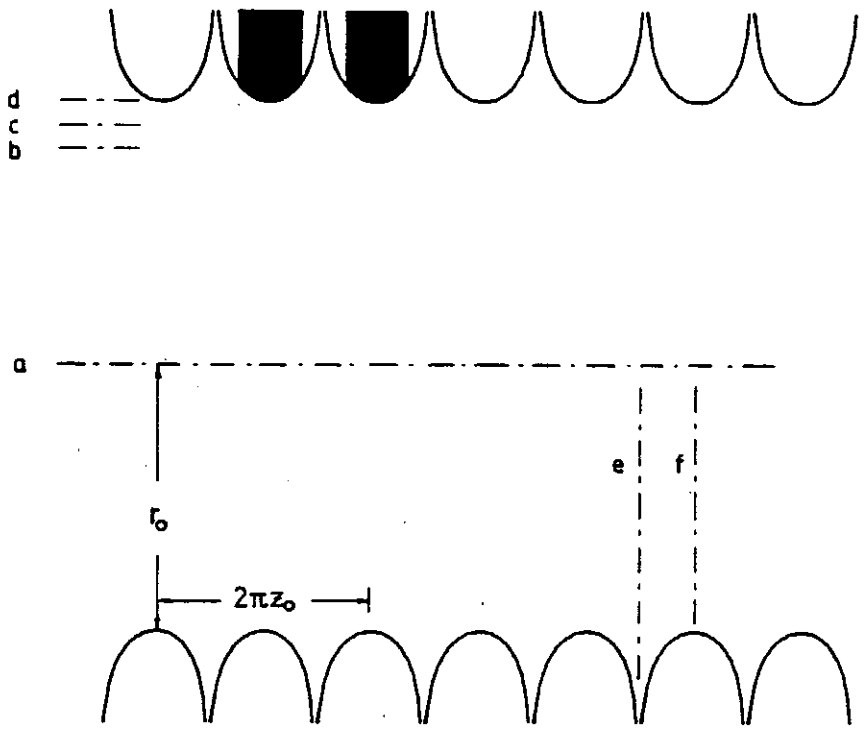

Figure 7. Equipotential lines of a rotationally symmetric ring electrode trap, defined in Eq. (34). The actual shape of the electrodes in marked in black (see Section III E). The letters a–f indicate locations along which Fig. 8 shows cuts through the effective potential.

The advantage of this potential is that it decreases exponentially with increasing $\hat{x}$, and, as such, one can start trajectories in an almost field-free region and study the influence of single reflections. Finally, Laplace's solutions of the very important class of multipole fields has been treated by Friedman et al. (1982) and Szabo (1986) and shall be discussed separately in Section II D.

Potentials for more complicated boundary value problems can be expressed as a infinite sum over a complete set of adequate general solutions making use of the superposition principle. A typical example is the calculation of the electrostatic potential and the resulting effective potential of a Paul trap with cylindrical rather than hyperbolical electrodes (Lagadec et al., 1988).

For those situations where simple analytical methods fail, many numerical methods have been developed for obtaining potential functions under given boundary conditions. Usually the problem is reduced to the solution of linear algebraic equations. One general method, based on N discrete surface-charge distributions, has been used recently to optimize a simple electrode structure for the approximation of a quadrupole trap (Beaty, 1987). Another method has been proposed and examined theoretically (Matsuda and Matsuo, 1977), whereby the parameters of a 12-wire arrangement were varied to obtain an optimal representation of a hyperbolic quadrupole field.

In order to calculate the potential of some realistic arrangement of electrodes with a circular profile and to account for other special laboratory situations like geometrical distortions and external field penetration, we have developed a computer program (Scherbarth, 1984) based on the superposition of $N = 96$ pairs of line charges. Some results of these calculations will be presented in Section II D.

3. *Effective Potentials*

To determine the effective potential we must first know the potential $\Phi = \Phi_s + \Phi_{rf}$, which itself depends on the geometry and the applied potential, Φ_0, as shown explicitly in several examples presented in Section II C 2. For the time and amplitude dependence of Φ_0, we generally use the form

$$\Phi_0 = U_0 - V_0 \cos \Omega t, \tag{36}$$

which means that a static voltage U_0 and a sinusoidal time-dependent voltage with amplitude V_0 are applied to the electrodes. The minus sign is in accordance with the convention used for the description of quadrupoles (Dawson, 1976). Concerning the amplitudes, there is some confusion in the literature, which has recently been discussed (March and Hughes, 1989). For our boundary conditions, used, for example, in the derivation of Eq. (34), Eq. (35), and Eq. (39), the potentials applied to two adjacent electrodes are

$+\Phi_0 = U_0 - V_0 \cos \Omega t$ and $-\Phi_0 = -U_0 + V_0 \cos \Omega t$. This leads to an electrode to electrode potential difference of $2U_0 - 2V_0 \cos \Omega t$. With these definitions and conventions we are consistent with March and Hughes (1989).

If the rf part, Φ_{rf}, of the potential is known, it is straightforward to determine $\mathbf{E}_0$, E_0^2, and $|\nabla E_0|$. With these expressions one obtains the effective potential V^* from Eq. (13) and the stability parameter η from Eq. (21). An illustrative example is the effective potential created by the ring electrode arrangement depicted in Fig. 7. The amplitude of the oscillatory field, $\mathbf{E}_0$, is calculated from the gradient of the potential given in Eq. (34), where Φ_0 is replaced by V_0:

$$\mathbf{E}_0 = (E_r, E_z) = \frac{V_0}{z_0}\left(-\mathbf{I}_1(\hat{r})/\mathbf{I}_0(\hat{r}_0)\cos\hat{z},\ \mathbf{I}_0(\hat{r})/\mathbf{I}_0(\hat{r}_0)\sin\hat{z}\right). \tag{37}$$

A detailed description of the the modified Bessel functions, and the relation $\mathbf{I}_0'(\hat{r}) = \mathbf{I}_1(\hat{r})$ used in the derivation of $\mathbf{E}_0$, can be found in Abramowitz and Stegun (1964). Inserting $|\mathbf{E}_0|^2$ into Eq. (13) leads immediately to the effective potential

$$V^* = \frac{q^2 V_0^2}{4m\Omega^2 z_0^2}\left[\mathbf{I}_1^2(\hat{r})\cos^2\hat{z} + \mathbf{I}_0^2(\hat{r})\sin^2\hat{z}\right]/\mathbf{I}_0^2(\hat{r}_0). \tag{38}$$

Several cuts through this potential, the positions of which are specified as *a–f* in Fig. 7 are plotted in Fig. 8. The left panel shows two radial cuts, *e* and *f*, the right panel the four axial cuts, *a–d*, at different distances from the centerline. For comparison, the effective potentials of a quadrupole and an octopole are also included in Fig. 8. Multipole devices and their analytical representations of V^* and η will be discussed in Section II D.

D. Two-Dimensional Multipoles

1. *The Ideal Multipole*

Among the most important electrode systems for the purpose of this chapter are the two-dimensional multipoles. The most prominent member, the quadrupole, is probably one of the best described and most thoroughly characterized devices. A general treatment of the entire class of multipoles, however, is rarely found in literature. Some theoretical background and various proposals for the use of multipoles to focus beams and confine ions were given in Gapanov and Miller (1958) and Miller (1958a, 1958b). The first experimental realization of an octopole was described by Gerlich (1971), and a general description of its function within the effective potential approximation was published in Teloy and Gerlich (1974). Additional details

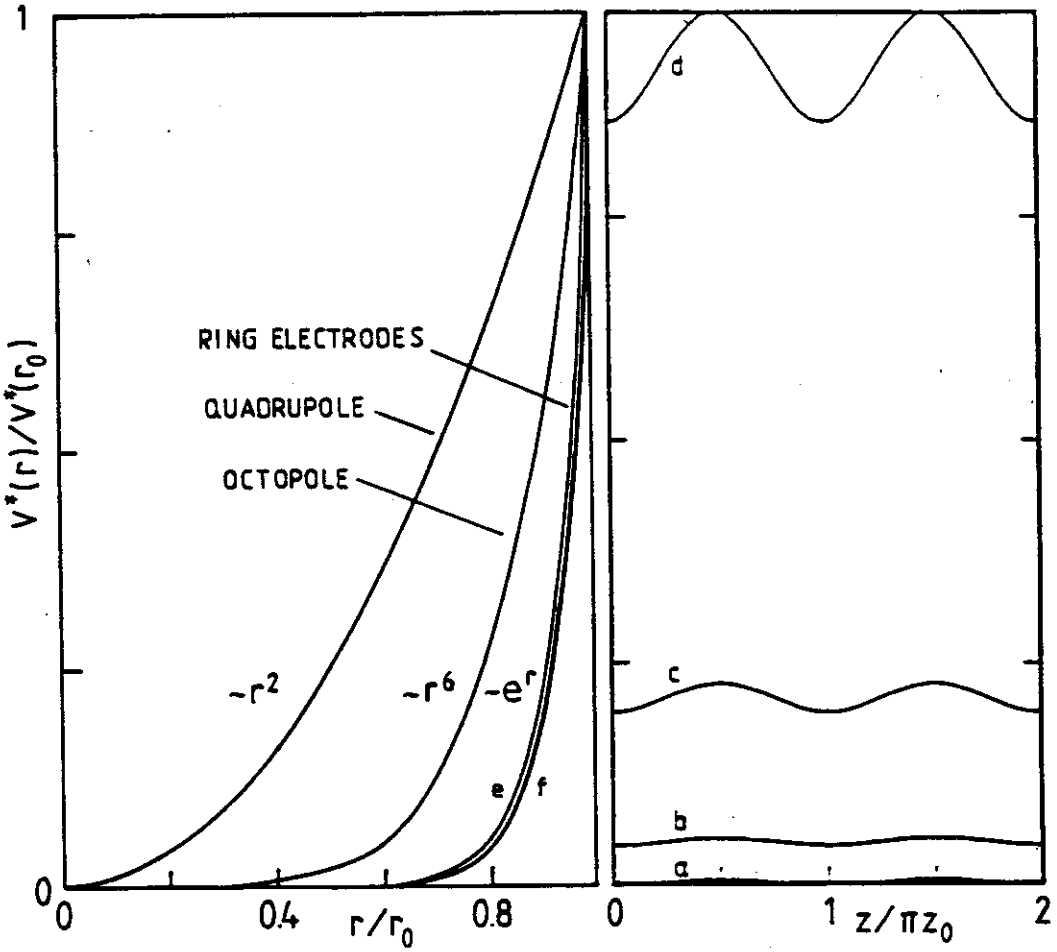

Figure 8. Effective potentials V^*. The left panel illustrates that for the ring electrode trap V^* increases proportional to e^r, in comparison to the r^2 and r^6 dependence of the quadrupole and the octopole. The letters a–f refer to locations marked in Fig. 7. In the axial direction (right panel) the effective potential of the ring electrode trap has a weak corrugation (a–c), which only becomes pronounced very close to the electrodes (d).

on multipole devices were reported more recently (Gerlich, 1986). There are a few additional references (Friedman et al., 1982; Szabo, 1986) that compile some fundamental facts and basic information about multiple potential functions and present the equation of motion of ions moving therein.

The potential of a multipole field can be obtained from Eq. (29) by setting $\Phi(r = r_0, \varphi) = \Phi_0 \cos n\varphi$ and $\Phi(r = 0, \varphi) = 0$, and by using the reduced variable $\hat{r} = r/r_0$:

$$\Phi(r, \varphi) = \Phi_0 \hat{r}^n \cos n\varphi. \tag{39}$$

The n dependence of these potentials, the hyperbolic equipotential lines, and the shape of the $2n$ electrodes have been discussed and depicted in several figures in Friedman et al. (1982) and Szabo (1986). The influence of deviations from the exact structure will be discussed in Section II D 4.

The polar components of the electric field, $\mathbf{E} = (E_r, E_\varphi)$, are obtained as the gradient of Φ;

$$\mathbf{E} = -\left(\frac{\partial}{\partial r}\Phi, \frac{1}{r}\frac{\partial}{\partial \varphi}\Phi\right) = \frac{\Phi_0}{r_0} n \hat{r}^{n-1}(-\cos n\varphi, \sin n\varphi). \tag{40}$$

The differential equation, Eq. (3), describing the motion of an ion in a two-dimensional multipole field, has been discussed in detail in Friedman et al. (1982) and Szabo (1986). Using the cartesian representation of the electric field,

$$(E_x, E_y) = \frac{\Phi_0}{r_0} n \hat{r}^{n-1}(-\cos(n-1)\varphi, \sin(n-1)\varphi), \tag{41}$$

and replacing Φ_0 by the sum of the static and rf potential from Eq. (36), we obtain the equation of motion in cartesian coordinates $\hat{\mathbf{r}} = (x/r_0, y/r_0)$

$$\ddot{\hat{\mathbf{r}}} + F(t)\hat{r}^{n-1}(-\cos(n-1)\varphi, \sin(n-1)\varphi) = 0. \tag{42}$$

For abbreviation and further reference we introduce the explicit time-dependent function

$$F(t) = n\frac{qU_0}{mr_0^2} - n\frac{qV_0}{mr_2^0}\cos\Omega t. \tag{43}$$

It is evident that for $n > 2$ this differential equation is nonlinear and, in contrast to the quadrupole, additional complications arise because the x and y motions are no longer decoupled. As such, it is advantageous to obtain a general characterization of the solutions within the adiabatic approximation.

To derive the effective potential V^* and the adiabaticity parameter η for a multipole field, we must determine $|E_0|$ and ∇E_0 according to the general definitions given in Eq. (13) and Eq. (21), respectively. The absolute value of the amplitude of the oscillatory field,

$$|E_0| = \frac{V_0}{r_0} n \hat{r}^{n-1}, \tag{44}$$

follows directly from Eq. (40), whereby Φ_0 is replaced by V_0 according to Eq. (36). Inserting Eq. (44) and the static multipole potential, $qU_0\hat{r}^n \cos n\varphi$, into Eq. (13) leads to the representation of the effective potential:

$$V^* = \frac{n^2}{4}\frac{q^2}{m\Omega^2}\frac{V_0^2}{r_0^2}\hat{r}^{2n-2} + qU_0\hat{r}^n\cos n\varphi. \tag{45}$$

With this potential we can rewrite Eq. (16) such that

$$E_m = \tfrac{1}{2} m\dot{\mathbf{R}}_0^2 + V^*(\mathbf{R}_0). \tag{46}$$

The adiabaticity parameter, defined in Eq. (21), can be easily derived with Eq. (44), since the vector

$$\nabla E_0 = \left(\frac{\partial}{\partial r}, \frac{1}{r}\frac{\partial}{\partial \varphi}\right)|\mathbf{E}_0|$$

has only a radial component, and one obtains

$$\eta = 2n(n-1)\frac{qV_0}{m\Omega^2 r_0^2}\hat{r}^{n-2}. \tag{47}$$

Finally, the reduced amplitude, $\hat{\mathbf{a}} = \mathbf{a}/r_0$, can be determined from Eq. (5) and Eq. (41).

$$\hat{\mathbf{a}} = \frac{qV_0}{m\Omega^2 r_0^2} n\hat{r}^{n-1}(-\cos(n-1)\varphi, \sin(n-1)\varphi). \tag{48}$$

Some of the results can be explained with the help of Fig. 9, which depicts a stable motion ($\eta_m = 0.3$) of an ion in an octopole. This trajectory corroborates the physical picture of a smooth motion of the guiding center under the influence of the quasipotential and a superimposed wiggling motion, which is seen especially during the reflections. The circle marks the radius where $\frac{1}{2}m\dot{\mathbf{R}}_0^2 = 0$, and the positions of the turning points near the circle indicate that the energy is conserved. Note the hole in the center, a region avoided by the trajectory, that is due to conservation of angular momentum of the ion motion. Since the absolute value of the electric field, $|\mathbf{E}_0|$, is independent of the azimuthal angle, φ, the rf part of the effective potential becomes rotationally symmetric. This has the important consequence that, within our high-frequency approximation, the interaction between the ion and the rf field results in a pure central force. In the absence of a superimposed static field U_0, there is a second constant of the motion, the angular momentum $\mathbf{L}$, and the total kinetic energy is composed of the radial term and a centrifugal term:

$$\tfrac{1}{2}m\dot{\mathbf{R}}_0^2 = \tfrac{1}{2}m\dot{R}_0^2 + \mathbf{L}^2/2mR_0^2. \tag{49}$$

It must be emphasized, however, that both the total energy and the total

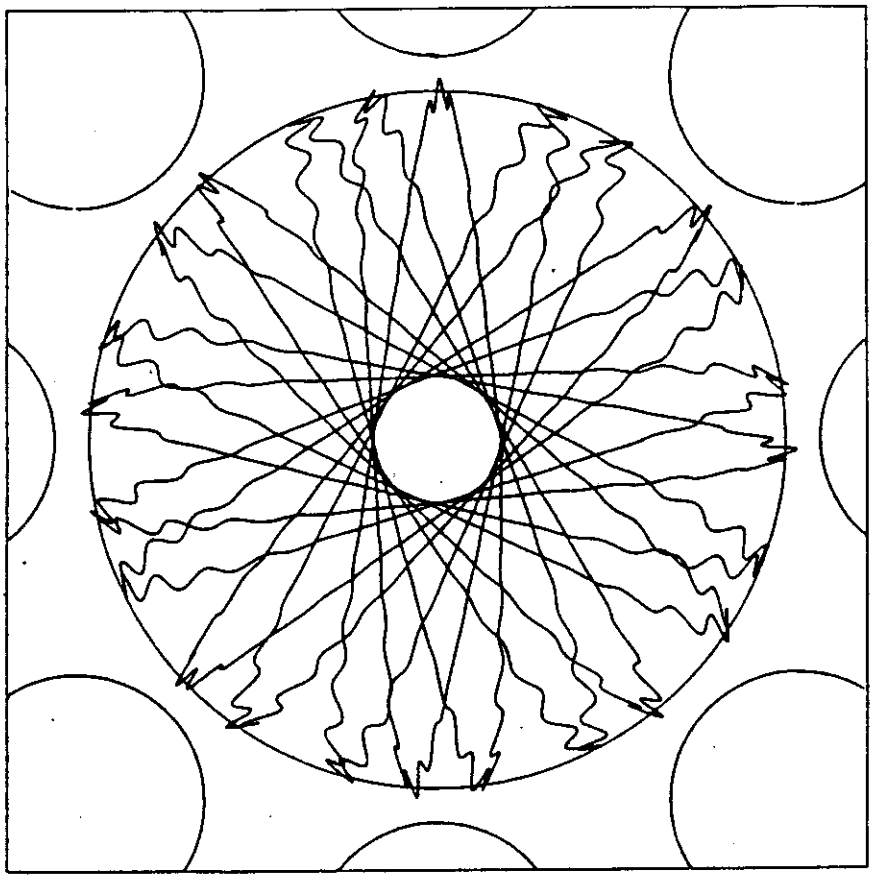

Figure 9. Typical trajectory of an ion in an octopole determined by direct numerical integration of the exact equation of motion, Eq. (42), for $\eta_m = 0.3$. The circle marks the turning radius, as determined from the effective potential approximation.

angular momentum are oscillating and that they are conserved only on average.

A trajectory which becomes unstable ($\eta_m \sim 0.55$) is plotted in Fig. 10 for an ion in a 32-pole. Here, the angular momentum is no longer conserved. The trajectory shown changes its closest approach to the center, and after a few more reflections, the ion will be lost. This figure further illustrate one of the most important features of higher-order multipoles, that is, the wide field-free region bordering on very steep potential walls. Most of the time the ion moves along straight lines and the interaction with the rf wall is very short ranged.

To evaluate numerically V^* and η in the case of multipoles, it has proven useful (Gerlich, 1986) to introduce an additional parameter, the characteristic energy ε, which combines the important parameters mass, frequency, and radius r_0:

$$\varepsilon = \frac{1}{2n^2} m\Omega^2 r_0^2. \tag{50}$$

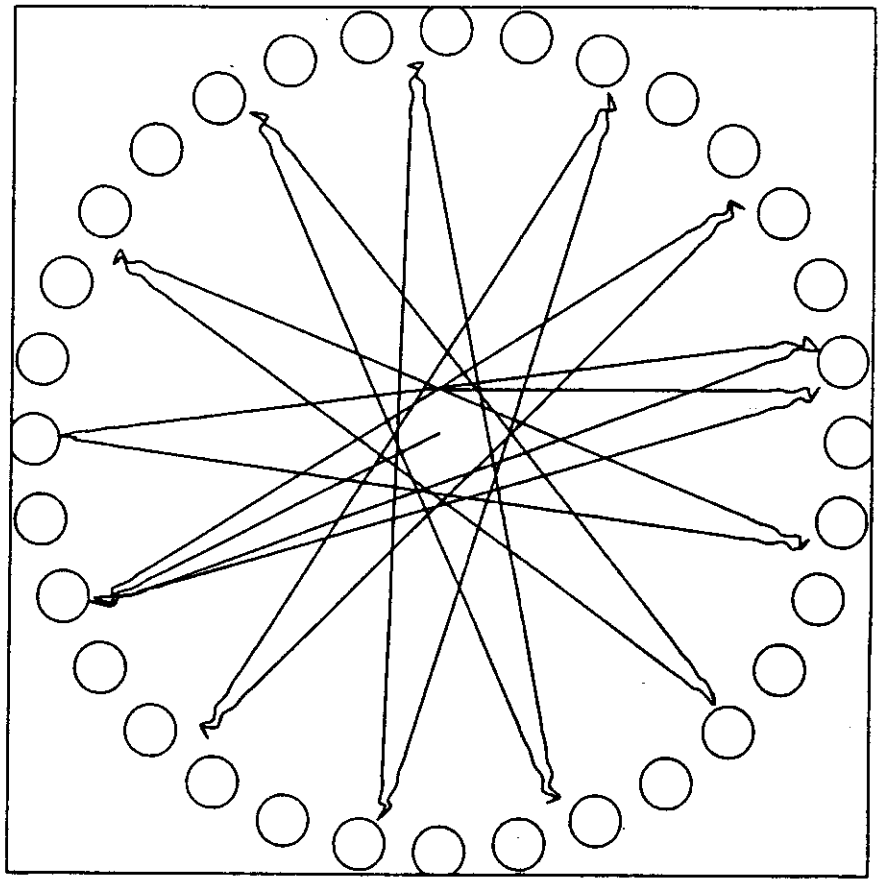

Figure 10. Trajectory in a 32-pole ($\eta_m \sim 0.55$). The ion is moving most of the time in a wide field-free region. After a few more reflections, the depicted trajectory will be lost. In contrast to Fig. 9, the closest approach of the trajectory to the center changes, indicating that here the orbital angular momentum is no longer conserved. This is a hint that the condition for the adiabatic approximation is no longer fulfilled.

This term allows one to rewrite Eq. (45) and Eq. (47) in the following simpler forms

$$V^* = \frac{1}{8}\frac{(qV_0)^2}{\varepsilon}\hat{r}^{2n-2} + qU_0\hat{r}^n \cos n\varphi \tag{51}$$

and

$$\eta = \frac{n-1}{n}\frac{qV_0}{\varepsilon}\hat{r}^{n-2}. \tag{52}$$

The energy ε is not simply an abbreviation; it also has a physical interpretation. It corresponds to the kinetic energy of an ion cycling in phase with the rf on a radius r_0. It is obvious that for adiabatic behavior the actual ion energy must be much lower than ε.

2. *Safe Operating Conditions*

As was mentioned in our discussion on adiabaticity and stability, characterization of necessary or sufficient operating conditions of rf devices depends on the desired application. In this section we summarize a few analytical formulas that permit one to calculate conditions for operating multipoles in such a manner that the adiabatic approximation remains valid everywhere within given spatial boundaries, that is, those defined by the electrode surfaces. For a complete characterization, only the multipole parameters (n, r_0, Ω, V_0), the mass m, and the energy E_m are needed. Adiabatic conservation of energy ensures that safe transmission or storage of ions does not depend on the individual initial conditions, but only on their transverse energy.

The situation and the η restriction discussed in Section II B are illustrated in Fig. 11, which shows several trajectories, all starting in the center of an

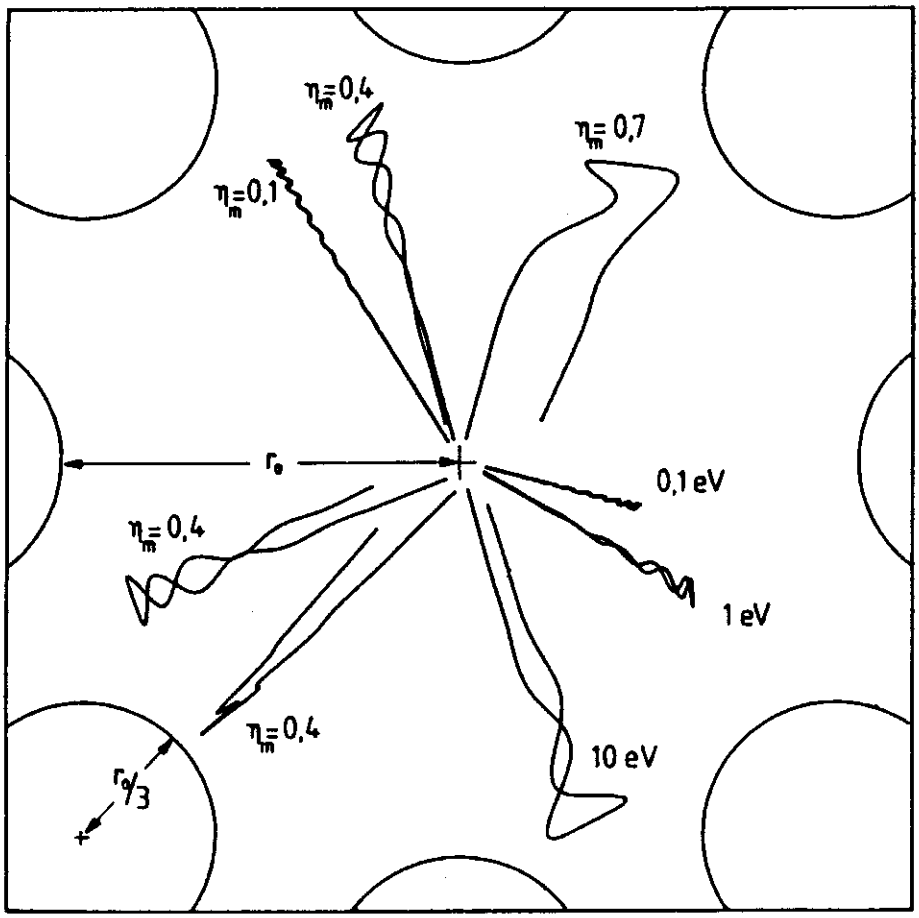

Figure 11. Characteristic ion trajectories in an octopole illustrating different operating conditions. All ion trajectories start in the center of the octopole. The examples with $\eta_m = 0.1$, 0.4, and 0.7 illustrate that with increasing η the amplitude of the wiggling motion increases and that the number of oscillations during one reflection from the rf wall decreases. For the three energies (0.1, 1, and 10 eV) the values ε and V_0 are constant. In the remaining trajectories ($\eta_m = 0.4$) only the starting angle has been changed. In one case, the small oscillations $\mathbf{R}_1(t)$ are parallel to the secular motion $\mathbf{R}_0(t)$; in the other, they are orthogonal.

octopole (i.e., $\mathbf{L} = 0$), but under different initial conditions. For $\eta_m = 0.1$, the energy and angular momentum are conserved. The ion with $\eta_m = 0.7$ is reflected once, but the energy and the angular momentum have already increased significantly. The three trajectories with $\eta_m = 0.4$ are all stable; however, one already sees small perturbations of the motion from nonradial forces. These results lend further support to the limitation $n_m = 0.3$ given in Section II B 3. The three remaining trajectories have been calculated for fixed values of ε and V_0, but with different starting energies $E_m = 0.1$ eV, 1 eV, and 10 eV. The turning radius of the 10-eV trajectory is so large that, with a different starting angle, this ion would hit the electrode. For the formulation of safe operating conditions, such trajectories must be excluded.

Since η increases proportionally to $\hat{r}^{n-2}$, according to Eq. (52), we can use the maximum turning radius, $\hat{r}_m$, for determining in good approximation the maximum of the adiabaticity parameter, $\eta(\hat{r}_m)$. To guarantee that the trajectories remain bound, $\hat{r}_m$ must remain smaller than 1, and since there must be some space for the wiggling motion, we normally require (Gerlich, 1986) for safe operating conditions that

$$\hat{r}_m < 0.8$$

and

$$\eta(\hat{r}_m = 0.8) < 0.3. \tag{53}$$

The correlation between the maximum allowed transverse energy E_m and $\hat{r}_m$ can be derived from adiabatic conservation of energy, which is expressed for multipoles in Eq. (46). For this purpose we apply Eq. (49), where the kinetic energy of the secular motion, $\frac{1}{2}m\dot{\mathbf{R}}_0^2$, is separated into its radial and centrifugal components, and make use of the fact that the radial component, $\frac{1}{2}m\dot{R}_0^2$, vanishes in the turning points. In the absence of a static field, the maximum energy E_m can be calculated from

$$E_m = \frac{1}{8}\frac{(qV_0)^2}{\varepsilon}\hat{r}_m^{2n-2} + L^2/2mr_m^2. \tag{54}$$

The centrifugal energy decreases with r^2 and is therefore usually rather rather small at the turning radius. In addition, the ions usually start very close to the centerline, resulting in a small angular momentum L. This allows us to neglect this energy term, especially since we wish to derive safe operating conditions.

From Eq. (52) and Eq. (54) the minimal characteristic energy ε and the smallest necessary amplitude V_0 for guiding an ion with a given maximal

energy can be expressed by the three quantities $\hat{r}_m$, E_m, and η_m:

$$qV_0 = 8\frac{n-1}{n}\frac{E_m}{\eta_m \hat{r}_m^n} \tag{55}$$

and

$$\varepsilon = 8\frac{(n-1)^2}{(n\eta_m \hat{r}_m)^2} E_m. \tag{56}$$

Equation (55) shows the interesting result that the minimal amplitude expressed in terms of $\hat{r}_m$, η_m, and E_m is independent of m and Ω. Using, for example, $n = 4$, $\hat{r}_m = 0.8$, $\eta_m = 0.3$, and $E_m = 1$ eV, it is found that an amplitude above 48.8 V is needed to store a singly charged particle ($q = 1e$) in accordance with the formulated requirements. This is independent of whether it is an electron, a proton, or a heavy cluster ion. For a given mass m and radius r_0, the minimal frequency follows from Eq. (56) and Eq. (50). The specified numbers lead to $\varepsilon = 78.1$ eV. Solving Eq. (50) for Ω with $r_0 = 0.3$ cm and $m = 1$ u, results in $f = \Omega/2\pi = 26$ MHz. For such numerical evaluations it is useful to use the units cm, MHz, and V, the mass unit u, the charge unit e, and the energy unit eV. In these units, Eq. (50) becomes

$$\varepsilon = 1.036\frac{1}{2n^2} m\Omega^2 r_0^2 \quad \text{(units eV, } u\text{, cm, MHz)}. \tag{57}$$

To guide an electron in a quadrupole ($n = 2$, $r_0 = 0.5$ cm) with a transverse energy $E_m = 0.1$ eV, an rf voltage of $V_0 = 2$ V is needed at a frequency $f = 70$ MHz. One must, however, pay attention here that the wavelength may become comparable to the dimensions of the device. An application at the other extreme of the frequency scale, the storage of charged microparticles in a quadrupole at $f = 53$ Hz, has been discussed by Wuerker et al. (1959a).

Safe conditions for simultaneous confinement of two masses $m_1 < m_2$ with a common maximum transverse energy E_m can also be calculated from Eq. (55) and Eq. (56) by replacing η_m with

$$\eta'_m = (m_1/m_2)^{n/(2n-2)}\eta_m, \tag{58}$$

and using in Eq. (57) the larger mass m_2. The optimum choice of the number of poles depends on the desired mass range, for example, for a relative range of a factor of 100, an octopole is best suited. Here we have used the obvious criterion of the lowest frequency and amplitude, and assumed the radius r_0 to be fixed.

As a typical numerical example for an octopole, where $m_1 = 1$ u, $m_2 = 100$ u, $n = 4$, $r_0 = 0.3$ cm, and $E_m = 0.1$ eV, the minimal values are $V_0 = 105$V and

$f = 17.8\,\mathrm{MHz}$. For a wider mass range, for example, a factor of 10,000, a decapole is preferred. Such a range might be needed for simultaneous storage of electrons and ions. In a hypothetical example, where $m_1 = 1\,u, m_2 = 10{,}000\,u$, $n = 5$, $r_0 = 0.3\,\mathrm{cm}$, and $E_m = 1\,\mathrm{eV}$, minimal values of $V_0 = 20\,\mathrm{kV}$ and $f = 110\,\mathrm{MHz}$ are needed. The derivation of conditions for the simultaneous

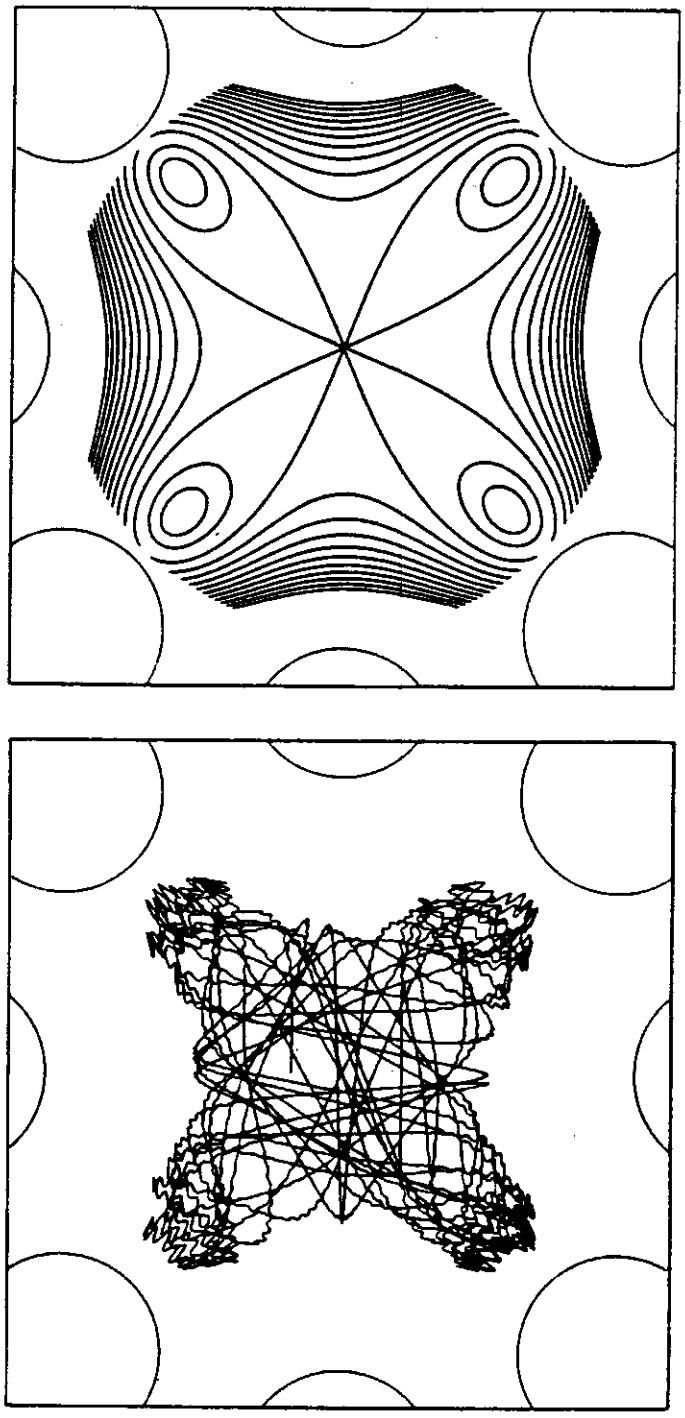

Figure 12. Upper figure illustrates the effective potential in an octopole with a superimposed static field, Eq. (45). The trajectory in the lower panel shows that the ion spends most of its time in the four potential minima located in the vicinity of the negatively biased rods.

storage of ions with different masses and with different energies is straightforward.

In nearly all applications described thus far, multipoles with $n > 2$ have been operated in the rf-only mode, that is, with no static potential U_0. The effective potential of a multipole with a superimposed dc potential [see Eq. (51)] is illustrated in the upper panel of Fig. 12. It is evident that the effective potential has lost its rotational symmetry. Since the static portion of the effective potential decreases proportional to $-\hat{r}^n$ in the direction of the negatively biased poles, and the rf portion increases as $\hat{r}^{2n-2}$, one obtains potential minima close to the negative rods for multipoles with $n > 2$. This is illustrated by the trajectory in the lower panel of Fig. 12, which shows that the ions avoid the positively biased poles. To ensure that ions started near the center of a multipole with $U_0 > 0$ do not hit the rods, it is necessary that $V^*(\hat{r} = 1) > 0$, and one obtains directly from Eq. (51) the relation

$$qU_0 < \frac{1}{8}\frac{(qV_0)^2}{\varepsilon}. \tag{59}$$

Since ε is proportional to the mass, Eq. (59) also shows that any multipole can be operated as a low-pass filter, transmitting only masses below a certain limit. Critical operating conditions will be discussed further in Section III C 4.

For determining safe operating conditions in the presence of a static field, the correlation between the maximum allowed transverse energy E_m and radius $\hat{r}_m$ can be established analogously to Eq. (54). It is also straightforward to derive corresponding formulas for stable confinement of ions that start in the vicinity of one of the potential minima located near the negatively biased rods (see Fig. 12).

3. *Is There an (a_n, q_n) Stability Diagram?*

It has already been mentioned in Section II A that for the special case of a quadrupole field, the region of stable trajectories is completely characterized by the well-known (a, q) stability diagram (see Fig. 24). In an attempt to generalize these parameters for multipoles, we define the parameters a_n and q_n,

$$q_n = 2n(n-1)\frac{qV_0}{m\Omega^2 r_0^2} = \frac{n-1}{n}\frac{qV_0}{\varepsilon} \tag{60}$$

and

$$a_n = 4n(n-1)\frac{qU_0}{m\Omega^2 r_0^2} = 2\frac{n-1}{n}\frac{qU_0}{\varepsilon}, \tag{61}$$

which leads to a simplification of Eq. (59):

$$a_n < \frac{n}{4(n-1)} q_n^2. \tag{62}$$

For a quadrupole this expression, $a_2 < \frac{1}{2}q_2^2$, is identical to the first term in the expansion of the lower (a_2, q_2) boundary limit of stability (Dehmelt, 1967; Wuerker et al., 1959a). Motivated by this similarity, one could be attempted to start from Eq. (62) and construct an (a_n, q_n) stability diagram for multipoles. However, one has to be aware of several restrictions that may render this approach impossible. First, Eq. (62) is only valid in the range of adiabaticity, and the question arises whether there is any meaningful generalization to extend the border lines to $q_n > 0.3$. Second, comparison of Eq. (60) with Eq. (47) reveals that q_n is only identical to the adiabaticity parameter η for $n = 2$, while to fully characterize the multipole one needs the $\hat{r}$ dependence of η, which can be expressed as

$$\eta = q_n \hat{r}^{n-2}. \tag{63}$$

Finally, it is important to remember that the underlying differential equations, Eq. (42), are nonlinear and coupled for $n > 2$.

An attempt to search for an (a_n, q_n) stability diagram, based on a similar analogy and numerical tests, was reported by Szabo (1986). His "analytical theory of multipole devices" began by comparing the canonical form of the Mathieu equation with the general equation of motion, Eq. (42), substituting the time t by the dimensionless parameter $\xi = \Omega t/2$. With this substitution, the function $F(t)$, given in Eq. (43), could be rewritten in the form $a_{n_s} - 2q_{n_s}\cos 2\xi$, and from this expression, Szabo defined the parameters (a_{n_s}, q_{n_s}). The index s was introduced here because for $n > 2$ there is a slight difference between the definition given by Szabo and our difinition given in Eq. (60) and Eq. (61). Taking our convention for U_0 and V_0 (see Section II C 3), the relation between (a_n, q_n) and (a_{n_s}, q_{n_s}) is given by

$$q_{n_s} = \frac{n^2}{4(n-1)} q_n \quad \text{and} \quad a_{n_s} = \frac{n^2}{4(n-1)} a_n. \tag{64}$$

This comparison shows that Szabo's "derivation" of the (a_{n_s}, q_{n_s}) parameters is not unequivocal because for $n = 2$, also, our definition is consistent with the canonical form of the Mathieu equation if we use the slightly different substitution, $\xi = \Omega t/2(n-1)^{1/2}$. Yet another possibility would be to introduce

the time scale $\xi = \Omega t n/4(n-1)$, resulting in

$$q'_n = q_n \quad \text{and} \quad a'_n = \frac{4(n-1)}{n^2} a_n, \tag{65}$$

and in a somewhat simpler form of Eq. (62),

$$a'_n < \frac{1}{n} q'^2_n. \tag{66}$$

For all three substitutions of the time t by ξ, Eq. (42) is transformed to the same canonical form when $n = 2$, thus indicating an ambiguity in the definition of the characteristic parameters.

In a subsequent series of papers, Hägg and Szabo (1986a, 1986b, 1986c) examined the transmission properties of the hexapole and octopole in terms of their generalized parameters (a_{n_s}, q_{n_s}), numerically solving Eq. (42) for selected initial conditions where the ions were started suddenly, off-axis, at full local field. The large computational effort resulted in sets of diffuse (a_{n_s}, q_{n_s}) diagrams. Conclusions of general validity set forth by these authors are (i) a simple classification within such diagrams is not possible especially since they depend on the initial conditions and (ii) multipoles with $n > 2$ are suited for transporting, guiding, and collimating ion beams but probably not for mass analysis.

Unfortunately, there are other conclusions presented by these authors that are not due to properties of the multipoles themselves, but rather are a consequence of the selection of initial conditions used in their computations. One example is the reported correlation between the region of total stability and the size of the entrance hole. A second is the quoted dependence of the stability range on the number of poles. It is generally not true that an octopole or hexapole is better suited than a quadrupole for confining a beam close to the axis. In fact, for a specified transverse energy, the preceding statement must be completely reversed. There are other inferences reported that are simply a consequence of the initial conditions chosen. The sudden start of the ions at full local field leads to a phase-dependent additional transverse energy that increases with r and decreases with n. Such initial conditions have to be questioned, even from a practical point of view. Experimentally, it is advisable that the incoming ions see a slow, that is, adiabatic, rise of the rf amplitude. This will be discussed further in Section IV B 1.

Finally, there is a more conceptional problem related to Hägg and Szabo's attempt to extend the stability diagram. More serious than the ambiguity in the definition of (a_n, q_n) is their failure to observe the nonlinear $\hat{r}^{n-1}$

dependence in Eq. (42), which, in our adiabatic treatment, is reflected in the $\hat{r}$-dependent stability parameter, $\eta = q_n \hat{r}^{n-2}$. The fact that the region of stability in a multipole ($n > 2$) is better characterized with $\eta(r)$, rather than q_n, can be nicely illustrated by results presented in Hägg and Szabo (1986c). Figure 4 in this paper shows an ion-beam cross section with a maximum radius $\hat{r} < 0.2$. The operating conditions correspond to $\eta = 5.33\hat{r}^2$, leading to $\eta(\hat{r} < 0.2) < 0.21$, that is, one obtains safe and stable conditions. The conditions of their Fig. 6 result in $\eta = 37.5\hat{r}^2$. Here, many ions have access to regions $\hat{r} \geqslant 0.14$ where η is equal to 0.7 or higher. Therefore, one can expect further loss of ions before the residual cloud remains close enough to the center axis, where one always finds a finite region of stability, since $\eta(\hat{r} = 0) = 0$ for $n > 2$.

These two examples illustrate that our concept of a local stability parameter $\eta(r)$ is superior. The extremely large range of stability reported in Hägg and Szabo (1986b) is simply a consequence of defining the stability parameter only at the electrode surface, $\hat{r} = 1$. Even more important, our definition of η is based on a completely general analysis of the structure of solutions from the general equation of motion, and not on simple analogies. It can be concluded that the only adequate description of multipoles presently available is that based on the η field. Unfortunately, this method is only valid in the adiabatic limit, and it is not straightforward to extend the characterization of stability in multipoles toward higher η values. It is, however, mandatory that any generalization should merge into the conditions derived in this section, such as that given in Eq. (62).

One possible way to map out regions of stability at higher η values has been mentioned in Section II B 4. A systematic search for stable oscillatory equilibria (in the Liapunov sense) could be started from regions where the adiabatic approximation holds and where one can make use of the adiabatic constants of the motion, E_m and $\mathbf{L}$. To illustrate this idea, we have determined the period T of a full oscillation of the secular motion by integration of Eq. (46). If the motion goes through the center, that is, $\mathbf{L} = 0$, the frequency $\omega = 2\pi/T$ can be expressed by η

$$\omega/\Omega = C_n \eta(r_m), \tag{67}$$

where the constant C_n is obtained from an elementary integral, which must be evaluated numerically for $n > 2$. For the quadrupole, where $C_2 = 1/8^{1/2}$ and $\eta = q_2$, one obtains the well-known ratio between the harmonic secular motion with frequency ω and the rf frequency Ω. For $n > 2$, the potential V^* is no longer harmonic and the period T depends on the amplitude r_m, which enters into Eq. (67) via $\eta(r_m)$. Using this relation, initial conditions for stable periodic trajectories with prescribed Ω/ω can be narrowed down. For

example, one predicts for an octopole with $C_4 = 0.152$ and $\Omega/\omega = 10$ an initial velocity corresponding to $\eta_v = 0.66$. This is in good agreement with the numerically determined value of $\eta_v = 0.645\cdots$ (see Section II B 4). Similar comparisons can be made to locate the positions of other integer Ω/ω values in Fig. 4 and to predict initial conditions for periodic trajectories with angular momenta $L > 0$.

This example illustrates that there are mathematical methods (Arnold, 1988; Kruskal, 1962; Lichtenberg and Lieberman, 1983), which may be used for a more general description or classification of ion motion in multipoles or other rf devices. It is unlikely that such an approach will result in a simple (a_n, q_n) diagram and in sharp transitions from stability to instability, which could be easily used for mass or phase-space selection. However, it may lead to new theoretical insight, and to the development of new rf devices, or even to new applications of existing devices in an η range, which in this chapter has been deemed *unsafe*. At present we recommend for most applications operating under *safe* working conditions, that is, to restrict the ion trajectories to regions where $\eta(r) < 0.3$.

4. *Potentials of Realistic Multipoles*

Another question often discussed is the influence of deviations on the ideal electric field. There are several sources of deviations. These include the surfaces of the field defining conductors, which practically never coincide with the mathematically defined boundary conditions. Also, the relative alignment of the electrodes can be perturbed and, often, the metal surfaces are not exact equipotential surfaces. At high ion densities ($> 10^5\,\mathrm{cm}^{-3}$), space-charge effects can greatly contribute to perturbations, and, in this case the potential has to be determined explicitly from Eq. (26). A costly approach to closely approximating ideal fields is to use precisely machined metal pieces. Typically, however, mechanically simple and relatively low cost arrangements of electrodes are used, for example, rods, wires, metal plates, and so on, since many undesired imperfections can be minimized by adequate selection of geometrical and electrical parameters.

The ideal equipotential lines of multipoles were given in Eq. (39). In practice, $2n$-pole devices are usually composed of $2n$ circular rods, equally spaced on a inscribed circle with radius r_0. As a first approximation, the diameter d of the rod can be determined from the radius of curvature of the hyperbolic potential and one obtains

$$r_0 = (n-1)d/2. \tag{68}$$

Use of nonideal electrode structures leads to perturbations in the field that can be expanded in a series of higher-order multipole terms, as given in

Eq. (29). This problem has often been discussed (Busch and Paul, 1961b) in the case of quadrupoles. By minimizing the lowest-order term in the multipole expansion, Dayton et al. (1954) have shown that for a quadrupole with round rods, the rod diameter should be slightly larger than that given by Eq. (68), that is, $d/2 = 1.148r_0$. Denison (1971) has shown that if one accounts for the cylindrical tube which commonly surrounds the rods, a diameter $d/2 = 1.1468r_0$ should be used. To accurately determine the effective potential or adiabaticity parameter, Eq. (45) and Eq. (47), respectively, the higher-order multipole terms should be taken into account. However, it is not necessary to minimize these terms if ion guidance or ion trapping rather than sharp mass selection is intended, since small geometrical deficiencies do not influence the general properties of these devices. This will be demonstrated using numerical examples.

Rather than using precisely positioned rods, very good approximations of given electric fields can be achieved by an arrangement of wires surrounded by a metal cylinder. This has been briefly described in Section II C 2 and has been used, for example, to approximate quadrupole fields (Matsuda and Matsuo, 1977). We have also used this method as a numerical means of studying the influence of field imperfections on the effective potential. Realistic octopole structures have been represented by 96 pairs of line charges, as illustrated in Fig. 13. The boundary conditions imposed by each rod are fulfilled at 12 points, indicated by the solid squares, while image charges are used to simulate the position and potential of the shielding cylinder (dashed line). This method reduces the boundary value problem to a simple algebraic problem, and thereby allows one to study many details of the electrostatic and the effective potential, for example, the influence of the pole shape, misalignment, electrical distortions, and also field penetration from surrounding ring electrodes.

Figure 14 shows the effective potential of a realistic octopole whose dimensions are given as defined in Eq. (68). The inner equipotential lines have almost perfect rotational symmetry and their positions are in excellent agreement with the values calculated from the analytical expression given by Eq. (45). There are some slight perturbations close to the electrodes, especially between the rods where the effective potential is somewhat weakened. This effect is even more pronounced in the lower part of Fig. 14, where the shape of four rods has been modified significantly, for example, for passing a crossed molecular beam. Note that in both cases ions with a transverse energy of less than 0.5 eV see almost circular equipotential lines. It is a general fact that the actual field converges to that of an ideal multipole as one moves farther away from the rods. One example illustrating the influence of a mechanical misalignment is depicted in Fig. 15. The significant shift in the position of one pole on the right perturbs the total symmetry

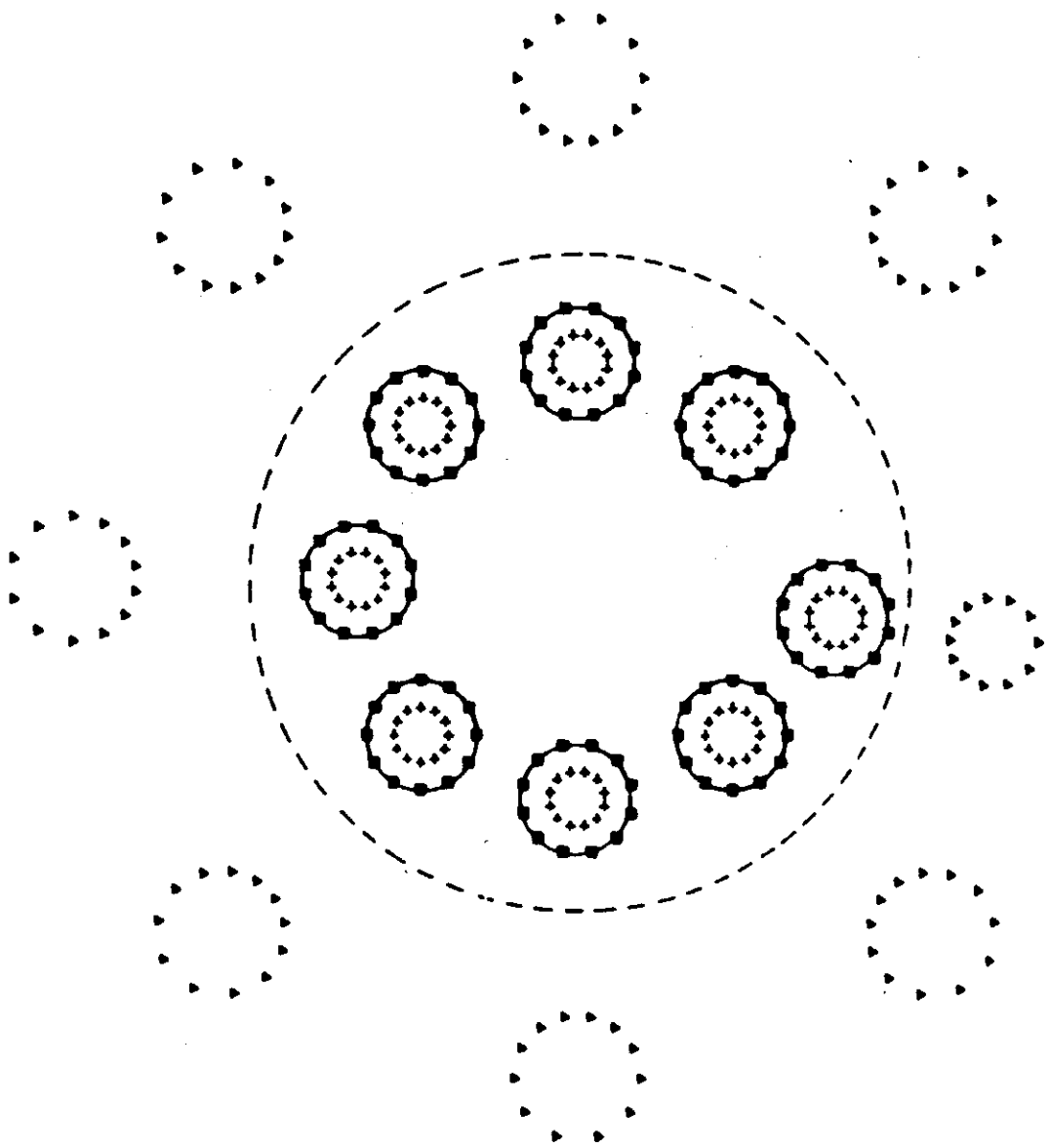

Figure 13. Positions of 96 pairs of line charges (+, ▶) used for numerical determination of realistic octopole potentials. The rods (circles) are approximated by imposing the desired boundary values in the positions (■). The dashed line represents the shielding cylinder. This example shows the arrangement of an octopole with a slightly distorted geometry; the resulting potential is plotted in Fig. 15.

and influences the inner potential lines. Nonetheless, this octopole can still be used to guide ions safely with transverse energies up to 4 eV. All three examples clearly demonstrate that the use of multipoles as ion guides does not require very accurate electrode shapes, and that the alignment is also rather uncritical.

More serious problems and significant distortions are usually caused by changes in the work function, contact potential imperfections, or contamination of the rods. The build up of charge on insulating layers of the electrode surface is less critical for an ion guide than for a mass filter,

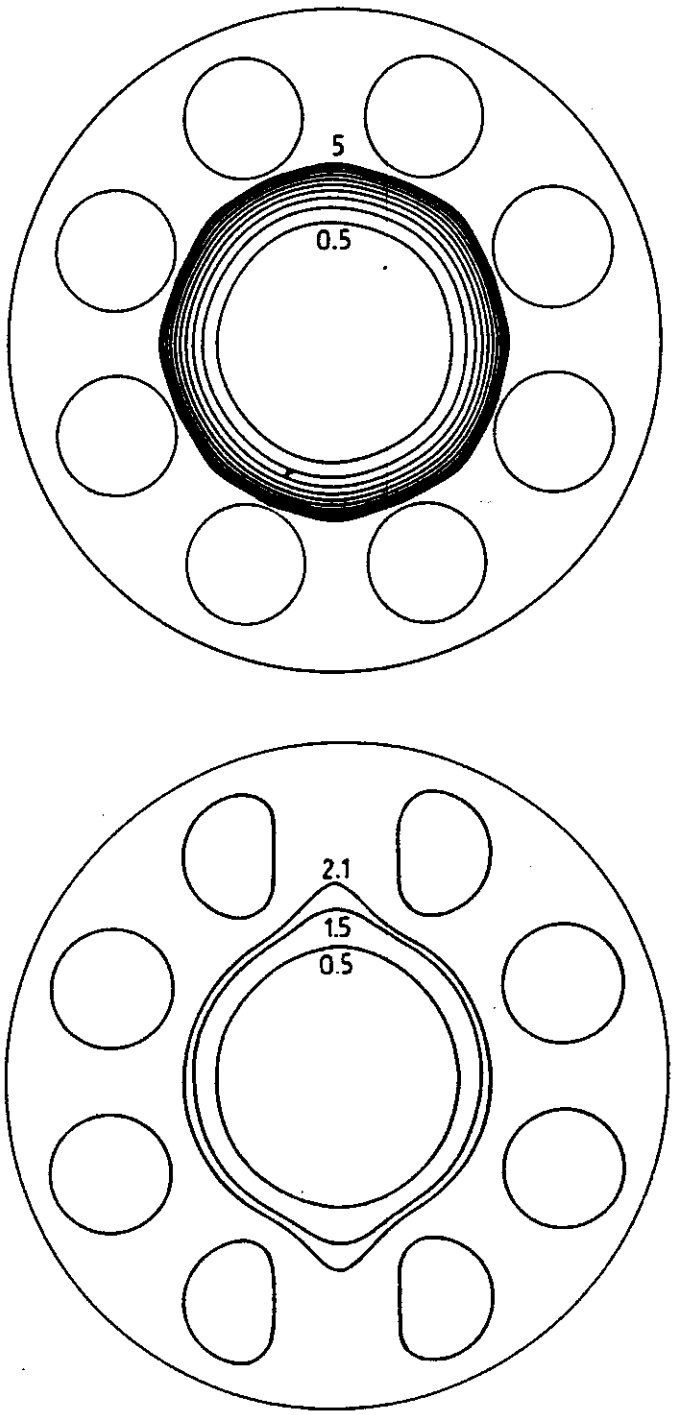

Figure 14. Contour plot of the effective potential (in eV) of an octopole with circular rods, diameter given in Eq. (68). The result illustrated is very similar to the potential obtained with ideal hyperbolic electrodes; the graphic resolution is not sufficient to demonstrate the differences. Only the equipotential lines close to the rods show slight deviations from the rotational symmetry. The lower panel shows the influence of a significant deformation of the electrodes (e.g., geometry for a crossed-beam arrangement).

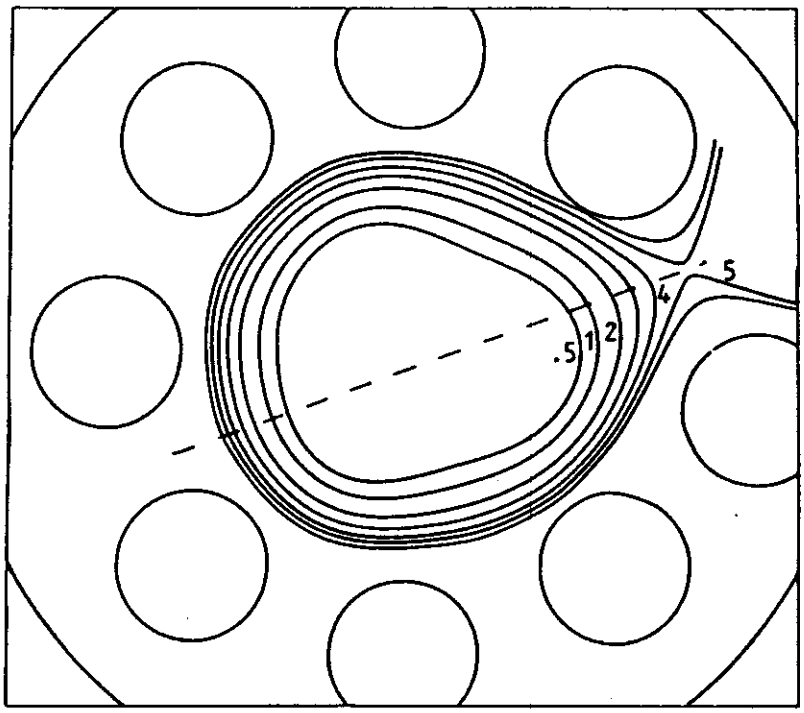

Figure 15. Contour plot of the effective potential (in eV) from a mechanically distorted octopole (see Fig. 13), illustrating that geometric precision is not required for using multipoles as ion guides.

since in the former all ions are usually transmitted, while in a quadrupole the surfaces are continuously under ion bombardment. The effect of an additional dc voltage applied to a single rod in an octopole is illustrated in Fig. 16. The effective potential becomes half-moon shaped, and the distortion pushes the ions toward the other half of the ion guide. A cut through the effective potential along the dashed line is shown in the lower part of Fig. 16 for several rf amplitudes. This figure illustrates that the minimum energy path is a function of V_0. This feature can be used to test a device for a surface distortion localized on a single rod. However, according to our experience, it is more reasonable to assume a patchiness of distortions distributed statistically both in the r and φ directions. Since the influence of the distortions is least significant in the center, operating the beam guide at high rf amplitudes so that the ions are compressed close to the center line, is usually superior. Further discussion of surface problems follows in Section III C 2.

A final example of a numerically determined potential distribution is given in Fig. 17 and shows the influence of a cylinder surrounding an octopole. In order to display the very small effect of the field penetration, the rf and the dc potentials have been set to zero. The equipotential lines are given as a fraction of the externally applied voltage, U_{ext}. It can be seen for the geometry shown that the center of the octopole is raised by 2.5 mV per 1 V applied to the cylinder. Using short cylinders, local potential barriers can be created.

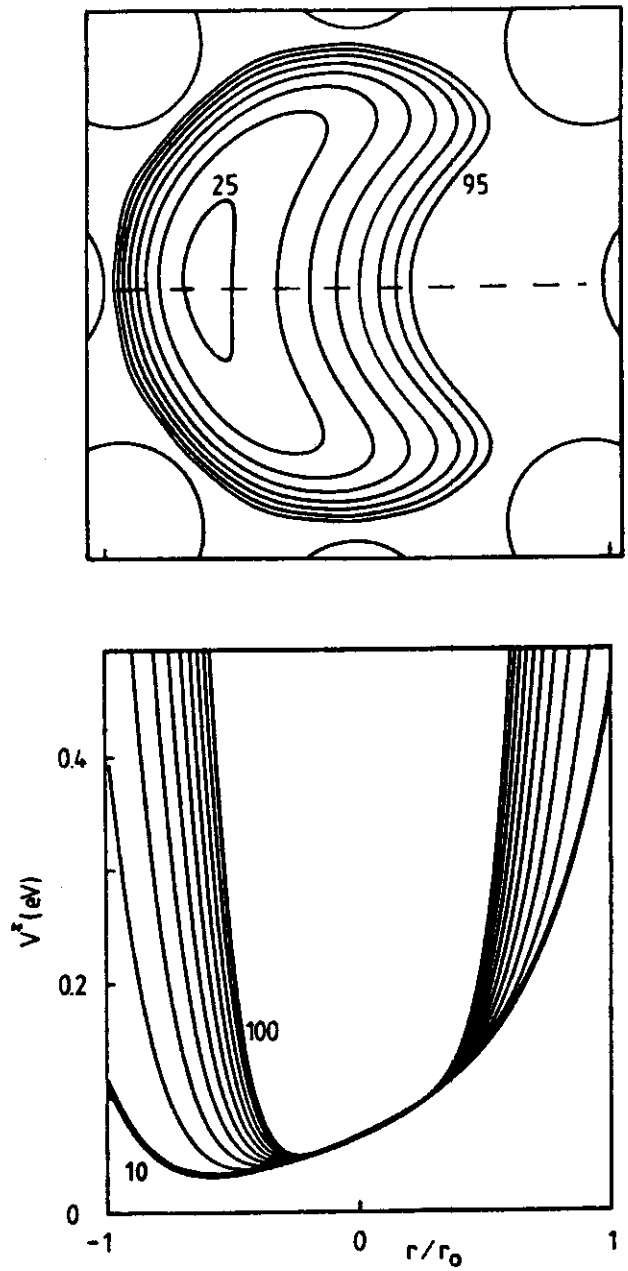

Figure 16. Influence of an electrostatic potential distortion. In this example one rod on the right is charged to +0.5 V. The upper panel shows a contour plot of the effective potential (in meV, 10-meV steps) for a low rf amplitude of 10 V. The lower panel is a cut through the potential along the dashed line and illustrates the influence of the rf amplitude as it is increased in 10-V steps.

Such ring electrodes have gained practical importance both for localizing potential distortions and for forming and trapping extremely slow ion beams. Here again we refer to Section III C.

In summary, it is not necessary that the contour of the cross section of the electrode have the exact shape given by Eq. (39) in order to achieve the best possible performance. The required accuracy of a multipole field depends strongly on the desired application. When using rf electrodes for guiding and

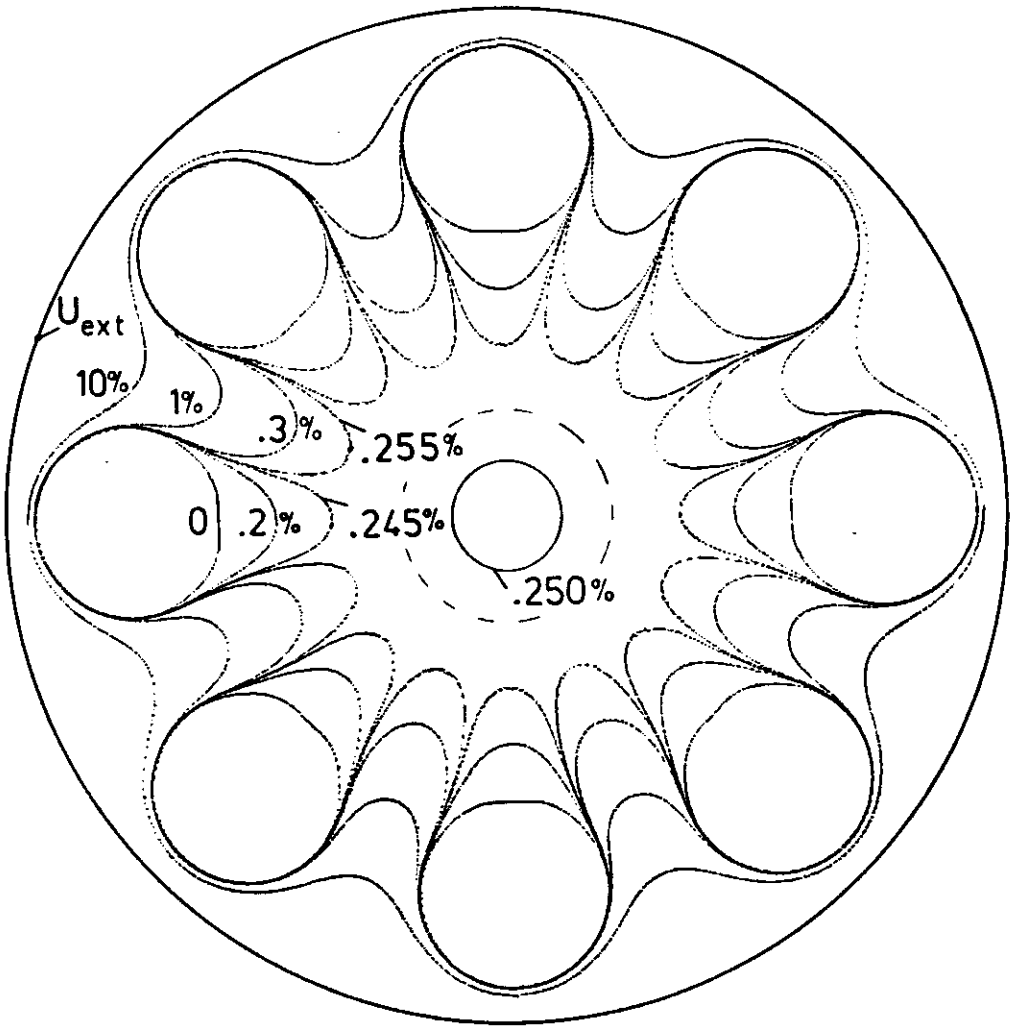

Figure 17. Contour plot of the electrostatic potential inside an octopole caused by a voltage U_{ext} applied to the surrounding cylinder. The potential of the eight rods is set to zero. The height of the equipotential lines is given relative to the external voltage. For the geometry shown, the potential on the centerline is shifted by 0.25%.

storing ions within the safe adiabatic limit, the approximation of the field geometries by real electrodes is not critical, in contrast to the quadrupole mass filter where sharp mass selection is intended. As a general rule, it is advisable to avoid sharp edges or small bending radii since they cause steep field gradients, and therefore large local $\eta(r)$ values, according to Eq. (21). Of course the situation becomes different if one finds, for a well-defined potential, some application where critical operation at the border between stability and instability is demanded. There, the requirements for the experimental realization of the ideal boundary conditions become the same as those for mass selective quadrupole fields, and may possibly be even more critical. Finally, one should be aware of the fact that problems due to potential distortions of the metal surfaces are often more critical than deviations from mechanically ideal electrodes.

E. Energy Distributions

To aid in the interpretation of experiments employing stored or guided ions, it is often necessary to understand the distortion of the ion kinetic energy distribution caused by the confining rf field. One extreme is the process of rf heating, which couples kinetic energy from the micromotion (i.e., from the rf field) into the secular motion. Such heating processes have been considered for acceleration of ions to high velocities (Motz and Watson, 1967) or for mass-selective ejection (Busch and Paul, 1961a), and are predominantly based on resonant approaches. In contrast, most of the applications in this chapter deal with slow ions and make use of adiabatic conservation of energy by working at high frequencies, as has been discussed in Section II B.

Several models and mathematical methods have been developed to examine kinetic energy distributions of ions stored in quadrupole traps, especially under the inclusion of collisions and space-charge effects. The results have been summarized in several reviews (March and Hughes, 1989; Todd et al., 1980; Vedel, 1991). Energy distributions in quadrupole fields are significantly inferior to those in higher-order multipole fields or other suitable electrode arrangements. This can be understood qualitatively based on several of the preceding figures. For example, Fig. 2 shows stable confinement; however, it is nearly a worst case example with respect to the kinetic energy distribution because the wiggling motion is always rather intense. Even in the minimum of the effective potential, the ion interacts strongly with both the dc and rf fields. Damping of this wiggling motion by inelastic collisions would lead to a drift into regions of weaker rf field, and finally, to a loss at the outer cylinder. All multipoles feature a weak-field region close to the center, which becomes broader with increasing number of poles, as can be seen from comparison of Fig. 9 and Fig. 10. Similar qualitative conclusions can be drawn from the steepness of the effective potential. For example, Fig. 8 shows that the ring electrode trap is superior to an octopole.

In the following section, we first describe the time dependence of the momentary kinetic energy of an ion during its reflection from an rf wall and derive time-averaged energy distributions. The influence of collisions with neutral molecules will then be treated for a few special cases using numerical simulations.

1. *Instantaneous and Time-Averaged Energy*

We have shown in Section II B that on average the system behaves like a conservative one if the condition for the adiabatic approximation, $\eta < 0.3$, is fulfilled. This means that the total energy, E_m, as defined by Eq. (16) or Eq. (46), is conserved within narrow limits. The example given in Fig. 4 nicely illustrated that the relative energy changes are typically below 10^{-6}

if η remains smaller than 0.3. It was discussed, however, in Section II B that the effective potential is in reality the average of the kinetic energy of the fast oscillatory motion. This means that there is a continuous exchange between the two different forms of translational energy, the wiggling motion and the secular motion.

For deriving an expression for the total instantaneous kinetic energy within the adiabatic theory, we assume for simplicity a constant static potential, that is, $\Phi_s = \text{const}$. The exact motion, $\mathbf{r}(t)$, is represented in first-order approximation by the superposition of the secular motion, $\mathbf{R}_0(t)$, and the wiggling motion, $\mathbf{R}_1(t)$, as discussed in detail in connection with Eq. (6). The relation between the effective potential energy, $V^*(\mathbf{R}_0)$, and the kinetic energy, $\frac{1}{2}m\dot{\mathbf{R}}_1^2$, has been emphasized by the representation chosen in Eq. (18) and is depicted in Fig. 18. This figure refers to an ion that has been started in the center of an octopole with an initial kinetic energy E_m. The smooth line indicates the effective potential energy, which reaches its maximum $V^* = E_m$ in the turning point of the secular motion, while the oscillatory line shows the kinetic energy $\frac{1}{2}m\dot{\mathbf{R}}_1^2$ along the same trajectory $\mathbf{R}_0(t)$. This kinetic energy fluctuates between 0 and $2V^*$ during the reflections from the rf wall. The absolute maximum can reach $2E_m$, depending slightly on the rf phase δ.

The *total* instantaneous kinetic energy has to be calculated from the sum of the two velocity vectors $\dot{\mathbf{R}}_0$ and $\dot{\mathbf{R}}_1$;

$$E_{\text{kin}}(t) = \tfrac{1}{2}m[\dot{\mathbf{R}}_0(t) + \dot{\mathbf{R}}_1(t)]^2. \tag{69}$$

Assuming the extreme case, that the smooth and the oscillatory motions are parallel, and expressing $\dot{\mathbf{R}}_0^2$ and $\dot{\mathbf{R}}_1^2$ by the effective potential using Eq. (16) and Eq. (18), respectively, one obtains for the momentary total kinetic energy the simple relation

$$E_{\text{kin}}(t) = [(E_m - V^*)^{1/2} + (2V^*)^{1/2} \sin \Omega t]^2. \tag{70}$$

It is obvious that the total instantaneous kinetic energy is identical to E_m in the field-free region, that is, for $V^* = 0$, and that it becomes equal to $2E_m \sin \Omega t$ for $V^* = E_m$. It is also easy to show that the absolute maximum of the total kinetic energy, $3E_m$, is not reached at the turning point of the secular motion, but rather at that position in the field where two-thirds of the total energy is converted into oscillatory motion and one-third remains in smooth motion. During one reflection, E_{kin} oscillates between 0 and $3E_m$, as can be seen from the dashed line in Fig. 19.

Note that Fig. 19 also allows one to gain an impression of the high quality of the first-order adiabatic approximation. The heavy line shows the exact kinetic energy, $\frac{1}{2}m\dot{r}^2$, obtained by direct numerical integration of the equation

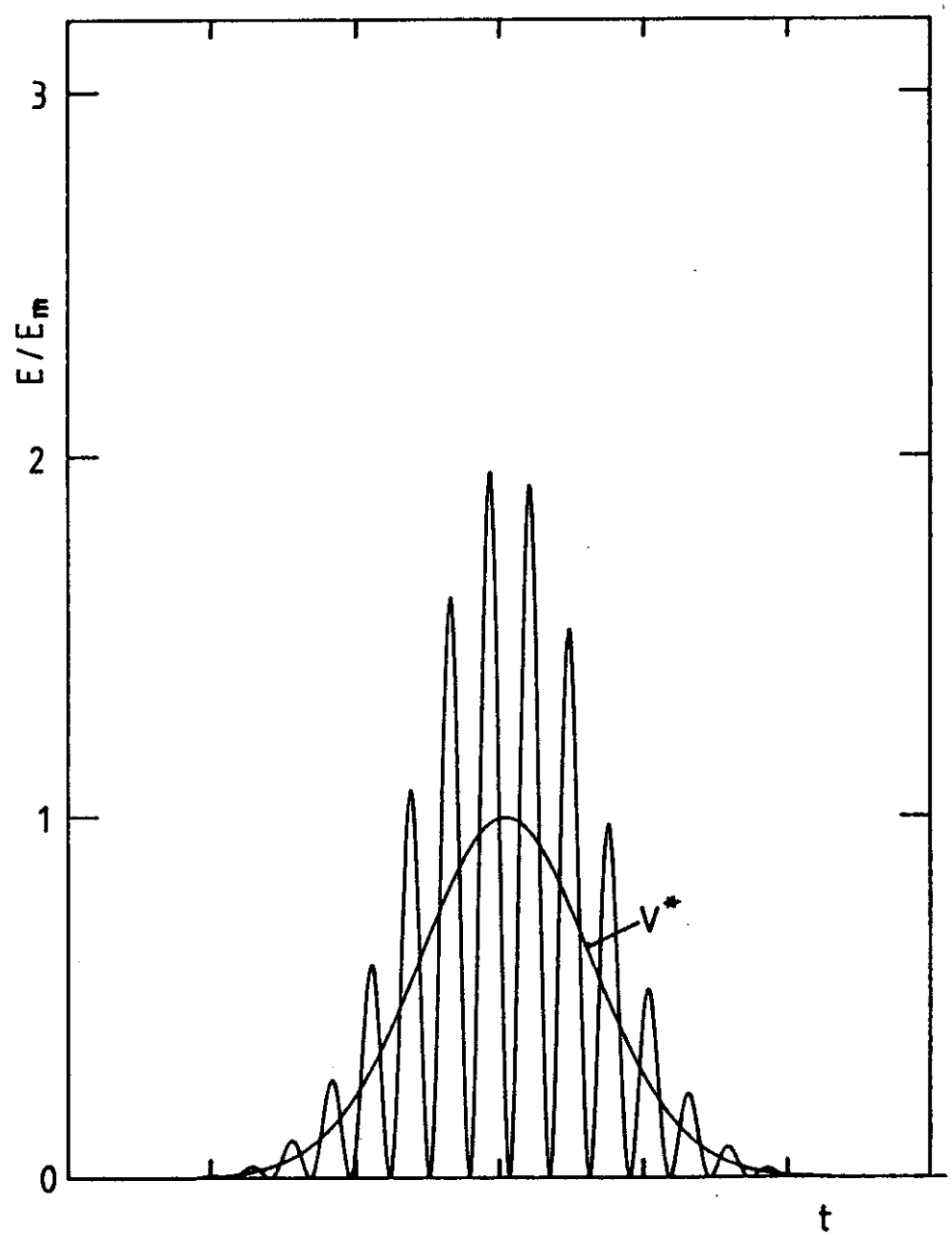

Figure 18. Time dependence of the kinetic energy ($\frac{1}{2}m\dot{\mathbf{R}}_1^2$) and of the effective potential energy V^* during one reflection from an rf wall. The oscillatory line represents the kinetic energy of the wiggling motion, which varies between 0 and $2E_m$. The smooth line shows the increase of the effective potential energy along $\mathbf{R}_0(t)$.

of motion. The dotted line, which has been calculated for $\eta_m = 0.3$, clearly shows that higher-order microoscillations contribute only with small corrections to the results derived within the first-order adiabatic approximation. The two curves become practically indistinguishable for $\eta_m < 0.2$.

The opposite extreme of relative orientation of $\dot{\mathbf{R}}_0$ and $\dot{\mathbf{R}}_1$ in Eq. (69) is obtained when the oscillatory motion is orthogonal to the smooth motion. This occurs, for example, in a multipole for a motion along those lines where

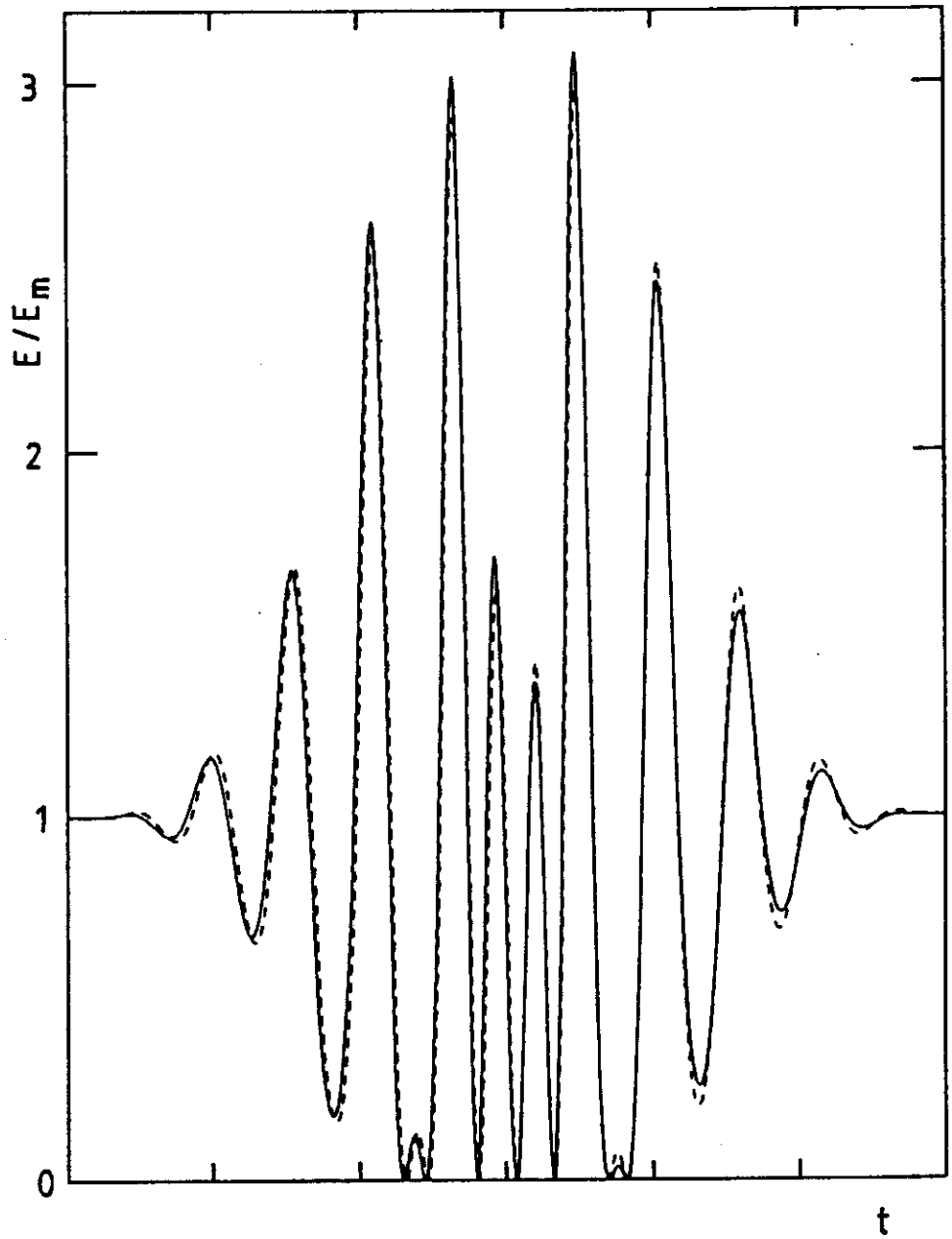

Figure 19. Total instantaneous kinetic energy of an ion during one reflection from an rf wall. The dashed line has been calculated within the adiabatic approximation, $\frac{1}{2}m(\dot{\mathbf{R}}_0 + \dot{\mathbf{R}}_1)^2$, while the solid line is the numerically exact solution, $\frac{1}{2}m\dot{\mathbf{r}}^2$.

$\cos n\varphi$ vanishes [see Fig. 11 or Eq. (39)], since in this case the two vectors $\mathbf{E}_0$ and ∇E_0 are orthogonal. In this situation, the total kinetic energy is just the sum of the two kinetic energies and oscillates only between 0 and $2E_m$. It should be emphasized that Eq. (70) is valid for all field geometries. Note, however, that the energy E_m only accounts for those degrees of freedom that are affected by the rf field, while energy contributions from other degrees of freedom, for example, the axial motion in an octopole, remain unperturbed.

For most applications, it is more important to know the time-averaged distribution of the momentary kinetic energy. Such results have been

computed by following ion trajectories with different initial conditions and by continuously recording their energies (usually in 96 steps per rf period). A typical result, accumulated over 3×10^5 rf periods, is shown in Fig. 20 for an octopole using $\eta_m = 0.25$. The kinetic energy is measured relative to the initial energy E_m. The most probable value, which in this case is arbitrarily normalized to 1, is slightly below $E/E_m = 1$. Instances in which the energy reaches the predicted maximum of $3E_m$ are very rare, and in Fig. 20 are not

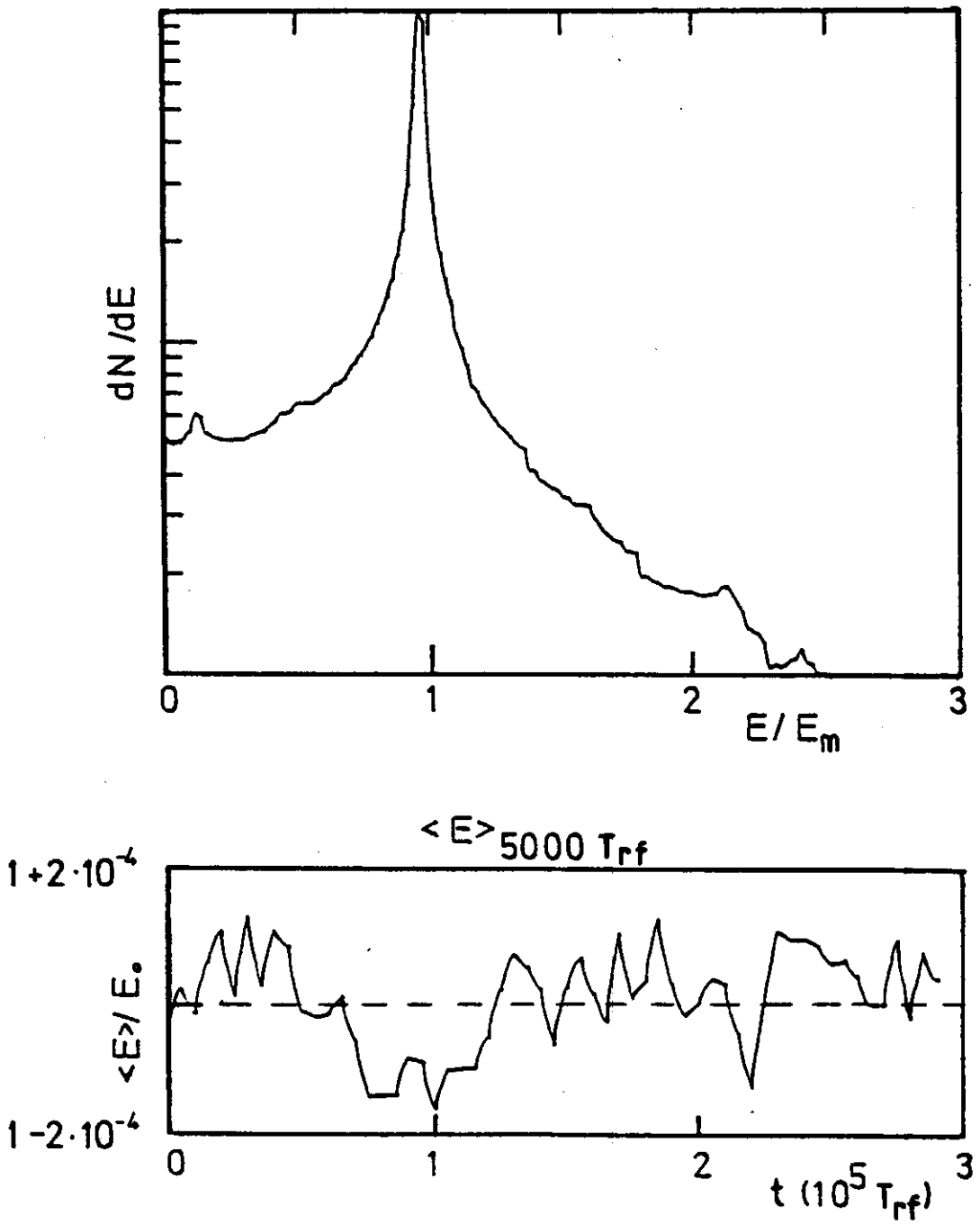

Figure 20. Numerically determined kinetic energy distribution of an ion moving in an octopole accumulated over 3×10^5 rf periods T_{rf} ($\eta_m = 0.25$). The lower panel shows the fluctuations of the mean energy averaged each time over 5000 rf periods.

on scale. The time dependence of mean values, $\langle E \rangle$, averaged in each case for 5000 rf periods, is plotted in the lower part of Fig. 20. The fluctuations are on the order of 10^{-4} and are due more to the statistics of the interrogation intervals rather than to a real fluctuation of the total energy. This result agrees qualitatively with that shown earlier in Fig. 4. Note, however, that Fig. 20 shows the energy averaged along the whole trajectory, while in Fig. 4 the energy is probed only at a single point in the field-free center.

As already indicated by the trajectories shown in Fig. 9 and Fig. 10, the storing field perturbs the ion energy to a smaller extent as the number of poles is increased. A quantitative comparison between numerically determined energy distributions for a 16-pole and a 32-pole is shown in Fig. 21. The extremely narrow widths of the distributions indicate that the ions spend most their time in field-free regions. The energy distributions have also been studied as a function of η_m. It was found that there are no significant changes as long as η remains smaller than 0.3.

In summary, the modulation of the kinetic energy by the rf field can often be neglected, especially in ion-beam guides where only the transverse part of the energy is affected and where usually either no or single-collision conditions prevail. The situation changes completely if the stored ions undergo many collisions with a buffer gas. This leads, on the one hand, to a thermalization of the ion energy if the energy exchange takes place in a field-free region. If, on the other hand, one of the collisions occurs in the rf field, the adiabatic energy exchange between the ion and the rf field breaks down. The consequences of collisions are discussed in the following section.

2. *Influence of Collisions*

As a means of determining the velocity and spatial distributions of stored ions under the inclusion of collisions, we have carried out a series of numerical simulations (Kaefer, 1989; Scherbarth, 1984). Since our primary goal was to obtain realistic energy distributions for H^+ and C^+ ions stored in a cold hydrogen buffer gas under actual experimental conditions, this work did not systematically study different parameter dependencies. Calculations have been performed for linear $2n$-pole traps ($n = 2, 4$, and 8) and for the ring electrode trap (see Section III E).

The computer program consists of our standard code for the numerically exact description of the ion motion in a particular time-dependent field and a subroutine for simulating collisions. The trajectory calculations take advantage of the fact that the potential of a cylindrical multipole field, Eq. (39), or a ring electrode trap, Eq. (34), depends only on two coordinates. During collisions, however, the relative motion is treated in three dimensions. The trapping fields have been assumed to be infinitely long, that is, effects from electrostatic gates or barriers used to close a real trap are ignored.

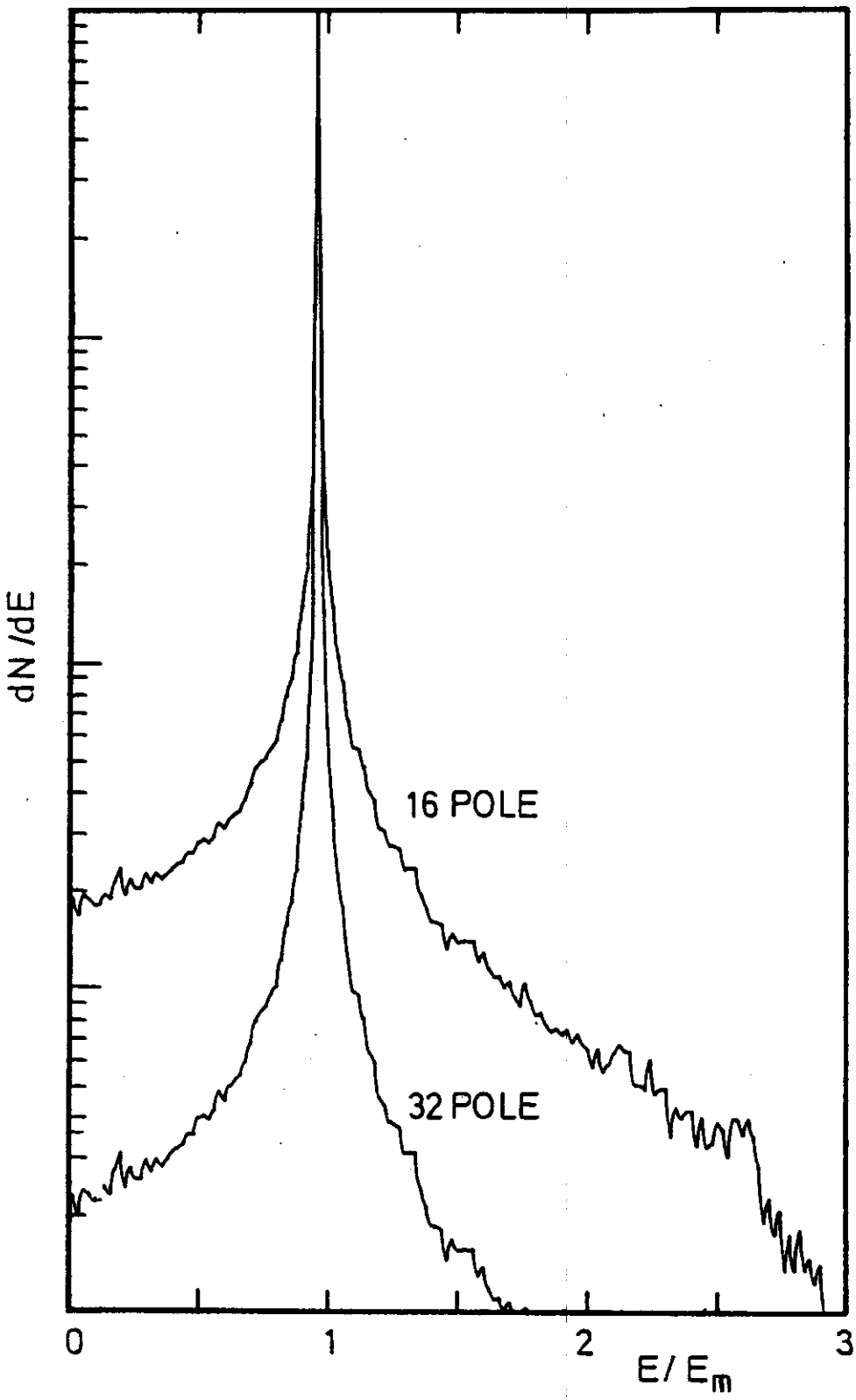

Figure 21. Numerically determined kinetic energy distributions of an ion moving in a 16-pole or a 32-pole averaged over 3×10^5 rf periods ($\eta_m = 0.25$).

The temperature of the hydrogen target gas was either 80 K or 300 K. The random selection of the target velocity, simulated by a three-dimensional Maxwell–Boltzmann distribution, and the thermal population of the individual rotational H_2 states were accounted for by properly weighted random selection. Usually we chose normal-H_2, although in some calculations pure para-H_2 was used. The time between collisions, on average 200 rf periods, was also chosen randomly, as was the rf phase. The collision rate was about 10 times higher than in typical experiments; however, it was kept low enough to avoid correlation between subsequent collisions.

The $H^+ + H_2$ collision process has been modeled in great detail using experimentally verified state-to-state differential cross sections, derived from a dynamically biased statistical theory (Gerlich 1977, 1982; Gerlich et al., 1980) and accounting for ortho–para transitions (Gerlich, 1990). $C^+ + H_2$ collisions were described in a similar way, since in this system, also, formation of a long-lived complex determines the collision mechanism at the low energies of our study (Gerlich et al., 1987). The laboratory motion of both collision partners was described independently and in all three dimensions. Details of the necessary forward–backward transformations between laboratory and center-of-mass frames are described in Gerlich (1989a).

To avoid additional expenditure with the initial conditions of the ion, we make use of the fact that these are essentially randomized after a few collisions. Therefore, it was sufficient to simulate the energy distribution by following a single ion over a long period of time and over many collisions. For low ion densities, the results were identical with an average over an ensemble of stored ions. The program was tested by switching off the rf field, leading to a perfect thermal energy distribution of the ions.

A few typical results are shown in Fig. 22 and Fig. 23. Each of the distributions is the result of 10^4 collisions. The parameters in mV correspond to potential distortions and are explained subsequently. The distributions obtained are not purely thermal; however, they can be composed in good approximation by a weighted sum of two Maxwell–Boltzman distributions, resulting in two characteristic temperatures T_1 and T_2, and related weighting factors.

The aim of the presentation in Fig. 22 is to emphasize the high-energy tail and the influence of the multipole order. It can be seen that the distribution of ions stored in an octopole with H_2 at 300 K has an extremely hot tail. The 16-pole also exhibits a high-energy tail, which is comparable to a 700 K Maxwell–Boltzmann distribution, shown for reference in the third panel of Fig. 22. Indeed, the fraction of very fast ions is rather small (10^{-6} and below); however, they can obstruct the observation of rare processes like radiative association if these products compete with products from endothermic

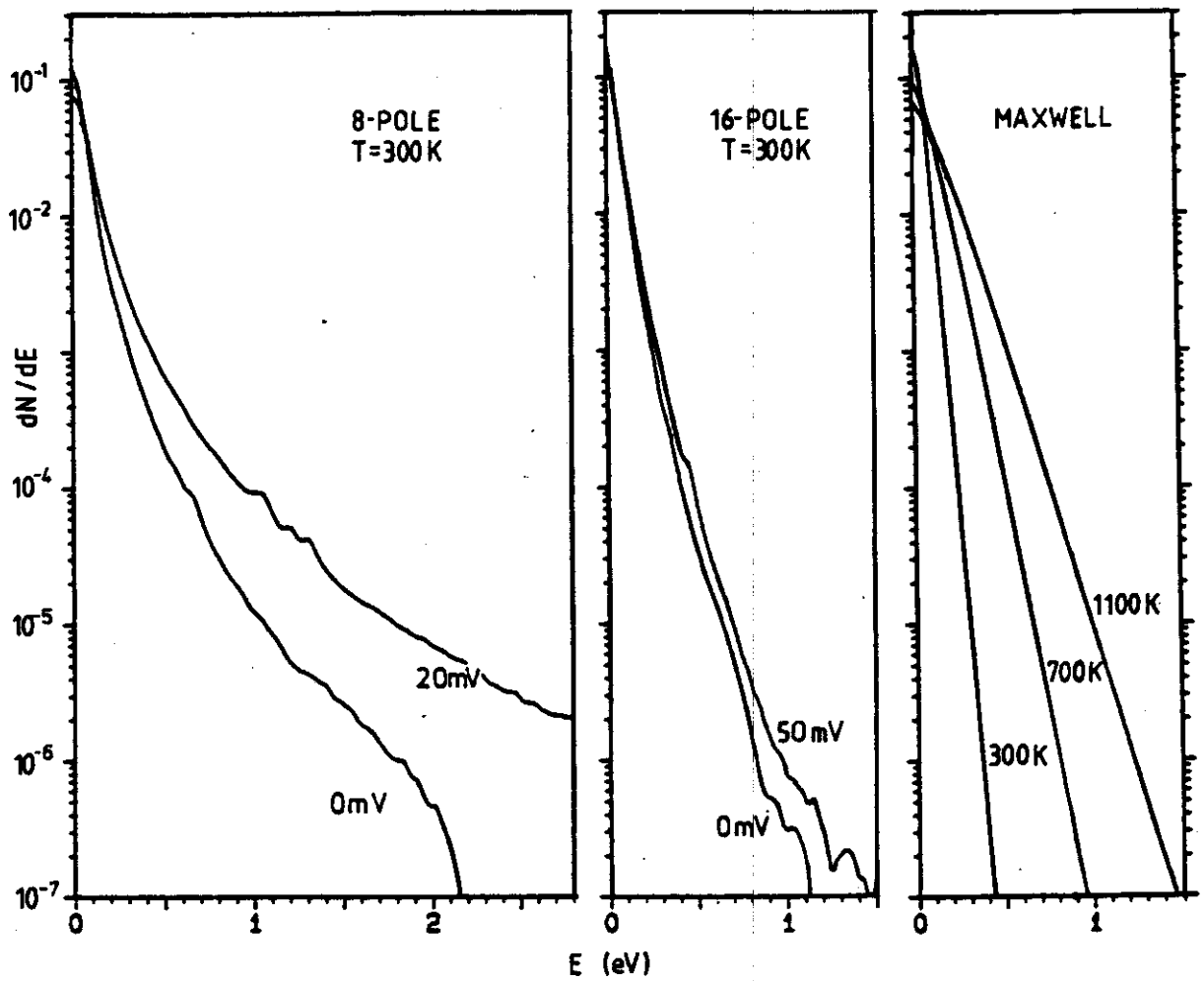

Figure 22. Numerically determined kinetic energy distributions calculated for H^+ under inclusion of collisions with room-temperature normal-H_2. The details of the model are described in the text. The two left panels show results for an 8-pole and a 16-pole. For comparison, the right panel depicts thermal distributions at three temperatures. The scales have been chosen to stress the high-energy tail of the distributions. For an octopole, a weak potential distortions of only 20 mV has a dramatic effect.

channels. One example is the formation of H_2^+ in fast $H^+ + H_2$ collisions via charge transfer.

A presentation that allows one to view simultaneously the low- and the high-energy regimes is given in Fig. 23 (although the logarithmic energy scale can lead to a somewhat erroneous visual weighting of the area normalized distributions). In these two examples, H^+ and C^+ ions are stored in a ring electrode trap ($r_0 = 0.5$ cm) with 80 K normal-H_2. An analysis of the H^+ distribution, plotted in the upper panel, indicates that 75% of the H^+ ions can be described by a 80 K thermal distribution. An additional 25%, however, resides in a 200 K hot tail. This heating is partly caused by too low of an rf frequency (27 MHz) and by the unfavorable mass ratio (light ion in a heavier buffer gas). Both effects are significantly reduced if one goes to C^+, as shown

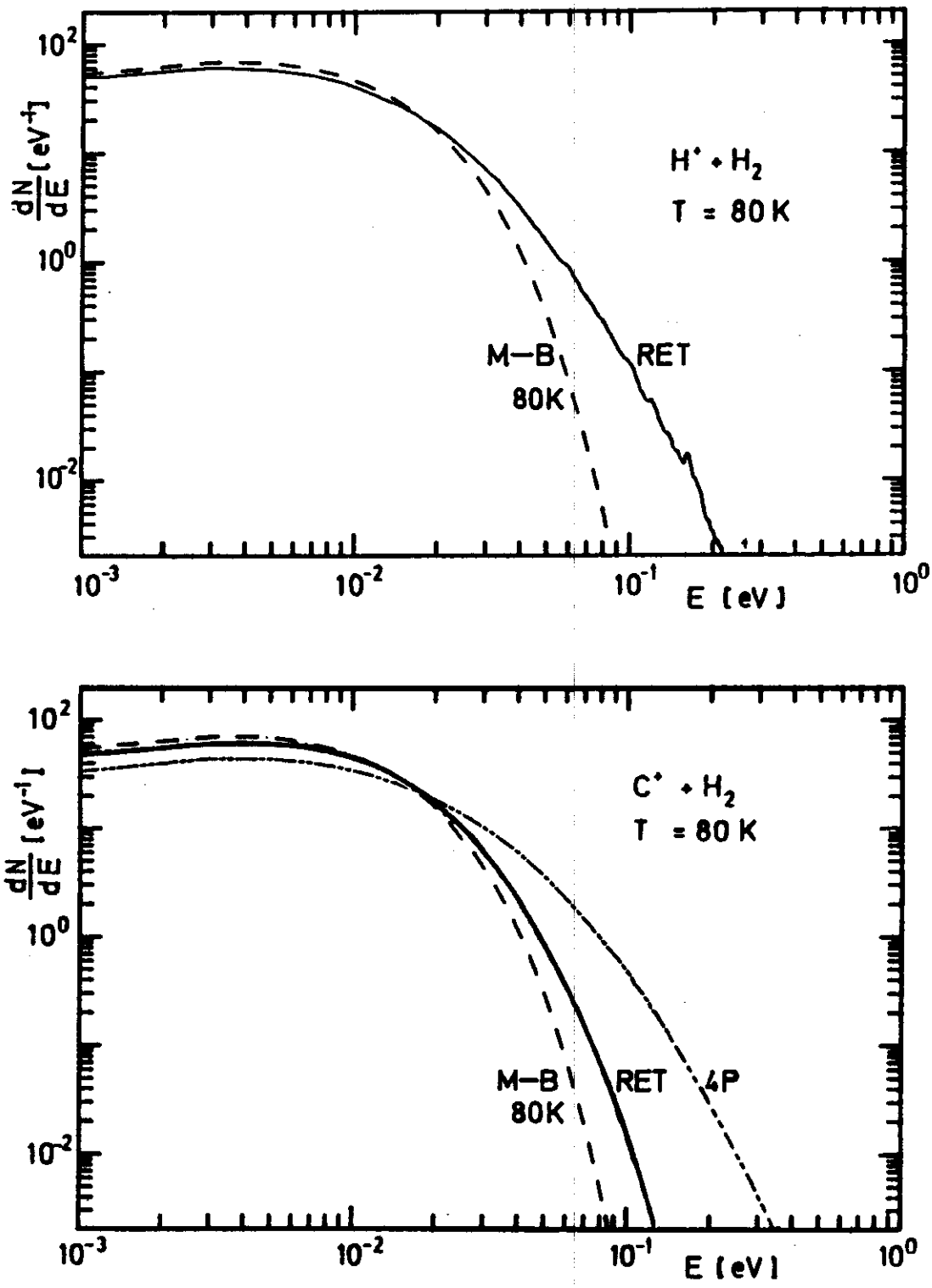

Figure 23. Log/log representation of numerically determined energy distributions for H^+ (upper panel) and C^+ (lower panel) stored in a ring electrode trap (RET) with 80 K H_2 buffer gas. The comparison with the 80 K thermal Maxwell–Boltzmann (M–B) and the quadrupole trap (4P) distributions is discussed in the text.

in the lower panel. To account for the small fraction of fast ions in this distribution, we only need a 160 K Maxwell distribution with a relative weight of 10%. An energy distribution of ions stored in a linear quadrupole trap is also compared quantitatively in this figure. Since in such a trap the ions are under the influence of the rf field for a much longer time, the energy distribution becomes significantly broader. In the example shown, more than 50% of the ions stored in the quadrupole are characterized by a temperature of 300 K.

There are several possible distortions that can increase the duration of the interaction of the ions with the rf field and cause additional perturbation of the energy distributions. Superimposed static field gradients, as shown for example in Fig. 12, or surface potential distortions, seen in Fig. 16, can attract ions toward the electrodes. A similar effect can result from repulsion by space charge. For modeling such an effect, we have performed calculations using a potential wall, raised in the center of the trap, with a mean range of $0.5r_0$. The left panel in Fig. 22 shows that in an octopole a barrier of only 20 mV causes a significant increase in the number of fast protons. If n is increased, the effect becomes smaller, as seen in the middle panel for the case of a 16-pole.

Although the examples presented are rather special cases, some general conclusions can be drawn from this section. It is evident that the rf field always has some influence on the ion energy distribution; however, under collision-free conditions, the effect is usually negligible. For collisional ion cooling, the rf frequency, the mass ratio, and the trap geometry all play an important role. The frequency should be as high as possible, the buffer gas should be light relative to the ion mass, and the rf trap should have a wide field-free region with steep confining walls. If collisions play a role, quadrupole ion traps should be avoided. However, for laser cooling of trapped ions, Paul traps are superior, since the harmonic effective potential simplifies the optical side-band spectrum.

III. EXPERIMENTAL APPLICATIONS AND TESTS OF SEVERAL RF DEVICES

A. Introduction

The preceding section surveyed the development of the theory related to the interaction of oscillatory electric fields with charged particles. In this section we describe detailed applications and experimental tests of several rf devices including the focusing quadrupole, octopoles, rf ion sources, and the ring electrode trap. As an introduction, we briefly review a few applications in addition to those just mentioned, some of which have a more historical significance. Included are experiments where laser fields or microwave fields interact with electrons or low-frequency fields with microparticles. The range

of rf frequencies, $\Omega/2\pi$, of the selected examples extends from 10^2 to 10^{14} Hz, while the charge to mass ratio, q/m, ranges from 1.76×10^8 to 10^5C/g for electrons and heavy ions, to less than 10^{-6}C/g for microparticles. Characteristic lengths L of the field geometries range from cm to μm, and are either determined by a typical distance of the electrode structures, or given by the wavelength, as in the case of microwaves or optical waves. The interdependence of Ω, q/m, and L is given by Eq. (21), and a crude estimate of the relation between q/m and Ω can be obtained by using $\eta = 0.3$ and approximating the gradient of the field, ∇E_0, simply by E_0/L.

As in Section II A, we begin by examining the interaction between electrons and electromagnetic fields. One of the first experimental attempts to observe scattering of electrons by standing waves was reported in 1965 (Bartell et al., 1965), and later, with the availability of very intense laser beams, it became possible to provide safe experimental evidence (Bucksbaum et al., 1987) that an inhomogeneous laser field can create an effective potential wall, causing elastic scattering of free electrons. Many correlated problems occur in experiments on the ionization of atoms in strong radiation fields since the ejected photoelectron is created in a region of high laser field. Provided that the spatial and also the temporal variations of the field are slow, that is, change adiabatically, the electron–laser interaction can be explained on the basis of the conservative quasipotential derived in Section II. Nonconservative behavior has recently been demonstrated with ultrashort laser pulses (Bloomfield, 1990; Bucksbaum et al., 1988).

An interesting and illustrative experiment has been performed by Weibel and Clark (1961) who verified experimentally that a beam of electrons can be guided in stable orbits along the axis of a circular wave guide. This axis coincides with one nodal line of the microwave field and is therefore the locus of a two-dimensional effective potential minimum. The electron-beam guide consisted of a 20-cm-long section of a circular, properly terminated wave guide, operated with a frequency of $\Omega/2\pi = 9.29$ GHz. The cavity was fed with 250 kW of rf power in pulses of 2 μs duration. The well depth of the effective potential, achieved with a peak electrical field of 52 kV/cm, was as deep as 400 eV for electrons, and the frequency of the secular motion was reported as $0.033\,\Omega$ (corresponding to $\eta < 0.1$). Their measurement of the guided electron current was in good agreement with their estimate based on the adiabatic theory (Weibel, 1959). Other experiments using microwave resonance cavities have been surveyed by Motz and Watson (1967).

We now wish to shift our focus to rf confining devices that use quadrupole fields. The three-dimensional quadrupole, the Paul trap, has become very popular as a universal ion storage device. Early spectroscopical applications were pioneered by Dehmelt (1969) who employed a variety of different ingenious detection schemes. The last decade has been dominated by sensitive

probing of a few ions or even a single ion via laser-induced fluorescence (Neuhauser et al., 1978). Applications to chemical problems have greatly expanded in the 1980s with the advent of the technique of mass-selective ejection and detection (March and Hughes, 1989). A reminiscence of the development of the quadrupole trap has been presented recently by Paul (1989) in his Nobel prize lecture. Among the first fundamental papers (Fischer, 1959) on the quadrupole ion trap is the experiment by Wuerker et al. (1959a), who suspended charged iron and aluminum particles ($q/m = 5 \times 10^{-6}$ C/g) in a low-frequency (100 Hz) rf field and was able to verify directly, by photographic observation, many details of the kinematics of the particle motion. Other experiments with microparticles and charged droplets (Owe Berg and Gaukler, 1959) have been summarized in Dawson (1976).

The question of the kinetic energy distribution of stored ions is a fundamental problem for spectroscopical as well as for collisional studies, and different attempts to determine or to reduce the ion motion have been made. Effective cooling of the ion motion can be obtained by interaction with a buffer gas (viscous "drag"), as was nicely demonstrated by the crystallization of macroscopic particles moving through air (Wuerker et al., 1959a). A necessary condition is that the neutrals are sufficiently lighter than the ions. Other interesting approaches include adiabatic cooling by slowly lowering the effective potential well (Dehmelt, 1969), or dissipation of the ion energy into an external resonant tank circuit, as has been successfully applied to cool stored protons (Church, 1969). Significant progress in obtaining ultracold ions has been made by laser sideband cooling of trapped ions (Neuhauser et al., 1980), leading to extremely low temperatures, for example, 50 μK (Diedrich et al., 1989), and also to interesting new physical phenomena such as the arrangement of the stored ions into crystals (Blümel et al., 1989; Wineland et al., 1987).

It is impossible in the context of this introduction to refer to the variety of operational modes, applications, and experimental tests that have been performed with the linear quadrupole. Note that in most cases the quadrupole is operated in the narrow band pass mode at q_2 values which are outside the range of validity of the adiabatic approximation, and, therefore, this mode is not considered in this chapter. There are, however, interesting applications and operational modes below $q_2 = 0.4$, which will be mentioned in Section III B.

Besides quadrupole fields, various other types of inhomogeneous rf fields have been used to create effective potential minima. Included are several quadrupole-like electrode structures that use spherical (Owe Berg and Gaukler, 1959) or cylindrically shaped electrodes (Lagadec et al., 1988). By bending the electrodes of a quadrupole into a circular or "racetrack" shape (Church, 1969), a closed structure has been obtained. In such a storage ring,

ion-confinement times of several minutes have been achieved. A curiosity is a six-electrode rf trap that was driven with a three-phase ac generator (Wuerker et al., 1959b).

The use of more complex electrode arrangements for ion confinement was discussed in outlines by Gaponov and Miller (1958) and Miller (1958a, 1958b). As one of the simplest realizations, these authors proposed quasielectrostatic higher-order multipole fields. According to our knowledge, however, no such device was constructed and tested experimentally until the end of the 1960s. At this time, it was recognized by E. Teloy at the University of Freiburg that one can utilize multipole and other electrode geometries to store ions in wide field-free regions and to study low-energy ion-collision processes. The first experimental tests were performed with a ring electrode structure (Bahr et al., 1969; Wernes, 1968 see Section III E). In the subsequent year, several modifications of the electrode structure improved the performance of the trap as an ion source, the first octopole was constructed and tested, and these rf elements were assembled together resulting in the first version of the guided-ion-beam apparatus (Gerlich, 1971; Henchman, 1972). Further improvements and developments of the guided-ion-beam apparatus will be discussed in Section IV A.

B. Quadrupole

In Section II we occasionally referred to the quadrupole for illustrative purposes, since it is utilized in so many areas of science and is undoubtedly the best known rf device. Its features as a mass filter or an ion guide are well documented in many papers, review articles, and books (Dawson, 1976; March and Hughes, 1989). Nonetheless, there are several not generally recognized modes of operation and application that make use of dynamic focusing, time and spatial selectivities, long-time trapping and multiple traverses, and rf amplitude modulation or superimposed auxiliary rf fields. Some of these features are discussed in the following.

In general, the functioning principle of the quadrupole mass filter is fully described by the Mathieu equation, the solutions of which can be classified with the help of the (a_z, q_z) stability diagram. Of practical importance is only the lowest zone of stability, $q_z < 1$. The triangularly shaped border lines, plotted in Fig. 24, enclose the range of (a_z, q_z) parameters where the ion motion is simultaneously stable in the x and y direction. Usually, this range is further restricted, either to region (1), which is defined by the condition $q_z < 0.3$, or to region (2), which is close to the tip of the triangle, $(a_z, q_z) = (0.237..., 0.706...)$. Most commonly, the quadrupole is operated in this tip where one obtains high mass resolution, but at the expense of perturbation of the kinetic energy of the transmitted ions. This mode is thus well suited for mass analysis, but not for the preparation of a monoenergetic

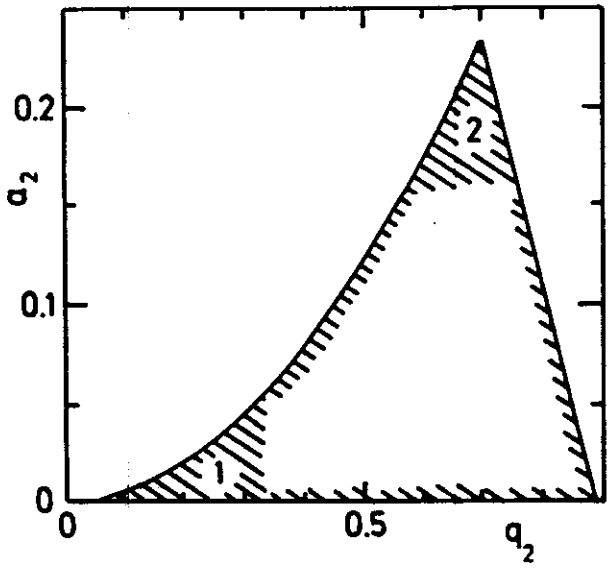

Figure 24. Lowest zone of stability of the Mathieu (a_2, q_2) diagram. The boundary lines are given by $a_2 = \frac{1}{2}q_2^2 - \frac{7}{128}q_2^4 \cdots$ and by $a_2 = 1 - q_2 - \frac{1}{8}q_2^2 \cdots$ (Dawson, 1976). Region 2 is used for high-resolution mass filter operation. In region 1 the adiabatic approximation is valid.

ion beam. Restriction of q_2 to region (1) has the advantage that the device operates within the range of validity of the adiabatic approximation. This ensures conservation of energy, as is discussed in detail in Section II E. In addition, it simplifies the understanding of specific transmission features of quadrupole fields since one can make use of the effective potential approximation.

1. *Low-Mass Band Pass*

One of the obvious applications of operating a quadrupole at low q_2 values is to use it as a low-mass band pass. Since the guiding force derived from the effective potential decreases with increasing mass, the device can be operated such that only ions with masses below a certain limit are transmitted. The condition,

$$m < qV_0^2/(\Omega^2 r_0^2 U_0), \tag{71}$$

can be derived directly from Eq. (59). The cut-off toward higher masses can be very sharp and efficient, as illustrated in the following example in which we have applied this method for the preparation of an extremely pure beam of protons (Scherbarth, 1984). In this case, a 20-cm-long quadrupole with $r_0 = 0.78$ cm was used. At an rf amplitude $V_0 = 100$ V, a dc difference $U_0 = 3$ V, and a frequency $\Omega/2\pi = 10$ MHz, one obtains for $m = 1$ u from Eq. (57), Eq. (60), and Eq. (61), $\varepsilon = 311$ eV, $q_2 = 0.1608$, and $a_2 = 0.0096$, respectively. The (a_2, q_2) parameters fulfill the condition given in Eq. (62); however, for $m = 2$ u, the point (0.0804, 0.0048) lies outside the stability triangle, and the H_2^+ ions are thus accelerated toward the rods and lost, as illustrated by the curved trajectories in the upper panel of Fig. 3. In an actual experiment performed with a pulsed beam (Scherbarth, 1984), a peak count rate of 10^9

H^+/s with an impurity of only $4\,H_2^+$/s was obtained. Accounting for the H^+/H_2^+ ratio in the storage ion source, this corresponds to a suppression of H_2^+ by more than nine orders of magnitude. It is important to note that for high resolution, a low axial energy of typically 50–100 meV is required.

2. *Focusing Properties*

Another important feature of quadrupole fields is their ability to create a phase-space-conserving image, for example, they are able to focus all trajectories starting from one point onto another point, a direct consequence of the harmonic electric (and also effective) potential. Conditions for obtaining periodic solutions of the Mathieu equation are well known (Meixner and Schäfke, 1954). It was suggested by von Zahn (1963), in connection with the monopole, to utilize focusing conditions to improve the resolution of the mass analyzer. Additional aspects of focusing and results from trajectory calculations were reported by Lever (1966) and reviewed by Dawson (1976), although in none of these references have experimental advantages been presented. A more recent discussion on spatial focusing in an rf-only quadrupole was given by Miller and Denton (1986). In their experiment, pronounced transmission minima and maxima were observed as a function of the rf amplitude, most probably caused by a combination of the imaging features of the ion guide with spatial discrimination of the subsequent detector. These authors provided several suggestions to minimize this unwanted effect. We, on the other hand, make use of these properties to achieve energy and mass filtering for ion creation and beam preparation.

Within the adiabatic approximation, it is straightforward to derive conditions for operating a quadrupole in the focusing mode. It can be seen from Eq. (51) that for $n = 2$, the effective potential V^* is harmonic. Therefore, one can separate Eq. (14) into two harmonic oscillator differential equations, describing independently the x and the y components of the smooth motion, $\mathbf{R}_0(t)$. Both oscillate with different secular frequencies,

$$\omega_{x,y} = \tfrac{1}{2}\beta_{x,y}\Omega, \tag{72}$$

with

$$\beta_{x,y} = (q_2^2/2 \pm a_2)^{1/2}. \tag{73}$$

In the absence of a superimposed dc difference, the two frequencies are identical and the value of β changes as a function of q_2 simply as

$$\beta = 2^{-1/2} q_2. \tag{74}$$

With an added dc potential that is, $a_2 > 0$, the oscillation in the x direction

becomes faster than that in the y direction. Note that for $q_2 < 0.3$, Eq. (73) defines in very good approximation the well-known iso-β lines, and that Eq. (74) is in good agreement with the function $\beta(q_2, a_2 = 0)$, as reported by Miller and Denton (1986).

As discussed thus far, all transmission conditions depend only on the operating point in the (a_2, q_2) plane. However, if additional boundary conditions are imposed, for example, by using mechanical apertures, deflection plates, or time-of-flight selection, transmission through the quadrupole requires spatial and/or time focusing. An early version of such a mass and velocity filter was described in Teloy and Gerlich (1974). This filter was operated in the rf-only mode and employed two separate stages and three off-axis apertures. A mechanically simpler version of a focusing quadrupole with much higher transmission was described in Gerlich (1986). This device, assembled in several lengths and with different rod sizes, is used successfully in our apparatuses (see, for example, Fig. 45, Fig. 46, and Fig. 58). Ions are injected through a central entrance hole, the rf field focuses them onto a point at the exit of the quadrupole, and this point is then imaged onto an aperture using an electrostatic lens system, which is also used to pulse and correct the direction of the ion beam. The functioning principle of the focusing quadrupole is illustrated in Fig. 25, which shows the x and y projection of calculated trajectories for an (a_2, q_2) combination in which ω_x is ten times larger than ω_y. To obtain an erect or inverted image of the central entrance aperture onto the exit hole, both numbers of half cycles, N_x and N_y, must be integers. Therefore, the flight time t must obey the two equations,

$$t = N_x \pi / \omega_x$$

and

$$t = N_y \pi / \omega_y. \tag{75}$$

Both conditions are fulfilled in the illustration on the left-hand side of Fig. 25, since both foci coincide with the exit aperture. The figure on the right shows the effect of a slight increase in the kinetic energy. Here, the focus of the trajectories is shifted so that the ions are no longer transmitted. In contrast to the suggestion of this figure, which was calculated assuming ideal conditions, the experimental resolution is primarily determined by the fast x motion, rather than the y motion. This will be discussed below.

An experimentally determined transmission function for C^+ and CH^+ ions is shown in Fig. 26. In this example, the parameters $\Omega/2\pi = 12.25$ MHz, $r_0 = 0.42$ cm, and $U_0 = 0.247$ V were held fixed and only the amplitude V_0 was varied. Based on these values, and on an axial energy of 0.25 eV and

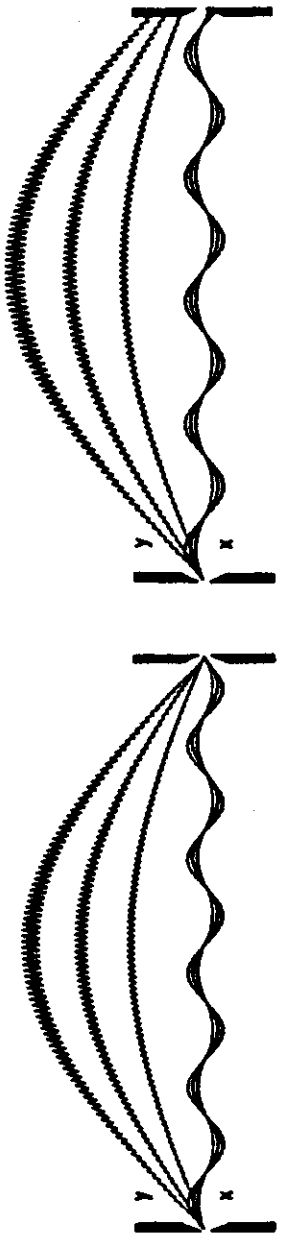

Figure 25. Illustration of the focusing properties of a quadrupole. Both panels depict trajectories, projected onto the x and y plane, respectively, for three different starting angles and for $N_x = 10$ and $N_y = 1$ half cycles. In the left panel, the common starting point is focused exactly into the exit hold. A slight increase of the axial energy leads to a loss of the ions, as illustrated in the right panel.

a quadrupole length of 25 cm, the numbers of half waves of the secular motions, N_x and N_y, have been calculated. The resulting values are shown in the two scales in the upper part of the figure. Although the dc difference is very small ($a_2 = 0.000152$), the two frequencies, ω_x and ω_y, differ significantly since the rf amplitude is varied in the vicinity of the border line, $a_2 = \frac{1}{2}q_2^2$. The observed C^+ intensity maxima can be assigned to $(N_x, N_y) = (27, 4)$ and $(29, 11)$. In the depicted example, a_2 and the injection conditions were optimized for the preparation of a C^+ beam in the $(27, 4)$ mode. The discrimination of the higher-mass CH^+ ion is simply achieved by operating so close to the border of the stability triangle that its y motion is unstable. If, on the other hand, one wishes to favor CH^+ ions and to suppress C^+, one could make use, for example, of the transmission gap between $N_x = 28$ and 29. High mass resolution requires additional energy

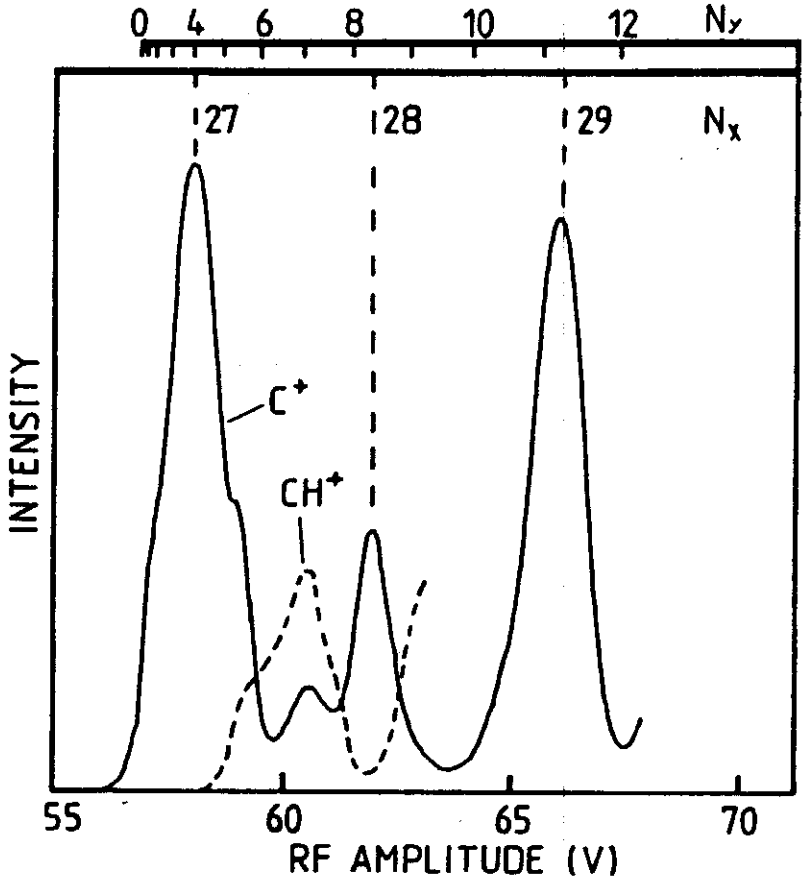

Figure 26. Measured transmission of C^+ and CH^+ ions through a focusing quadrupole as a function of the rf amplitude. The numbers on top refer to the number of half cycles of C^+ trajectories (compare Fig. 25). The C^+ intensity maxima are obtained for $(N_x, N_y) = (27, 4)$ and $(29, 11)$. Owing to its larger mass, the onset and the structure of the CH^+ intensity is shifted to higher amplitudes.

selection, and, therefore, we usually operate the device in a pulsed mode making use of time-of-flight selection. For preparing an ion beam with a very narrow energy spread, the axial energy usually must be below 100 meV.

It is important to note that the resolution is predominantly determined by the high-frequency component ω_x, while, as can be seen, for example, from the $N_x = 27$ peak in Fig. 26, contributions from $N_y = 2$–5 are only indicated as fine structure. This is primarily due to the much larger acceptance angle in the x plane, since, here, both the dc and the rf fields confine the ions close to the axis. In contrast, the guiding field in the y direction is very weak, and, as such, even small imperfections in the work function of the metal surfaces can cause significant perturbations. These are especially ciritical in regions where the ions come very close to the rods. This always leads to some asymmetries, and, therefore, operation of a focusing quadrupole at low energies and low guiding fields requires careful tuning of the injection and extraction conditions, as well as slow adjustment of the dc and rf fields to obtain stable surface conditions.

3. *Photoionization Source*

Single- and multiphoton ionization is gaining rapid acceptance as a technique for preparing state-selected ions. Combination of this method with the focusing properties of a quadrupole has lead to the development of an efficient ion source, shown in Fig. 27. Here, the focus of a pulsed laser is located in the interior of a quadrupole. Two cylindrical electrodes surrounding the quadrupole in the ionization region and one repeller allow one to shift the dc potential in the vicinity of the laser focus relative to the dc potential of the rest of the quadrupole and to adjust the kinetic energy in this region to typically 100 meV. Making use of the focusing properties of the guiding field,

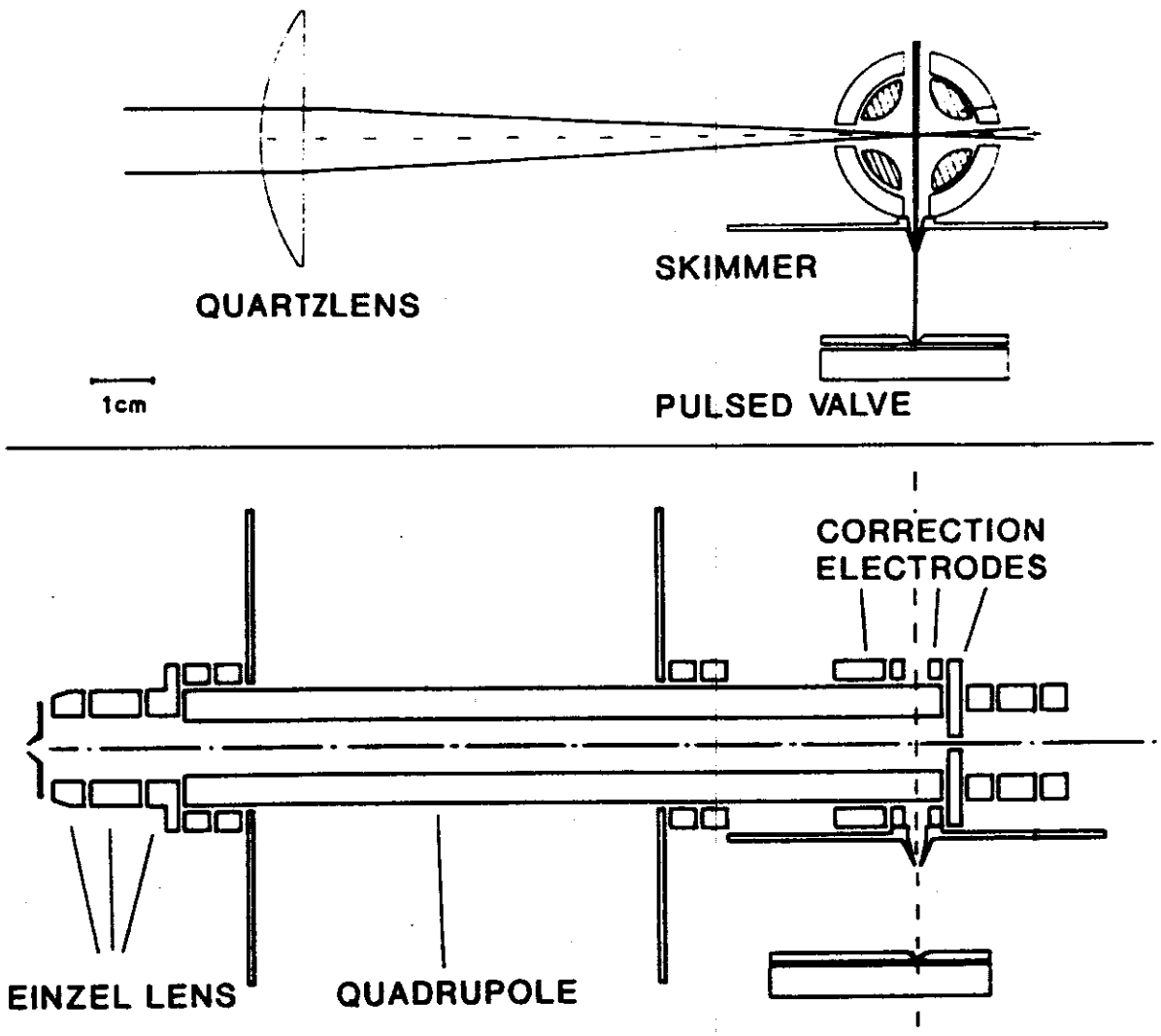

Figure 27. Quadrupole used as a multiphoton ionization source. Ions are formed inside the quadrupole in the intersection of the focused laser beam and the skimmed pulsed molecular beam. The correction electrodes allow one to create an axial dc potential gradient in the focal region, leading to a weak acceleration of the ions in the axial direction. Using the focusing properties of the quadrupole, the well-defined ionization volume can be mass selectively imaged to the exit hole.

the well-defined ionization volume can be imaged onto the exit hole at the other end of the quadrupole. This leads to a high collection efficiency without the need for strong extraction fields. In addition, the mass selectivity of the device can help suppress fragment ions. This is especially important for the ionization of molecules, where dissociative ionization or fragmentation often compete with the state-selective preparation of the molecular ion. The high time resolution of a laser (or of the light pulses from a synchrotron) also allows for time-of-flight selection. Further improvements can be imagined by synchronizing the ionization event with the rf field, leading to a well-defined starting phase.

In the ion source depicted in Fig. 27, a pulsed supersonic nozzle beam is used to create cold neutral precursors. The neutral beam, the quadrupole axis, and the laser are all orthogonal to each other, reducing the risk of collision-induced relaxation of the created ions. A skimmer plate separates

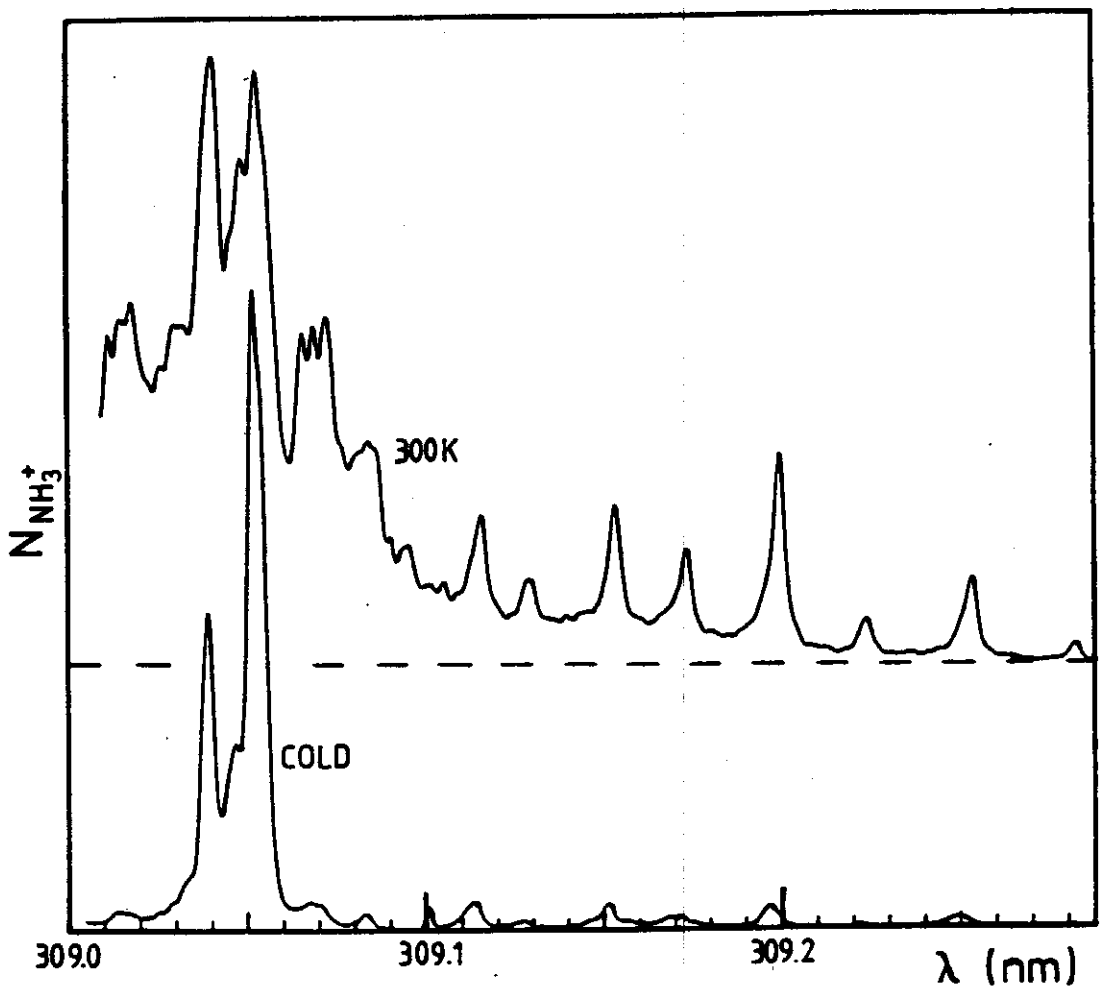

Figure 28. Multiphoton ionization spectrum of NH_3 recorded using the quadrupole photoionization source (Fig. 27). The lower curve shows NH_3^+ formed in the pulsed supersonic beam. The upper curve was recorded with such a long delay between the gas pulse and the laser firing that only the remaining 300 K effusive background gas was ionized.

the supersonic beam from the effusive background gas and eliminates the need for an additional differential pumping stage. Figure 28 shows a multiphoton ionization spectrum of NH_3 obtained with this source. The bottom spectrum was obtained by optimum synchronization of the laser and pulsed beam, while in the upper curve, the laser was delayed sufficiently long so that only the remaining NH_3 background gas was ionized.

4. *Resonant Excitation by Auxiliary Fields*

Another important modification of operating quadrupoles is to superimpose an auxiliary dipole or quadrupole field alternating at a lower frequency $\Omega' < \Omega$ with an amplitude V'_0. The mathematical problem of solving the resulting inhomogeneous Mathieu differential equation under the inclusion of such an additional term has been treated in Kotowski (1943). The principle has also been described in one of the first publications on quadrupoles (Paul et al., 1958). One early application of this technique was to separate different isotopes by resonant ejection of specific masses (Busch and Paul, 1961a). Recently, this method has found renewed interest (Watson et al., 1989) and has been coined as a notch rejection filter (Miller and Denton, 1990).

The procedure of resonant excitation is easy to understand if the quadrupole is operated within the limit of the adiabatic approximation. As described previously, the secular motion corresponds to a two-dimensional harmonic oscillator with frequencies ω_x and ω_y [see Eq. (72)]. If one superimposes on the quadrupole field a weak homogeneous field in the x direction oscillating at the frequency $\Omega' = \omega_x$, the corresponding motion becomes resonantly excited. This leads to a *linear increase* of the amplitude of the x component of the secular motion, and, finally, to the loss of all ions with the critical mass $m(\omega_x)$ determined by Eq. (72) and Eq. (73). This method of mass-selective ejection is a standard technique used in ICR cells, Penning traps, and also Paul traps (March and Hughes, 1989). On the other hand, superimposing a quadrupole distortion field leads to parametric excitation when $\Omega' = 2\omega_x$ and results in an *exponential increase* of the amplitude of the secular motion (Busch and Paul, 1961a). Parametric heating can also be achieved by modulating the rf amplitude with a frequency Ω' such that one of the two secular frequencies, $2\omega_x$ or $2\omega_y$, coincides with $\Omega - \Omega'$. Note that resonant excitation is restricted to harmonic potentials, that is, to quadrupoles. In all other potentials, the period of the ion secular oscillation depends on the amplitude, as has been derived for multipole fields in Eq. (67). As a result, accumulation of energy from the resonating field causes the ion motion to drift out of phase, and, for ejection, a continuous adjustment of the excitation frequency would be required.

Combining one of the previously described methods, for example, high mass cut-off and/or selective focusing, with resonant ejection usually leads to a

very pure preparation of an ion beam. It is normally advisable to operate under conditions such that the desired mass m is just at the stability limit given by Eq. (71). This suppresses higher mass ions $m' > m$ very efficiently. In addition, the weak guiding field has the advantage that resonant excitation of an unwanted lower mass, for example, $m-1$, perturbs only slightly the mass m since the two frequencies, $\omega_y(m)$ and $\omega_y(m-1)$, are well separated, as can be derived from Eq. (73). Recall that it is important to operate at sufficiently low q_2 values to guarantee adiabatic conservation of energy.

C. Octopole Beam Guide

After quadrupoles, the octopole beam guide is the second most used rf device, and, although its use is not nearly as widespread as that of the quadrupole, it has seen expanded application in a number of laboratories. It is now applied routinely in many experiments where one wishes to guide very slow ions and where 4π collection efficiency of product ions is required. An overview of the different appratuses that employ octopoles will be given in Section IV A. In this section we begin by making a few general remarks concerning the characterization of transmission features of an octopole. We then discuss applications of ring electrodes to localize potential distortions and describe a procedure to calibrate the axial energy of a slow guided ion beam. The last part of this section describes an experimental test for obtaining a correlation between the transverse energy of ions and the minimum rf amplitude needed to confine them.

1. *Transmission Properties*

Recently, an experimental (Tosi et al. (1989b) and a theoretical (Hägg and Szabo, 1986c) attempt to characterize the transmission properties of an octopole ion guide have been reported. The theoretical approach has already been discussed in Section II D 3. Unfortunately it was based on trajectory calculations with experimentally unrepresentative initial conditions. Tosi et al. (1989b) have experimentally investigated the transport of different ions through an octopole as a function of the rf amplitude. They gave several interpretations of their measured transmission functions, and, in addition, they attempted to compare their findings to those limits we have recommended in Gerlich (1986) and in Section II D 2 for safe operation of an octopole as an ion beam guide. Unfortunately, these authors overlooked the fact that these proposed operating conditions are *sufficient* conditions, and their observation that transmission also occurs outside of these limits is therefore not surprising.

The principal difficulty in determining conditions that are simultaneously *sufficient* and *necessary* for ion transmission have already been discussed in Section II D 3 in context with adiabaticity and stability. Besides the

theoretical uncertainties in defining border lines between stability and instability, there is the added experimental difficulty that the observed transmission is not only a feature of the octopole, but also a complicated function of the initial conditions and the acceptance of the detection system (see Section IV B). For a fundamental study of the transmission function of a multipole, it is mandatory to account for such perturbations.

It seems to be necessary to repeat here in this context that we do not yet know of any practical reason to use an octopole outside the range of validity of the adiabatic approximation, and therefore, we do not present any transmission functions extending outside this range. Operating below $\eta_m = 0.3$ ensures that the transmission depends only on the transverse energy, as defined in Eq. (54). From this equation we have derived the conditions for safe operation of the ion guide, that is, for 100% transmission. Equation (54) also allows one to derive critical operating conditions for the maximum confined transverse energy. This and a corresponding experimental test will be discussed in Section III C 4.

The strength of the effective potential, which determines the transmission features, depends on the shape and the position of the rf electrodes, and, in addition, on the potential of the metal surfaces that surround the octopole. In order to use directly the formula for V^*, as given by Eq. (51), it is advisable that the ratio of the rod diameter d and the radius r_0 be close to that given in Eq. (68). In some experiments (Ervin and Armentrout, 1985), smaller r_0/d ratios have been used. This weakens the effective potential between the rods (see Fig. 14) and, for a quantitative estimate of ion transmission, V^* must be calculated from the correct boundary conditions using, for example, the method described in Section II C 2. As an extreme case, we have performed an experimental test with an octopole constructed from eight thin wires with $d = 0.03$ cm arranged on a circle with $r_0 = 0.4$ cm (Müller, 1983). The effective potential was calculated as described in Section II C using the boundary conditions shown in Fig. 6. It is evident that with such an open structure the field penetration from surrounding electrodes becomes significantly larger than that depicted in Fig. 17. The transmitted ion intensity, measured as a function of amplitude and external field, was in good agreement with the calculated predictions (Müller, 1983).

2. *Potential Distortions, Ring Electrodes*

One of the most poorly characterized problems affecting the transmission properties of octopoles and other rf devices is that arising from nonuniformities of the surface potentials of the electrodes. It is well known that patchiness of the work function of metal surfaces can be caused by dust particles, insulating layers, chemisorption, or other sources. Experimentalists working with slow charged particles in electron-energy analyzers, electrostatic

lens systems, ion traps, or other electrode arrangements have developed a variety of methods for treating the metal surfaces to reduce such impairments. In the following, we describe a procedure (Gerlich, 1984, 1986) that allows one to obtain detailed information about potential distortions along the axis of an octopole, and then make a few remarks on the treatment of the surfaces of the octopole rods.

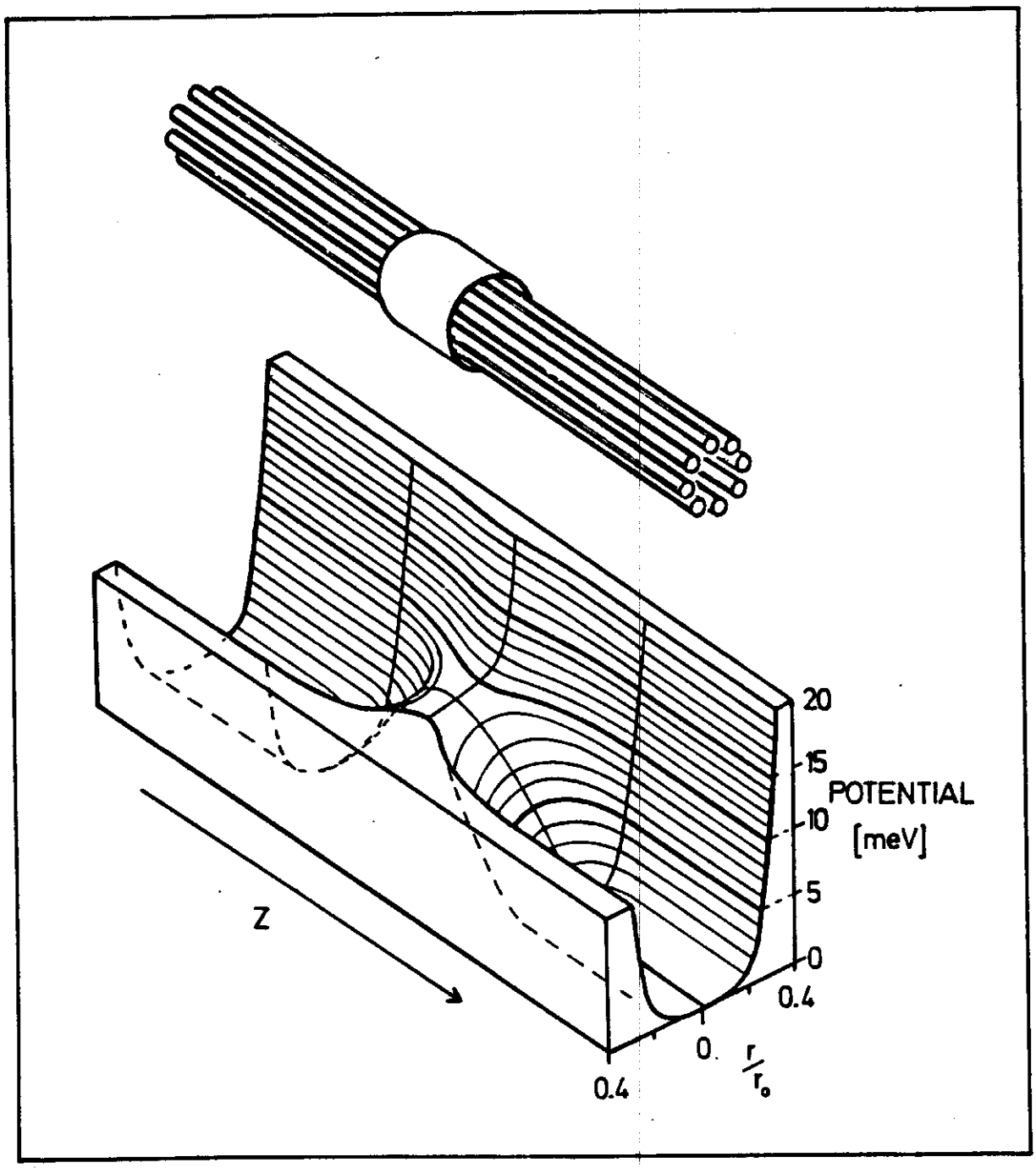

Figure 29. Perspective view of the sum of the effective potential and a dc potential distortion caused by a cylindrical ring electrode in an octopole. The penetrating field creates a local barrier of a few millivolts per volt applied to the ring.

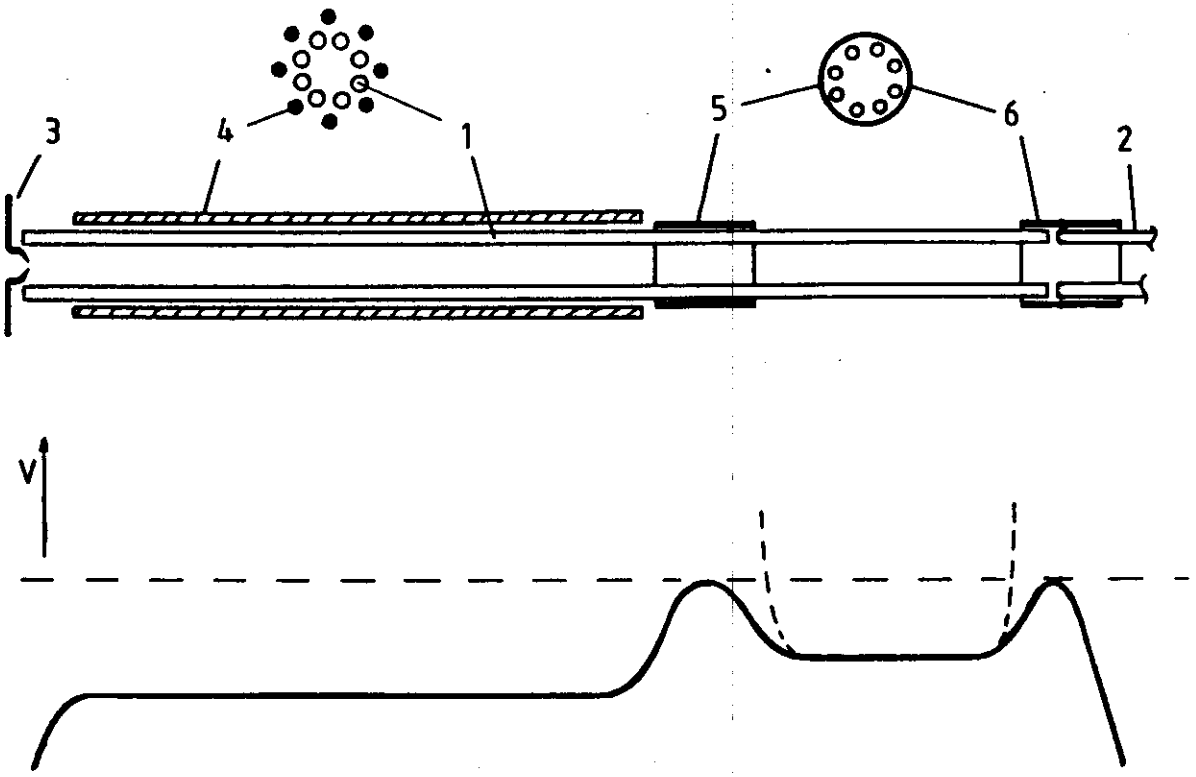

Figure 30. System of two octopoles (1, 2) with electrodes for ion injection (3) and for field correction (4–6). Correction electrode (4) consists of eight rods, staggered as indicated, (5) and (6) are cylinders. The lower panel shows a schematic representation of the dc potential along the axis of the system. In this example, the electrode (4) was used to lower the potential slightly, while (5) and (6) were used to create barriers.

The test procedure makes use of two or more cylindrical ring electrodes that surround the octopole; see Fig. 29 and Fig. 30. Choosing the dimensions as depicted in Fig. 17, a ring voltage of 1 V shifts the octopole potential in the vicinity of the axis typically by 2–3 mV. Superimposing this weak dc field with a rather strong rf guiding field leads to an effective potential with a variable local barrier, as plotted schematically in Fig. 29.

Figure 30 shows a part of the octopole system (1, 2) from our universal guided-ion-beam apparatus (Gerlich, 1986; Gerlich et al., 1987; Scherbarth and Gerlich, 1989), which is described further in Section IV B. Important for the present discussion is the region between the ring electrodes (5) and (6). Here, the electrodes determine the entrance and exit of the scattering cell. The lower part of this figure is a schematic representation of the dc potential along the axis of the ion guide. The electrode (4) is used to slightly lower the potential in the first part of the octopole, while the ring electrodes (5, 6) create two potential barriers. If an ion is injected into this octopole with a kinetic energy below the energy marked by the horizontal dashed line in Fig. 30, it will be reflected at (5) and lost. If the ion has a higher energy, it is transmitted

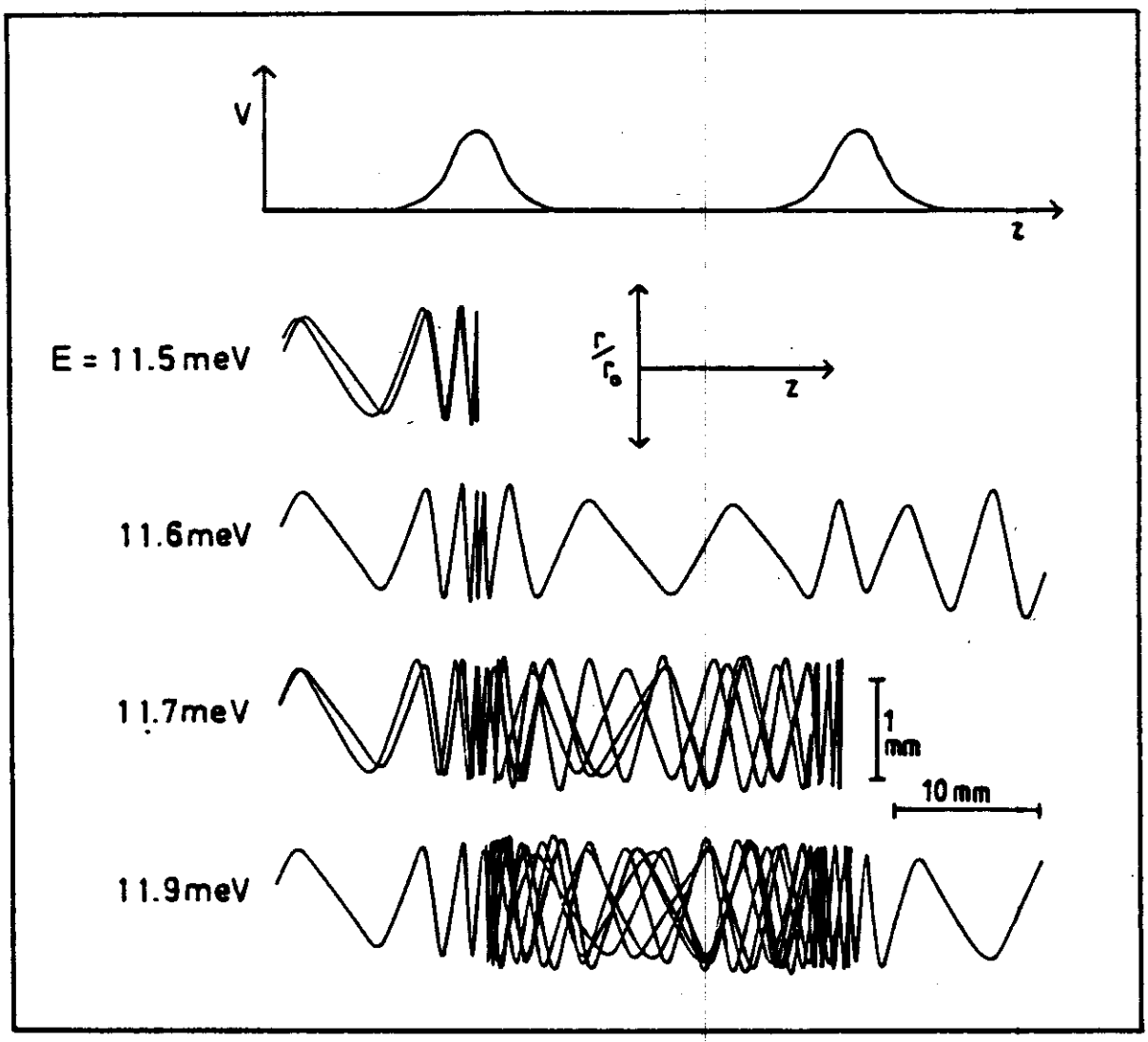

Figure 31. Model calculations of ion trajectories in an octopole with two equally high potential barriers. Several sequences of reflections at the barriers are obtained depending on the kinetic energy and the angle of the incoming ion.

directly. However, under certain conditions, there is also a small energy window where the ion can be trapped for a few reflections between two equally high potential barriers. This is illustrated in Fig. 31 based on a simple model calculation (Schweizer, 1988). In this numerical example, ions with an energy between 11.5 and 12 meV can be trapped, depending on the initial conditions. Necessary for this behavior is a weak coupling between the axial and the transverse motion.

Experimentally observed reflection signals of He^+ ions are plotted in Fig. 32. In this case, an intense, few microsecond short pulse of slow ions was injected into the octopole. From the approximately 50-meV-wide energy distribution, the slow part is reflected at electrode (5) and lost, while the fast part is transmitted directly (not shown in figure). The well-resolved individual peaks originate from those ions whose energies are close to the barrier height

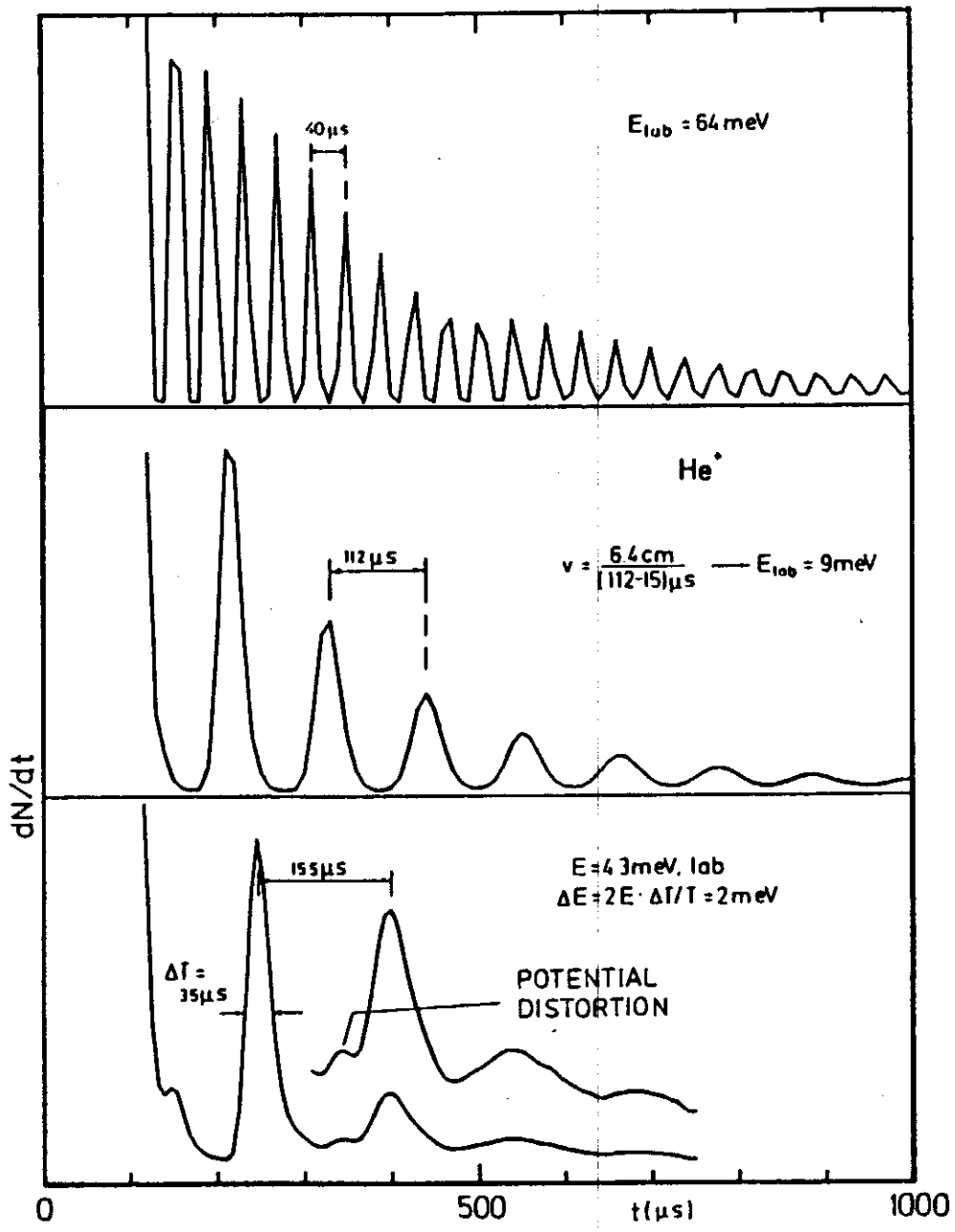

Figure 32. Measured time-of-flight distributions of He^+ ions trapped between the two ring electrodes (5) and (6) shown in Fig. 30. The external voltages correspond to barriers of 64, 9, and 4.3 meV. For a precise calculation of the energy, it is important to know that the potential at ring (5) is raised after passage of the ions, while ring (6) remains semitransparent. The effective distance between the rings is 3.2 cm and the turn around time in ring (6) is 15 μs. In the lowest panel, the additional structure is indicative of other potential distortions.

imposed by ring electrodes (5, 6) and are therefore trapped for a certain number of oscillations. The upper panel depicts a time-of-flight distribution recorded with a barrier corresponding to 64 meV. Here one can see contributions from ions that have been reflected back and forth more than 20 times. Most probably they escape because of a coupling of the axial energy to other sources of energy. Lowering both ring electrode potentials reduces

the barriers and leads to the capture of slower ions, as shown in the lower two panels. The lowest panel shows an oscillating ion beam with a mean energy of only 4.3 meV. Here, the marked additional structure in the time-of-flight spectrum is due to an additional potential barrier caused by surface distortions.

Such a low-potential distortion is not straightforward to obtain owing to the previously mentioned surface problems. Usually, before an octopole is assembled, the surfaces (here stainless steel) are carefully treated using standard methods such as mechanical or electrolytic polishing and ultrasonic cleaning in different solvents. Nonetheless, distortions between the two rings (5) and (6) following such a cleaning are typically 30–50 meV. In order to further reduce these barriers, we have developed a method of cleaning the octopole—using a fine metal brush and blowing the region continuously with pressurized nitrogen—without removing it from the apparatus. After each such cleaning, the apparatus is pumped down and the positon of the highest perturbation is determined as described previously. According to our interpretation (Scherbarth, 1984; Schweizer, 1988), our treatment probably creates different random distributions of distortions that cancel with a certain probability close to the octopole axis. For obtaining very low distortions, it is necessary that the critical range, in our case the length of the scattering cell, be as short as possible and that the cleaning, pumping, and testing cycles be very fast in order to repeat them often. With the described octopole system, cycles of 1–2 h are possible. We have found that it is always possible to reduce the potential distortions below 10 meV after many iterations (24 in the depicted example). It is very important to note that the obtained potential distribution remains very stable, even over a period of months.

The described procedure employing two potential barriers is of course more than just a test for potential distortions. It is a unique method for selecting ions (typically a few 100 per pulse) with an extremely small energy spread of 1–2 meV, and for forming a pulsed, trapped ion beam with a well-defined kinetic energy that can be easily varied between 5 and 100 meV. For a precise determination of the kinetic energy, the semitransparent barriers (heavy line in the lower part of Fig. 30) have the disadvantage that the turning points are somewhat undefined within the region of the ring electrodes and that here the ions move very slowly. Therefore, the potential barrier (5) is usually raised as the desired ions are reflected from (6), while (6) is raised when the ion bunch is reflected from (5). This results in very steep and well-defined potential walls, as indicated by the dashed lines in Fig. 30. Also, under these conditions, the time spread of the enclosed ion bunch is very small. This has been tested by opening the trap after several round trips. Finally, it should be noted that the conservation of the time structure over a period of milliseconds, as can be seen for example from the upper panel

in Fig. 32, indicates either that the coupling between the axial and the transverse motion is very weak or that the transverse energy is extremely small.

3. *Calibration of the Axial Energy*

In studying collision processes, the kinetic energy distribution of the ions in the interaction region must be known. The previously described method has the advantage that both energy selection and calibration are performed in the octopole itself, resulting in an overall accuracy of a few meV. To operate at high ion intensities, it is necessary to inject an externally prepared ion beam. In general, the energy distribution of the ions in the octopole depends on several factors such as ion source conditions, resolution of energy selectors, impairment by varying fields (pulsed electrodes, rf fields, low-frequency noise, etc.), and by potential inhomogeneities in the scattering cell. In some applications of guided ion beams, it may be sufficient to determine the beam energy by using the octopole as a retarding field analyzer; however, for studies at laboratory energies below 0.5 eV, we always employ a time-of-flight analysis.

A very precise calibration procedure consists of several steps. Intially, following the method described in Section III C 2, the potential inhomogeneities in the scattering cell are tested and reduced to the desired accuracy. Then, the potential of the external electrode (4) is adjusted such that the mean velocity is the same in both parts of the octopole (1), as can be tested by reflecting ions alternatively between (6) and (5), or (6) and (3). Next, one has to prepare externally a pulsed ion beam with a narrow energy distribution and a sufficiently small time width. Finally, one has to perform the following calibration routine, the attainable accuracy of which depends significantly on the quality of this beam.

At energies above a few tenths of an eV, it is usually sufficient to assume a linear dependence of the nominal laboratory energy E_1 on the voltage U applied to the field axis of the octopole

$$E_1 = -q(U + \Delta U). \tag{76}$$

It is advisable to measure U relative to the actual ion source potential, since then the correction ΔU only has to account for possible shifts due to space charge or differences in the work function. If only the voltage U of the octopole (1) is changed, while all other potentials are kept constant, the total flight time t of the ions through the apparatus can be separated into a voltage-dependent part t_u and constant part t_c

$$t = t_u + t_c. \tag{77}$$

The two constant parameters, ΔU and t_c, are determined experimentally by recording ion time-of-flight distributions, dN/dt, at different octopole voltages and by characterizing them with the mean flight time

$$\langle t \rangle = \int t(dN/dt)dt \Big/ \int (dN/dt)dt. \tag{78}$$

Several potentials between 2 and 10 V are used to calculate an average value of t_c. A second set of measurements is performed between 0.2 and 2 V for obtaining ΔU. The attainable accuracy of ΔU is typically better than 10 m*V*.

At laboratory energies below a few tenths of an eV, where the mean energy of the ion cloud and its half width become comparable, it is no longer sufficient to characterize the beam simply by its mean flight time. In this case, each measured time-of-flight distribution dN/dt is transformed numerically into an energy distribution dN/dE_1 and the mean energy is determined from

$$\langle E_1 \rangle = \int E_1(dN/dE_1)dE_1 \Big/ \int (dN/dE_1)dE_1. \tag{79}$$

Such obtained energy distributions are plotted in Fig. 33. In this example, the nominal energy E_1, as determined from Eq. (76), was in good agreement with $\langle E_1 \rangle$, since the energy half width of the ion beam was rather small (25 meV). Comparison of the distributions, however, reveals some changes in their shape with different energies.

To characterize the overall accuracy of the calibration routine, we usually record the mean energy $\langle E_1 \rangle$ and the total transmitted intensity as a function of the nominal energy E_1 between 10 mV and 1 V, as depicted in Fig. 34. The upper panel shows that under favorable conditions E_1 and $\langle E_1 \rangle$ are identical down to 50 meV. Further lowering of the octopole voltage leads to deviations due to cutting off of slow ions. In this example, the slowest ion beam with $\langle E_1 \rangle = 25$ meV was obtained at $E_1 = 10$ meV with a remaining intensity of 30%.

The lower panel of Fig. 34 illustrates that potential barriers in the octopole can lead to a significant shift of the retarding field curve. Here, the ring electrode (5) is used to create a 100 mV distortion. This leads to a corresponding shift of the onset of the intensity, although the energy of the ions is unchanged in the octopole with exception of the region at the localized distortion. The mean energy $\langle E_1 \rangle$ determined by time of flight is also slightly perturbed, since the total flight time in the octopole (1) is slightly increased by the barrier.

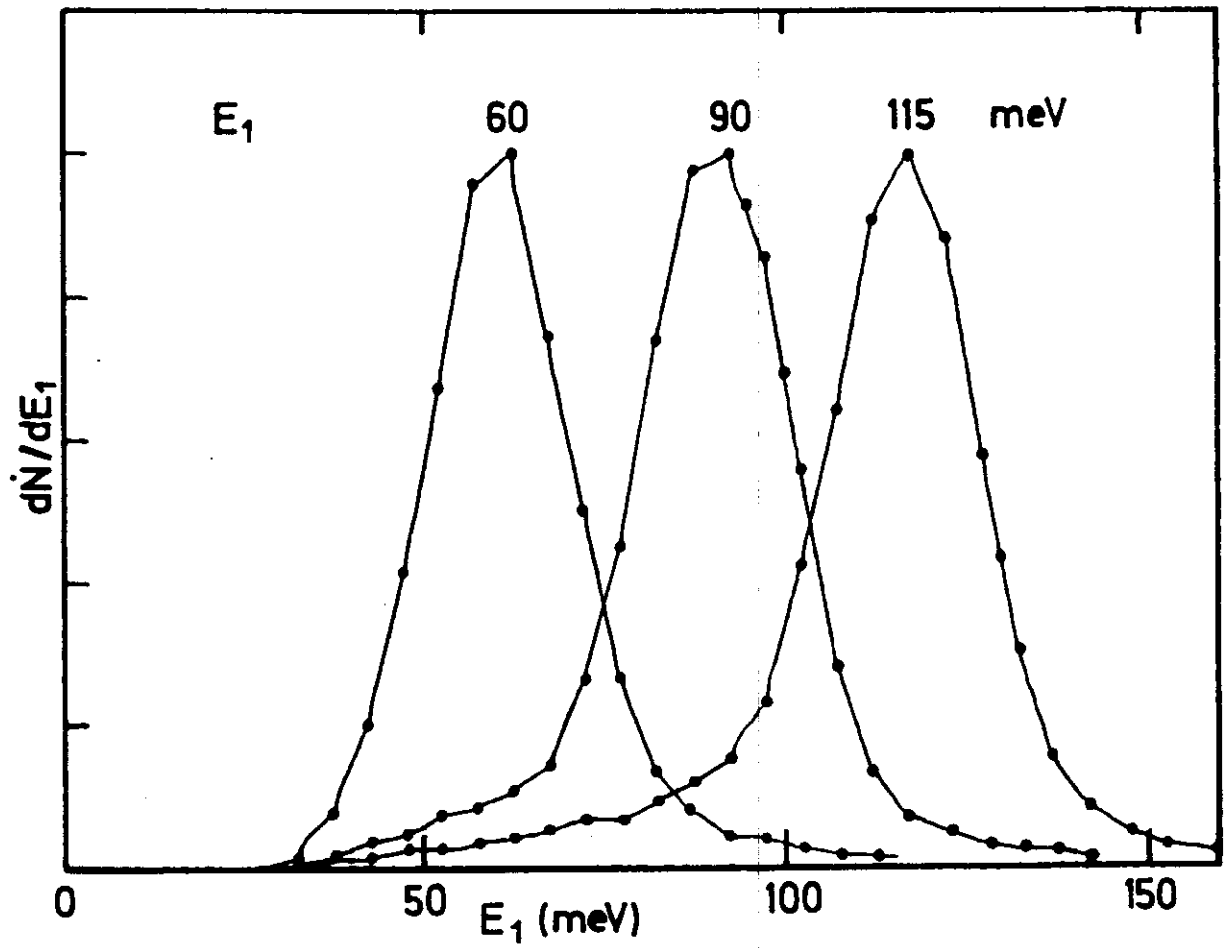

Figure 33. Kinetic energy distributions of a slow guided D_2^+ ion beam measured by time of flight at three octopole voltages U. The nominal energies $E_1 = -q(U + \Delta U)$ are in excellent agreement with the derived mean energies $\langle E_1 \rangle$. The energy half width is 24 meV.

This example shows that for a precise time-of-flight calibration of the ion energy the overall potential homogeneity is important. There are additional sources of error that must be considered. Since the flight time corresponds only to the axial component of the ion velocity, it is important to avoid injection conditions that lead to a wide angular spread, that is, it is not recommended to use a strong deceleration field between the injection electrode (3) and the octopole (1). Other problems can arise from time focusing effects caused by ion acceleration in the pulsed electrodes, which usually results in a nonlinear $\langle E_1 \rangle$-E_1 dependence.

4. *Maximum Confined Transverse Energy*

Since in most applications one is interested in operating at 100% collection and transmission efficiency, we have postulated in Section II D 2 safe conditions which ensure that the ions will not collide with the rods ($\hat{r}_m < 0.8$). However, under ideal conditions, the ions can be allowed to come much closer to the electrodes, and the maximum tolerable kinetic energy can be

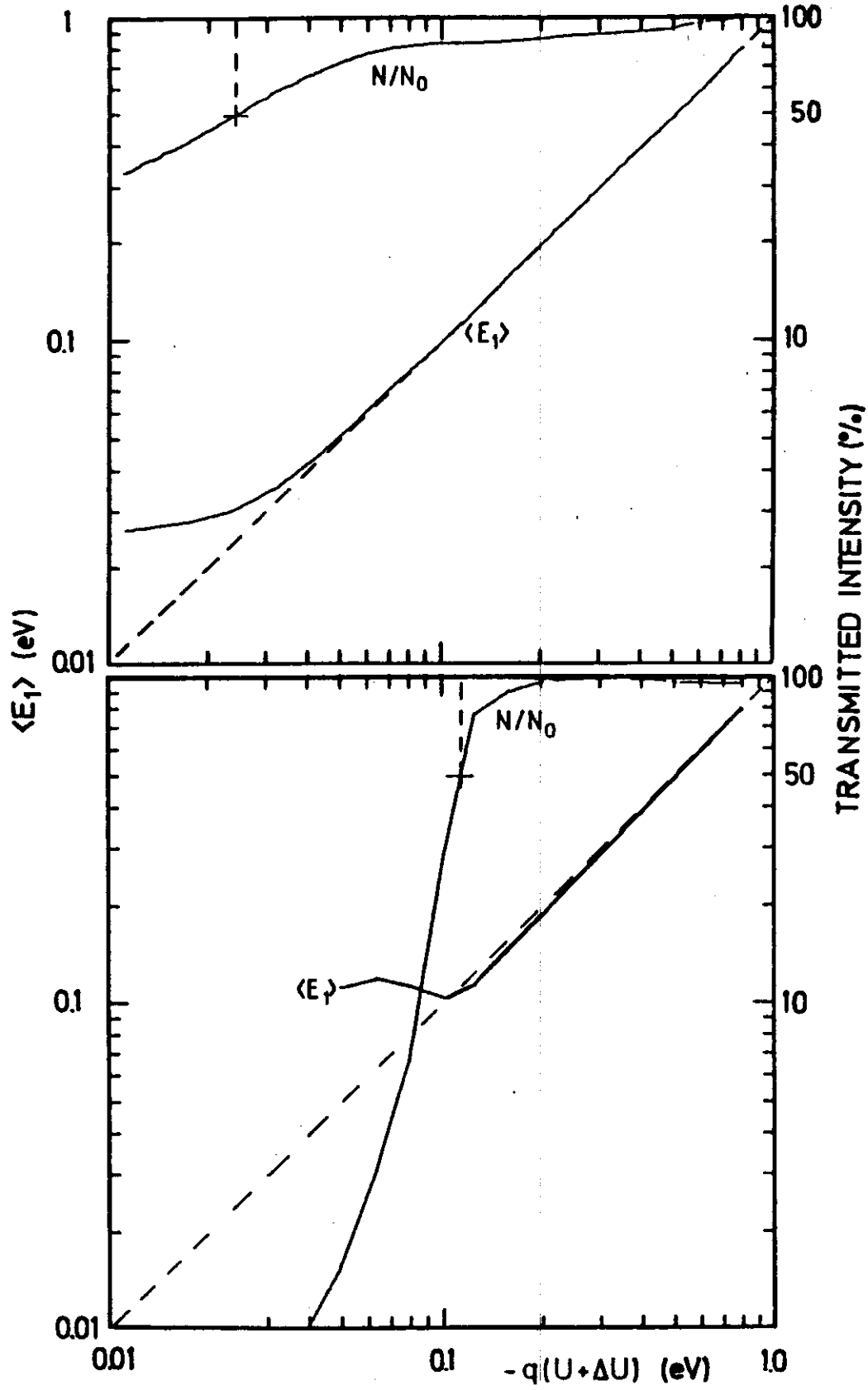

Figure 34. Experimental characterization of ion transport in an octopole. The figure depicts the dependence of the relative transmitted ion intensity N/N_0 (scale on right) and the mean kinetic energy $\langle E_1 \rangle$ on the nominal energy $E_1 = -q(U + \Delta U)$. The upper panel shows good agreement between $\langle E_1 \rangle$ and E_1 over a wide range, and that laboratory energies below 30 meV are accessible. The curves in the lower panel were recorded with a local potential distortion of 100 meV. Comparison with the upper curve reveals a corresponding shift of the retarding potential curve. The marked 50% value (+) is displaced from 24 meV to 115 meV.

significantly larger than given by Eq. (54) for $\hat{r}_m = 0.8$, since the effective potential increases steeply toward the rods. In determining critical operating conditions of an ion trap or an ion guide, it is necessary to find a relation between the initial conditions of ion trajectories and their closest approach to the electrodes. Within the adiabatic approximation, this correlation can be derived in general from Eq. (16). For multipoles the situation is even simpler, as discussed in detail in Section II D.

In first-order adiabatic approximation, the ion trajectory is given by $\mathbf{r} = \mathbf{R}_0 + \mathbf{R}_1$; see Eq. (6). The region where the risk of hitting an electrode is largest is that along the lines given by $\cos n\varphi = 1$. Here, the gap between a given equipotential line and the rod surface has its smallest value. In addition, the oscillatory motion, $\mathbf{R}_1$, in this region is directed toward the surface (see Fig. 9). In order to avoid colliding with the rod, the closest approach of the ion must fulfill the condition $R_0 + R_1 \leqslant R_0 + a < r_0$. Therefore, the secular motion R_0 must be restricted by $R_0/r_0 < \hat{r}_c$, where the critical radius is defined in reduced units by

$$\hat{r}_c = 1 - \hat{a}_c. \tag{80}$$

The critical amplitude $\hat{a}_c$ depends itself on $\hat{r}_c$, as given by Eq. (48):

$$\hat{a}_c = \frac{1}{2n}\frac{qV_0}{\epsilon}\hat{r}_c^{n-1}. \tag{81}$$

From these two equations, $\hat{r}_c$ can be calculated; for example, for an octopole, one obtains a third-order equation. Using the thus obtained critical radius, we define the critical effective potential

$$V_c^*(\hat{r}_c) = \frac{1}{8}\frac{(qV_0)^2}{\epsilon}\hat{r}_c^{2n-2}. \tag{82}$$

An exact, numerically determined amplitude dependence of this potential is shown in Fig. 35. For most practical applications it is easier to calculate the critical radius from the amplitude at $\hat{r} = 1$ and to use the simple approximation

$$\hat{r}_c \simeq 1 - c\frac{1}{2n}\frac{qV_0}{\epsilon}, \tag{83}$$

where c is a constant. Choosing $c = 0.81$ leads to excellent agreement with the exact result, as can be seen in Fig. 35. This figure also shows for

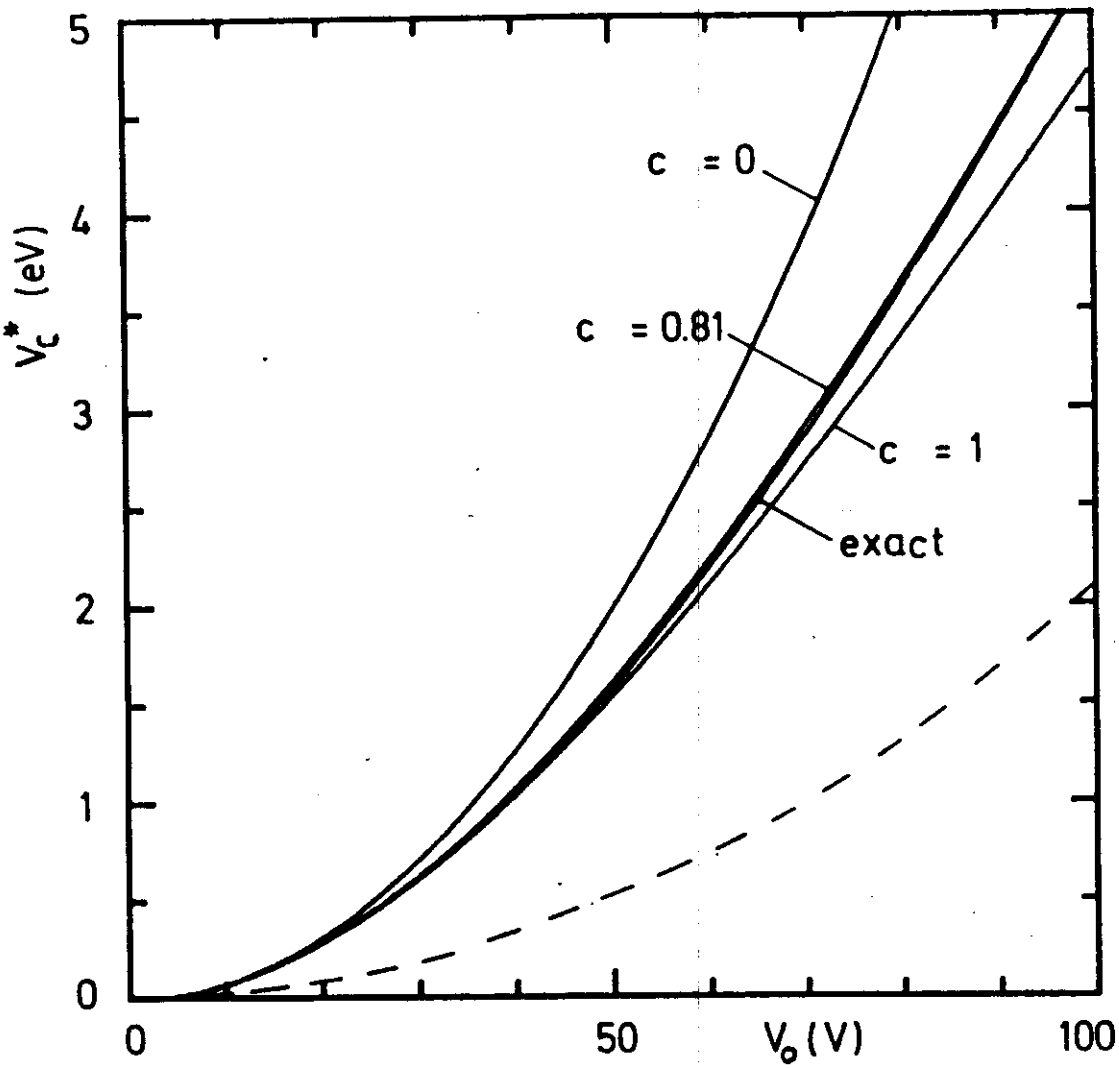

Figure 35. Critical effective potential V_c^* of an octopole calculated as a function of the rf amplitude V_0. The parameters used are $m = 20$u, $\Omega/2\pi = 8.3$ MHz, and $r_0 = 0.3$ cm. The curve $c = 0$ corresponds to the effective potential at $\hat{r} = 1$. For deriving safe guiding conditions, one has to account for the oscillatory motion. The different approximations are explained in the text. The dashed line corresponds to the safe operating condition, where $\hat{r}_m = 0.8$.

comparison $V_c^*(\hat{r}_c)$ for $c = 0$ and 1. The first case neglects the oscillatory motion, while $c = 1$ leads to a slight overestimation of the amplitude. At very low values of the adiabaticity parameter η (low amplitudes or high frequencies), the difference between the various approximations becomes very small. Recall that for high values of V_c^*, the operating conditions must always be maintained such that $\eta(\hat{r}_c) < 0.3$.

With the critical radius and the critical effective potential, specific limits for guiding ions can be derived from Eq. (45) and Eq. (46). For $U_0 = 0$, one obtains

$$E_m = \frac{1}{8}\frac{(qV_0)^2}{\epsilon}\hat{r}_c^{2n-2} + \frac{L^2}{2mr_c^2}. \tag{84}$$

In this case, the transmission depends only on the two adiabatic constants of motion, the total energy E_m and the orbital angular momentum L, that is, one obtains an (E_m, L) "stability diagram." As was discussed in Section II D 2, the centrifugal energy can be neglected in those cases where the ions start close to the centerline.

Setting $U_0 > 0$, and assuming for simplicity that the ion kinetic energy is zero at $\hat{r} = 0$, that is, $E_m = 0$, the ions will be accelerated in the direction of the negatively biased rods (see Fig. 12). Ion confinement requires at $\hat{r}_c$ the energy balance

$$qU_0\hat{r}_c^n = \frac{1}{8}\frac{(qV_0)^2}{\epsilon}\hat{r}_c^{2n-2}. \tag{85}$$

Comparing Eq. (84) for $L = 0$ with Eq. (85) reveals that the initial kinetic energy E_m and the kinetic energy gained from the electrostatic potential difference, $qU_0\hat{r}_c^n$, are equivalent. In both cases, the ion is lost as soon as this energy surmounts the critical effective potential $V_c^*(\hat{r}_c)$.

An experimental test has been performed to verify the validity of the derived relations. In this test ions were injected into an octopole close to the centerline. The axial energy was about 100 meV, corresponding to a negligible transverse energy with our injection conditions. The transmitted ion intensity was measured as a function of the rf amplitude V_0 at several different dc voltages U_0. Some typical results are shown in Fig. 36. As expected, the onset is shifted to higher amplitudes V_0 as U_0 is increased. A quantitative comparison is made in Fig. 37 where one can see directly that the experimentally determined correlation between V_c^* and U_0 is in good overall agreement with results (dashed line) from Eq. (85). The deviation at low guiding fields is most probably caused by potential distortions, which have been discussed in Section III C 2. Under favorable conditions they may indeed average out along the centerline of the octopole; however, it is reasonable to assume that on the surfaces there are still local distortions as high as 100 mV.

These uncertainties may also be responsible for the transverse energy resolution, which is on the order of 100 meV, as seen from the differentiated curve in the inset of Fig. 36. Because of this large uncertainty, we use the experimentally determined relation between U_0 and the rf amplitude for calibration purpose, rather than the theoretical dependence. For special ion trajectories, for example, those that are reflected from the rf wall between the rods, the transverse energy limit can be somewhat larger than given by Eq. (84). For transverse energy analysis it is therefore advisable to use low axial velocities, low orbital angular momenta L, and a long octopole in order to obtain many reflections from the guiding field.

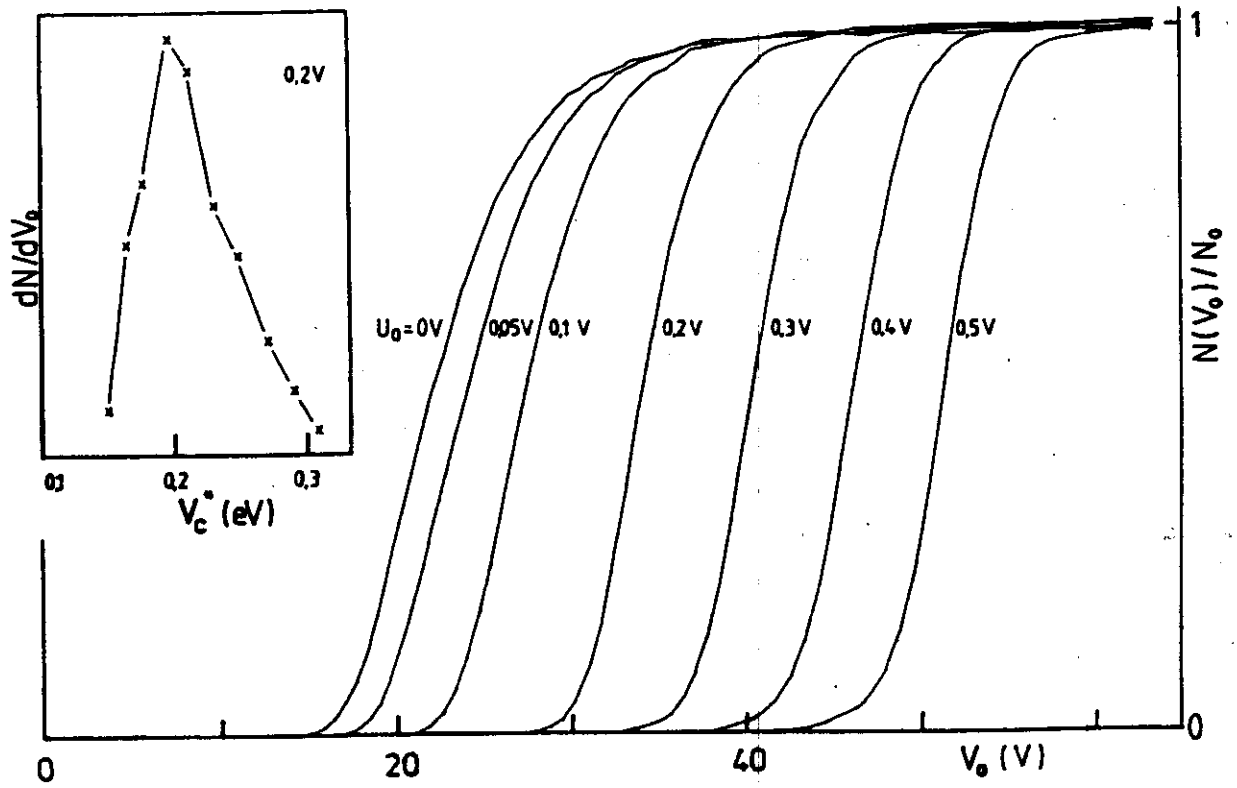

Figure 36. Transmitted ion intensity measured as a function of the octopole rf amplitude V_0 for several fixed dc voltages U_0. (The dc difference between neighboring rods is $2U_0$.) Parameters are $m = 40$ u, $\Omega/2\pi = 12$ MHz, and $r_0 = 0.3$ cm. The inset shows the differentiated 0.2 V curve as a function of V_c^*, indicating a transverse energy resolution of about 100 meV.

D. Traps as Ion Sources

The combination of rf ion trapping with ion formation has lead to the development of different storage ion sources. The advantages of such sources include high collection efficiency without the use of energy-perturbing extraction fields, accumulation of ions for obtaining intense short pulses, thermalization by inelastic collisions, and chemiionization by secondary reactions.

Quadrupole ion traps have been used in some experiments as ion sources (Dawson, 1976), and they are now widely applied for analytical purposes (March and Hughes, 1989); however, they are not suited for preparing a well-defined ion beam owing to difficulties in ion extraction resulting from geometrical restrictions. Many of these inherent problems can be overcome by making use of the fact that the effective potential can be tailored according to specific experimental needs, as recognized by Teloy, who reported the first use of an rf ring electrode trap as an electron-impact ion source (Bahr, 1969; Bahr et al., 1969). Several improvements of the shape of the storage volume have lead to better suited arrangements. Especially important was the separation of the ionization region from the ion source exit by using a

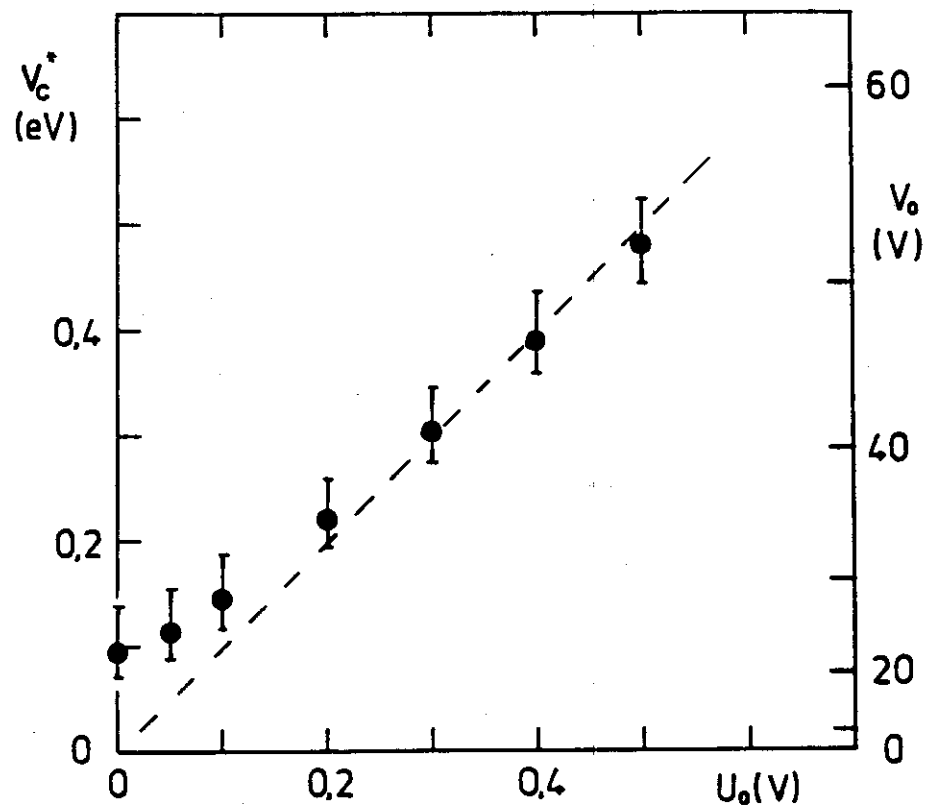

Figure 37. Correlation between the critical effective potential V_c^* and the dc voltage U_0. The rf amplitude, shown at the right-hand side, is converted into V_c^* using Eq. (82) and Eq. (83). The dashed line corresponds to the theoretical dependence given by Eq. (85). The dots are the 50% values of the transmission curves from Fig. 36, and the error bars indicate the 20–80% transmission range.

U-shaped storage volume (Gerlich, 1971). This rf storage ion source has been described thoroughly in Teloy and Gerlich (1974). A very similar version has been characterized in Sen and Mitchell (1986).

A slightly modified construction (Gerlich, 1977) is depicted in Fig. 38. The uppermost part shows the filament holder, the repeller, and the plate for electron extraction, which can also be used to pulse the electron beam. The U-shaped storage volume is defined by a stack of plates separated by ruby balls. The plates are alternately connected to the two phases of an rf generator. The top and bottom of this storage volume is limited by an adequate dc bias voltage applied to the two L-shaped endplates, each containing a small slot for the electron beam. In the exit region, the ions are guided in a field which changes smoothly to that of an octopole. Presently, we are using a storage ion source with a different electrode shape, as depicted in Fig. 46. This geometry has the advantage of being transparent in the axial direction for laser applications. In addition, the ion source has two equivalent filaments and ionization regions, and two symmetric ion exits that are useful for diagnostic purposes.

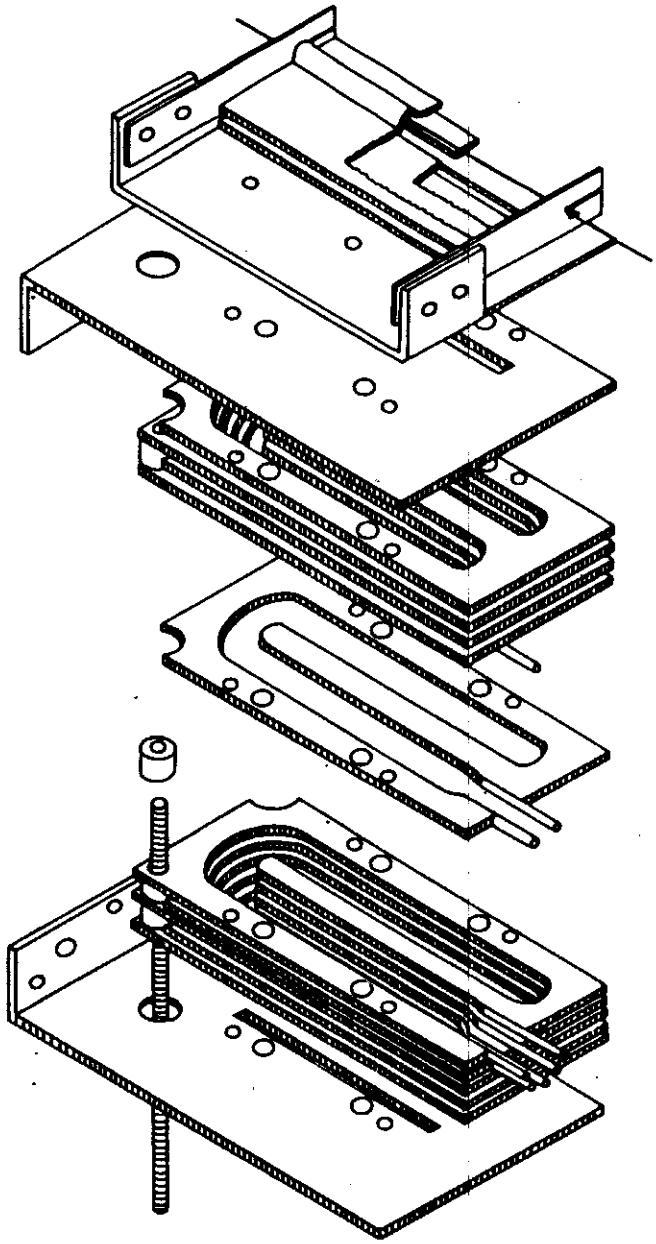

Figure 38. Schematic view of an rf storage ion source.

We limit our discussion here to a few examples that illustrate the advantageous features of the rf storage ion source. For the preparation of an intense, slow, and nearly monochromatic pulsed beam of protons (Gerlich, 1977; Teloy, 1978), we make use of the accumulating and mass-discriminating ability of the effective potential. Since in this case the trap is operated at the space-charge limit, it is important to avoid storage of undesired H_2^+ and H_3^+ ions by applying a weak dc difference and by properly adjusting the rf amplitude and H_2 pressure. On the other hand, the trap can be operated using a high pressure of H_2, such that more than 98% of the outgoing ions are H_3^+, formed by reactive $H_2^+ + H_2$ collisions. Collisional quenching of vibrationally excited ions has been demonstrated in several cases, for example,

production of partially cooled H_2^+ ions was achieved by operating with a H_2/Ne mixture (Sen and Mitchell, 1986). Suppression of metastable atomic ions has also been demonstrated for N^+ (Frobin et al., 1977; Gerlich, 1984). Chemical quenching in the source can be used very efficiently, for example, to discriminate C_2H^+ from $C_2H_2^+$ formed by electron-impact ionization, as seen in the mass spectrum in Fig. 39. Using a mixture of 5% C_2H_2 and 95% H_2, the undesired species could be completely eliminated, since C_2H^+ reacts much faster with H_2 than $C_2H_2^+$ (Ikezoe et al., 1986). The resulting higher masses are suppressed by the high mass cut-off feature of the quadrupole following the ion source (see Fig. 46). In some cases, thermodynamical equilibrium cannot be reached in the trap within an acceptable storage time. One example is the population of the two $Ar^+(^2P_I)$ fine structure states (Scherbarth and Gerlich, 1989). Another is the quenching of metastable Ar^{2+}. Admixture of $Ar^{2+}(^1D)$ has been tested by single charge transfer in Ar^{2+} + He collisions. The Ar^+ product velocity distribution in Fig. 40 shows changes in the metastable population with storage conditions; however, the slow

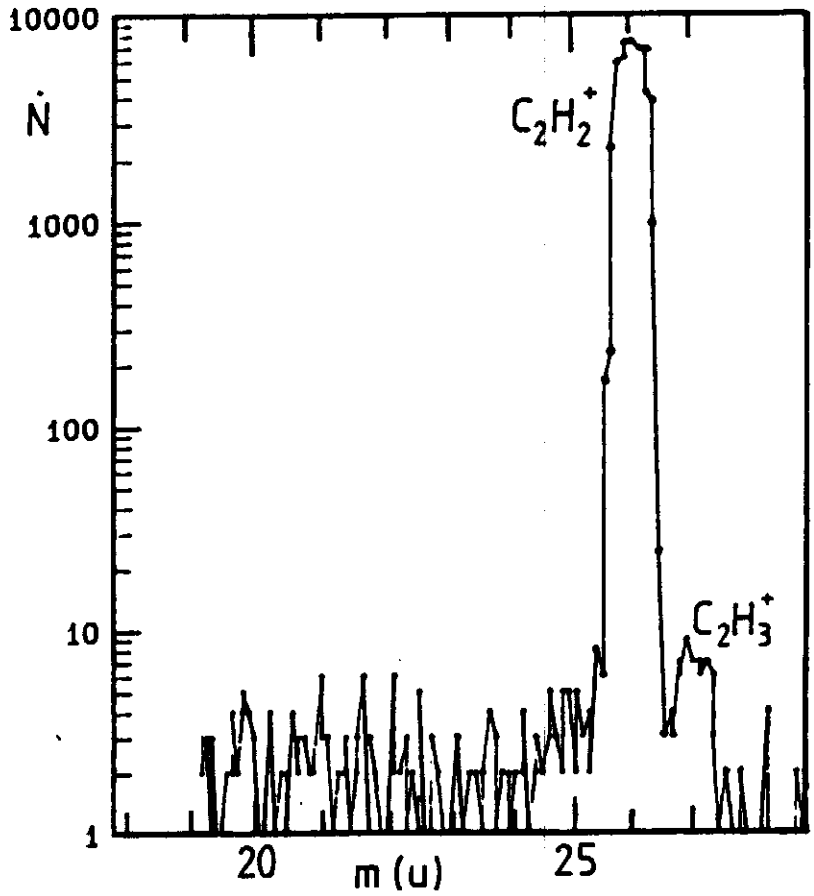

Figure 39. Preparation of a $C_2H_2^+$ beam by chemical quenching of C_2H^+ with H_2 in the storage ion source and by suppressing higher masses using the band-pass properties of the subsequent quadrupole.

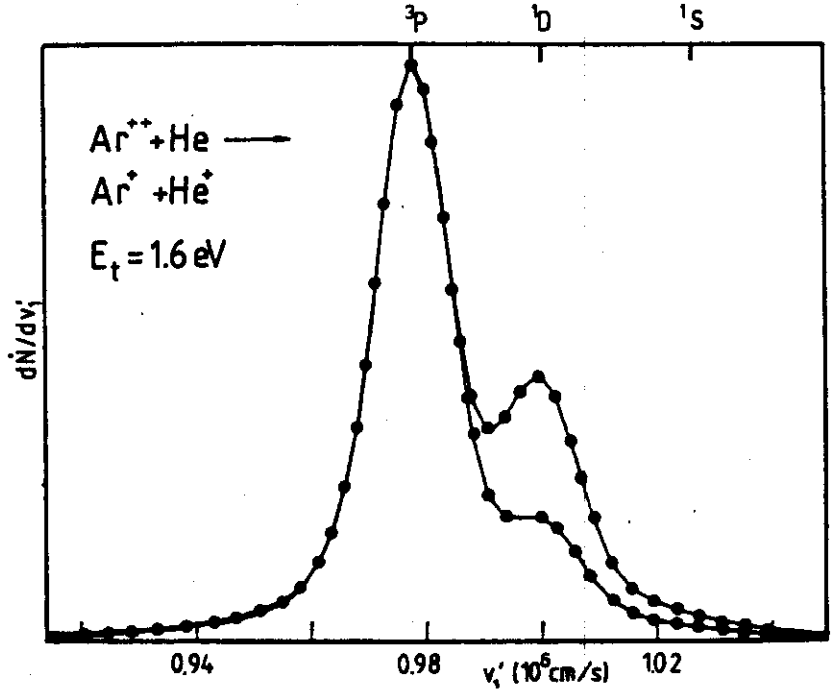

Figure 40. Quenching of metastable Ar^{2+} ions. The fraction of ions in the ^1D or ^1S state can be reduced by increasing the storage time in the rf source. Using the differential scattering apparatus, shown in Fig. 52, the composition of the initial Ar^{2+} beam has been analyzed by the charge transfer reaction $Ar^{2+} + He \rightarrow Ar^{+} + He^{+}$.

relaxation rate and the experimentally required duty cycle impeded complete relaxation.

In addition to the storage ion source and the previously mentioned combination of a quadrupole with photoionization, there are other possible combinations of guiding fields with ion formation. A photoionization source, combining a molecular beam of neutral precursors, monochromatized VUV light, and an oval 12-pole guiding field was described in Anderson et al. (1981). The oblong ionization volume, adapted to the exit slit of the monochromator, was converted smoothly into an octopole geometry using properly shaped electrodes. Another version of a stack-of-plates trap with a complicated labyrinth structure has been used by Anderson and coworkers (Hanley et al., 1987) for cooling metal-cluster ions in a He buffer gas. This group has also developed a method to produce boron-cluster ions by laser ablation in the interior of a specially designed rf ion trap (Hanley et al., 1988).

E. Ring Electrode Trap

The rf ring electrode ion trap has been proven over the past few years to be a very useful tool for obtaining low-temperature thermal rate coefficients of ion-molecule collisions owing to its unique sensitivity and efficient trapping capability (Gerlich and Kaefer, 1987, 1989; Gerlich et al., 1990). As was

mentioned in the preceding section, the ring electrode device was pioneered by Teloy and Bahr (Bahr et al., 1969), who utilized the trap to obtain information on thermal rate coefficients from temporal changes of ion concentrations (Bahr, 1969). Progress in our applications (Kaefer, 1989; Paul, 1990) is due to mass-selected ion injection and developments that allow one to vary the trap temperature over a wide range. The axial symmetry of the trap provides easy access at both ends for ion injection and extraction. Moreover, the geometry is also well suited for studying ion–laser interactions and for product detection by optical methods. Integration of the trap in a complete instrument will be described in Section IV E.

Two different electrode arrangements are shown in Fig. 41. The dominant construction problem was the need to operate the trap at cryogenic

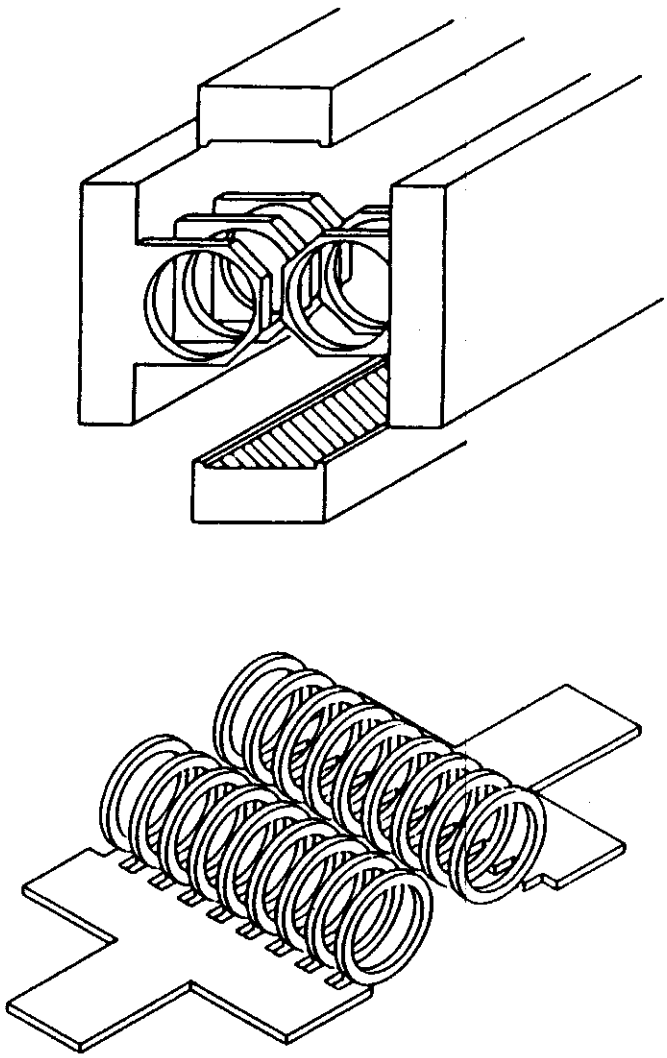

Figure 41. Illustration of two ring electrode traps. In the trap shown above the solid ring holders are cooled directly with liquid nitrogen. The lower trap has been designed for mounting on the head of a liquid helium cryocooler. The perspective views show the two groups of electrodes slightly removed from each other. The function of the two graphite-coated ceramic covers (hatched area in the upper figure) is explained in the text.

temperatures. An early version (Gerlich and Kaefer, 1987) not shown in Fig. 41, could only operate down to 170 K due to heating by absorbed rf power. To overcome this problem, a second version, upper structure in Fig. 41, was constructed (Gerlich and Kaefer, 1988, 1989), whereby the entire device is cooled directly by running liquid nitrogen through the massive ring holders using electrically insulated feedthroughs. The liquid nitrogen flows from one half of the trap to the other using stainless-steel tubing. The tubing is bent into the shape of a coil such that the inductance L of this coil and the capacitance c of the trap are used directly as a Lc-resonance circuit (Kaefer, 1989), which can be easily excited by inductive rf coupling. Typical frequencies and amplitudes are 25–35 MHz and up to 100 V, respectively.

1. *The 10–350 K Trap*

A third version (Paul, 1990) has been designed for mounting directly onto the cold head of a closed-cycle liquid helium refrigeration system (Leybold Heraeus, RD 210).The perspective view in the lower part of Fig. 41 shows the two identical halves slightly removed from each other. Each half can be machined from a solid copper block; however, experience has shown that the rf power absorbed in the rings is so low that one can simply hard solder or weld the rings onto the bottom plates using either copper or stainless steel. The two plates are attached to the cold head and a 0.1-mm-thin sheet of a special insulating material (Denka, BFG 20) is placed between the plate and the cold head to obtain good electrical insulation and sufficient heat conductivity, as has also been applied successfully for a similar purpose by Hiraoka (1987). The advantage of this material is its flexibility at low temperatures; however, the material is not best suited for our vacuum conditions and its heat conductivity decreases toward low temperatures. We are presently performing tests with sapphire insulation, the heat conductivity of which is even higher than that of copper at temperatures below 80 K. As indicated in Fig. 58, the trap is surrounded by a 80 K heat shield, which is connected to the first stage of the cryocooler. All connections to the trap, including the gas inlet and the wires to the external rf coil, are also precooled to 80 K. At full rf amplitude, the total required cooling power at the second stage of the cryocooler is less than 0.2 W and the lowest achievable temperature of the electrodes is 10 K.

The kinetic energy distribution of ions stored in the wide field-free region of the ring electrode trap has been discussed in detail in Section II E. The effective potential has been derived in Section II C 3 and is shown in Fig. 8. The relation between the actual shape of the electrodes and the mathematical boundary conditions used to describe this trap are compared in Fig. 7. Typical dimensions of the trap are $r_0 = 0.5$ cm, while the thickness of the rings and their separation is 0.1 cm, resulting in $2\pi z_0 = 0.4$ cm. The shape of the ion

cloud has an almost cylindrical form with a volume of about 1 cm^3. The maximum observed ion density is $10^6\ cm^{-3}$, which is close to the space-charge limit. Most experiments are performed with typically 10^3–10^4 ions per cm^3. At these low ion densities space-charge effects and ion-ion collisions are negligible.

The problem of surface potential distortions, discussed in Section III. C 2, also perturbs the functioning of the ring electrode trap. In this case, the ions are thermalized and trapped; however, trapping can occur in regions of local potential minima, and, as a result, the ions are not distributed throughout the trap. This can lead to an augmentation of rf heating, as discussed in Section II E. In addition, this localized trapping can significantly increase the time needed for extraction. To aid in ion extraction, as well as correct the position of the trapped ion cloud, we make use of field penetration from external electrodes. As electrodes we use the graphite-coated ceramic plates, indicated in Fig. 41 by the hatched area, which are also used to confine the buffer gas. Applying a voltage of about 100 V across the ends of the graphite coating creates a constant axial potential gradient toward the exit. This voltage is pulsed on during the extraction period and shortens the time needed to evacuate the ions from the trap. With an additional voltage applied to a contact in the center of the correction electrode, a V-shaped field can be generated, which leads to a concentration of the ions close to the middle of the trap. This well can be made sufficiently deep to confine the ions in the axial direction.

The maximum achievable storage time of ions in the trap is usually limited by the extent of reactive-loss processes. Storage loss is very unlikely, since the confining potential wall is usually several eV and the chance that an ion can accumulate sufficiently high energy is rather low. Examples that illustrate the change of the ion composition in the trap as a function of storage time are given in Fig. 42. The upper panel shows a fast conversion of primary H^+ ions into D^+ products (Gerlich and Kaefer, 1987), the sum of these ions indicates no loss on the millisecond time scale. Ternary association of CD_3^+ with $2D_2$ (Gerlich and Kaefer, 1989) is plotted in the middle panel. Here, the time constants are in the range of seconds. The sum of the two ion intensities declines with a mean life time of 12 s, most probably due to formation of nonrecorded products. The lowest panel shows storage of He^+ ions over several minutes at 10 K. A dominant loss channel is due to reaction with background N_2 (density $5 \times 10^5\ cm^{-3}$).

2. *Collision Temperature*

A general difficulty with all ion traps is the determination of the actual collision "temperature." The precise ion energy distribution is a complex function of parameters such as the temperature of the electrodes, the walls,

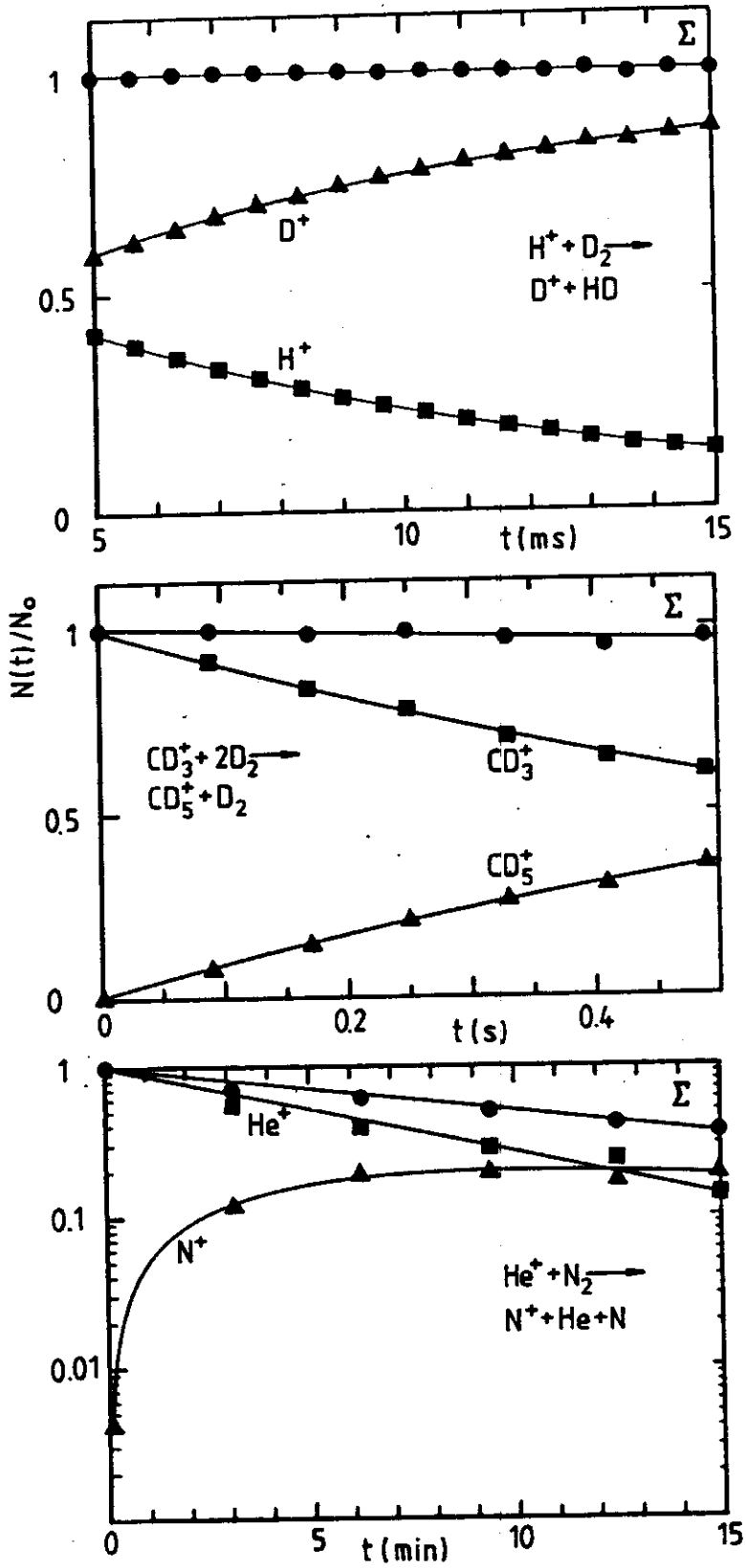

Figure 42. Change of ion composition in the trap as a function of storage time. The upper panel depicts a typical fast reaction; the time scale is in the millisecond range for target densities between 10^{12} and $10^{13}\,cm^{-3}$. The middle panel shows a ternary association reaction; time constants are in the range of seconds. The lowest figure shows storage of He^+ ions over several minutes. The loss of ions in this case is predominantly due to reactions with traces of the background gas, for example, N_2.

and the buffer gas. The rf influence on the ion energy has been discussed in Section II E. This can be investigated experimentally, based either on known temperature dependencies of rate coefficients or by determination of a thermodynamical equilibrium. One example is the slightly endothermic reaction $N^+ + H_2 \rightarrow NH^+ + H$, for which the endothermicity ΔH^0 has been established as 17 ± 2 meV from CRESU data (Marquette et al., 1988) and phase-space evaluation (Gerlich, 1989b). These results are compared to our ring electrode trap results (Gerlich et al., 1990) in Fig. 43. If we explain the slight deviation on the basis of a higher temperature in our experiment, we obtain a difference of 10 K between our nominal temperature and the actual temperature. However, the discrepancy may also be explained by incomplete thermalization of the $N^+(^3P_J)$ fine structure states. Our results are in perfect agreement with the statistical theory if we change the endothermicity ΔH^0 from 17 to 15 meV. Another test is the three-body association reaction $He^+ + 2He \rightarrow He_2^+ + He$ for which we have obtained a ternary rate coefficient $k_3 = 6 \times 10^{-31}$ cm^3/s at a nominal trap temperature of 10 K. This value compares well with results obtained from a liquid-helium-cooled drift tube (Böhringer et al., 1983). Accounting for possible errors in the determination of the He density and the absolute rate coefficient, the resulting uncertainty of the temperature is again 10 K.

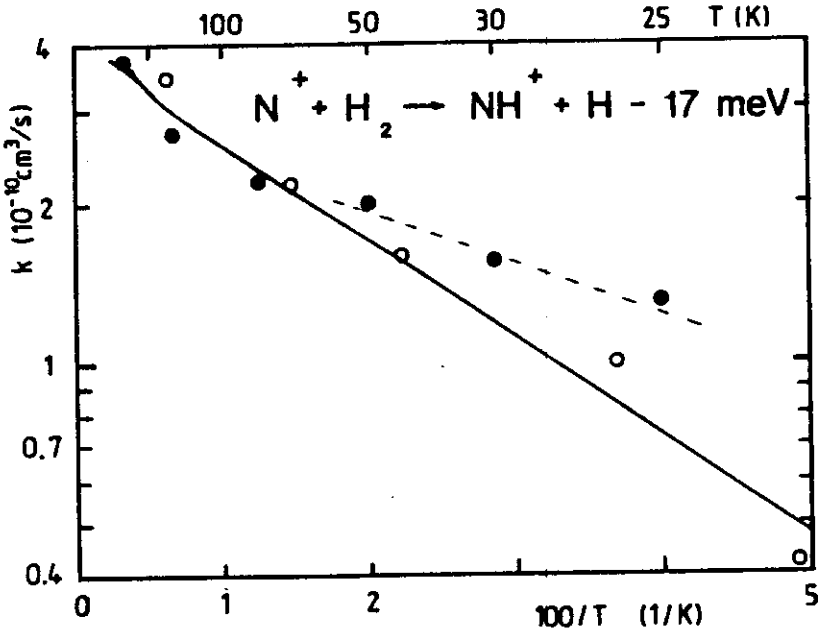

Figure 43. Arrhenius plot of the temperature dependence of the rate coefficient for the endothermic ion–molecule reaction $N^+ + H_2 \rightarrow NH^+ + H$. The phase-space calculation (Gerlich, 1989b) (solid line) has been adjusted to the CRESU results (Marguette et al., 1988) (○) by using $\Delta H^0 = 17$ meV. Possible explanations for the slight deviations from our trap measurements (●) are given in the text.

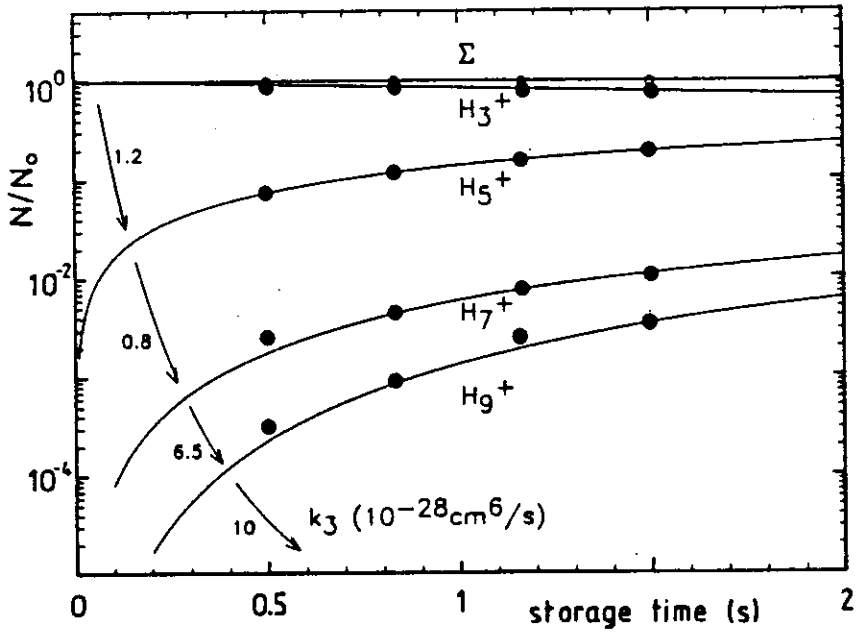

Figure 44. Consecutive formation of hydrogen clusters at a temperature of 25 K. H_3^+ primary ions were injected into the ring electrode trap containing normal $-H_2$ at a rather high density of $3.7 \times 10^{13}\,cm^{-3}$. The lines are solutions from the corresponding rate equation system. The numbers on the arrows are the resulting ternary rate coefficients in $10^{-28}\,cm^6/s$.

Determining the collision temperature based on thermodynamical equilibrium has the advantage that it is independent of the neutral density. At temperatures above 80 K, we have stored H^+ ions in a known H_2/D_2 mixture and measured the resulting H^+/D^+ equilibrium, the temperature dependence of which is well known (Gerlich, 1982; Henchman et al., 1981). At low temperatures, the $H_3^+ \cdot (H_2)_n$ cluster-size distribution can also be used as a thermometer over a wide range, based on recently published cluster binding energies (Hiraoka, 1987). Figure 44 shows the consecutive formation of hydrogen clusters following injection of H_3^+ into our trap containing H_2 at a nominal temperature of 25 K. From these data, the rate coefficient for cluster growth can be derived; however, the storage time was too short to reach thermodynamical equilibrium at this low temperature. The equilibrium can be established more quickly if one injects larger hydrogen cluster ions.

IV. DESCRIPTION OF SEVERAL INSTRUMENTS

In this section we begin with a short, mainly chronological, overview of various guided-ion-beam instruments used in different laboratories in which one or more of the rf devices described in Sections II and III are combined for stydyng processes in gas-phase ion physics and chemistry. Mostly these instruments are used to investigate low-energy ion–molecule collisions, but we will also refer briefly to a few spectroscopic applications. In Sections

IV B–IV E we describe in detail four apparatuses used in our laboratory, that is, an universal guided ion beam, a differential scattering, a merged beam, and a ring electrode ion trap apparatus. Some fundamentals of kinematic averaging and data analysis are compiled to compare the various experimental methods. Examples that illustrate special features of the instruments are also given in this section, while a more complete overview of specific applications follows in Section V.

A. Overview: Instruments Using rf Devices

One of the early uses of an rf field as an ion-beam guide was reported by von Zahn (Tatarczyk and von Zahn, 1965; von Zahn and Tatarczyk, 1964) for studying metastable decay of excited polyatomic ions in the time window between 0.1 and 1 ms. In this experiment, a mass-selected ion beam was injected into a 314-cm-long quadrupole operated in the rf-only mode ($a_2 = 0$). The field parameters were chosen such that a wide range of masses were transmitted, that is, to guide the parent ions and to simultaneously confine their fragments. The ions were analyzed in a subsequent quadrupole mass spectrometer. Decay rates on the order of $10^4\ s^{-1}$ were reported for several hydrocarbon ions.

Related experiments are now performed using so-called triple quadrupole mass spectrometers. These instruments were developed initially (McGilvery and Morrison, 1978; Vestal and Futrell, 1974) to study laser photodissociation processes in the center rf-only quadrupole, and their use has expanded to include among others the study of collision-induced dissociation of polyatomic ions. Such instruments and more complicate ones, for example, penta quadrupoles, are now available and are used routinely for analytical purposes, see, for example, Dolnikowski et al. (1988) and references therein. For obtaining accurate cross sections for collision processes, however, such arrangements are often insufficient. Unsuitable injection conditions lead to poorly defined collision energies, and inefficient product collection can result from unsafe ($\eta > 0.3$, see Section II D 2) operating conditions of the rf-only quadrupole or from a mismatch of the product phase space to the mass analyzer or to the ion detector.

The development of the first guided-ion-beam apparatus began in the late 1960s in the group of Ch. Schlier by E. Teloy (Bahr, 1969; Bahr et al., 1969, 1970; Werner, 1968), with the combination of a ring electrode trap ion source, described in Section III, and a magnetic mass spectrometer followed by the construction of the storage ion source and the first octopole (Gerlich, 1971). Early results obtained using this instrument have been mentioned in Henchman (1972), while a complete description of the first guided-ion-beam apparatus and several integral cross sections were published in Teloy and Gerlich (1974). Further results are given in Frobin et al. (1977) and Ochs and

Teloy (1974). An improved and more universal version of this apparatus will be described in Section IV B. A differential scattering apparatus consisting of several rf devices, including a 1-m-long octopole for product time-of-flight analysis, has also been constructed by the same group (Gerlich, 1977; Teloy, 1978). Details of this apparatus will be given in Section IV C.

The incorporation of rf octopoles and other special rf devices in different laboratories has proceeded rather slowly. At the end of the 1970s the guided-ion-beam technique was combined with the photoionization method in the group of Y.T. Lee (Anderson et al., 1981). This instrument consisted of a molecular-beam photoionization source, a He discharge lamp (Hopfield continuum), and vacuum ultraviolet monochromator, coupled with an octopole beam guide, scattering cell, and quadrupole mass spectrometer detector. With this apparatus effects of both reagent translational and vibrational energy have been studied for several reaction systems (Houle et al., 1982; Turner et al., 1984).

During the 1980s the guided-ion-beam technique became more popular and several groups successfully contributed to its further development. A discussion of the fundamental functioning of an octopole ion guide and some performance tests were published by Okuno (Okuno, 1986; Okuno and Kaneko, 1983) who studied one- and two-electron capture of Ar^{2+} and Kr^{2+} in their own gases.

Anderson and coworkers have extended the use of the guided-ion-beam technique into different fields. In their group they developed an apparatus for measuring integral cross sections of cluster ion reactions (Hanley and Anderson, 1985). A unique feature of their instrument is an rf storage trap with labyrinthine geometry, which is used to collisionally cool sputtered cluster ions (Hanley et al., 1987). In another instrument, state-selective preparation of ions via multiphoton ionization has been combined with a tandem guided-ion-beam spectrometer (Orlando et al., 1989). The influence of different vibrational modes on the reaction dynamics of several collision systems are discussed in more detail in Anderson's chapter of this book.

Also, the group of Armentrout started in the early 1980s (Ervin and Armentrout, 1985; Ervin et al., 1983), to utilize guided-ion-beam instruments for investigating various reactions, among others, those between first- and second-row atomic cations and isotopic hydrogen molecules. Some of their results have been reviewed in Farrar (1988). A recent experimental modification has been made to cool the octopole and scattering cell to near liquid nitrogen temperatures (Sunderlin and Armentrout 1990). In the past year, this group has also completed the construction of a new guided-ion-beam mass spectrometer, the design and capabilities of which have been described in Loh et al. (1989). This mew instrument has been developed to study collision-induced dissociation dynamics of cold metal-claster ions.

Ng and coworkers have made extensive use of photoionization coupled in various combinations with octopole beam guides and quadrupole mass filters (Flesch et al., 1990; Liao et al., 1990; Ng, 1988), including a crossed ion–neutral-beam photoionization instrument (Liao et al., 1984, 1985) and a triple-quadrupole double-octopole photoionization apparatus (Liao et al., 1986). A unique demonstration of the high sensitivity of the guided-beam technique is the differential reactivity method developed in this group (Liao et al., 1985). With this method it is possible to determine the internal energy of product ions by reacting them in the second octopole with a probing gas. The power of this method for obtaining state-to-state information, as well as further details of these instruments, are documented in Ng's chapter of this volume.

For several years the group of D. Zare (Conaway et al., 1987; Morrison et al., 1985) has applied resonance enhanced multiphoton ionization to the production of vibrationally state-selected ion beams (see Anderson's chapter, this volume). Using a tandem quadrupole arrangement with a static gas collision cell, ion molecule reactions have been studied. In order to improve the product collection efficiency and the accessible energy range, they have recently built a quadrupole-octopole-quadrupole system (Posey et al., 1991).

In order to complete, hopefully without omission, the list of guided-ion-beam instruments, we also wish to mention the investigations of Tosi et al. (1989b) who have recently completed the construction of such an instrument and have used it in a crossed beam arrangement to study $Ar^+ + H_2$ reactions (Tosi et al., 1989a). A very recent combination of photoionization with octopole guiding fields became operational in Orsay (Guyon et al., 1989). Special features of this apparatus include ion preparation using monochromatized synchrotron radiation in combination with the threshold photoelectron– photoion coincidence method, and also the ability to determine integral cross sections and to measure product velocity distributions using a short scattering cell in a system of two octopoles similar to that described in Section IV B. Finally, there are some spectroscopical applications which employ rf guiding fields. A molecular ion spectrometer consisting of a long rf octopole for guiding or storing ions has been developed in the group of Lee. An application of this device was to study the spin-forbidden radiative decay of $O_2^+(a^4\Pi_u)$ (Bustamente et al., 1987). Also, using tunable IR lasers, fragmentation of several cluster ions has been studied including $H_3^+(H_2)_n$ and $H_3O^+(H_2O)_n$ (Okumura et al., 1988; Yeh et al., 1989).

B. The Universal Guided-Ion-Beam Apparatus

The apparatus described here is, on the whole, comparable to the first guided-ion-beam apparatus (Teloy and Gerlich, 1974); however, there are many improvements and extensions that require elaboration. A fundamental capability of both instruments is the ability to precisely determine integral

cross sections with high sensitivity. In the improved guided-ion-beam apparatus, the range of laboratory energies of guided ions has been extended to below 10 meV (Gerlich, 1984). Expansions of the capabilities of this apparatus include the ability to measure photons from chemiluminescent reactions and to detect coincidences between photons and mass selected product ions (Gerlich and Kaefer, 1985). Product angular distributions can also be obtained by a procedure that combines time-of-flight analysis with variation of the guiding field (Disch et al., 1985). A rather detailed description of this procedure and several applications have been reported in Gerlich (1986) and will be further discussed in Section IV B 3. The modular design of the apparatus allows for simple replacement of the scattering cell with a crossed pulsed supersonic beam, thereby improving the kinetic energy resolution. This led to the discovery of an oscillatory structure in the integral cross section for the reaction $C^+ + H_2 \rightarrow CH^+ + H$ (Gerlich et al., 1987). The geometry of the ion source and the off-axis detection system allow for ease of integration of various laser systems to state selectively prepare reactants and/or to analyze reaction products (Gerlich and Scherbarth, 1987). A detailed study of the $Ar^+ + O_2$ charge transfer, including the determination of rovibrational product state distributions by laser-induced predissociation, has been published recently (Scherbarth and Gerlich, 1989) and demonstrates the versatility of this instrument.

1. *Description of the Apparatus*

Figure 45 shows schematically the most important elements of a simple guided-ion-beam apparatus. An rf storage ion source is used (see Section III D) to trap and internally thermalize ions generated by electron bombardment. The trap is usually operated in a pulsed mode by opening the ion gate for a few μs leading to a rather high momentary peak current. For energy and mass filtering the ions must pass very slowly, typically 0.1 eV axial energy, through the focusing quadrupole, as described in Section III B 2. Additional time-of-flight selection is achieved by pulsing the beam a second time at the center element of the lens system following the quadrupole. In order to avoid interference with the rising and falling edges of the pulse, this lens element is divided into equal halves that are connected to two properly adjusted counter propagating pulses. Usually the lens system focuses the ions into the injection electrode; however, in some cases, to reduce the angular divergence of the injected ion beam, all lens elements are operated at the same voltage. Typical octopole dimensions are $d = 0.2$ cm and $r_0 = 0.3$ cm, fulfilling the relation given by Eq. (68). The scattering cell usually consists of a 3–15-cm-long cylinder containing the target gas. The vacuum conductance of this cell is reduced by two small tubes that closely surround the octopole. As described in Section III C 2 and illustrated in Fig. 30, the

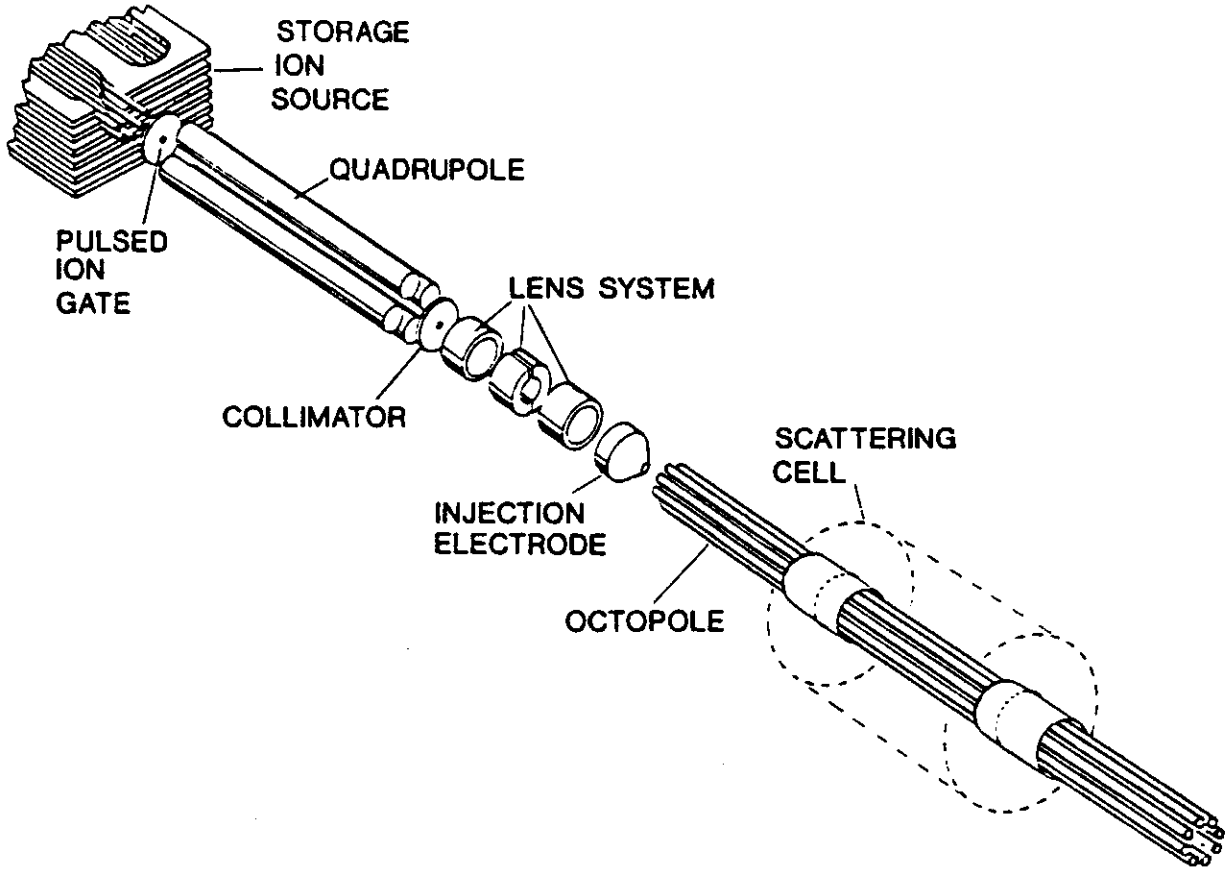

Figure 45. Perspective view of the major elements of a typical guided-ion-beam apparatus. Ions are created in a storage ion source, are mass and energy selected in a quadrupole and are injected into an octopole via a funnellike electrode. The scattering cell usually consists of a gas-containing cylinder surrounding the octopole. The ion beam is pulsed by opening the gate at the exit of the ion source and by pulsing the two halves of the middle element of the lens system.

field penetration of these cylindrical electrodes is used for diagnostic purposes, ion trapping, and so on.

A detailed illustration of our universal guided-ion-beam apparatus (Gerlich 1986; Scherbarth and Gerlich, 1989) is depicted in Fig. 46. It consists of the just described rf source for ion creation and preparation. Alternatively, this source can be easily exchanged with the multiphoton ionization source described in Section III B 3. The primary ions are injected into a tandem octopole arrangement with a short scattering cell. Primary and product ions are mass analyzed by a magnetic mass spectrometer and detected using a scintillation detector. The two octopoles are coupled mechanically such that the rf field does not change in the joint, yet the ions can be accelerated or decelerated by using different dc potentials.

Calibration of the kinetic energy of the ion beam in the octopole has been described in detail in Section III C 3. For some applications it may be sufficient to use the octopole as a retarding field analyzer; however, it is normally advisable to calibrate the difference between the onset of the ion

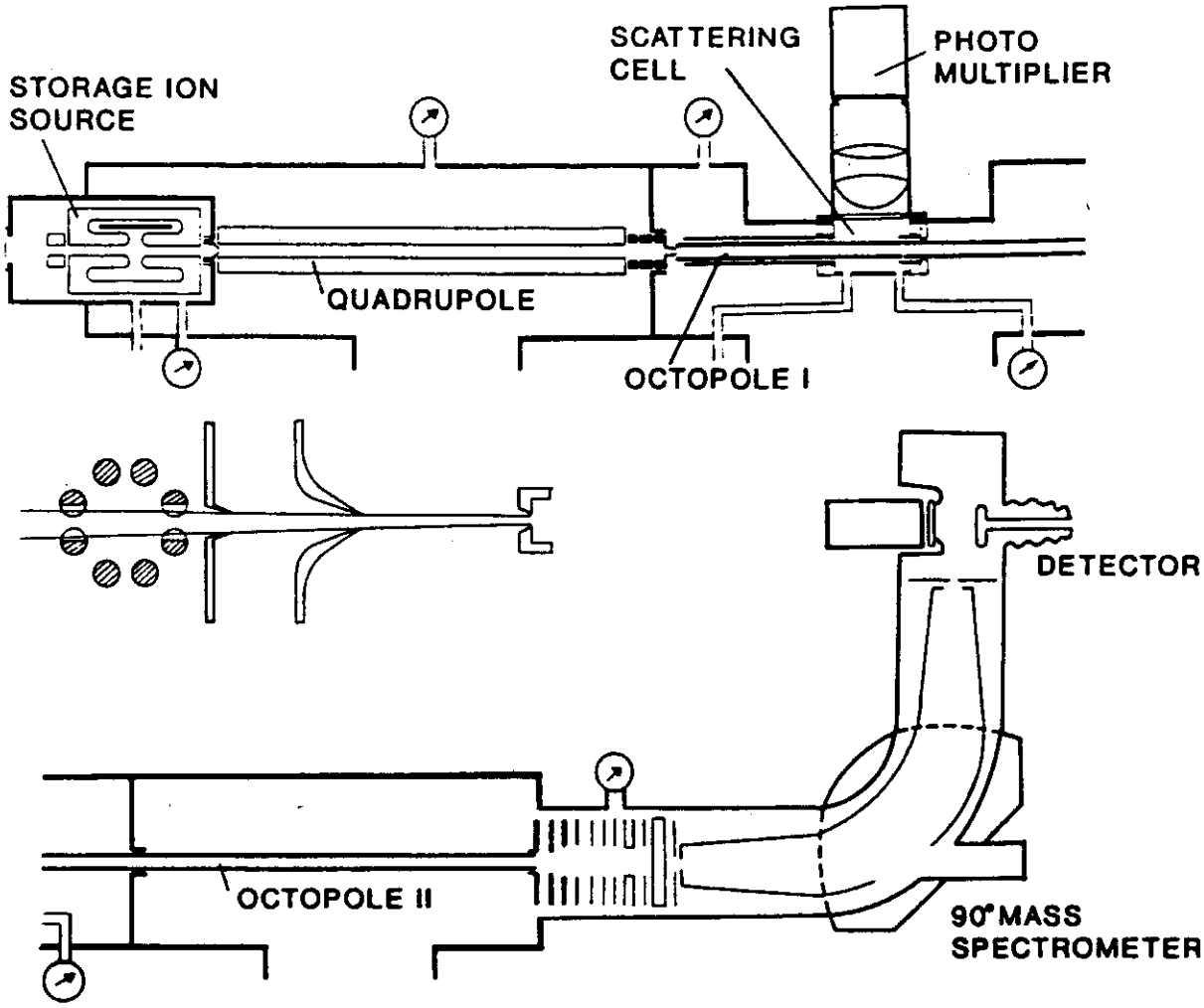

Figure 46. Schematic of the universal guided-ion-beam apparatus (the lower part of the figure is a continuation of the upper). The bakable vacuum system is pumped separately by three turbomolecular pumps. The crossed-beam arrangement, depicted between the two parts of the figure, can be used in place of the scattering cell/photomultiplier arrangement. Most electrodes are shown approximately to scale. The length of the quadrupole is 26 cm, octopoles I and II are 14 cm and 46 cm long, respectively. The 90° magnetic mass spectrometer has a 15 cm radius.

intensity and the energy zero point by time of flight. In order to avoid loss in accuracy, all measurements are made in the pulsed mode under the same conditions the time-of-flight calibration procedure was performed.

Problems related with the injection of ions into rf multipoles have been briefly mentioned in Sections II and III; however, a few additional comments and some practical hints are needed. Going from a pure dc field into an ideal multipole rf field, the ions traverse a region in which they are under the influence of a combined dc and rf field, which has both axial and transverse components. This always leads to perturbations of the energy and angular distributions of the injected ions. In order to minimize these effects, several precautions should be taken. An rf-field-free region along the multipole axis

can be attained if the mechanical geometry is accurate and the amplitudes of the two rf voltages are symmetric and exactly opposite in phase. Note that it is also necessary to block the rf from the dc electrodes using capacitors. Under such conditions, an ion beam that is injected very close to the axis with a small angular divergence remains unperturbed. In cases where for intensity reasons, or for passage of a laser beam, one has to use entrance holes with dimensions up to $r/r_0 < 0.5$, it is important to avoid rapid entrance of the ions into the rf field, since the impairment of their kinetic energy is significantly increased if one works under nonadiabatic conditions in the transition region. A slow entrance can be achieved by a gradual spatial variation of the field using adequate electrodes or electrical-field-shielding devices, as known from quadrupoles. Alternatively, it is also possible to pass the critical region very slowly, that is, during several rf periods. In general, we operate in the transition region with ion energies of a few tenths of an eV. The injection field is defined by a conelike electrode, as can be seen in Fig. 30 or Fig. 45. This electrode is centered in a precisely machined ceramic part, which also holds the multipole rods in their exact position.

Neutral reactants are introduced either diffusively into a scattering cell or as a pulsed supersonic beam; see Fig. 46. The gas cell is rather short to reduce potential distortions, as discussed in Section III C 2, and for product time-of-flight analysis. Determination of the neutral gas density n_2 and the effective scattering length L have been described previously (Gerlich et al., 1987). The amplitude and the frequency of the rf field are always chosen such that all primary and product ions are confined in the octopole and guided toward the mass spectrometer detector. In the laboratory system, backward-scattered ions can be reflected forward by operating the ion beam and the injection electrode in a pulsed mode. Under such conditions, the octopole can guarantee 4π collection efficiency. Nonetheless, there are other possible sources of errors in determining absolute cross sections, for example, those caused by local potential distortions and the limited phase-space acceptance of the detection system.

Local potential barriers in the scattering cell can lead to trapping of slow product ions and their loss, for example, by secondary reactions. More critical, especially at low laboratory energies, is the trapping of scattered primary ions in the scattering cell. This often leads to a significant increase in the formation of products, especially if the cross section is large at low collision energies. These problems can be tested and partially avoided by applying adequate potentials to the two ring electrodes (5) and (6), depicted in Fig. 30. An external potential barrier at the entrance of the reaction zone reflects slow ions and reduces the extent of trapping. A barrier at the exit can increase the effect for diagnostic purposes. An example of a reaction that is very sensitive to potential barriers is the $N^+ + CO$ charge transfer, as

discussed in Gerlich (1984 and 1986). Similar effects have been observed for the $Ar^+ + O_2$ charge transfer.

Difficulties in matching the phase space of the ions emerging from the octopole to the phase space accepted by the mass analyzer and detector have already been discussed in detail in Teloy and Gerlich (1974). Most of the newer guided-ion-beam instruments mentioned in Section IV A utilize quadrupole filters for mass analysis. However, according to our experience, it is not easy to avoid discrimination effects if the reaction products have large transverse velocities or if the rod diameter of the quadrupole filter is too small. In our universal guided-ion-beam apparatus, the ions are gradually accelerated via several lens elements with large apertures to 2–3 keV, then focused by two independent electrostatic einzel lenses to the entrance slit of a large magnetic mass spectrometer. The Daly-type detector is preferred over open ion multipliers owing to its large area and very uniform detection efficiency.

2. *Kinematic Averaging*

So far, the majority of the guided-ion-beam experiments has been performed by passing the octopole through a scattering cell. The influence of the random thermal motion of the target gas on the distribution of the collision energy has been treated often (Berkling et al., 1962; Chantry, 1971; Schlier, 1988; Teloy and Gerlich, 1974) and the impairment of the product energy distributions has recently been discussed in Gerlich (1989a). In a few experiments (Gerlich et al., 1987; Sunderlin and Armentrout, 1990), the target temperature has been reduced by operating with a cooled scattering cell. Significant improvement, however, can only be achieved by replacing the scattering cell with a supersonic beam. Two successful approaches in which a neutral beam was crossed with a guided ion beam at a right angle have been described in Gerlich et al. (1987) and recently in Tosi et al. (1989a). The kinematic conditions can be further improved if the crossed beams are replaced by merged beams, as will be described in Section IV D. To better compare the different arrangements, it is necessary to summarize a few facts concerning kinematic averaging.

In an ideal experiment, with two well-collimated monochromatic beams of velocities $\mathbf{v}_1$ and $\mathbf{v}_2$, the number of molecules reacting per unit time in the scattering volume $d\tau$ is given by (Gerlich, 1989a; Levine and Bernstein, 1974)

$$d\dot{N} = g\sigma(g)n_1 n_2 d\tau. \tag{86}$$

Here, $g = |\mathbf{g}| = |\mathbf{v}_1 - \mathbf{v}_2|$ is the relative velocity, n_1 and n_2 are the projectile and target densities, respectively, and $\sigma(g)$ is the intrinsic integral cross section. The corresponding intrinsic rate coefficient is denoted as $k = g\sigma(g)$. In

contrast to the ideal case, the kinematic conditions of a realistic experiment are less well defined, and the actually obtained product rate $d\dot{N}$ is the average over the velocities of the reactants $\mathbf{v}_1$ and $\mathbf{v}_2$. The number of molecules reacting per unit time in the scattering volume $d\tau$ is given by the six-dimensional integral

$$d\dot{N} = \int_{\mathbf{v}_1} d\mathbf{v}_1 \int_{\mathbf{v}_2} d\mathbf{v}_2 g\sigma(g) n_1(\mathbf{r}, \mathbf{v}_1) n_2(\mathbf{r}, \mathbf{v}_2) d\tau. \tag{87}$$

Assuming that the velocity distributions are independent of the spatial coordinate $\mathbf{r}$, the density functions $n_i(\mathbf{r}, \mathbf{v}_i)$ can be factorized using normalized probability functions $f_i(\mathbf{v}_i)$ $(i = 1, 2)$

$$n_i(\mathbf{r}, \mathbf{v}_i) = n_i(\mathbf{r}) f_i(\mathbf{v}_i). \tag{88}$$

With $f_1(\mathbf{v}_1)$ and $f_2(\mathbf{v}_2)$, we define $f(g)$, the distribution of the relative velocity

$$f(g)dg = \int_{\mathbf{v}_1} d\mathbf{v}_1 \int_{\mathbf{v}_2} d\mathbf{v}_2 f_1(\mathbf{v}_1) f_2(\mathbf{v}_2). \tag{89}$$

$f(g)dg$ denotes the probability that the relative velocity lies in the interval $[g, g + dg]$. The asterisk indicates symbolically that the integration must be limited to that subspace of $(\mathbf{v}_1, \mathbf{v}_2)$ where $|\mathbf{v}_1 - \mathbf{v}_2|$ falls into this interval. With the mean relative velocity $\langle g \rangle$,

$$\langle g \rangle = \int_0^\infty g f(g) dg, \tag{90}$$

we define the *effective cross section* with a somewhat more general distribution function $f(g)$ than usual as

$$\sigma_{\text{eff}}(\langle g \rangle) = \int_0^\infty \frac{g}{\langle g \rangle} \sigma(g) f(g)\, dg. \tag{91}$$

With this definition of σ_{eff}, we obtain a result that is very similar to Eq. (86)

$$d\dot{N} = \langle g \rangle \sigma_{\text{eff}} n_1(\mathbf{r})\, n_2(\mathbf{r})\, d\tau. \tag{92}$$

Similarly,

$$k_{\text{eff}} = \int_0^\infty g\sigma(g) f(g)\, dg \tag{93}$$

corresponds to the effective rate coefficient.

For the description of the special case of a monoenergetic ion beam passing through a scattering cell with target gas at a temperature T_2, $f_1(\mathbf{v}_1)$ and $f_2(\mathbf{v}_2)$ in Eq. (88) are replaced by a δ-function and a Maxwellian $f_M(\mathbf{v}_2; m_2, T_2)$, respectively. The resulting integral can be reduced analytically, leading to the well-known generalized Maxwell–Boltzmann distribution (Chantry, 1971; Teloy and Gerlich, 1974)

$$f(g) = f^*(g; v_1, T_2)$$
$$= (m_2/2\pi k T_2)^{1/2} \frac{g}{v_1}\left[\exp\left(-\frac{m_2}{2kT_2}(g-v_1)^2\right)\right.$$
$$\left. - \exp\left(-\frac{m_2}{2kT_2}(g+v_1)^2\right)\right]. \tag{94}$$

At low ion velocities v_1, this function approaches a normal Maxwellian $f_M(g; \mu_2, T_c)$ with a reduced temperature $T_c = m_1/(m_1+m_2)\,T_2$, as illustrated in Fig. 47. In most experiments, this limit is only reached for mass ratios

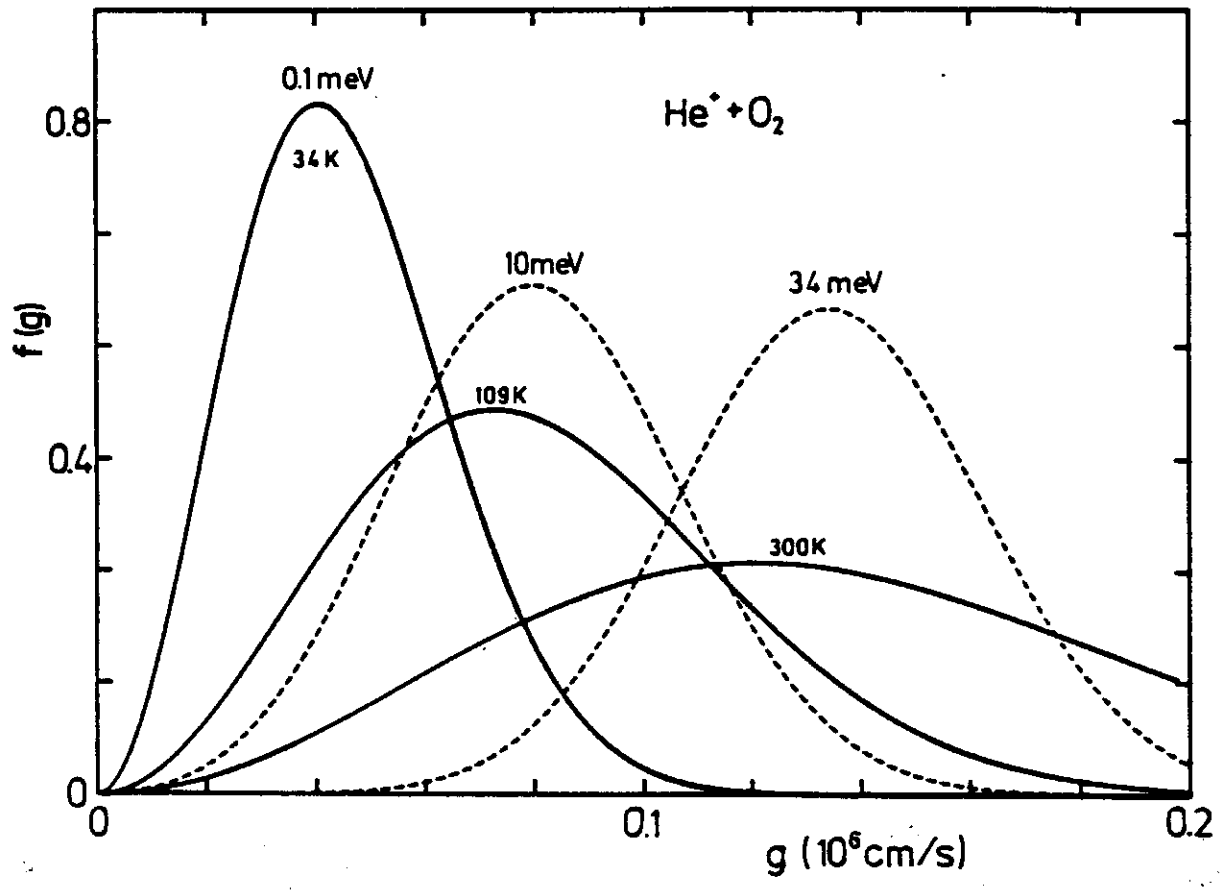

Figure 47. Relative velocity distributions $f(g)$ calculated using Eq. (89). The dashed lines are generalized Maxwell–Boltzmann distributions $f^*(g; v_1, T_2)$ [Eq. (94)] describing the relative motion between monoenergetic He^+ ions (0.1, 10, and 34 meV_{lab}) and $T_2 = 300$ K thermal O_2 neutrals. For comparison, the solid lines show thermal distributions $f_M(g; \mu, T)$ [Eq. (112)] having the same mean velocities $\langle g \rangle$.

$m_1 \gg m_2$ (Ervin and Armentrout, 1987; Teloy and Gerlich, 1974), and the lowest attainable collision temperature is therefore $T_c \sim T_2$. The trapped-ion-beam technique, described in Section III C 2, allows one to store nearly monoenergetic ions at such low energies that the velocities of the ions and the neutrals become comparable, even for mass ratios like He^+ and O_2. For this system, we have performed experiments with He^+ ions trapped at energies as low as 9 meV and obtained collision temperatures T_c that are significantly lower than T_2. The resulting effective cross sections are presented in Fig. 61.

3. *Low-Resolution Differential Cross Sections*

The direct combination of the short scattering cell surrounding the end of the first octopole with the second much longer octopole (see Fig. 30 and Fig. 46) allows one to extract information on product velocities with very high sensitivity and in an energy range that is inaccessible in standard crossed-beam experiments. Moreover, by varying the guiding field potential, information on the transverse velocity component can be obtained, and, thus, product angular distributions can be determined. The principle of this method is based on the fact that, under ideal conditions, the projection of the velocity of an ion onto the octopole axis is conserved. Therefore, this velocity component can be measured directly by time-of-flight analysis. The correlation between the transverse energy and the required rf amplitude was discussed in Section III C 4. Indeed, the angular resolution is limited, but several examples have shown that it is sufficient to gain important additional insight into the mechanisms of low-energy ion–molecule reactions.

The scattering process is illustrated schematically in the upper part of Fig. 48. A beam of primary ions with an angular divergence of less than 10° is moving in the axial direction with a velocity v_1. The products formed in reactive collisions with the target gas are scattered through certain angles and move with velocities $\mathbf{v}'_1$, which can be decomposed into parallel and transverse components (v'_{1p}, v'_{1t}). Since the primary ions remain close to the octopole axis, we ignore for simplicity the angular momentum L in Eq. (49). Owing to the axial symmetry of the guiding field, this method integrates over the azimuthal angle φ. This has the advantage of intensity gain and avoids the need for mathematical corrections for the azimuthal acceptance of the detector. Direct information on the forward–backward symmetry of all products is obtained by operating the octopole with a sufficiently high amplitude that all ions are guided. Using a very low guiding field, only the forward–backward cone of products is detected. In general, we measure an entire set of time-of-flight distributions for different rf amplitudes, spaced according to the desired resolution.

The overall resolution is limited by the time spread resulting predominantly from the finite length of the scattering cell and field imperfections of

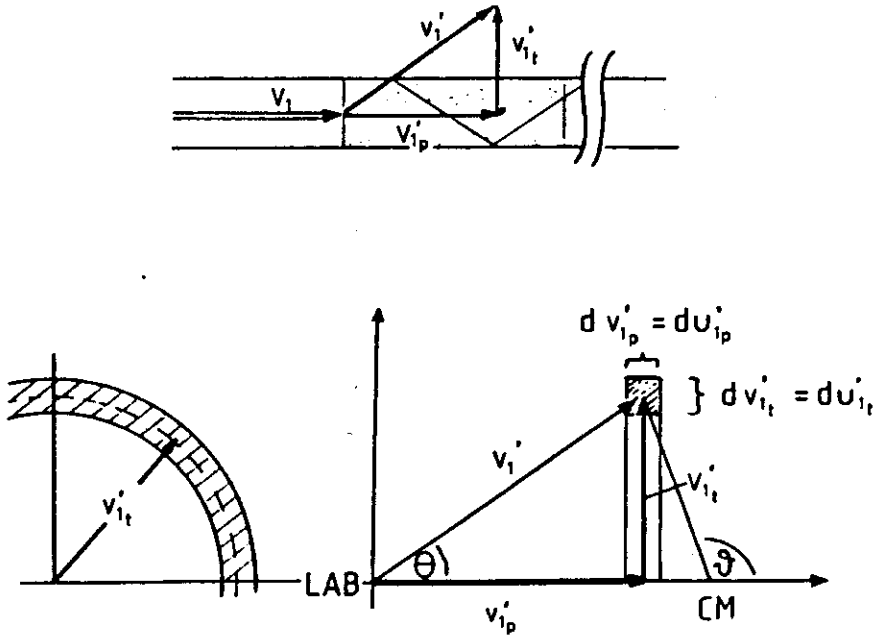

Figure 48. Scattering in an octopole. The upper part illustrates schematically the parallel and the transverse components of the product velocity vector $\mathbf{v}'_1 = (v'_{1p}, v'_{1t})$. The lower part shows the cylindrical ring volume element in the velocity space, needed to define the doubly differential cross section $d^2\sigma/du'_{1p}du'_{1t}$. In the figure on the right, θ and ϑ are the laboratory and center-of-mass scattering angles, respectively.

the octopole. These are partly due to mechanical inaccuracies and the connection between octopoles I and II, but the major perturbations are caused by surface potential distortions. The transverse energy calibration procedure described in Section III C 4 corrects for some of the uncertainty, but presently the resolution is limited to about 100 meV. The resolution in the axial direction depends strongly on the ion–target mass ratio and the energetics of the reaction. The thermal motion of the target gas can also have a significant influence on the product ion kinetic energy distribution. Several related details have been discussed recently in Gerlich (1989a). In order to simplify the following discussion, we assume the target to be at rest.

Since the experimental method differs from the standard differential scattering experiment, a few formulas must be compiled to explain the presentation of our results. The differences are primarily due to the fact that the previously described method is based on a two-dimensional differential detector ($dv'_{1p}dv'_{1t}$), shown schematically in the lower part of Fig. 48, while in a standard scattering experiment, a differential detector that selects in three dimensions is used. For example, in a spherical polar coordinate representation, the detector acceptance is usually given by $(dv'_1 d\Omega) = (dv'_1 \sin\Theta\, d\Theta d\varphi)$. In principle, however, both methods provide the same information as long as the reactants are randomly oriented, since the scattering is cylindrically symmetric with respect to the initial relative velocity.

One therefore usually speaks of a doubly differential cross section and writes $d^2\sigma/d\Omega dv'_1$ instead of $d^3\sigma/d\Omega dv'_1$. We shall use the last expression to emphasize the differences between the two methods.

The number of products detected per unit time within the cylindrical ring depicted in Fig. 48, that is, $\mathbf{v}'_1$ must lie between (v'_{1p}, v'_{1t}) and $(v'_{1p} + dv'_{1p}, v'_{1t} + dv'_{1t})$, is given by (Gerlich, 1989a)

$$\frac{d^2\dot{N}}{dv'_{1p}dv'_{1t}}\Delta v'_{1p}\Delta v'_{1t} = n_1 n_2 d\tau\, g \frac{d^2\sigma}{dv'_{1p}dv'_{1t}}\Delta v'_{1p}\Delta v'_{1t}$$

$$= n_1 n_2 d\tau\, g \frac{d^2\sigma}{du'_{1p}du'_{1t}}\mathfrak{J}\Delta v'_{1p}\Delta v'_{1t}. \tag{95}$$

These equations define the laboratory and center-of-mass differential cross sections, respectively. It can be easily seen from Fig. 48 that for the simple geometry of our detector the appropriate Jacobian is given by

$$\mathfrak{J} = \frac{du'_{1p}du'_{1t}}{dv'_{1p}dv'_{1t}} = 1. \tag{96}$$

As previously mentioned, in a standard differential scattering experiment a differential detector with a laboratory angular acceptance $\Delta\Omega = \sin\Theta\Delta\Theta\Delta\varphi$, positioned at the laboratory angles Θ and φ, is used together with a device for velocity filtering, selecting only products in the interval $(v'_1, v'_1 + \Delta v'_1)$. A typical example of such an experiment for measuring triply differential cross sections will be described in Section IV C. The correlation between the number of products detected per unit time and the differential cross section is then given by (Levine and Bernstein, 1987)

$$\frac{d^3\dot{N}}{d\Omega\, dv'_1}\Delta\Omega\Delta v'_1 = n_1 n_2 d\tau\, g \frac{d^3\sigma(\vartheta, u'_1)}{d\omega du'_1}\mathfrak{J}\Delta\Omega\Delta v'_1. \tag{97}$$

For a chemical reaction with many product states the Jacobian is given by

$$\mathfrak{J} = \frac{d\omega}{d\Omega}\frac{du'_1}{dv'_1} = \frac{v'^2_1}{u'^2_1}. \tag{98}$$

A comparison of the two different methods used to obtain differential cross sections is presented in Fig. 49. In both cases, the single electron charge transfer in $Ar^{2+} + N_2$ and $Ar^{2+} + CO$ collisions, respectively, leads to a narrow Ar^+ intensity ridge surrounding the center-of-mass origin. The upper

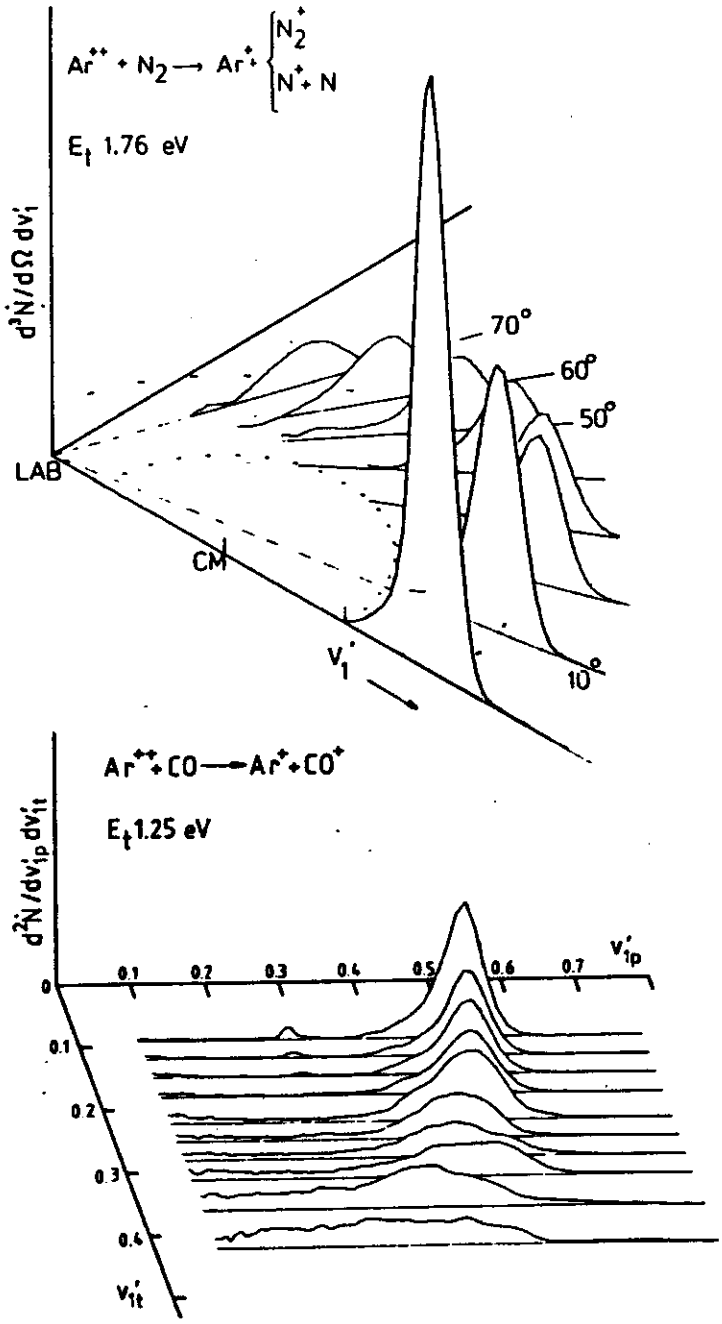

Figure 49. Illustration of product velocity distributions determined by two different experimental methods. The upper panel shows velocity distributions $d^3\dot{N}/d\Omega dv_1'$ [Eq. (97)] for Ar^+ products recorded with a traditional rotating detector at laboratory scattering angles $\theta = 0°$–$70°$. The velocity distributions $d^2\dot{N}/dv_{1p}' dv_{1t}'$ [Eq. (95)] shown in the lower panel were measured using the guided-ion-beam apparatus.

part of the figure shows results from our differential apparatus with a movable detector (Section IV C). Several Ar^+ time-of-flight distributions have been measured at laboratory scattering angles between $\Theta = 0°$ and 70°. The results in the lower plot were obtained using our guided-ion-beam apparatus by varying the effective potential. Plotted are the differences of adjacent time-of-flight distributions recorded for a set of properly chosen rf amplitudes.

In order to derive a relation between the two methods, we must divide the measured intensity $(d^3\dot{N}/d\Omega dv'_1)\Delta\Omega\Delta v'_1$ by the velocity space volume element $v'^2_1\Delta v'_1\Delta\Omega$. This leads to the *density of the product flux in the velocity space*

$$D(v'_1, \Theta, \varphi) = \frac{d^3\dot{N}}{v'^2_1 d\Omega dv'_1}. \tag{99}$$

It is common to present $D(v'_1, \Theta, \varphi)$ as a contour map, called the *cartesian map*, which should not be confused with the *flux–velocity contour map* (Levine and Bernstein, 1987). Integration over the azimuthal angle results in a density function $D(v'_1, \Theta)$

$$D(v'_1, \Theta) = \int_0^{2\pi} D(v'_1, \Theta, \varphi) v'_1 \sin\Theta \, d\varphi. \tag{100}$$

It is easy to show that this two-dimensional product flux density is identical with

$$D(v'_{1p}, v'_{1t}) = \frac{d^2\dot{N}}{dv'_{1p}dv'_{1t}}. \tag{101}$$

Note that $D(v'_{1p}, v'_{1t})$ is measured directly in the guided-beam experiment without moving any mechanical parts and without any mathematical manipulation of the data. Figure 50 shows the distributions, depicted in the lower part of Fig. 49, as a contour plot of $D(v'_{1p}, v'_{1t})$, emphasizing that the mean value of the translational exoergicity is independent of the scattering angle. This graphical presentation has the further advantage of showing isotropic scattering, that is, $d\sigma/d\vartheta = \text{const}$, as circles concentric relative to v_c. In the depicted example, the forward-peaked distribution actually is due to the reaction dynamics. The more common presentation of such data in the form of a three-dimensional product flux density $D(v'_1, \Theta, \varphi)$, has the disadvantage of superimposing at $\Theta = 0°$, a $1/\sin\Theta$ singularity for an ideal detector.

Less detailed distributions can be readily derived from this distribution by integrating over a corresponding subspace. For example, integration over the center-of-mass scattering angle within the adequate velocity intervals leads to translational exoergicity distributions. Angular distributions are derived by integration over v'_1. Finally, integration over v'_{1p} and v'_{1t} leads to integral cross sections that are, of course, also measured directly. This method

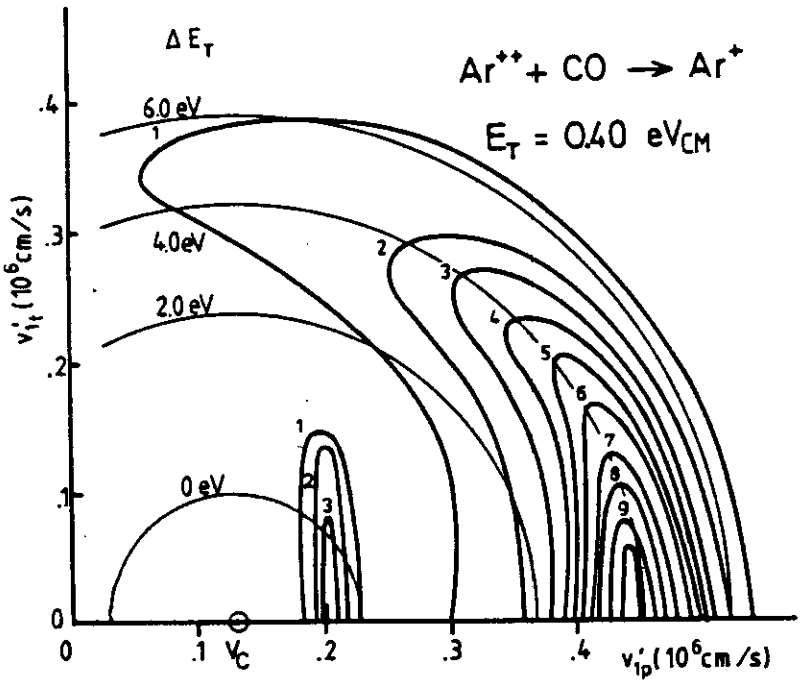

Figure 50. Contour map of $D(v'_{1p}, v'_{1t})$. The results depicted in the lower part of Fig. 49 are plotted here as Ar^+ equiflux contour lines. Shown is the two-dimensional flux as defined by Eq. (101). The circles mark loci of constant translational exoergicity ΔE_T, the most probable value being $\Delta E_T \sim 4$ eV. The small peak close to v_c is due to a small number of Ar^+ ions coming directly from the ion source.

is therefore uniquely capable of determining precise absolute values for differential cross sections.

4. *Combinations with Optical Methods*

The universal guided-ion-beam apparatus depicted in Fig. 46 can also be used in combination with different optical methods, as mentioned briefly in Section IV A. For example, photons created in the scattering cell, either by chemiluminescence or by laser-induced fluorescence, can be detected by a photomulitiplier via a quartz window. Two additional windows at the ion source and the mass spectrometer allow one to pass a laser beam coaxially through the entire apparatus. The narrowest beam restriction is usually dictated by the octopole entrance electrode, which has a typical diameter of 3 mm. For some applications, for example, for the multiphoton ionization source described in Section III B 3, the laser beam can also be directed transverse to the apparatus axis.

The instrument has been used to study chemiluminescent ion–molecule reactions at low collision energies. With an appropriate imaging system and optical filters, different wavelength ranges could be selected. Absolute integral cross sections for photon emission were determined by calibrating the optical system (Kaefer, 1984) based on known integral cross sections. The geometrical

restrictions due to the octopole rods resulted in a light transmission of only a few percent. Nonetheless, the sensitivity was high enough to detect the photons in coincidence with mass-selected product ions. This simplified the observation of weak luminescent product channels in the presence of strong emitters and was also used to identify spectroscopically unknown emitters. Operating with a continuous ion beam and using the photon as start signal for a multichannel scaler, time-of-flight distributions of chemiluminescent products can be recorded. In this way, one can identify cascading transitions, since information is obtained simultaneously on the ion kinetic energy and the photon energy.

In addition to single-photon ionization and resonance-enhanced multiphoton ionization, there are several other schemes that can be used to prepare primary ions in selected states. We have demonstrated that the guided-ion-beam apparatus can be used to study reactions with electronically excited ions provided their lifetimes are at least in the μs range. In this case, the laser excites the ground-state primary ions during their passage through the scattering cell prior to reaction with the neutral collision partner. It is also conceivable to modify in a controlled manner the internal state population of the reactant ions created in the electron bombardment source by methods such as optical pumping, photofragmentation, or infrared excitation.

Laser methods can also be used for state-selective detection of product ions. We have explored the possibilities of laser-induced fluorescence (Scherbarth, 1988) using thermal CO^+ ions produced in the storage source. Unfortunately, with the present setup, the signal-to-noise ratio is only satisfactory if we store about 10^5–10^6 ions between the octopole ring electrodes, and this method is therefore not sensitive enough to determine nascent product distributions. We have, however, developed a very efficient state-detection scheme based on laser-induced predissociation of product ions. In contrast to the fluorescence photons, the photofragments can be formed throughout the entire length of the octopole and are confined and detected with nearly 100% efficiency. This method was used successfully for the study of O_2^+ charge-transfer products formed in the a-state (Scherbarth and Gerlich, 1989). Detecting the absorption of a laser photon via fragmentation has the additional advantage that one can operate in the regime of saturation. Extrapolation to total fragmentation results in a signal that is independent of optical transition probabilities. As an illustration, Fig. 51 shows a small portion of an O_2^+ fragment spectrum for three different laser pulse energies.

Predissociation of a molecular ion with a single photon is not a generally applicable method. Therefore, we are presently exploring the possibility of fragmenting product ions in subsequent steps with two photons. State

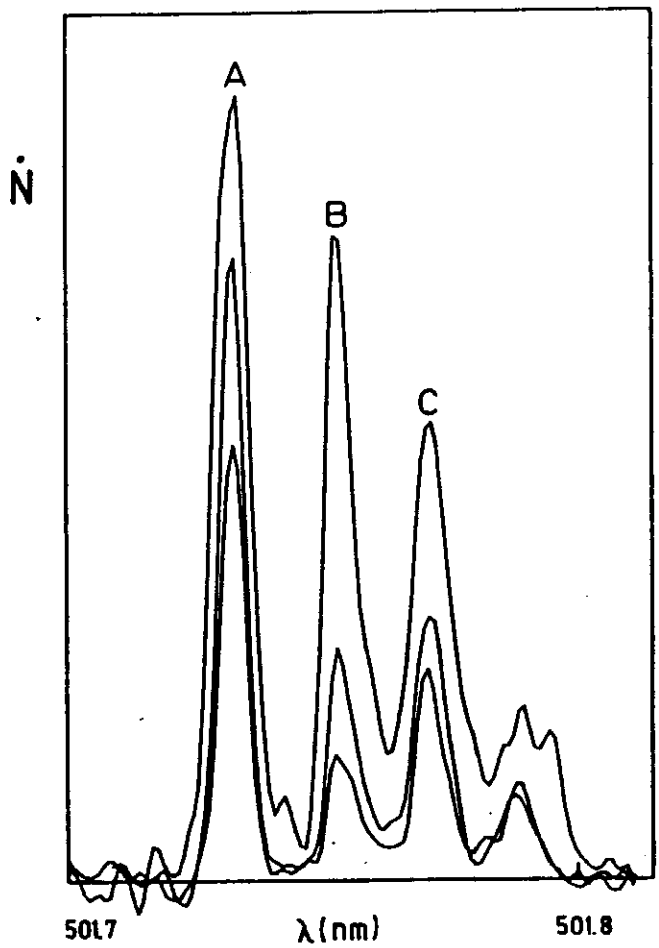

Figure 51. Laser fragmentation spectrum of O_2^+ for three laser energies. The spectra were recorded at pulse energies of 0.1 mJ, 0.2 mJ, and 1.7 mJ. Note that line *A* is strongly saturated. The energy necessary to reach 63.2% fragmentation is different for each of the depicted transitions, 0.13 mJ for *A*, 0.52 mJ for *B*, and 0.21 mJ for *C*.

selectivity is obtained in the first bound–bound transition and can be followed by any transition to a dissociative state.

C. Differential Scattering Apparatus

Over the past several years, significant progress has been made in experimental studies of high-resolution angular and velocity distributions of scattered product ions. Owing to continued improvements in energy analyzers and other instrument details, a kinetic energy resolution on the order of 10 meV is now possible. The chapter by G. Niedner-Schatteburg and P. Toennies on doubly differential proton scattering gives some insight into the present state of such high-resolution instruments. For chemical systems with closely packed rovibrational states, single-state resolution can only be achieved by optical methods. Nonetheless, angular and medium resolution velocity distributions are needed and provide important insight into the reaction dynamics, as can be seen from J. Futrell's chapter on crossed-molecular-beam studies of ion–molecule reactions.

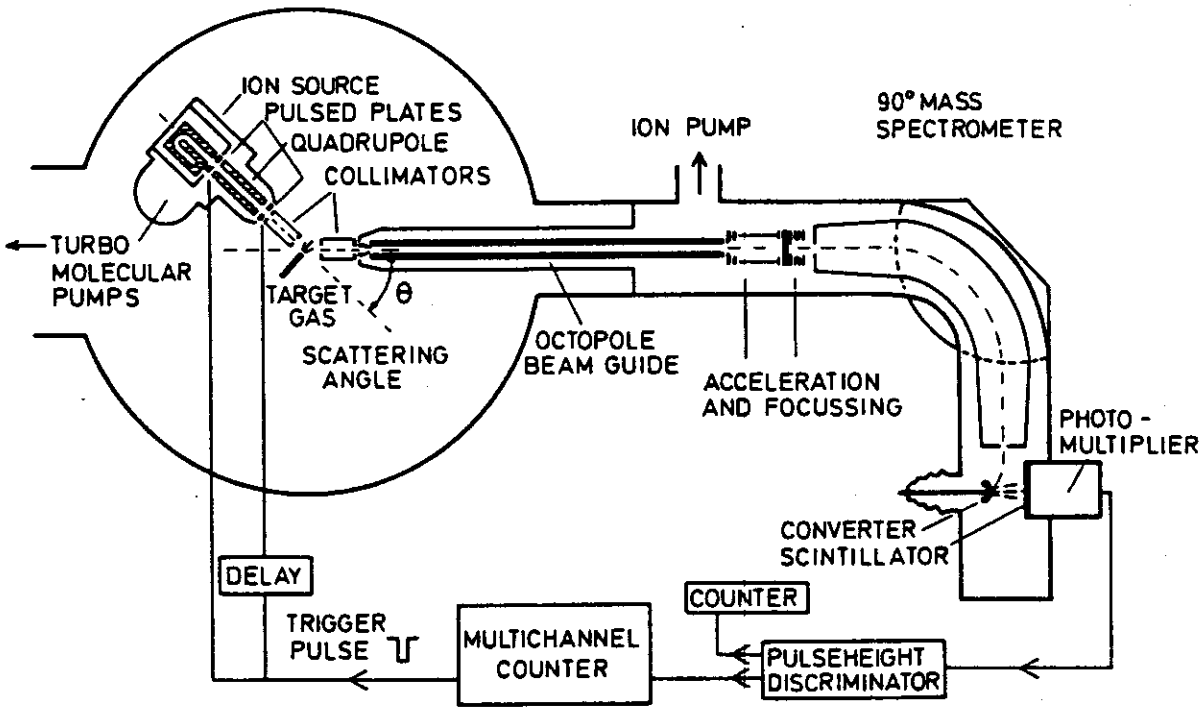

Figure 52. Schematic view of a differential scattering apparatus consisting of a rotating storage ion source and quadrupole, a scattering region, and a 1-m-long octopole for time-of-flight analysis of reaction products (Gerlich, 1977; Teloy, 1978).

In this section we present a differential scattering apparatus that employs several of the rf devices described in Section III. This apparatus, depicted in Fig. 52, has been characterized in detail in Gerlich (1977), and a short description can also be found in (Gerlich and Wirth, 1986; Teloy, 1978). Preparation of the primary ions is performed similarly to that described in Section IV B 1, using a storage ion source in combination with a focusing quadrupole and time-of-flight selection. With two 1-mm-wide collimation slits, the beam divergence is limited to 1°. Operating all elements at a low voltage avoids deceleration and facilitates the formation of an ion beam with a low laboratory energy. A typical lower limit is 0.2 eV, below which the angular profile of the beam becomes significantly broadened. The laboratory scattering angle Θ is varied by rotating the entire source. The accessible range is between $-20°$ and $+70°$ when a small scattering cell is used. In the case of a target gas beam, scattering angles up to $+100°$ can be reached. A second two-slit collimator restricts the angular acceptance of the detector to 3°. Surface potential distortions are most critical in the region of the two collimators and the interaction volume. These distortions are reduced by coating all electrodes with graphite and by baking this region with infrared radiation.

The energy of the scattered products is determined by recording their flight times through a 1-m-long octopole with a fast multichannel scaler. The

use of an octopole guiding field results in a velocity analyzer with unique features. Since the ions are allowed to move very slowly in this region, a kinetic energy resolution of better than 5 meV can be obtained, even if the time spread of the primary beam amounts to several μs. The main distortions are due to influences of the rf field in the octopole injection region, as has been discussed in Section IV B 1. By accelerating the ions into the octopole, the energy range recorded within a given time window can be compressed. Deceleration, on the other hand, leads to a stretching of the time scale without a loss in ion intensity. The octopole is also used to calibrate the energy of the primary ion beam, as described in Section III C 3. Shifts between the potential of the scattering center and the octopole are typically ± 50 meV, as determined by other methods (Gerlich, 1977).

The influence of target motion on the product translational energy in such a differential scattering apparatus has been discussed recently (Gerlich, 1989a). Ideally, a beam–beam arrangement should be used. To obtain fast product ions the neutral beam should be seeded (Farrar, 1988). In order to achieve low collision energies, the two beams should be crossed at a small angle. In most cases, either for intensity reasons or experimental limitations, it is necessary to use a scattering cell or an effusive beam. In general, the thermal motion of the neutrals deteriorates the product energy resolution, with the magnitude of the broadening depending on the reaction system.

Using the described apparatus, we have obtained very detailed differential cross sections for proton deuteron exchange reactions in $H^+ + D_2$ collisions (Gerlich, 1977). By cooling the scattering cell to liquid nitrogen temperature and by taking advantage of the favorable kinematic conditions in this reaction, we have achieved an overall energy resolution sufficient to record partially resolved rovibrational distributions. Figure 53 gives an impression of the attainable energy resolution. It demonstrates also the long-time stability of the apparatus, which is very important for the study of reactive processes due to the long integration times required. A brief survey of the $H^+ + D_2$ results has been presented in Teloy (1978) and another example will be given in Section V B 3. The apparatus has also been used to study ortho–para transitions in $H^+ + H_2$ collisions, with hydrogen in different $j = 0$ and $j = 1$ mixtures at 80 K (Gerlich and Bohli, 1981). An analysis of these results based on a dynamically biased statistical model has been reported recently (Gerlich, 1990). Lower-resolution velocity distributions and flux–velocity contour maps have also been measured for reactions of N^+ with O_2 and CO (Gerlich and Wirth, 1986; Wirth, 1984).

D. Merged-Beam Apparatus

The first beam method capable of reaching meV collision energies was the traditional merged-beam apparatus pioneered by Trujillo et al. (1966) and further developed by Gentry et al. (1975). This method achieved very low

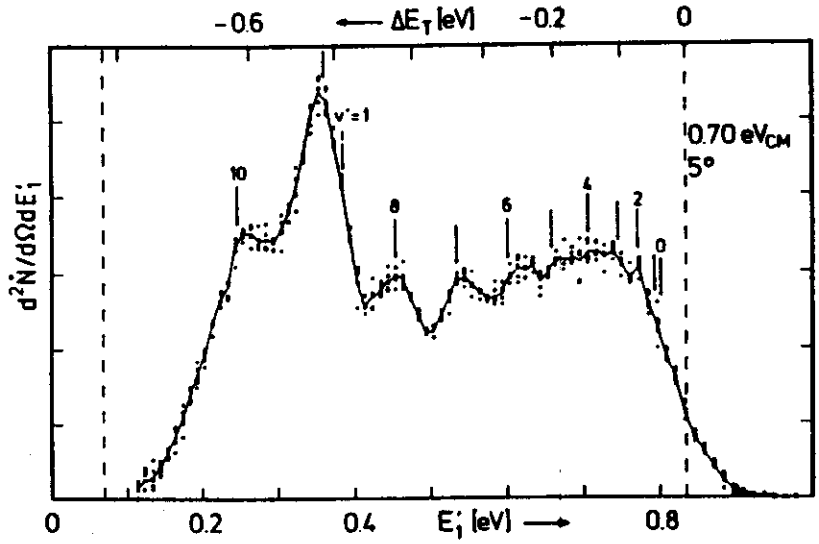

Figure 53. Laboratory energy distributions of D^+ ions produced in reactive $H^+ + D_2 \rightarrow D^+ + HD$ collisions (collision energy 0.70 eV_{cm}, scattering angle $5°_{lab}$). The partially resolved structure of the translational spectrum reflects excitation of rotational states of $HD(v' = 0, j')$ products, with the rise below $E_1' = 0.4$ eV due to contributions from $v' = 1$. The upper scale indicates the translational exoergicity ΔE_T. To demonstrate the overall stability of the instrument, five distributions are plotted, each accumulated over a period of 1 h. The line connects the average values of these measurements.

relative energies by merging two fast beams with parallel velocity vectors having the same magnitude. Operating at keV laboratory energies, kinematic compression allowed meV collision energies to be reached, even with beam energy spreads of several eV. Owing to these high energies, it was necessary to create the fast neutral target beam by charge exchange neutralization of an ion beam. Unfortunately, this led to a number of technical difficulties such as low reactant densities, a small and uncertain interaction volume, and a short interaction time. Other problems were due to the critical dependence of the energy resolution on the angular spread and the unknown internal excitation of the reactants, especially for molecular targets. All these drawbacks have impeded widespread use of this method. In this section, we describe a recently developed merged-beam instrument (Gerlich, 1989c; Kalmbach, 1989), where a slow ion beam is guided along the axis of a skimmed supersonic neutral beam. Despite the low laboratory energies involved, the kinematic compression resulting from the merged-beam geometry leads to surprising results. For advantageous systems, such as heavy ions and light targets, collision energies below 1 meV with corresponding resolution are obtainable.

1. *Description of the Apparatus*

A schematic diagram of the slow merged-beam apparatus is depicted in Fig. 54. For creation of the supersonic beam we use a piezoelectric driven pulsed valve (Gerlich et al., 1991). The fundamental principle is similar to

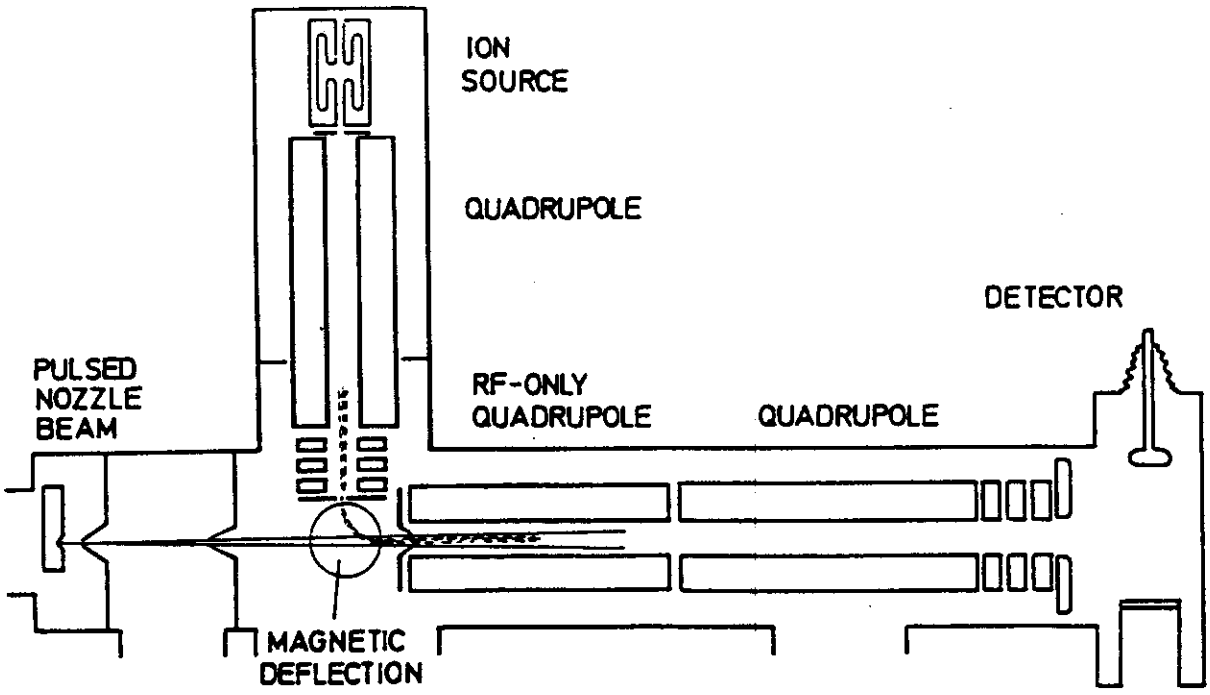

Figure 54. Schematic diagram of the merged-beam apparatus, superimposing a pulsed supersonic beam and a slow guided-ion beam. The ions are prepared in a storage source and merged into the neutral beam by deflection with a weak magnetic field. The interaction takes place in the weak guiding field of an rf-only quadrupole. Primary and product ions are detected via a quadrupole mass spectrometer.

that described by Cross and Valentini (1982); however, our valve can create pulses shorter than 20 μs and operate at repetition rates above 2 kHz. Two differential pumping stages are used to maintain a sufficiently low target-gas background pressure in the interaction chamber, while the density of the beam itself is on the order of $10^{11}\,\mathrm{cm}^{-3}$. Owing to the limited pumping speed, the beam intensity has to be rather weak and the valve is typically operated with a pulse width of 40 μs at 100 Hz. The use of a nozzle beam leads to cold molecules with a well-defined internal energy, for example, it is possible to prepare a beam of pure ground-state hydrogen molecules. The well-collimated neutral beam has a typical angular divergence of 2°.

The established combination of a storage ion source and focusing quadrupole is used to create an ion beam that is pulsed synchronously with the neutral beam. The mass- and energy-selected ions are deviated 90° in a weak magnetic field of less than 1 kG and then injected at the desired energy into a weak rf guiding field. There, they run along with the neutral beam and can react at low relative energies. At present, a quadrupole ion guide is preferred, since the harmonic effective potential confines the ion beam so close to the axis that full overlap with the neutral beam is guaranteed. Calibration of the ion axial energy, E_1, and determination of the actual

energy distribution is performed using the method described in Section III C 3. To measure the mean velocity $\langle v_2 \rangle$ and the spread of the neutral beam (FWHM, Δv_2), an additional differentially pumped ionization detector is mounted subsequent to the ion detector at a distance of about 1 m from the nozzle. In this arrangement we can operate routinely with ion laboratory energies down to 50 meV, and zero nominal relative velocity can be obtained for many mass ratios. In some cases, the neutrals must be seeded to operate at higher laboratory velocities.

Both primary and product ions are guided to the quadrupole mass filter and detected with a standard scintillation detector. In this experiment, the directed center-of-mass motion helps to reduce discriminating effects. Formation of products outside the quadrupole interaction region leads to an undesirable background signal. Contributions occurring in the short overlapping region in the magnetic deflection field and the injection electrode can be reduced by running the beams in these regions with a relative velocity at which the rate coefficient has a local minimum. Contributions from reactions in the quadrupole mass filter are usually small since it operates in the mass discriminating mode and at high axial energies between 5 and 20 eV; however, it causes some problems for endothermic reactions. Using very short neutral pulses (20 μs), and by properly adjusting the time overlap, these undesired reactions can be further reduced.

The reaction $H_3^+ + D_2 \rightarrow D_2H^+ + H_2$ has been studied by means of the traditional merged-beam technique (Dougless et al., 1982) and therefore offers an opportunity to compare the two experimental methods. The energy dependence of the integral cross section for this exothermic proton transfer is depicted in Fig. 55. Both sets of results show in good agreement that the reaction occurs with a cross section close to the Langevin limit. It is interesting to make a few quantitative comparisons of the two methods. In order to obtain a relative energy of 10 meV, we use a supersonic D_2 beam with a velocity $v_2 = 1.8$ km/s and an H_3^+ ion energy $E_1 = 0.13$ eV, in contrast to two fast beams with energies of 4427 eV and 4409 eV. The advantage of our experimental arrangement with respect to the density of the neutral target and the interaction time is clearly evident. Typical densities in our experiment are 3×10^{11} cm^{-3} compared to 10^6 cm^{-3}, and the interaction time is 35 μs rather than 0.27 μs. With these typical values and a reaction rate coefficient of $k = 10^{-9}$ cm^3/s, reaction probabilities of 10^{-2} and 10^{-10} are obtained for our slow merged-beam and the traditional merged-beam apparatus, respectively. To achieve a relative energy resolution of $\delta E_T/E_T = 0.3$ at $E_T = 10$ meV, the maximum tolerable angular divergences in the two instruments are 28° and 0.06°, respectively.

The minor deviation in the slopes of the cross sections in Fig. 55 may

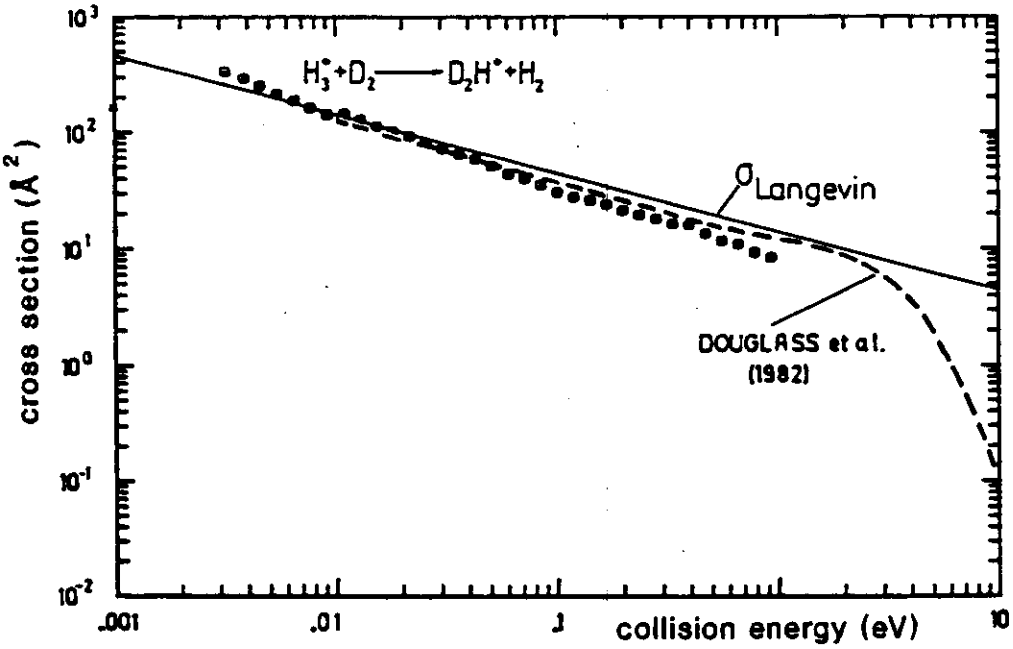

Figure 55. Comparison of the cross section for the proton transfer reaction $H_3^+ + D_2 \rightarrow D_2H^+ + H_2$ obtained with a conventional (dashed line) (Dougless et al., 1982) and our new slow merged beam apparatus (●).

be due to differences in the internal excitation of the D_2 target. In our experiment we use internally cold neutrals, while in the other, it is most probable that vibrationally excited D_2 is present. A related problem is the internal excitation of the ionic reactants. This becomes a real problem for the isotopically equivalent reaction $D_3^+ + H_2 \rightarrow H_2D^+ + D_2$, which is 29 meV endothermic. Figure 56 shows cross sections for this reaction using two different operational modes of our storage ion source. It can be seen that thermalization of the D_3^+ ions to the temperature of the ion source (~ 350 K) reduces the cross section. Nonetheless, the internal excitation of the reactants is larger than the endoergicity of the reaction. In order to observe the threshold onset, indicated schematically by the dashed line in Fig. 56, sufficiently cold ions have to be prepared.

To precisely determine the absolute integral cross section, the spatial overlap of the two merged beams and their local densities must be known. Here, the situation is simplified, since the ion beam is squeezed into the neutral beam and the neutral density n_2 is a simple function of z, the distance from the nozzle. Replacing in Eq. (92) the ion density n_1 by the ion flux $\dot{N}_1 = n_1 v_1 \Delta a$, where Δa is the cross section area of the ion beam, and substituting the volume element $d\tau$ by $\Delta a dz$, leads to the z-dependent differential product ion flux

$$d\dot{N} = \dot{N}_1(z) \frac{\langle g \rangle}{v_1} \sigma_{\text{eff}} n_2(z) dz. \tag{102}$$

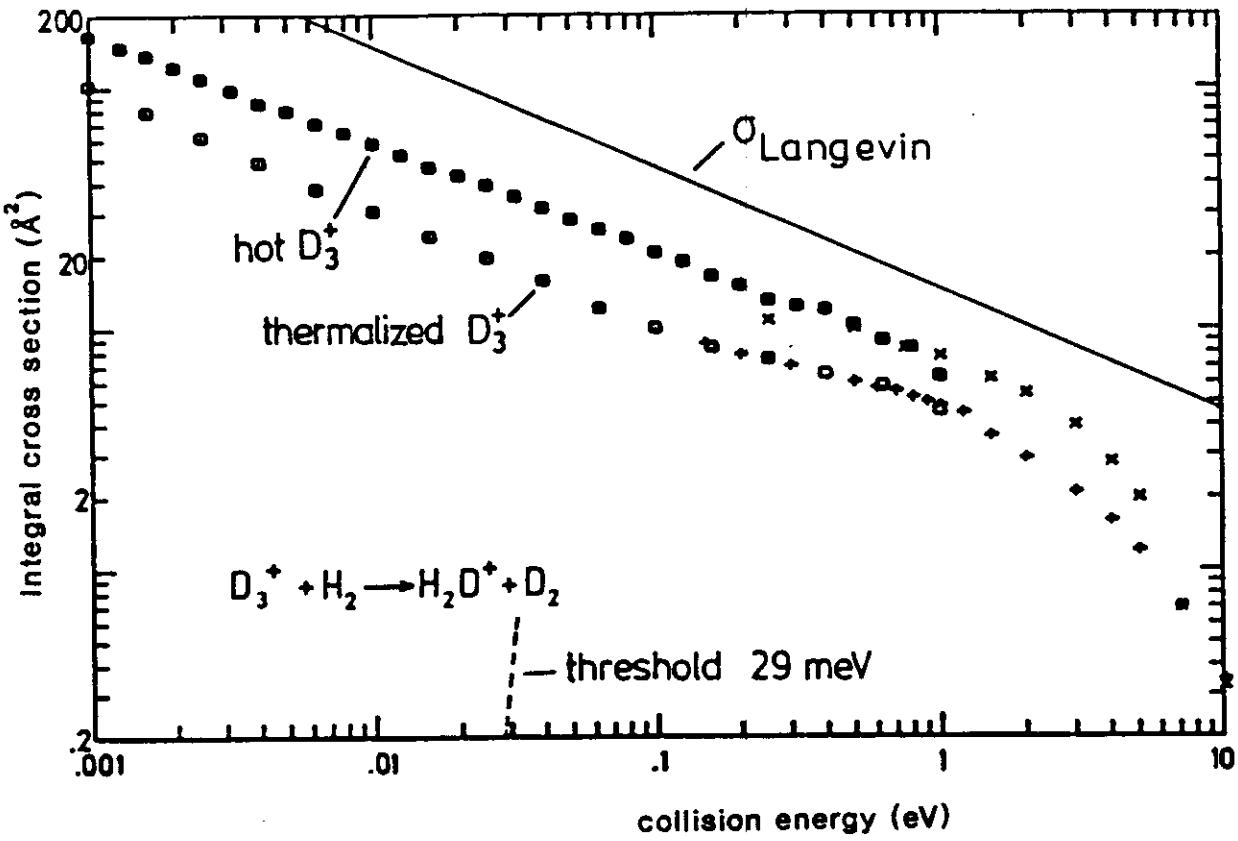

Figure 56. Integral cross sections for the 29 meV endothermic reaction $D_3^+ + H_2 \rightarrow H_2D^+ + D_2$ with hot D_3^+ ($\sim$2 eV internal energy) and $\sim$350 K thermalized D_3^+. The merged beam results (●, ⊙) are, in the overlapping energy range, in good agreement with earlier guided ion-beam experiments (Piepke, 1980), recorded under similar storage ion source conditions (+, ×). The cross sections are significantly lower than the Langevin value.

For weak attenuation of the primary beam, we can use in good approximation $\dot{N}_1(z) \sim \dot{N}_1$, and the effective cross section can be simply calculated from

$$\sigma_{\text{eff}} = \frac{\dot{N}}{\dot{N}_1} \frac{1}{\langle n_2 \rangle L} \frac{v_1}{\langle g \rangle}, \tag{103}$$

where $\langle n_2 \rangle$ is the average density determined by integration of $n_2(z)$ from the beginning of the interaction region, z_0, to the end, $z_0 + L$

$$\langle n_2 \rangle = L^{-1} \int_0^{z_0+L} n_2(z) dz. \tag{104}$$

The value $\langle n_2 \rangle L$ has been determined experimentally using reactions with known integral cross sections such as $Ar^+ + H_2$, D_2, and O_2.

2. *Kinematic Considerations*

The kinetic energy resolution of our merged-beam experiment can be characterized by three fixed parameters, the energy spread of the ion beam

ΔE_1, the velocity spread of the supersonic beam Δv_2, and the relative angular divergence between the two beams $\Delta\Lambda$. In general, we can assume rotational symmetry, and thus, the collision energy of the two reactants, colliding with velocities v_1 and v_2 under an angle Λ, can be expressed by

$$E_T = \tfrac{1}{2}\mu(\mathbf{v}_1 - \mathbf{v}_2)^2 = \tfrac{1}{2}\mu(v_1^2 + v_2^2 - 2v_1 v_2 \cos\Lambda). \tag{105}$$

As an illustrative example of the kinematic shifts caused by this vector addition, we compare in Fig. 57 guided-ion-beam results measured using a scattering cell and a crossed beam (Gerlich et al., 1987), with results obtained using the merged-beam arrangement. Shown is the threshold onset of the endothermic reaction $C^+ + H_2 \rightarrow CH^+ + H$ plotted as a function of the ion laboratory energy E_1. In the case of the scattering cell, the thermal random target motion causes an energy broadening of 300 meV, as can be derived from the distribution in Eq. (94). Crossing the two beams at a right angle significantly improves the resolution, and for $\Lambda = 90°$, the third term in Eq. (105) vanishes. Using merged beams, the rise of the product intensity is

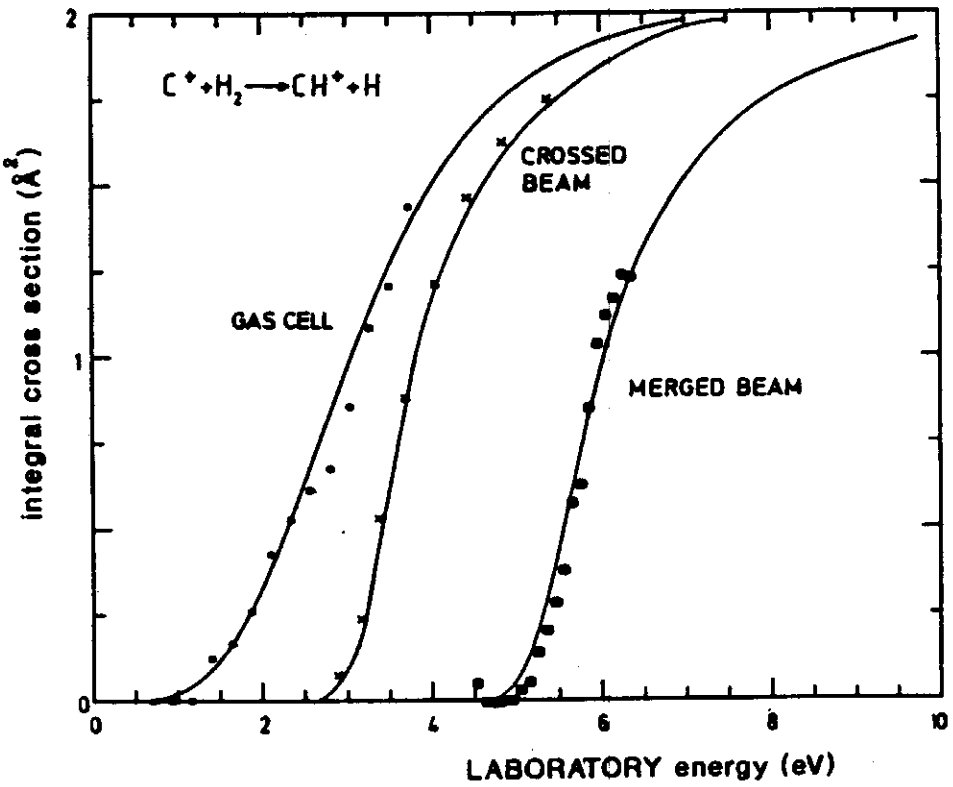

Figure 57. Integral cross sections for the reaction $C^+ + H_2 \rightarrow CH^+ + H$, measured in a beam gas cell, a crossed beam, and a merged-beam arrangement. In order to demonstrate the kinematic shift and energy broadening, the different results are plotted as a function of the C^+ laboratory energy.

again steeper and significantly shifted, that is, the laboratory energy of the C^+ ion has to be increased above $5\,eV_{lab}$ in order to reach the threshold. This is due to the fact that in the merged-beam arrangement the nominal value of Λ is 0° and the collision energy is reduced by $\mu v_1 v_2$.

To obtain better quantitative insight into the kinematic relations, we can calculate the broadening of the relative energy from Eq. (105) using error propagation:

$$\delta E_T = \left[\left(\frac{\partial E_T}{\partial v_1}\Delta v_1\right)^2 + \left(\frac{\partial E_T}{\partial v_2}\Delta v_2\right)^2 + \left(\frac{\partial E_T}{\partial \Lambda}\Delta\Lambda\right)^2 + \left(\frac{1}{2}\frac{\partial^2 E_T}{\partial \Lambda^2}\Delta\Lambda^2\right)^2\right]^{1/2}. \tag{106}$$

In the crossed-beam arrangement, a large contribution to δE_T is the angular divergence of the guided ion beam, entering in Eq. (106) for $\Lambda = 90°$ via the first-order term $(\partial E_T/\partial\Lambda)\Delta\Lambda$. In the depicted $C^+ + H_2$ example, one degree deviation from 90° causes an energy shift of 5 meV at $E_T = 0.4\,eV$ (Gerlich et al., 1987). Merging the two beams, the same resolution is obtained with a much larger angular divergence of ±8°. For this geometry of parallel velocities, that is, for $\Lambda = 0°$, $\Delta\Lambda$ contributes only in second-order and we obtain from Eq. (106)

$$\delta E_T = \left[\left(\frac{\mu g}{m_1 v_1}\Delta E_1\right)^2 + (\mu g \Delta v_2)^2 + \left(\frac{\mu}{2} v_1 v_2 \Delta\Lambda^2\right)^2\right]^{1/2}. \tag{107}$$

This formula can be used to get a quick estimate of the energy resolution based on the individual contributions and to determine the lowest relative energy attainable with the merged-beam arrangement. As an example, we assume for the system $N^+ + H_2$ an ion energy half width $\Delta E_1 = 50\,meV$ with an angular spread $\Delta\Lambda = 8°$, and a well-collimated supersonic hydrogen beam characterized by $v_2/\Delta v_2 = 20$ and $\langle v_2 \rangle = 2.7\,km/s$. A nominal relative energy of $E_T = 1\,meV$ is obtained for $E_1 = 0.57\,eV$, and at that energy, Eq. (107) predicts $\delta E_T = 1.4\,meV$ with equal contributions of 0.8 meV for the three terms.

At low relative energies such as these it is more accurate to determine numerically the distribution of the relative velocity $f(g)$ from Eq. (89). The distributions $f_1(\mathbf{v}_1)$ and $f_2(\mathbf{v}_2)$ are determined experimentally, or can be approximated by Gaussians. Owing to the rotational symmetry, the six-dimensional integral over $(\mathbf{v}_1, \mathbf{v}_2)$ can be replaced by an integration over (v_1, v_2, Λ) as derived in detail in Gerlich (1989a). This leads to rather asymmetric velocity distributions at low collision energies. A few typical results are depicted in the lower part of Fig. 63.

E. Temperature-Variable Ion Trap Apparatus

The liquid-helium-cooled ring electrode trap, described in Section III E, is integrated into a complete instrument (Gerlich and Kaefer, 1987, 1989; Gerlich et al., 1990), as depicted in Fig. 58. The ion source and the reaction region are differentially pumped with two turbomolecular pumps, resulting in a residual gas pressure of typically 10^{-9} mbar. At low temperatures, cryopumping leads to a significant improvement of the vacuum in the region of the ion trap. Typical applications using this apparatus include the determination of very slow binary (10^{-17} cm^3/s) and ternary rate coefficients as a function of temperature, the nominal value of which can be varied between 10 K and 350 K. In addition, we are especially interested in radiative association of small collision complexes, both in its spontaneous and laser induced form. For this purpose, as well as other laser applications, the system is transparent in the axial direction.

1. *Description of the Apparatus*

As in the previously described instruments, ions are formed by electron bombardment in an rf storage ion source, prethermalized to the source temperature, mass selected in the quadrupole, and then injected at low energies into the trap. Filling of the trap is achieved by properly setting or pulsing the voltages at the input and exit-gate electrodes, and by retarding and capturing the ions via inelastic collisions. Preparation of the primary ion kinetic energy is not very critical in this experiment; however, high mass discrimination is required to eliminate traces of product ions in the primary

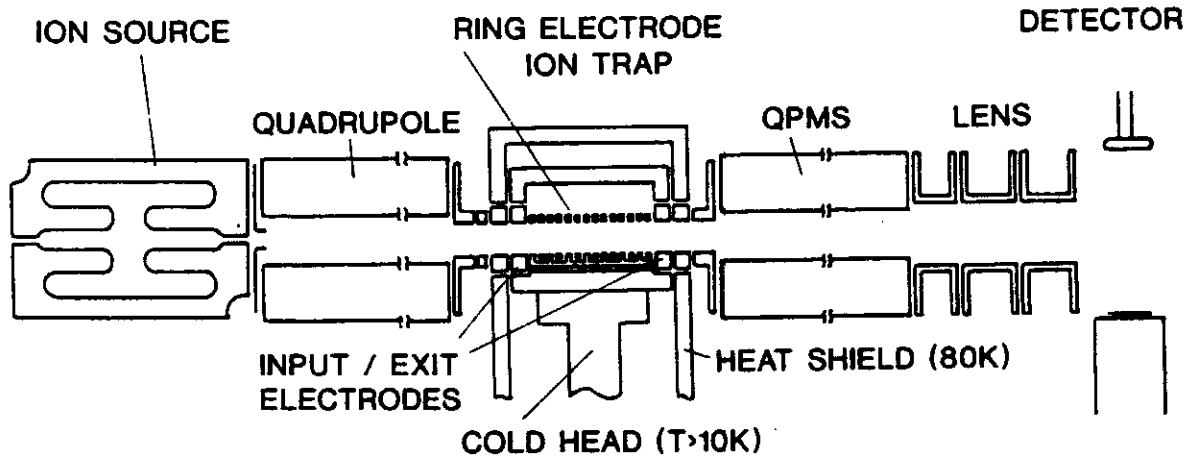

Figure 58. Schematic diagram of the ring electrode trap apparatus. Primary ions are created in a storage ion source, mass selected in a quadrupole, and injected into the trap by pulsing the input electrode. After a certain storage time (μs–min), the exit-gate electrode is opened, and the ions are mass analyzed with the quadrupole filter and detected with a scintillation detector. The temperature of the trap, which is mounted onto a cold head, can be varied between 10 K and 350 K.

ion beam. Filling times are between μs and ms and lead to typical ion densities ranging from 10^3 to 10^5 ions/cm^3. In the trap, the ions undergo many collisions with the target gas or an added buffer gas, usually He, thereby assimilating their translational and internal energy to the temperature of the trap environment. In certain cases, for example, for an endothermic reaction, an undesirable number of product ions is often formed during the filling and thermalization period. Provided these products are heavier than the primary ions, one can make use of the mass dependence of the effective potential and purify the contents of the trap. This method has been used very efficiently to reduce the H_3^+ background in the study of the radiative association reaction $H^+ + H_2 \rightarrow H_3^+ + h\nu$ (Kaefer, 1989; Gerlich et al., 1990).

After a selected storage time (μs–min), both the primary and product ions are ejected from the trap, mass analyzed, and detected with a scintillation detector. In the present apparatus, the acceptance and transmission of the detection system is less critical than in beam instruments, since the majority of the product ions are thermalized before they are extracted. This reduces the risk of discrimination in detecting the primary or product ions, which, in beam experiments, often occupy very different phase spaces. Nonetheless, it is necessary that the detection efficiency be independent of the storage time and that one always takes the same representative probe of the trap contents. For example, the change of the phase space of the injected ion cloud during thermalization can lead to a slight increase in the number of ions that reach the detector.

Opening the exit electrode usually results in an intense initial pulse of ions, and one has to be aware of the dead time of the counting system (200 MHz). The initial pulse is followed by a tail of slowly exiting ions that are delayed probably due to trapping by potential distortions. The emptying time can be significantly shortened by distributed acceleration of the ions using field penetration electrodes, as described in Section III E. In the case of endothermic reactions such as $C^+ + H_2 \rightarrow CH^+ + H$, one must take care that acceleration of the ions does not lead to additional formation of products. Even after a long opening time, it is conceivable that some ions remain in the trap. Therefore, it is advisable to completely empty the trap by switching off the rf amplitude for a short time prior to starting a new cycle.

The process of filling, storing, and extracting is repeated iteratively, with the delay time between injection and extraction being switched between a set of selected values. This delay defines the interaction time, which can be varied between μs and minutes. At the shortest reaction times the trap functions as a scattering cell, and the ions pass directly through as in the usual guided-ion-beam apparatus. The longest storage times are usually limited by primary ion loss due to reaction with the background gas or by loss due to operating at too low of an rf frequency and/or amplitude. Examples

demonstrating the range of different time constants are shown in Fig. 42. Since in most cases reactions with slow rates are studied, the repetition rate is typically 1–100 Hz; in some applications it is dictated by a laser (10–30 Hz).

Extracting the ion cloud for detection has the advantage of very high sensitivity and a large dynamic range; however, with such a detection technique one loses the thermally prepared ensemble of primary ions, which, in the case of slow reactions, is almost unattenuated. A better detection scheme would be to observe product ion formation while conserving the primary ions. In principle this could be achieved by monitoring the trap contents via laser-induced fluorescence, or the products by laser-induced fragmentation, as described in Section IV B 4. Eestimates show, however, that the overall sensitivity of these techniques is inferior to our destructive detection method. Another approach would be to select ions based on the energy dependence of the trapping field. For favorable exothermic reactions, the gained kinetic energy could allow the products to escape the trap over a properly tuned potential barrier at the exit electrode, without losing the stored primary ions. An example illustrating this principle will be given in Section V A. Other possibilities, such as the use of a mass selective rf barrier at the outlet, are also conceivable.

2. *Determination of Rate Coefficients*

Reaction rate coefficients are determined by fitting the parameters of an appropriate rate equation system to the measured temporal change of the ion composition. In a simple case, as shown for $H^+ + D_2$ in Fig. 42, a two-channel model is sufficient. Using Eq. (92) and integrating over the storage volume leads directly to the differential equation for the attenuation of the primary ions

$$\frac{dN_1}{dt} = -k_{\text{eff}} n_2 N_1(t), \tag{108}$$

that is, $N_1(t)$ decreases exponentially with the time constant

$$\tau = (k_{\text{eff}} n_2)^{-1}, \tag{109}$$

while the number of product ions, $N_2(t)$, augments complementary. For a low conversion efficiency, the increase of products can be approximated by a linear dependence

$$N_2(t) = N_1 \frac{t}{\tau}. \tag{110}$$

A slight decrease in the total number of ions, $N_1(t) + N_2(t)$, as shown in the middle panel of Fig. 42, can be accounted for by introducing a global time constant for ion loss. In many situations, this loss is predominantly due to additional, unrecorded product channels, for example, in the lowest panel of Fig. 42, to the formation of N_2^+ and other background gas ions. Other extensions of the rate equation system are needed if the product ions undergo further reactions, as, for example, in the reactions of H_3^+ depicted in Fig. 44. For product ions formed in very low abundance, such as from radiative association, it is necessary to determine their rate of loss in the trap in a separate experiment. For this purpose, the product species is directly prepared in the ion source in a sufficiently large amount, and its residence time in the trap is determined under otherwise identical storage conditions. In most cases of interest, very stable products are formed and reconversion to reactants by collision-induced dissociation can be neglected. For weakly bound systems, for example, ionic clusters, the rate equations have to account for forward and backward reactions.

To determine k_{eff} from Eq. (109) or Eq. (110), the density n_2, which can be varied between $10^6\,\text{cm}^{-3}$ and $10^{15}\,\text{cm}^{-3}$, must be known. At low densities, n_2 is determined by injecting primary ions, which react with the target gas at a known, fast, and temperature independent rate coefficient. One example is the reaction of He^+ with N_2 (Fig. 42). To determine the density of H_2 and D_2, we use the reaction with Ar^+. At higher densities, the target pressure is determined with a Leybold VISCOVAC VM 210, connected via a short tube to the interior of the trap. The gauge itself operates at room temperature and is calibrated with a quoted accuracy of 5%. The density n_2 is calculated from the indicated pressure p (mbar) and the trap temperature T(K) using the relation

$$n_2 = 4.2 \times 10^{17} p T^{-1/2}\,\text{cm}^{-3}. \tag{111}$$

The influence of thermotranspiration (Miller, 1963) can be neglected. At very low temperatures, the attainable density is limited by the vapor pressure of the target gas. For this and other reasons, we use He has a buffer gas. In experiments employing H_2, the temperature is maintained above 25 K to prevent condensation. One of the problems of the presently used system is the large entrance and exit apertures, which result in a rather steep density gradient of the target gas from the center toward the ends of the trap. To determine absolute rate coefficients, the ion cloud is concentrated in the middle of the ion trap where the pressure is actually measured. This is achieved by using the correction electrodes described in Section III E. The overall attainable accuracy of the absolute values is better than 20%.

Finally, to calculate the intrinsic reaction cross section $\sigma(g)$ from the

measured temperature dependence of the rate coefficient $k_{eff}(T)$ using Eq. (93), the distribution of the relative velocity $f(g)$ must be known. Ideally, both ions and neutrals are in thermal equilibrium in the trap at a common temperature T. Hence, $f(g)$, as defined by Eq. (89), is a Maxwell–Boltzmann distribution

$$f(g) = f_M(g; \mu, T) = (4/\pi^{1/2})(\mu/2kT)^{3/2} g^2 \exp\left(-\frac{\mu}{2kT} g^2 \right). \tag{112}$$

If the motion of the ions and the neutrals is characterized by different Maxwellians at temperatures T_1 and T_2, Eq. (112) still holds for a collision temperature given by

$$T = \mu(T_1/m_1 + T_2/m_2). \tag{113}$$

The problem of determining the actual temperature in the trap has already been discussed in Section III E, while the influence of the rf field on the ion energy has been treated in Section II E 2.

3. *Association Rate Coefficients*

The high sensitivity and efficiency of the ion trap apparatus enables one to study association reactions at rather low densities. Under typical operating conditions of swarm experiments, the buffer-gas density is so high that ternary association reactions prevail. At the other extreme of very low densities, for example, conditions of interstellar space, stabilization of the collision complex can only occur via spontaneous emission of a photon. Denoting the ternary rate coefficient as k_3 and the radiative association rate coefficient as k_r, the apparent second-order rate coefficient is given by

$$k^* = k_r + n_2 k_3. \tag{114}$$

This relation shows that to determine both k_r and k_3 it is advisable to vary n_2 in a range where the contributions of both processes have the same order of magnitude.

An example that shows the influence of temperature and target density on k^* is depicted in Fig. 59. The ternary rate coefficient k_3 for the association reaction $H_3^+ + 2H_2 \rightarrow H_5^+ + H_2$ increases by a factor of 2.5 as the nominal temperature is lowered from 80 K to 25 K. The absolute value $k_3(80\,\mathrm{K}) = 2.8 \times 10^{-29}\,\mathrm{cm}^6/\mathrm{s}$ is in very good agreement with an earlier obtained value of $2.5 \times 10^{-29}\,\mathrm{cm}^6/\mathrm{s}$ using our liquid nitrogen cooled trap (Kaefer, 1989). In this example, extrapolation to zero density, such that $k^* = k_r$, indicates that the radiative association rate coefficient is significantly smaller than

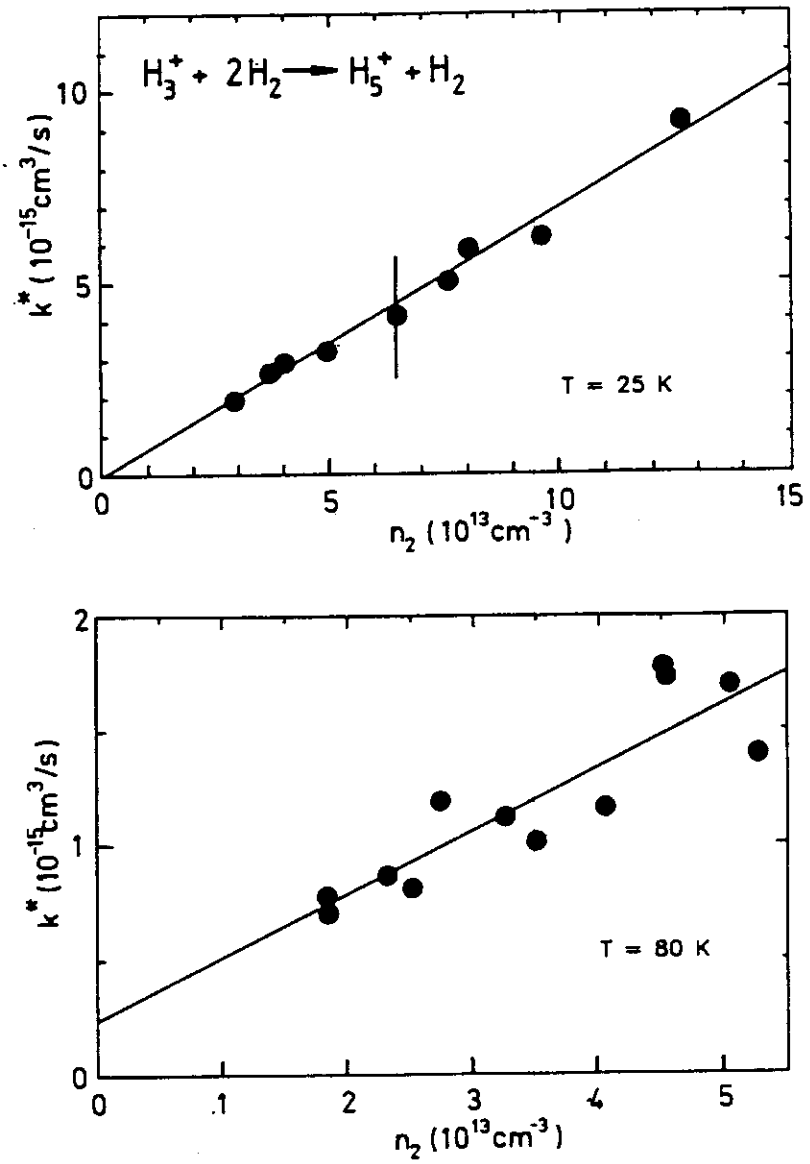

Figure 59. Apparent binary rate coefficient k^* for the ternary association reaction $H_3^+ + 2H_2 \rightarrow H_5^+ + H_2$, plotted as a function of the H_2 density n_2 (Paul, 1990). Increasing the nominal temperature of the ring electrode trap from 25 K to 80 K leads to a decrease of the ternary rate coefficient from 7×10^{-29} cm^6/s to 2.8×10^{-29} cm^6/s.

10^{-15} cm^3/s. For a more precise determination, measurements at densities below 10^{13} cm^{-3} are required. More results and other applications of this apparatus, for example, the measurement of radiative lifetimes, are described in Sections V A and V D.

V. STUDIES OF ION PROCESSES IN RF FIELDS: A SAMPLING

In Section III many of the technical details of special rf devices were described and various modes of operation were characterized and illustrated using selected examples. These rf devices have been combined in various instruments, as summarized in Section IV, and are used to study ion processes in

fields such as mass spectrometry, spectroscopy, and thermochemistry, but, predominantly, they are used in the field of reaction dynamics. In this section we present a sampling of studies of ion processes performed using these instruments.

We begin by presenting absolute integral cross sections and rate coefficients for simple charge-transfer reactions, the energy dependence of which shows interesting changes in the collision energy range between 1 meV and 1 eV, or in the temperature range between 10 K and 350 K. Differential product velocity and angular distributions are shown for representative systems in Section V B and illustrate that in favorable cases, near state-to-state information can be obtained. A sampling of the variety of experiments that can be performed by combining optical and laser methods with our instruments is given in Section V C. The final section presents a few special results from radiative association processes and related reactions. Although several examples illustrating various aspects of the versatility of guided-ion-beam apparatuses could be taken from other groups mentioned in Section IV A, we restrict our presentation to data obtained using the instruments described in Sections IV B–IV E.

One criterion for selecting the following reaction systems is that they illustrate several features of the rf apparatuses. For example, for the prototype ion–molecule reaction of H^+ with H_2 and isotopic variants, integral cross sections, differential state-to-state cross sections, and reaction-rate coefficients for ternary and radiative association are presented. The atom–atom system, $Ar^{2+} + He$, is an ideal test case for the method used to determine differential cross sections in an octopole. A detailed analysis of O_2^+ product states formed in He^+ and Ar^+ collisions with O_2 is performed by measuring product velocities and using the method of laser predissociation. Chemiluminescence detection and coincidence between photons and mass and/or time-of-flight-selected ions is illustrated for CO^+ products from the $N^+ + CO$ reaction. The CO^+ ion is also used to demonstrate the combination of the guided-beam technique with laser-induced fluorescence and laser-induced charge transfer. It is beyond the scope of this chapter to discuss in detail the dynamics of these reactions or even to give a complete survey of the existing literature. Therefore, we restrict the theoretical interpretation of the results to a few remarks that are required for the overall understanding of the experimental procedures.

A. Integral Cross Sections and Thermal Rate Coefficients

1. *Charge Transfer to Rare Gas Ions*

The integral cross section for the atom–atom charge-transfer collision $Ar^{2+}(^3P) + He(^1S) \rightarrow Ar^+(^2P) + He^+(^2S)$ has been determined as a function

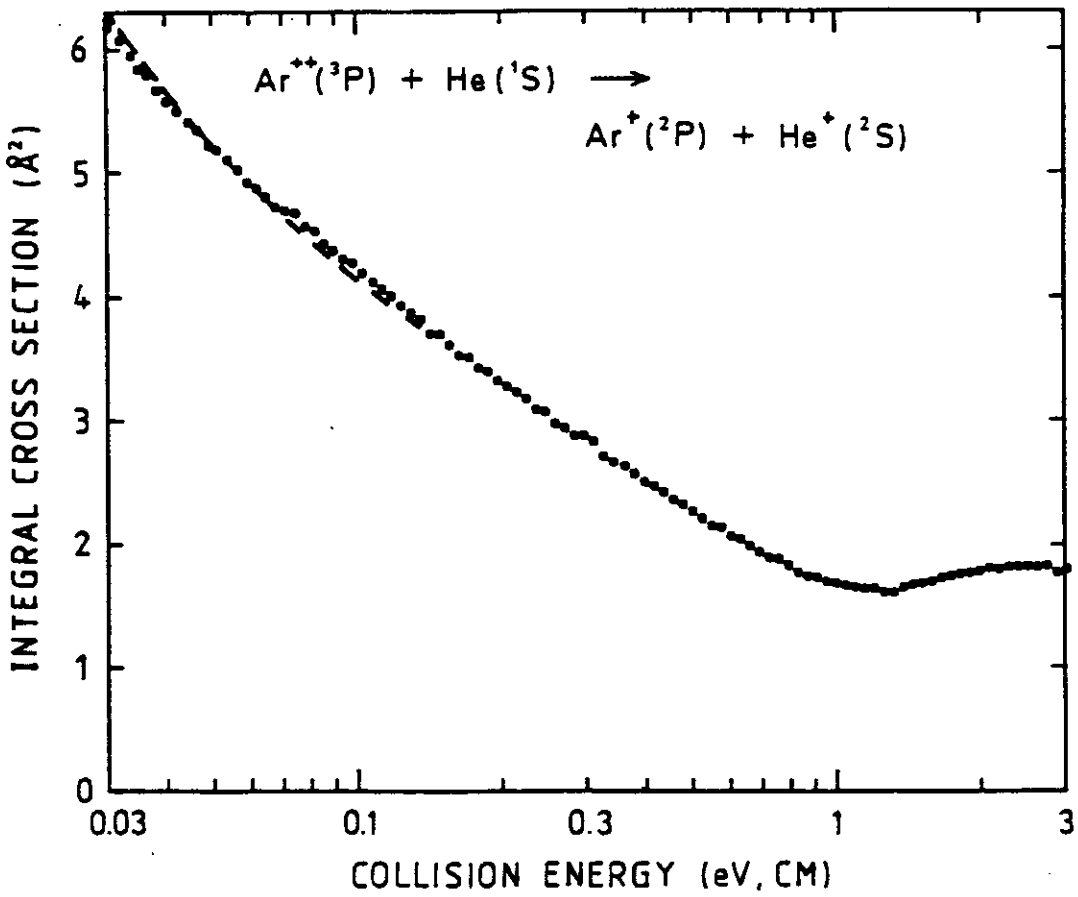

Figure 60. Integral cross section for the reaction $Ar^{2+} + He \rightarrow Ar^{+} + He^{+}$ measured in the universal guided-ion-beam apparatus. The dashed line corresponds to an effective cross section calculated using an analytical approximation for $\sigma(E_T)$ given in the text.

of collision energy using the guided-beam apparatus (Disch et al., 1985; Gerlich, 1986) and is depicted in Fig. 60. This system has been studied at low energies in the group of Z. Herman by crossed-beam scattering (Friedrich et al., 1984), and calculations of the differential cross section have been performed based on perturbation (Landau–Zener) techniques (Friedrich et al., 1986). The integral cross section, Fig. 60, has a shallow minimum at about 1 eV. The increase below 0.2 eV has been approximated by $\sigma(E_T) = 1.9 E_T^{-0.345}$. This function and the almost identical corresponding effective cross section as defined by Eq. (91) are shown as a single dashed line. Our experimental results have stimulated a comparison with quantum-mechanical calculations performed by Braga et al. (1986). The ab initio determined cross sections are about a factor of 2 larger; however, these authors have demonstrated that a good agreement can be obtained by slightly changing the diabatic potential. This illustrates the need for precise absolute values of integral cross sections at low energies. The experimentally measured minimum at about 1 eV was not reproduced in the calculation, and it has been supposed that this could be due to the channel leading to metastable $Ar^{2+}(^1D)$.

For this and the following charge-transfer systems, the nonadiabatic interaction is localized at a large internuclear distance R_c. At high collision energies, the impact parameter method (straight trajectories) can be used, and the cross section is simply described by $\sigma(E_T) = P(E_T)\pi R_c^2$, where $P(E_T)$ is the total charge-transfer transition probability averaged over the impact parameter. At the low energies of our experiment, however, the two reactants attract each other, for example, by the polarization potential

$$V_p = -7.2\alpha/R^4, \tag{115}$$

where α is the polarizability in $Å^3$, and the units of V_p and R are eV and Å, respectively. Accounting for the curved trajectories, one obtains

$$\sigma(E_T) = P(E_T)[1 - V_p(R_c)/E_T]\pi R_c^2. \tag{116}$$

For $E_T = -V_p(R_c)$, the orbiting radius becomes identical to R_c. At even lower energies, the polarization (or Langevin) cross section σ_p determines the charge-transfer cross section

$$\sigma(E_T) = P(E_T)\,\sigma_p, \tag{117}$$

where σ_p is given by

$$\sigma_p = 16.86\,(\alpha/E_T)^{1/2}. \tag{118}$$

All of the charge-transfer cross sections presented in this section have been measured close to or in this transition-energy range. In the $Ar^{2+} + He$ reaction, the crossing radius $R_c = 4.7$ Å is readily determined from the known exoergicity of 3.14 eV, from the Coulomb repulsion of the products $V_{cb} = 14.4/R$, and from Eq. (115), with $\alpha(He) = 0.22$ $Å^3$. Since $-V_p(R_c = 4.7\text{ Å}) = 13$ meV is smaller than our lowest experimental collision energy (30 meV), the experimental cross section can be fitted by Eq. (116) (dashed line in Fig. 60). Comparison of $\sigma(E_T)$ with the measured values results in the probability function $P(E_T)$, which has a local minimum of only 3% at 1 eV and increases slowly to 6.4% at 30 meV.

Larger transition probabilities have been derived for the dissociative charge transfer reaction $He^+ + O_2 \rightarrow O + He$. In Fig. 61 our measured integral cross section is compared with results obtained by other groups at high collision energies. The data between 0.07 and 10 eV were measured using the octopole guided ion beam, while the values between 10 and 100 meV were determined by the trapped ion beam method. Here, a beam of translationally cold ions ($\Delta E_{lab} = 2$ meV) is prepared in the octopole using

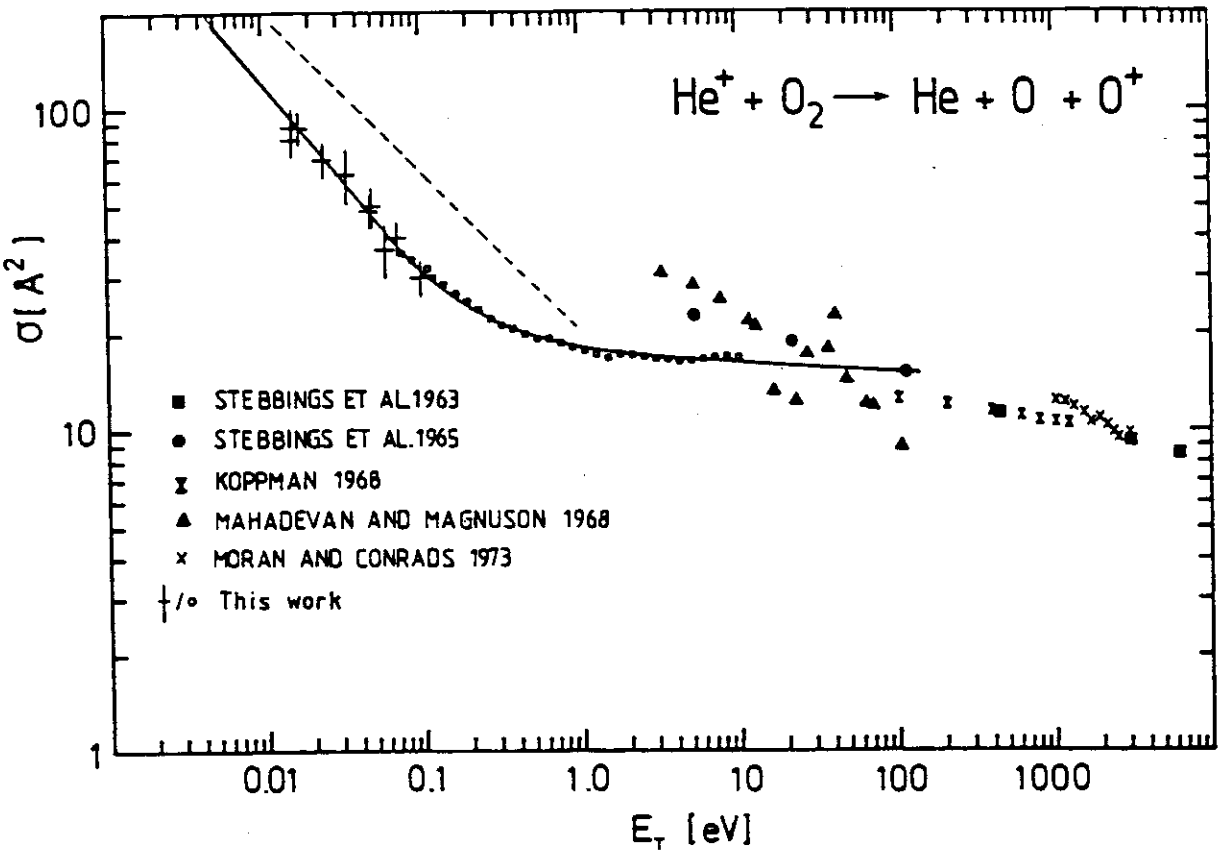

Figure 61. Integral cross sections for the dissociative charge transfer $He^+ + O_2 \rightarrow O^+ + O + He$. The guided-ion-beam results (○) have been extended to lower energies using the trapped ion beam method (+). The data at higher energies are from several other beam experiments, the references of which are compiled in Bischof and Linder (1986). The solid line is an effective cross section calculated using an analytical expression given in the text.

external potential barriers, as described in Section III C 2. This technique allows one to obtain effective rate coefficients at conditions corresponding to a translational temperature of about 100 K (see Fig. 47).

The measured integral cross sections have been evaluated based on the previously described model. A best fit to the measured effective cross section has been obtained for a crossing localized at $R_c = 3.5$ Å and with the transition probabilities

$$P(E_T > -V_p(R_c)) = 0.44E_T^{-0.02}$$

and

$$P(E_T \leqslant -V_p(R_c)) = 0.358E_T^{-0.1} \tag{119}$$

From Eq. (115) and the polarizability $\alpha(O_2) = 1.6$ Å^3, one obtains $-V_p(R_c = 3.5\text{ Å}) = 77$ meV. In contrast to the $Ar^{2+} + He$ system, here the change in the model cross section from Eq. (116) to Eq. (117) is within the energy range of our experiment, as can be clearly seen by the change in the slope in Fig. 61. For this atom–diatom system, the transition probability

$P(E_T)$ is almost energy independent at high energies (44%). Below 77 meV $P(E_T)$ increases slowly, and reaches a rather large value of 71% at 1 meV.

Thermal rate coefficients have also been measured for this system using the temperature-variable ring electrode trap. Rather than utilizing the standard technique for analysis, where all ions are extracted from the trap after a given interaction time (Section IV E 2), we have used here an alternative method. Since some of the created O^+ products are rather fast (see Section V B 2), one can adjust the trapping conditions such that these ions can escape from the trap, while the remaining He^+ ions are safely enclosed. Under these conditions the injected He^+ ions can be almost completely converted into reaction products. Figure 62 shows the O^+ intensity registered in a multichannel scaler after filling the trap with He^+ ions. This signal is directly proportional to the remaining number of He^+ ions, and therefore proportional to reactive decay rate kn_2 of the He^+ ion cloud. With this method, we have determined $k(350\,K) = 0.92 \times 10^{-9}\,cm^3/s$ and $k(80\,K) = 1.0 \times 10^{-9}\,cm^3/s$. These values agree, within the error limits, with the rate

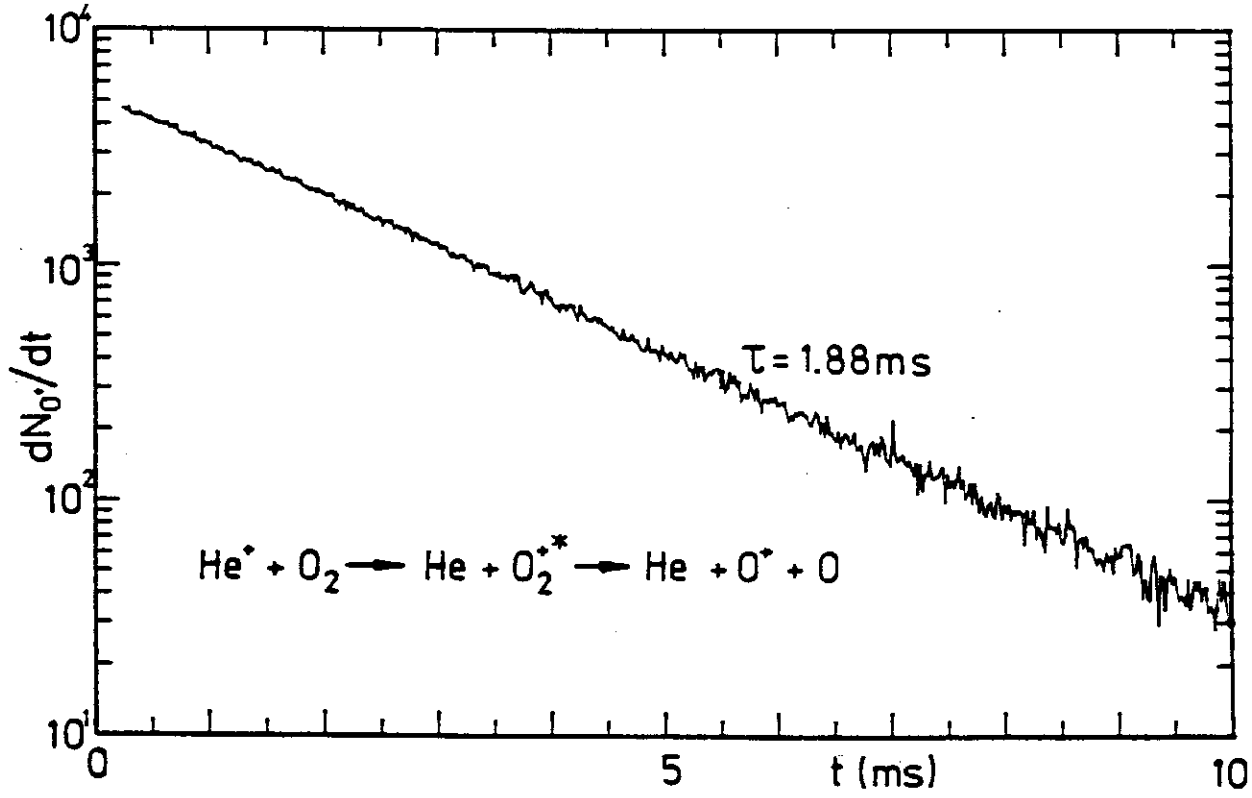

Figure 62. Measurement of the rate coefficient for the exothermic reaction $He^+ + O_2 \rightarrow O^+ + O + He$ by real-time registration of the O^+ products using a multichannel scaler. In this experiment, the He^+ ions are safely enclosed in the ring electrode trap, the only loss being due to reactions with O_2. A fraction of the fast O^+ products escapes over the properly adjusted dc barrier at the exit electrode. Their rate is directly proportional to the reactive decay rate kn_2 of the He^+ ion cloud.

coefficients $k_{eff} = 0.81 \times 10^{-9}\,cm^3/s$ and $0.92 \times 10^{-9}\,cm^3/s$ determined from Eq. (93) using the cross section σ defined by the parameters given in Eq. (119).

A third example, Fig. 63, shows the cross section for the $Ar^+ + O_2 \rightarrow O_2^+ + Ar$ charge transfer measured in our universal guided-ion-beam apparatus (Scherbarth and Gerlich, 1989) and our slow merged-beam instrument (Gerlich, 1989c; Kalmbach, 1989). Since the density of the O_2 beam was not determined directly, the relative cross sections measured in the merged-beam experiment were adjusted to the guided-ion-beam results at 0.1 eV. In the overlapping energy range above 40 meV the relative slopes are in excellent agreement. As in the case of the other two charge-transfer examples, the energy dependence deviates from the usual Langevin behavior

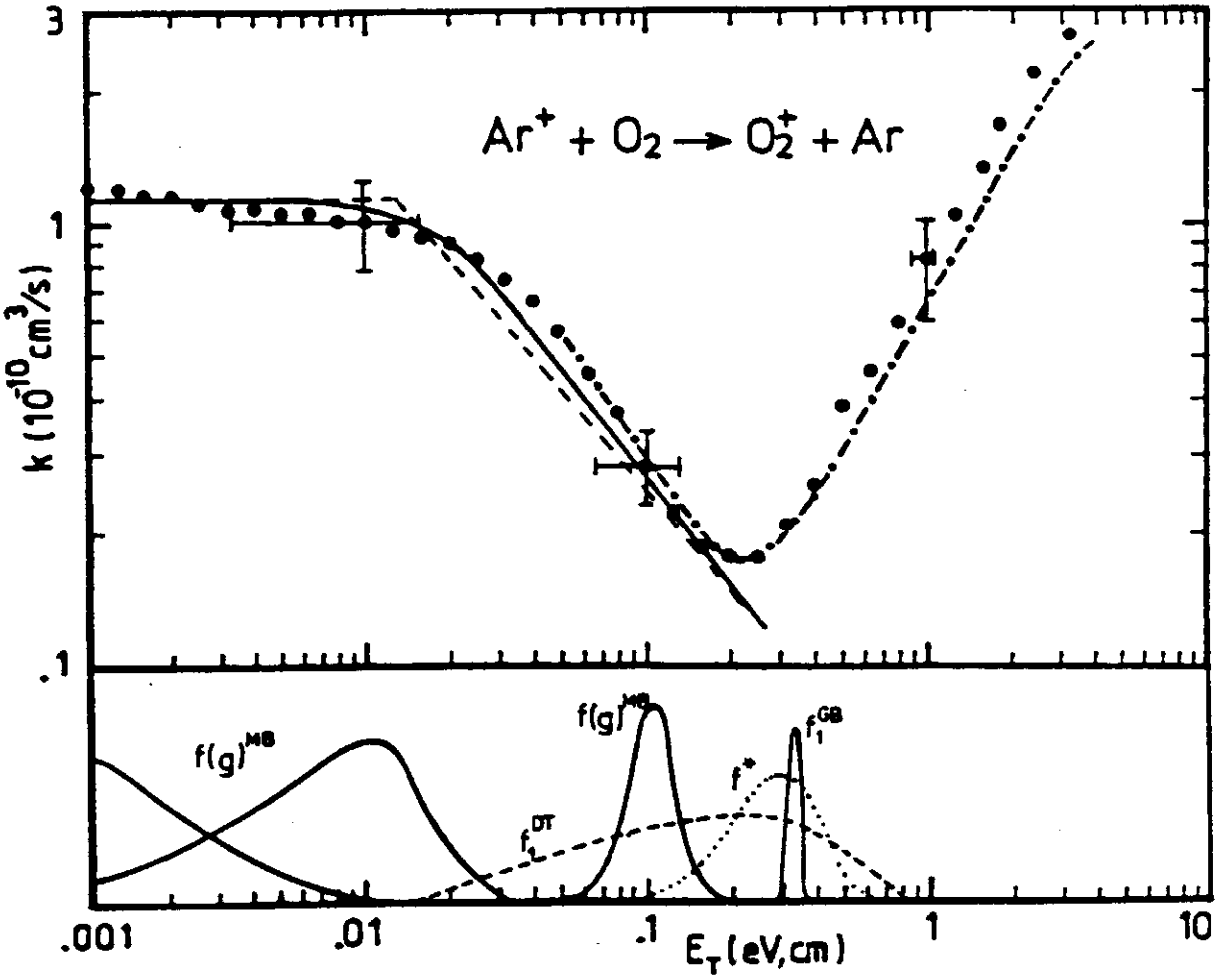

Figure 63. Integral cross section for the reaction $Ar^+ + O_2 \rightarrow O_2^+ + Ar$, measured with the merged beam (●) and the guided-ion-beam (●–●) methods (Scherbarth and Gerlich, 1989). The results are plotted as rate coefficients to emphasize the change in slope below 20 meV. The increase above 0.2 eV is due to the formation of $O_2^+(a\,^4\Pi_u)$. The low-energy behavior of the cross section has been approximated by the expression given in Eq. (120) (dashed line). Evaluation of Eq. (93) results in the effective rate coefficient (solid line). The lower part shows distributions of the relative velocity $f(g)^{MB}$ for the merged-beam conditions. For comparison the functions f_1^{GB}, f_1^{DT}, and f^* [see Eq. (94)] are given for the guided ion beam and DRIFT tube apparatuses.

and therefore gives some insight into the reaction mechanism. The increase above 0.2 eV is due to the formation of metastable $O_2^+(a^4\Pi_u)$ ions. This channel has been studied in detail using the method of laser fragmentation (Section IV B 4), a typical result of which is presented in Section V C 3.

The behavior of the cross section at low energies has been approximated by an expression predicted in Scherbarth and Gerlich (1989) on the basis of the guided-beam results and on thermal rate coefficients,

$$\sigma(E_T > 13\,\text{meV}) = 0.135 E_T^{-1.25}$$

and

$$\sigma(E_T \leqslant 13\,\text{meV}) = 3.5 E_T^{-0.5}. \tag{120}$$

The dashed line in Fig. 63 shows this function, while the solid line represents the effective cross section, calculated from Eq. (91), where the relative velocity distribution, $f(g)$, was determined from the measured ion and nozzle beam velocities using Eq. (89). The almost perfect agreement of this fit with the merged-beam results nicely corroborates the predicted analytical cross section, Eq. (120). The lower part of Fig. 63 shows several collision energy distributions obtained by numerical integration of Eq. (89). The speed ratio of the O_2 beam in these experiments was $v_2/\Delta v_2 = 5$, at an assumed angular spread of $\pm 10°$. The lowest attainable collision energy and energy resolution was mainly limited by the spread of the ion beam, which in this experiment was only 100 meV. Nonetheless, a mean collision energy of 3 meV was obtained at an Ar^+ laboratory energy of 0.15 eV. For comparison, we show the estimated ion energy distribution of a drift tube at a nominal collision energy of 0.3 eV; as well as the Ar^+ ion energy distribution in the guided-ion-beam apparatus, and the generalized Maxwellian f^* for this mass ratio, as given by Eq. (94).

Thermal rate coefficients, calculated from $\sigma(E_T)$ in Eq. (120), are also in accord with experimental rate coefficients measured using the ring electrode trap, $k(80\,\text{K}) = 1 \times 10^{-10}\,\text{cm}^3/\text{s}$ and $k(400\,\text{K}) = 4.4 \times 10^{-11}\,\text{cm}^3/\text{s}$. More details on this charge-transfer system, including a discussion of the reaction mechanism that explains the observed energy dependence of the cross section, can be found in Scherbarth and Gerlich (1989).

2. *The Prototype System $H^+ + H_2$*

Reactive collisions between $H^+ + H_2$ and isotopic variants $H^+ + D_2$ have been studied quite extensively using several experimental techniques and different theoretical models. At energies below 1.8 eV, proton–proton or proton–deuteron exchange are the only open reactive channels. The reaction mechanism is determined by the deep potential well of the H_3^+ intermediate, and the formation of a strongly bound complex allows one to use statistical

methods (Gerlich, 1982; Gerlich et al., 1980). Some restrictions of statistical behavior due to symmetry selection rules have been discussed recently (Gerlich, 1990). The low-energy behavior is also influenced by the differences in zero-point energies and the anisotropy of the long-range potential caused by the quadrupole moment of H_2.

Figure 64 shows the integral cross sections, plotted as rate coefficients, for the exothermic proton-deuteron exchange $D^+ + H_2 \rightarrow H^+ + HD$ at energies ranging from 1 meV to 1 eV. Above 30 meV, data from DRIFT measurements (Villinger et al., 1982) and guided-ion-beam results (Müller, 1983) are included. The different results agree with each other within the combined uncertainties. The heavy line has been calculated using a statistical model called the most dynamically biased (MDB) theory (Gerlich, 1982; Gerlich et al., 1980). The merged-beam apparatus has been used successfully

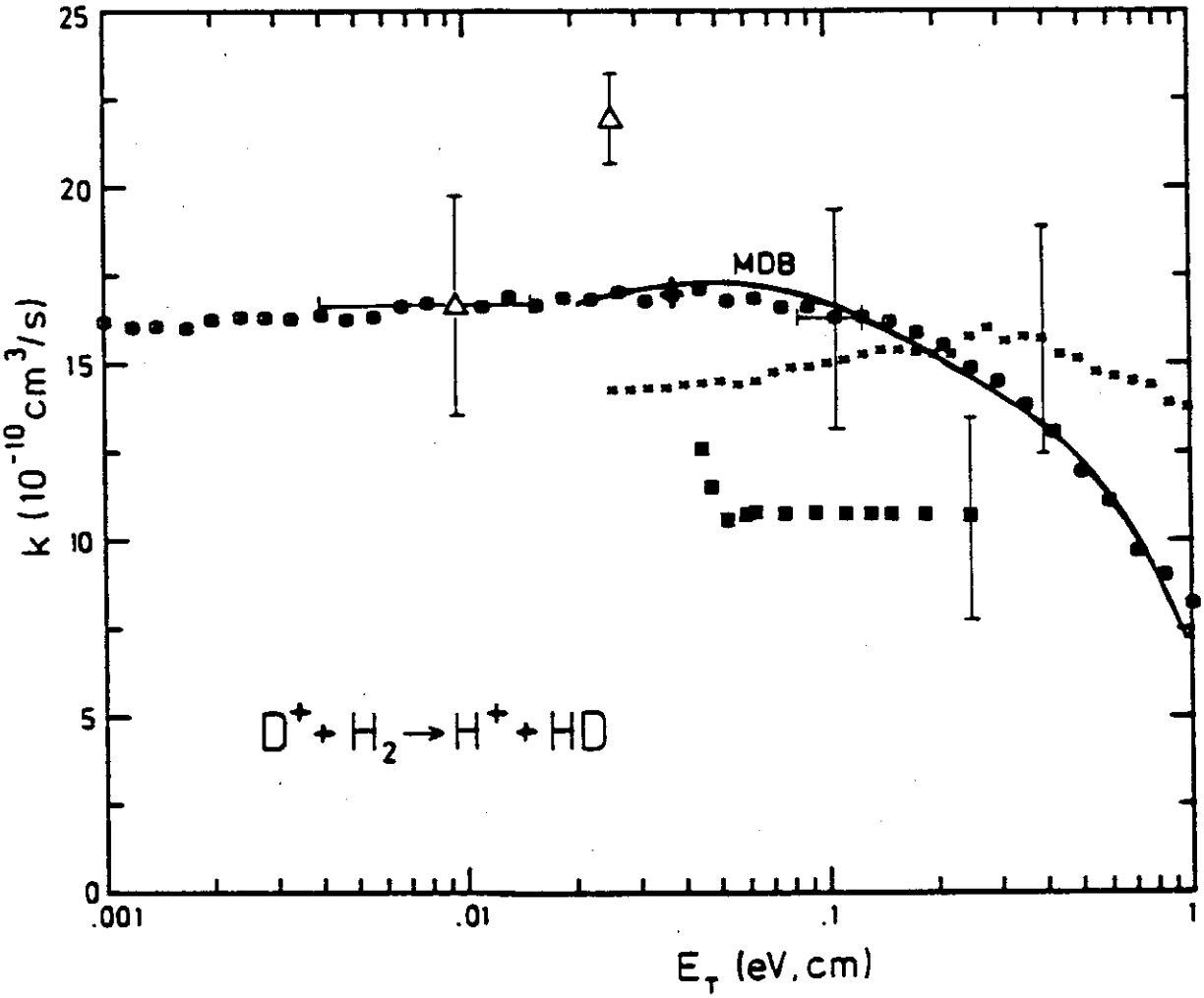

Figure 64. Energy dependence of the effective rate coefficients for the exothermic proton–deuteron exchange $D^+ + H_2 \rightarrow H^+ + HD$ measured with the merged beam (⊙), the guided ion beam (×) (Müller, 1983), and the DRIFT (■) methods (Villinger et al., 1982). The heavy line has been determined using the statistical MDB theory (Gerlich, 1982). The two triangles are thermal rate coefficients from a SIFT experiment (Henchman et al., 1981).

to extend the energy range down to a few meV. Here, the cross sections have been determined in absolute units by calibrating the density of the H_2 beam based on the well-known $Ar^+ + H_2$ reaction. The near perfect agreement with the theory is most probably fortuitous.

The decline of the cross section above 0.1 eV is understood within the MDB statistical theory. Below 0.1 eV, this reaction occurs with the typical Langevin cross section, resulting in a temperature independent rate coefficient. This can be seen from Fig. 65, which compares results from our

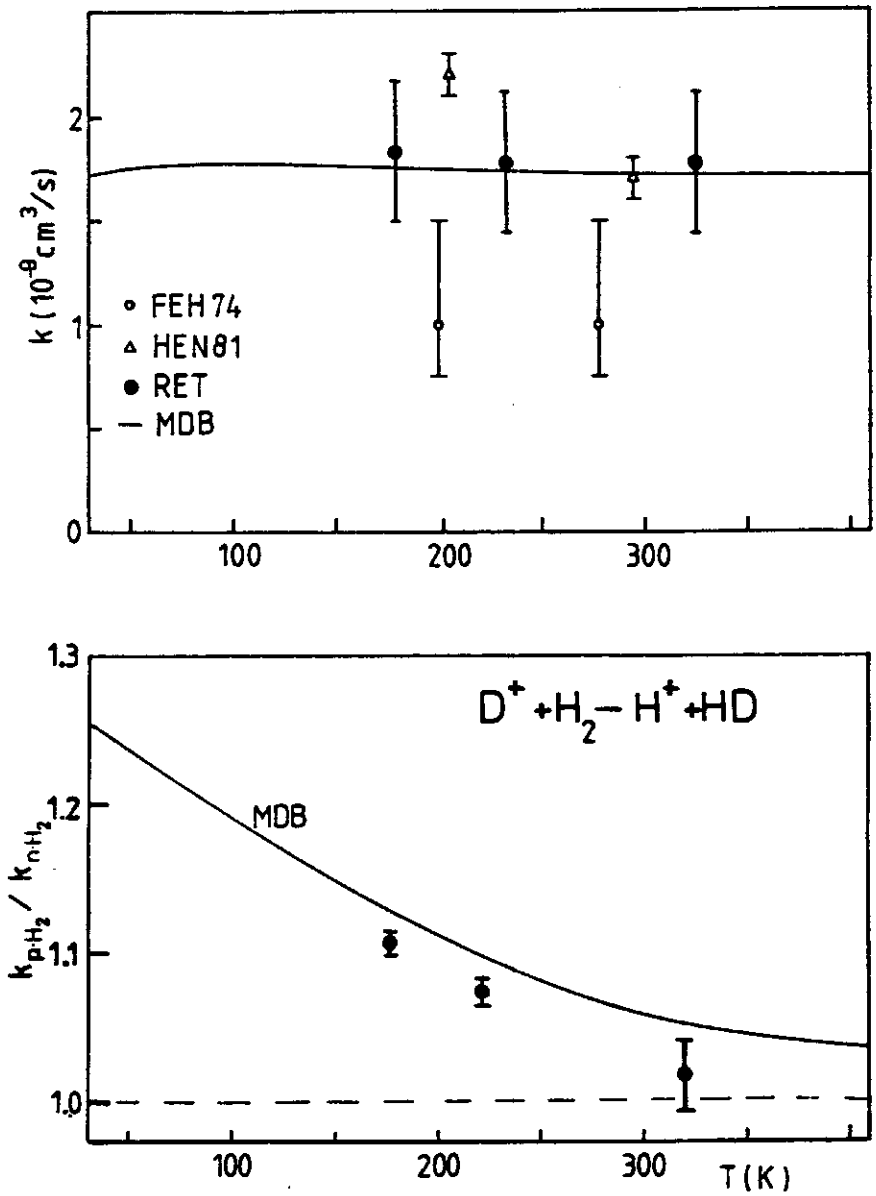

Figure 65. Thermal rate coefficients for $D^+ + H_2 \rightarrow H^+ + HD$. The upper panel shows a comparison of our ring electrode trap results (●) with those from a flowing afterglow (○) (Fehsenfeld et al., 1974) and a SIFT (Δ) (Henchman et al., 1981) apparatus. The solid line was determined using the statistical MDB theory (Gerlich, 1982). In all these experiments, normal-H_2 was used. The lower panel compares results obtained for 75% enriched para-H_2 and normal-H_2. The reaction rate with $H_2(j=0)$ increases with falling temperature due to the influence of the charge–quadrupole interaction, in reasonable accord with the statistical MDB theory.

first cooled ring electrode trap (Gaber, 1987) with those from a flowing afterglow (Fehsenfeld et al., 1974), and a SIFT (Henchman et al., 1981) apparatus. The reaction rate with nonrotating para-H_2 ($j = 0$) must increase with falling temperature due to the influence of the charge–quadrupole interaction. The lower part of Fig. 65 shows results obtained in the same trap with 75% enriched para-H_2 and normal-H_2 (Gaber, 1987). The observed increase is significant, although it is somewhat smaller than predicted from the statistical MDB theory.

The deuteron–proton exchange $H^+ + D_2 + D^+ + HD$ is 46 meV endothermic, which leads to a significant change in the low energy cross section, as seen from Fig. 66. Like the proton–deuteron exchange, this reaction has been studied extensively. The figure includes results obtained from two different guided ion beam apparatuses (Müller, 1983; Ochs and Teloy, 1974), DRIFT data (Villinger et al., 1982), and merged-beam results. Owing to the unfavorable mass ratio $m_1 : m_2 = 1 : 4$, the lowest attainable energy of the merged-beam apparatus is 20 meV. This, together with incomplete rotational

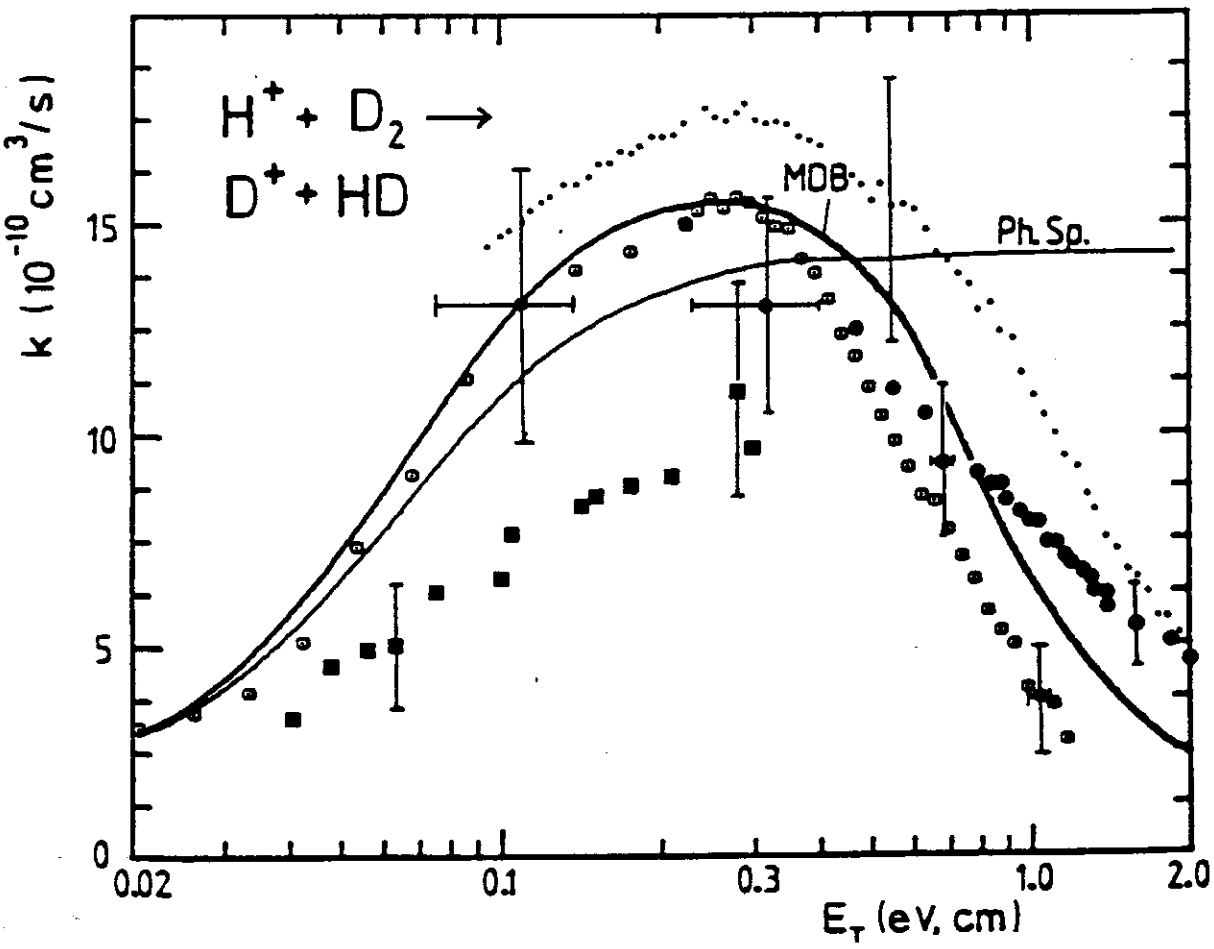

Figure 66. Energy dependence of the effective rate coefficient for the 46 meV endothermic proton–deuteron exchange $H^+ + D_2 \rightarrow D^+ + HD$ measured with different techniques [merged beam ⊙, guided ion beam ● (Ochs and Teloy, 1974), and • (Müller, 1983), DRIFT ■ (Villinger et al., 1982). The heavy line is the result from the statistical MBD theory (Gerlich, 1982), and the thinner line is the prediction based on conventional phase space theory.

relaxation of the D_2 target, leads to the broadening in the threshold region. At energies above 0.3 eV, the merged-beam cross sections may be somewhat too small owing to problems with the time overlap of the pulsed neutral and ion beam. The difference between our statistical MDB theory and the usual phase-space theory is small at low energies; however, there are significant deviations above 0.5 eV. More experimental results for the H_3^+ system will be presented in Sections V B 3 and V D 2.

3. *Small Rate Coefficients*

Most standard methods for determining thermal reaction rate coefficients are limited typically to values above 10^{-13} cm^3/s. In order to obtain a sufficient product signal for a very slow reaction, the experiments are often performed at high neutral densities, which results in several perturbations, for example, by ternary processes. With ion trapping methods, much smaller rate coefficients can be determined through long interaction times, thereby avoiding the need for high neutral densities. This is briefly illustrated in this section with two slow binary reactions. Radiative association and other slow processes that characterize the capabilities of the ring electrode trap follow in Section V D.

The first example, depicted on the left-hand side of Fig. 67, refers to collisions between C^+ and H_2. For this system, the binary or ternary products formed are CH^+ from the 0.398 eV endothermic bimolecular reaction, CH_2^+ from radiative association (see Section V D 1), or CH_3^+ produced by stabilizing the CH_2^+ collision complex during its lifetime via an additional H_2 molecule. The CH^+ and CH_2^+ products cannot be observed directly, since both undergo very fast secondary reactions with the ambient H_2 to give

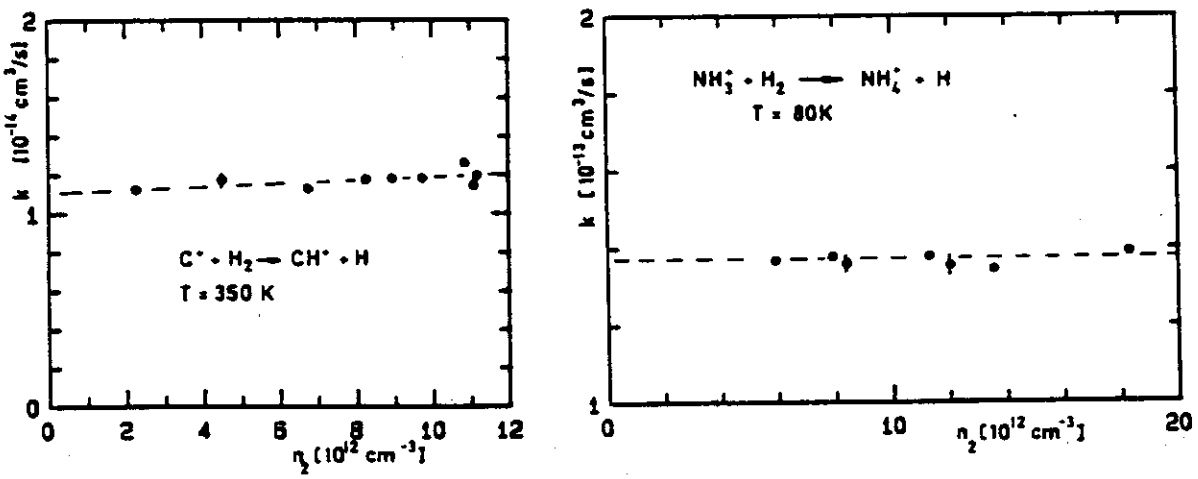

Figure 67. Thermal rate coefficients for two slow reactions as a function of the target density n_2. At the low density in the ring electrode trap, both reactions proceed predominantly via a bimolecular process. The slight increase in the rate coefficient for the $C^+ + H_2$ reaction indicates a minor contribution from ternary collisions.

CH_3^+. Owing to the large endothermicity, the binary reaction is very slow at room temperature. An estimate of the thermal rate coefficient can be obtained from the approximate formula $k(T) = 10^{-9} \exp(-4575\,\mathrm{K}/T)\,\mathrm{cm}^3/\mathrm{s}$, which fits in good approximation the results of our phase-space calculations (Gerlich and Kaefer, 1987; Gerlich et al., 1987) between 100 K and 600 K.

At room temperature, the binary reaction is so slow that it competes with ternary association, even at the low densities of our experiment. In order to increase the contribution of the binary reaction, the ion trap was not cooled, and rf heating of the electrodes led to an estimated temperature of about 350 K. Under these conditions an almost density-independent rate coefficient $k = 1.1 \times 10^{-14}\,\mathrm{cm}^3/\mathrm{s}$ is observed, that is, binary processes prevail. This experimental value is larger than the theoretical rate $k(T)$, suggesting a somewhat higher trap temperature. The slight increase of the measured effective rate with the hydrogen density indicates a small contribution from ternary reactions with $k_3 < 10^{-28}\,\mathrm{cm}^6/\mathrm{s}$. More discussion of this reaction at lower temperature is given in Section V D 1.

The second example in Fig. 67 refers to the formation of the ammonium ion from the abstraction reaction $NH_3^+ + H_2 \rightarrow NH_4^+ + H$. Although this reaction is exothermic, it is very slow (Barlow and Dunn, 1987). At 300 K the rate coefficient is three orders of magnitude smaller than the Langevin rate coefficient. It has a minimum of $1.5 \times 10^{-13}\,\mathrm{cm}^3/\mathrm{s}$ at about 80 K (Böhringer, 1985), but it increases toward lower temperature. This has been explained by an energy barrier and a quantum-mechanical tunneling mechanism. Since the reaction must proceed via formation of an intermediate complex with a rather long lifetime, significant perturbations can occur due to the presence of buffer gas at high density. The influence of third-body-assisted binary collisions has been examined in a selected ion drift tube (Böhringer, 1985), however, at densities above $10^{16}\,\mathrm{cm}^{-3}$. Our experiment has been performed at densities in the range of $10^{13}\,\mathrm{cm}^{-3}$, further reducing the influence of ternary collisions by three orders of magnitude. The resulting rate coefficient $k(80\,\mathrm{K}) = 1.4 \times 10^{-13}\,\mathrm{cm}^3/\mathrm{s}$ corroborates the previous results.

B. Differential and State-to-State Cross Sections

1. *Single-Electron Transfer in $Ar^{2+} + He$*

The integral cross section of the $Ar^{2+}(^3P) + He(^1S) \rightarrow Ar^+(^2P) + He^+(^2S)$ charge-transfer process was presented in Section V A and discussed on the basis of a localized crossing at 4.7 Å. This reaction is also well suited for characterizing the differential scattering guided-ion-beam apparatus and for testing the angular and energy resolutions of this new experimental method. A special feature of the one-electron charge transfer is that there is only one

input and one exit channel, since the exothermicity of 3.14 eV is not sufficient to populate excited states at low kinetic energies. The Ar^{2+} and Ar^{+} fine structure splitting, resulting in three reactant states and two product channels, are ignored, since they are not resolvable in the present experiment. For simplicity, we assume that metastable Ar^{2+} ions are quenched in the ion source (see Section III D). With these assumptions, the center-of-mass product velocity is well defined and the laboratory product velocity is easy to obtain, as illustrated in the Newton diagram in the upper part of Fig. 68.

To measure the differential cross section for this ideal collision system it is sufficient only to determine the projection of the product velocity, v'_{1p}, onto the axis defined by the primary velocity $\mathbf{v}_1$. In the guided-ion-beam experiment $\mathbf{v}_1$ coincides with the octopole axis and the distribution $d\dot{N}/dv'_{1p}$ is measured directly by time of flight. It is not necessary to determine the transverse component v'_{1t} of the product ions by varying the rf amplitude, as described in detail in Section IV B 3, since for this state-to-state process the scattering geometry is fully determined by v'_{1p} alone (see Newton diagram). A typical experimental Ar^{+} product velocity distribution $d\dot{N}/dv'_{1p}$ is shown in the lowest panel of Fig. 68. In the laboratory frame, all products are forward scattered, while in the center-of-mass frame, the distribution is symmetric relative the nominal center-of-mass velocity v_c. A similar symmetric form is obtained at a collision energy of 0.2 eV, while at 0.5 eV and above, the symmetry is lost, indicating a change in the differential cross section (Disch et al., 1985).

The experimental product velocity distributions are broadened by the angular spread of the ion beam, the time resolution, and the finite length of the scattering cell. For this particular system, however, a detailed analysis shows that the overall resolution in our beam/cell arrangement is mostly affected by thermal broadening. The influence of thermal broadening and the dependence on the nominal scattering angle ϑ is illustrated in the middle panel of Fig. 68. The simulated Ar^{+} product velocity distributions $d\dot{N}(\vartheta_0)/dv'_{1p}$ have been calculated using Eq. (95). For each distribution it was assumed that the differential cross section can be represented by a δ function, which peaks at different center-of-mass scattering angles [$d\sigma/d\vartheta = \sigma(E_T) \times \delta(\vartheta - \vartheta_0)$, $\vartheta_0 = 0°, 20°$, etc.]. The energy dependence of $\sigma(E_T)$ has been given in Section V A 1. More details of the method can be found in Gerlich (1989a). These simulated results show that thermal broadening leads to rather narrow but closely spaced velocity distributions in the forward and backward directions. If sideways scattering occurs, the angular resolution is better, although the distributions are wider. This example also shows that, for this system, the angular resolution of our experimental method is on the order of $\pi/4$.

To fit the measured distributions we superimpose the simulated distributions $d\dot{N}(\vartheta_0)/dv'_{1p}$ with properly chosen weights. A typical result of

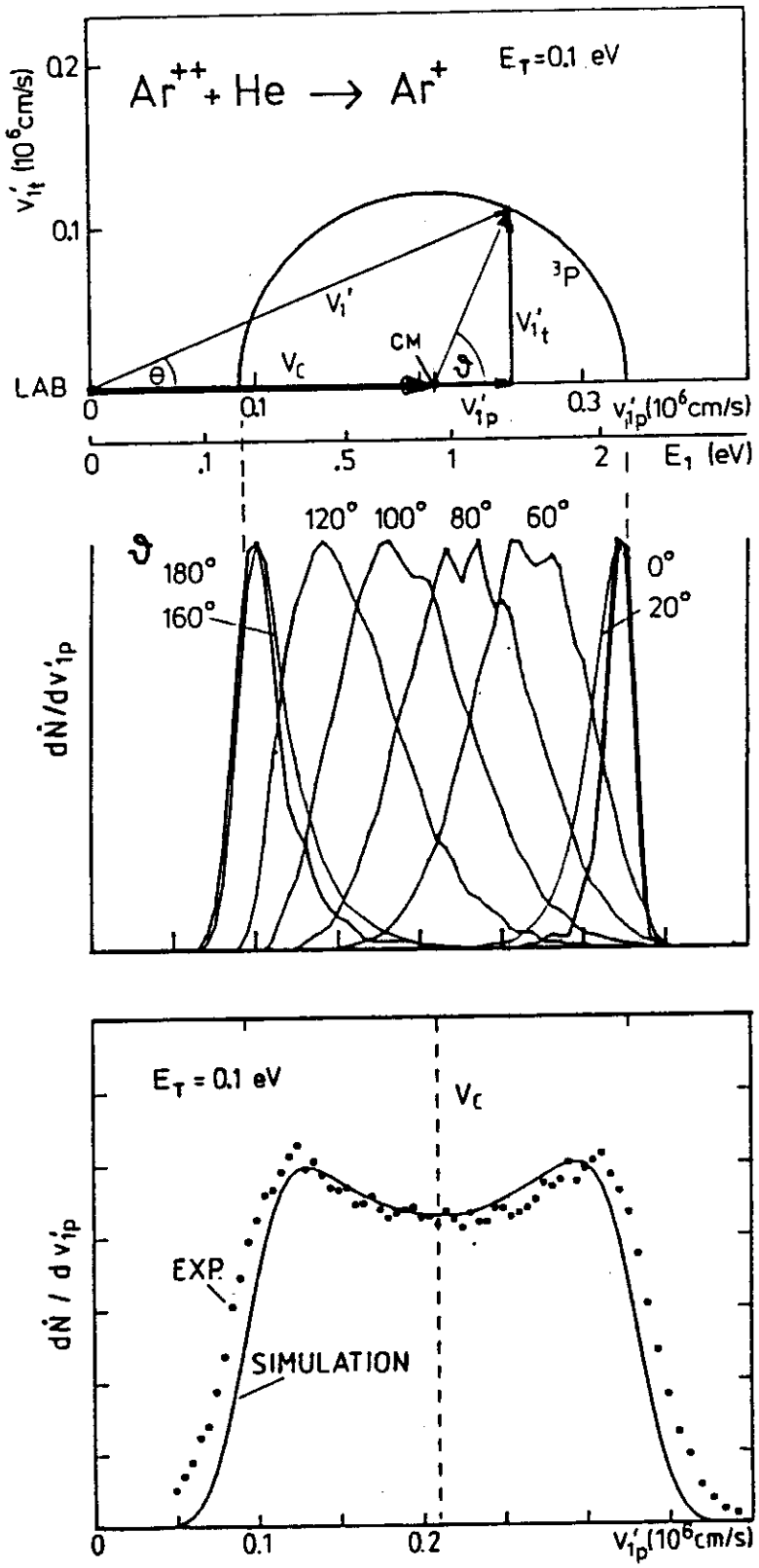

Figure 68. Differential scattering in the state-to-state charge-transfer reaction $Ar^{2+} + He \rightarrow Ar^{+} + He^{+}$ in the guided-ion-beam apparatus. The upper panel depicts a nominal Newton diagram scaled for a collision energy of 0.1 eV. CM marks the origin of the center-of-mass system; the He target is assumed to be at rest. The laboratory and center-of-mass scattering angles are θ and ϑ, respectively. The projection of the final velocity v'_1 onto the octopole axis, that is, the component v'_{1p}, is measured by time of flight. The product velocity distributions are broadened by the target motion, as illustrated in the middle panel. The lowest panel compares a measured velocity distribution with a simulation based on a weighted superposition of functions shown in the middle panel.

such a fit is compared to experimental data in the lowest panel of Fig. 68. The good agreement indicates that the thermal target motion causes most of the broadening. The slight differences are due to the previously mentioned effects, which were not included in this simulation. In an analogous manner these ϑ-dependent weights can also be used to simulate the transverse product velocity distribution $d\dot{N}/dv'_{1t}$. This distribution has also been measured independently by varying the rf guiding field and is given in Fig. 69. Comparison of the experimental data (dark line) with the simulation (dashed line) shows reasonable agreement if one compares the position of the maxima. As expected from the Newton diagram in Fig. 69 these maxima are positioned slightly above 1×10^5 cm/s. The deviation at low transverse velocities is due

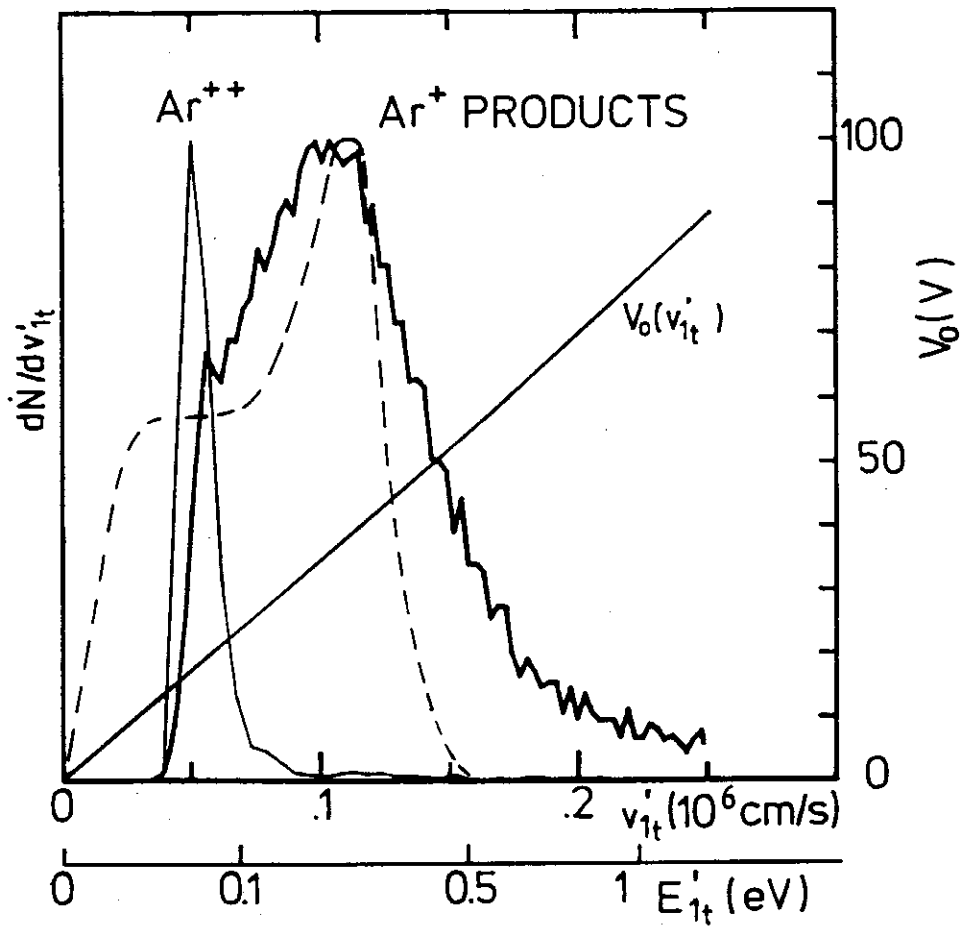

Figure 69. Ar^+ transverse product velocity distribution $d\dot{N}/dv'_{1t}$ (heavy line) for the state-to-state charge-transfer reaction $Ar^{2+} + He \rightarrow Ar^+ + He^+$, obtained by variation of the rf guiding field. The dashed line shows a simulation that only accounts for the thermal broadening. Deviations from the experimental Ar^+ curve are explained in the text. The maximum of the product distribution is situated slightly above $v'_{1t} = 1 \times 10^5$ cm/s in accordance with the Newton diagram in Fig. 68. The narrow Ar^{2+} distribution has been determined by differentiating the rf-dependent transmission function of the primary beam. The slightly curved line shows the relation between the maximum guided transverse velocity and the amplitude V_0, as obtained from Eq. (84).

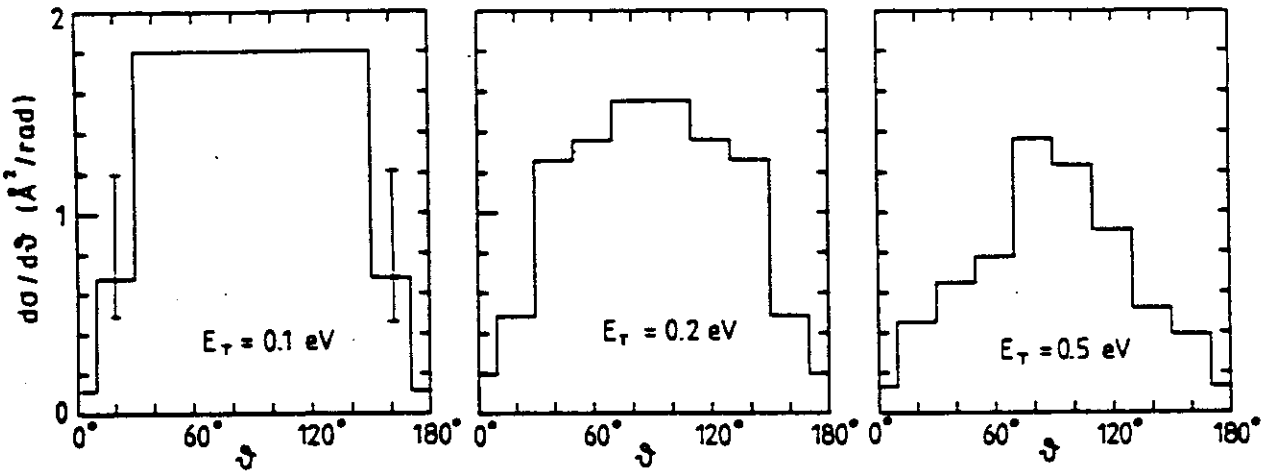

Figure 70. Differential cross sections $d\sigma/d\vartheta$ in absolute units (Å^2/rad) for the charge transfer reaction $Ar^{2+} + He \rightarrow Ar^{+} + He^{+}$. At 0.1 eV isotropic scattering prevails, that is, $d\sigma/d\vartheta$ is nearly constant, while at 0.5 eV the Ar^{+} products are mostly scattered sideways.

to potential distortions. It can also be seen from this figure that for guiding the primary Ar^{2+} beam, a minimum effective potential of about 50 meV is required. The additionl high-energy tail in the experimental distribution may be due to some unknown rf influence, but it can also be explained by the presence of metastable ions in our primary ion beam, which have been reported (Friedrich et al., 1984) to cause strongly sideways scattered products.

The most important results derived from the previously described fitting procedure are the ϑ-dependent weights, since they are directly proportional to the differential cross section. With these weighting factors and the measured integral cross section σ, one obtains the differential cross section $d\sigma/d\vartheta$ in absolute units. The angular dependence of $d\sigma/d\vartheta$ is depicted as a histogram in Fig. 70 at three collision energies. At 0.1 eV $d\sigma/d\vartheta$ is constant with exception of some uncertainty in the forward and backward directions, that is, isotropic scattering prevails. Increasing the collision energy to 0.2 eV and 0.5 eV leads to a preference for sideways scattering; however, the forward–backward symmetry is still maintained. At 1.6 eV, significant forward scattering prevails as can be seen immediately from the time-of-flight distribution in Fig. 71. These results can be compared with contour plots measured in a differential scattering experiment (Friedrich et al., 1984). Both the sideways scattering peak at $E_T = 0.53$ eV and the preference for forward scattering at $E_T = 1.6$ eV are in agreement with our observations. Some minor deviations may be due to an admixture of Ar^{2+} (^1D) ions which differ in the two experiments.

A self-consistency check of the differential guided-ion-beam method would be to detect the second ionic product, He^{+}. Since this light ion carries most of the reaction exothermicity (3.14 eV), one obtains a much larger

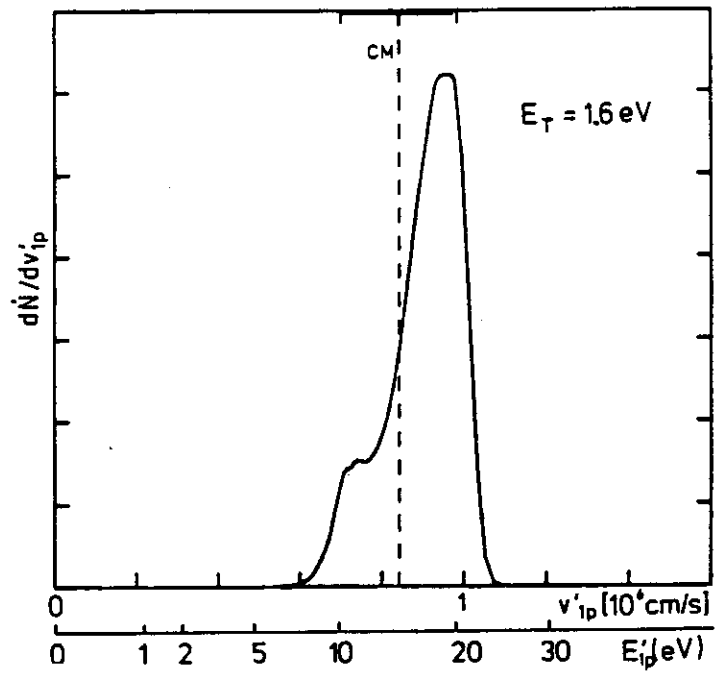

Figure 71. Product velocity distribution dN/dv'_{ip} for the charge-transfer reaction $Ar^{2+} + He \rightarrow Ar^{+} + He^{+}$ measured at a collision energy of 1.6 eV in the guided-ion-beam apparatus. The upper scale marks the position of the center-of-mass velocity and the range of the Newton circle. It is evident that at this energy forward scattering prevails.

Newton sphere and better angular resolution, but a large fraction of the products is scattered backward in the laboratory system. Owing to the high energy and low mass, one must operate the octopole at higher frequencies than used for guiding Ar^{2+} and Ar^{+}. The necessary operating conditions ($r_0 = 0.3$ cm, $E_m = 3$ eV, $\Omega/2\pi = 23$ MHz, $V_0 = 150$ V; see Section II D 2) are within the reach of our instrument, but the experiment has not yet been performed.

2. *Dissociative Electron Transfer in $He^+ + O_2$*

The universal guided-ion-beam apparatus has also been used to study the kinetic energy release in the dissociative charge transfer $He^+ + O_2 \rightarrow O^+ + O + He$. It was previously established (Gentry, 1979) that more than 99% of the charge transfer leads to the dissociation of the highly excited O_2^+. In our experiment the amount of detected O_2^+ was below 0.2%. Even after dissociation, an excess energy of 5.86 eV remains, which either results in fast fragments or can be lodged into exited products. In addition to the ground-state $O^+(^4S^0) + O(^3P)$ products, exited atoms $O(^1D)$ and $O(^1S^0)$, or excited ions $O^+(^2D^0)$ and $O^+(^2P^0)$, are accessible in different combinations.

Using a high-resolution crossed-beam apparatus, Bischof and Linder (1986) have studied the relative populations of the exited products, the accessible combinations of which have been denoted by I–VI. Integrating

over the scattering angle, they have derived the branching ratios depicted in Fig. 74. If these branching ratios are extrapolated from the lowest collision energy of 0.5 eV to thermal energies, a result is obtained that is in conflict with conclusions from an ICR trap experiment (Mauclaire et al., 1979). More details are discussed in Bischot and Linder (1986).

In order to clarify this discrepancy, we have measured axial and transverse velocity distributions (Scherbarth, 1988) using our guided-ion-beam apparatus. A typical result is shown in Fig. 72. The details of the data presentation have been discussed in Section IV B 3. The lower part of the figure shows that the angular distribution is rotationally symmetric relative to the laboratory origin. This corresponds, within our limited resolution, to the predissociation of an almost unperturbed, but excited O_2^+ formed by a large distance electron jump. This is in accordance with the crossing radius $R_c = 3.5$ Å, determined from the integral cross section. Such rotational symmetry relative to $v'_1 = 0$ is also observed at lower collision energies, since there the nominal center-of-mass velocity v_c is even closer to the laboratory origin. The dashed lines indicate the integration limits for deriving the intensity of the different product channels I–V. Since integration over our directly measured flux density $D(v'_{1p}, v'_{1t})$ requires no weighting factors, it can be seen directly from Fig. 72 that formation of exited $O^+(^2P^0)$ are ground state $O(^3P)$ is the dominant channel (denoted as V).

In order to demonstrate the attainable energy resolution, Fig. 73 shows axial product velocity distributions dN/dv'_{1p} recorded at several collision energies. These were measured at a very low guiding field, corresponding to a transverse energy of about 80 meV. A common feature of all the curves is the dominant peak at low product velocities and a partially resolved structure at higher velocities. In the bottom curve, the dashed lines indicate the estimated contributions from the channels I–VI. It is obvious that our method cannot compete with the much higher angular and energy resolution of a crossed-beam experiment; however, it has the unique ability of operating down to thermal energies and provides a fast and reliable overview of the scattering dynamics.

Changes in the relative populations are also shown in Fig. 73. For example, channel II becomes more important at higher energies. For a more quantitative comparison, the angle-integrated branching ratios have been calculated for collision energies between 0.06 eV and 6.5 eV, with the results plotted as open circles in Fig. 74. In the overlapping energy range they are in good overall agreement with the crossed-beam data from Bischof and Linder (1986); however, they deviate significantly from the near-thermal results derived from the ICR trap experiment (Mauelaire et al., 1979). Our guided-ion-beam results indicate that there is no dramatic change in the reaction mechanism below 0.5 eV. Note that our lowest collision energy

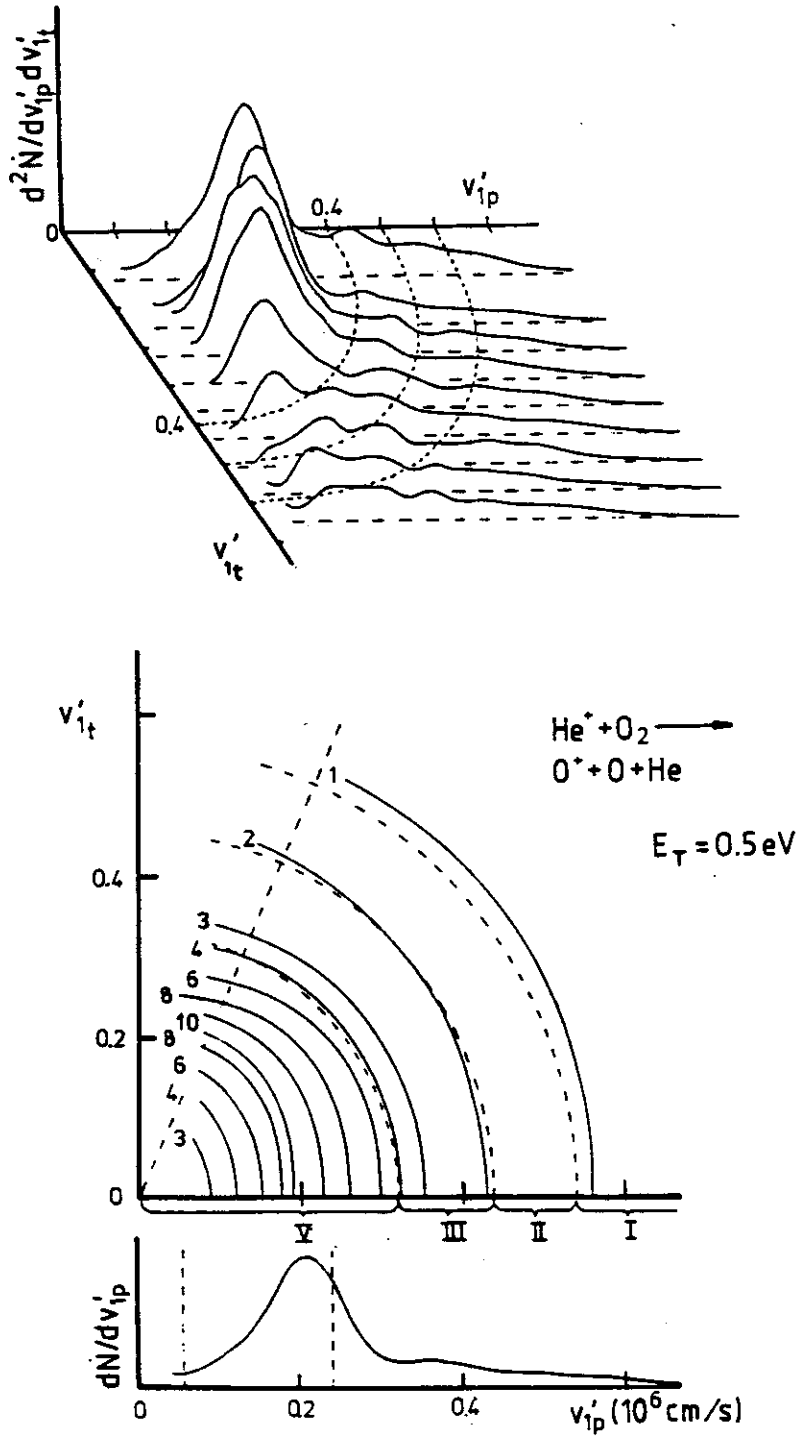

Figure 72. Doubly differential cross sections for the dissociative charge-transfer reaction $He^+ + O_2 \rightarrow O^+ + O + He$ determined in the guided ion beam apparatus. The O^+ product velocity distributions $d^2\dot{N}/dv'_{1p}\,dv'_{1t}$ are shown both perspectively and as a contour map of the two-dimensional product flux density, defined in Eq. (101). The dotted lines indicate the integration limits for deriving the intensity of the different product channels I–V; see text.

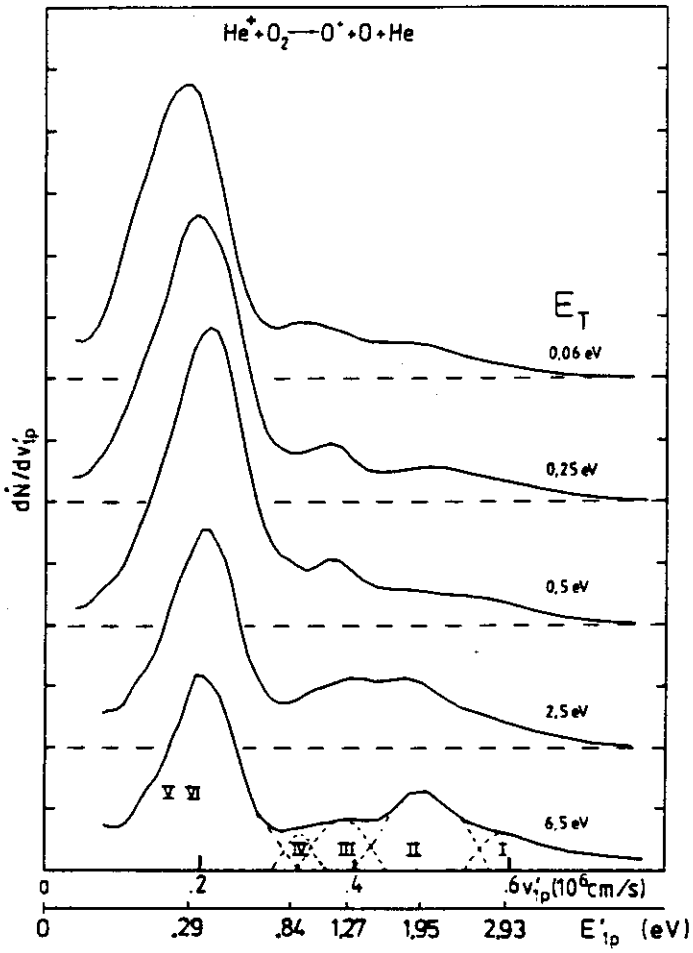

Figure 73. Axial product velocity distributions dN/dv'_{1p} measured for $He^+ + O_2 \rightarrow O^+ + O + He$ at a very low octopole guiding field. In the lowest curve, the dashed lines indicate the estimated contributions from channels I–V. Their relative populations changes slightly going from near thermal collision energies ($E_T = 0.06\,eV$) to $E_T = 6.5\,eV$; however, the slow peak is always dominant.

(60 meV) is already below the limit at 77 meV where the orbiting radius becomes larger than the crossing radius R_c, as shown in Section V A 1. For a detailed discussion of the reaction mechanism see Bischof and Linder (1986).

3. *Proton–Deuteron Exchange in $H^+ + D_2$*

It has been illustrated in Section V A 2 that integral cross sections and thermal rate coefficients for isotopic variants of the $H^+ + H_2$ reaction are in good agreement with the predictions of the MDB statistical theory (Gerlich, 1982; Gerlich et al., 1980). Here we want to demonstrate that the total energy available to the complex is distributed statistically among the open product channels. A survey of the results of this reaction, which has been studied in detail (Gerlich, 1977), has been reported in Teloy (1978).

High-resolution D^+ product velocity distributions for the reaction $H^+ + D_2 \rightarrow D^+ + HD$ have been measured by time of flight using the

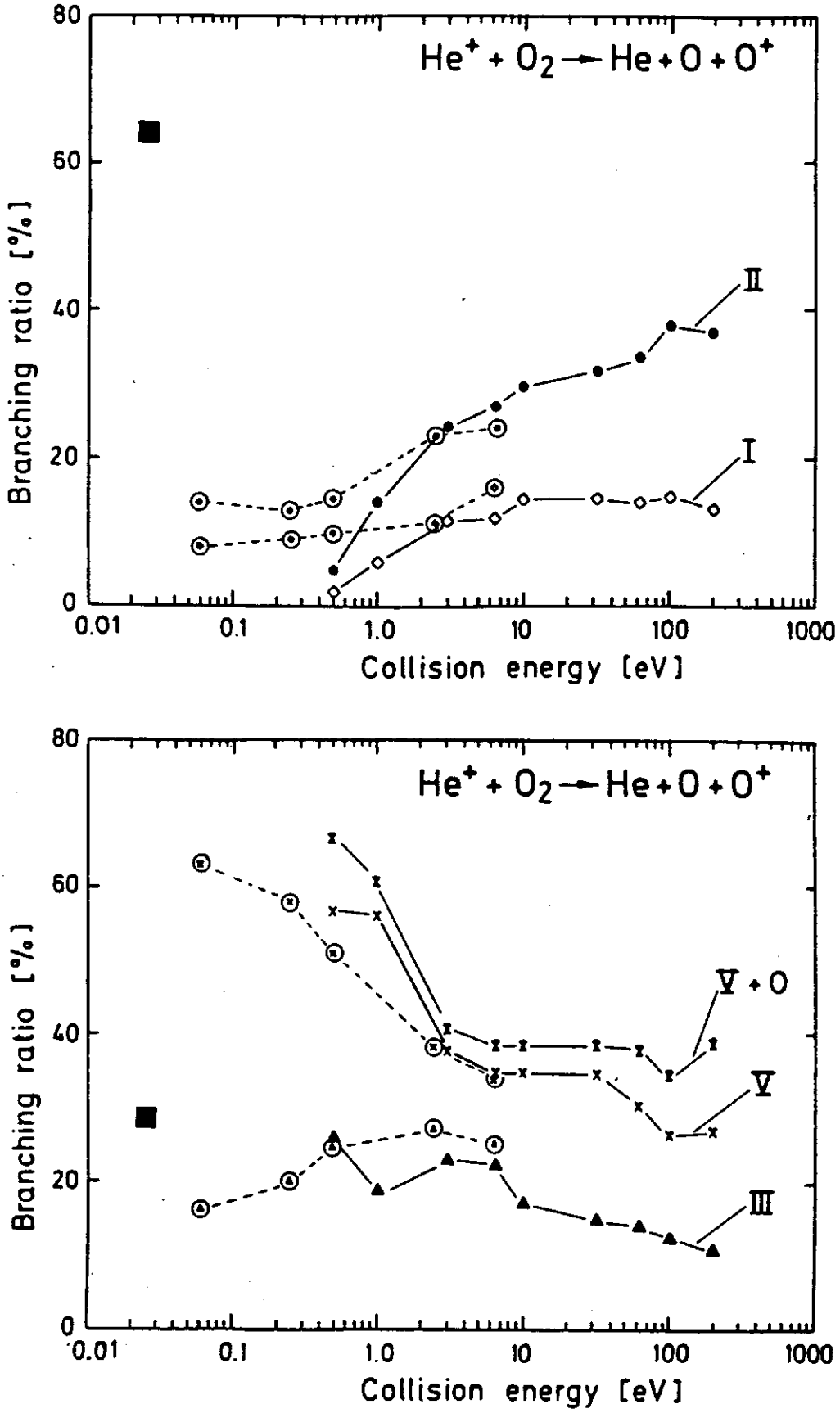

Figure 74. Branching ratios of the different $O + O^+$ channels (I–V) populated in dissociative charge-transfer collisions of He^+ with O_2. The data at high energies, connected with solid lines, were obtained with a differential scattering apparatus (Bischof and Linder, 1986). The two squares are near-thermal results, derived from an ICR trap experiment, combining channels (I + II) and (III + V) (Mauclaire et al., 1979). The guided-ion-beam results, connected with dashed lines, close the energy gap between thermal energies and those accessible in standard beam techniques.

differential scattering apparatus described in Section IV C. In this experiment, the target gas was cooled to liquid nitrogen temperature, the ion energy spread was 50 meV, and the angular resolution was 3°, resulting in an overall energy resolution of 80 meV. Product velocity distributions were determined by time of flight using a 1-m-long octopole as a flight tube. The recorded spectra were transformed numerically into laboratory energy distributions.

A selection of typical D^+ product distributions dN/dE'_1 is plotted in Fig. 75, the lines representing a smooth interpolation of the data. As can be seen by comparing the position of the $\Delta E_T = 0$ mark, this reaction has a strong tendency to convert collision energy into internal excitation. The structure of the distributions is due to partially resolved rovibrational states of the HD product molecule, the nominal positions of which are marked by arrows. In the depicted examples, the collision energy is varied in the threshold range

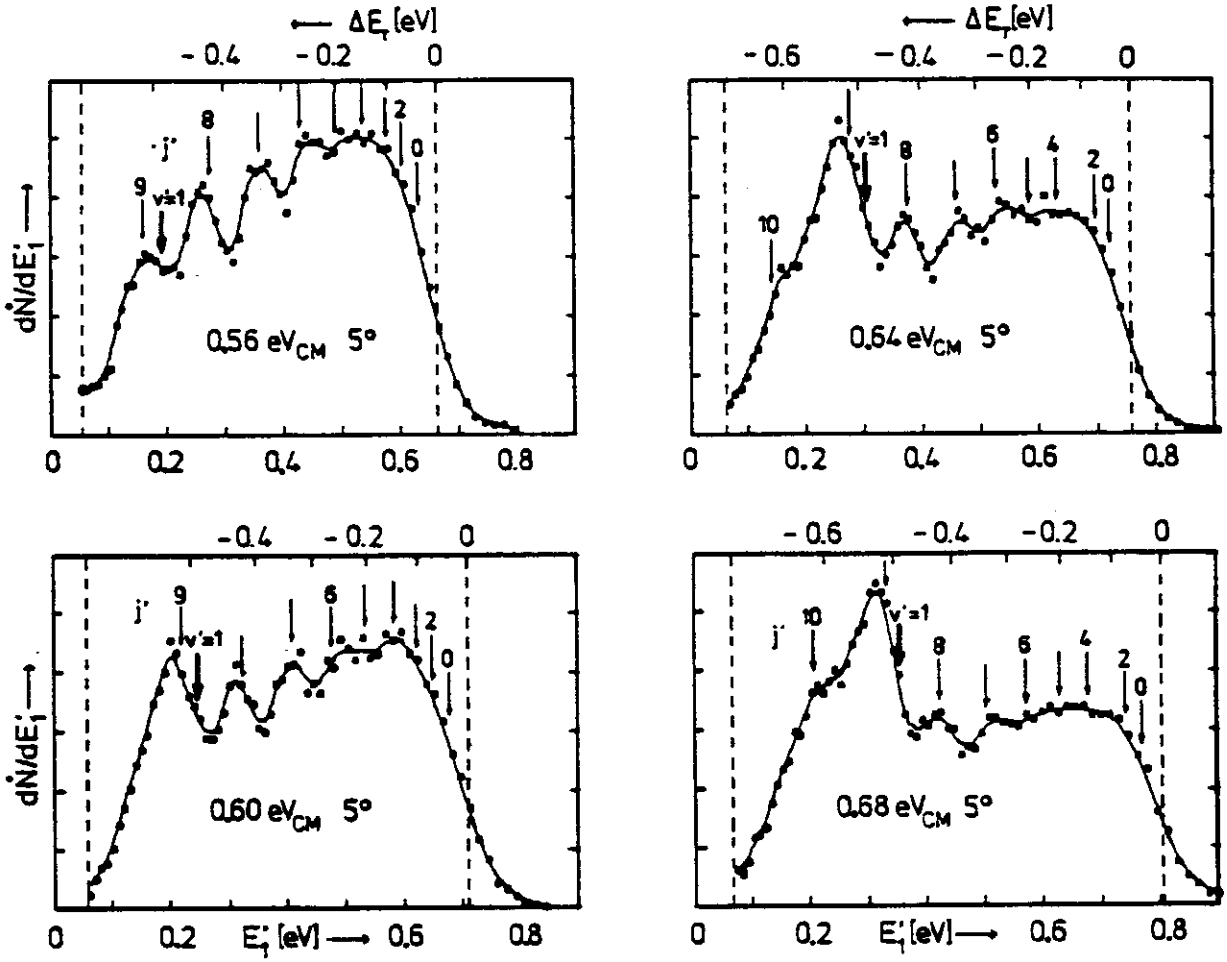

Figure 75. Product energy distributions dN/dE'_1 from reactive $H^+ + D_2 \rightarrow D^+ + HD$ collisions measured with a differential scattering apparatus at a laboratory angle of 5°. The upper scale shows the translational exoergicity $\Delta E_T = E'_T - E_T$. The dashed lines mark the positions $\Delta E_T = 0$ and $\Delta E_T = -E_T$. The partially resolved structure corresponds to rotational excitation of HD products. The collision energy is varied in the range of the threshold for formation of HD($v' = 1$), resulting in the formation of additional slow products (left side of the $v' = 1$ arrow).

for formation of HD in the first vibrational state. Contributions from the $(v' = 1, j')$ states, superimposed on the $(v' = 0, j')$ states, result in a steplike structure in the kinetic energy distribution of the D^+ products, which are marked by the $v' = 1$ arrow. A further increase of the energy to 2 eV leads to additional steps due to population of the vibrational states $v' = 2$–4 and to a dense manifold of rovibrational states (Gerlich, 1977; Teloy, 1978).

To compare calculated rovibrational distributions $P(v', j')$ with the experimental data, the probabilities must be convoluted with $F_T(E'_1, \theta, \Delta E_T)$, the overall resolution function of the apparatus. This function combines the influence of the energy spread of the ion beam, the resolution of the detector, and the influence of the target motion. Details of this procedure have been mentioned in Section IV C and are discussed in Gerlich (1989a). Rovibrational distributions have been calculated with the MDB theory; however, it has been shown (Gerlich, 1977; Gerlich et al., 1980) that the results are very similar to the microcanonical equilibrium distribution $P_0(v', j')$. Therefore, we use here for simplicity these probabilities, shown as sticks in Fig. 76, to illustrate the influence of the resolution of the apparatus. The calculated resulting smooth distributions, plotted in Fig. 76, agree well with the measured curves depicted in Fig. 75. They also allow one to obtain a quantitative estimate of the contributions from the $v' = 1$ states.

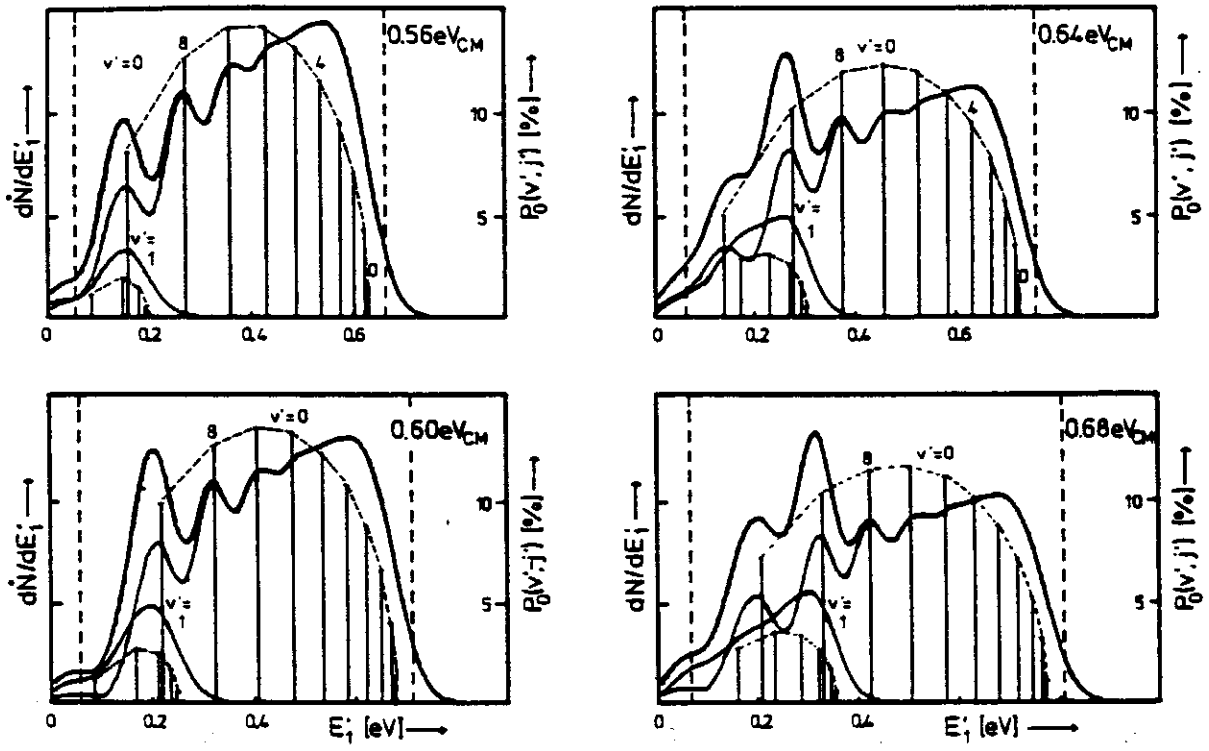

Figure 76. Simulation of the product energy distributions depicted in Fig. 75. The calculation is based on a statistical model that predicts the population probability $P_0(v, j)$ (stick diagram, scale at right). The smooth distributions were obtained by accounting for the overall resolution of the apparatus.

Corresponding high-resolution results have also been measured for $H^+ + H_2$ collisions, with emphasis on ortho–para transitions, and are reported in Gerlich (1990).

C. Applications of Optical Methods

Several possible combinations of the guided-ion-beam technique with optical methods have been mentioned in Section IV B 4. The following examples have been chosen to illustrate some of these capabilities. The $N^+ + CO$ reaction is used to demonstrate the sensitivity of the apparatus for detecting photons from a chemiluminescent reaction and to show two applications of the photon–ion coincidence technique. The use of intense laser pulses for multiphoton ionization is discussed in the chapter by Andersen; therefore, we present here only one brief example. Other laser applications described in this section include laser-induced charge transfer and laser-based analysis of products detecting fluorescence photons or fragment ions.

1. *Chemiluminescence*

The first application of a guided-ion-beam apparatus for the detection of photons from a chemiluminescent reaction was reported in Gerlich and Kaefer (1985). In this contribution it was shown that the observed B–X and D–X emission from N_2^+ products formed in $Ar^{2+} + N_2$ collisions (Neuschäter et al., 1979) are due to cascading transitions. This was proven directly by measuring photons, selected in wavelength using filters, in coincidence with product ions whose kinetic energies were determined by time of flight.

For the $N^+ + CO$ system, integral cross sections for several product channels have been reported based on a guided-ion-beam experiment (Frobin et al., 1977). The increase in the cross section toward higher energies, especially for CO^+, indicated contributions from exited products. By spectral analysis of the optical emission, Neuhauser et al. (1981) have shown that the dominant luminescent product is $CO^+(A\,^2\Pi)$. This reaction system has been studied in greater detail using luminescence and coincidence techniques in our universal guided-ion-beam apparatus (Kaefer, 1984).

Integral cross sections for luminescence in specific wavelength ranges, recorded using different filters, are shown in Fig. 77. The threshold onset at 2 eV coincides with the energy required for the formation of the exited $CO^+(A\,^2\Pi)$ state. At higher energies, the luminescence cross section increases to about 1 $Å^2$, corresponding to 30% of the total CO^+ cross section. Problems in calibrating the photon detection efficiency lead to an overall uncertainty of the absolute values of $\pm$ 50%. Accounting, in addition, for the differences in wavelength ranges, the agreement with previously published results (Neuschäfer et al., 1981) is satisfying.

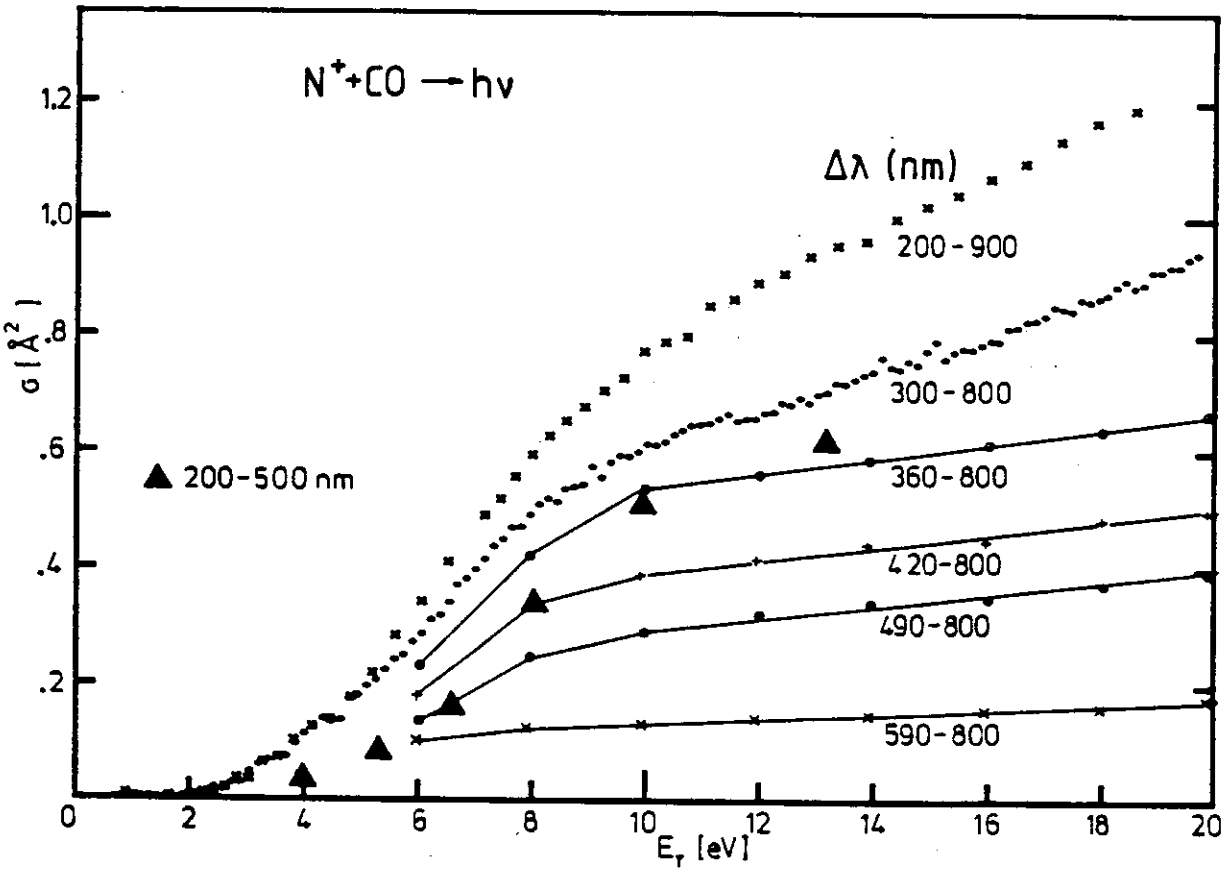

Figure 77. Integral cross sections for formation of luminescent products (CO^+, CN^+, etc.) in $N^+ + CO$ collisions recorded for selected wavelength ranges using the apparatus shown in Fig. 46. The triangles are from Neuschäfer et al. (1981).

A small contribution to the overall production of chemiluminescent photons is due to the formation of exited CN^{+*}. This specific products has been identified by detecting the photons in coincidence with mass-selected CN^+ ions. The integral cross section is plotted in Fig. 78 as a function of the total energy available for internal excitation of the products [$\Delta H^0(CN^+(a\,^1\Sigma)) = 2.97$ eV]. Identification of the emitting state, based only on a threshold onset at about $E_T - \Delta H^0 = 3$ eV, is not unequivocal since this threshold is significantly higher than the energy required to reach the $b\,^1\Pi$ state (1.03 eV), but below the $c\,^1\Sigma$ state (3.9 eV). A possible explanation is simultaneous excitation of both reaction products, for example, formation of the CN^+ ion in the $b\,^1\Pi$ state and the O atom in the ^1D state (1.97 eV).

Simultaneous excitation of both reactants has also been identified for the $CO^+(A\,^2\Pi) + N(^2D)$ product channel by using an even more complicated coincidence technique. In this case, photons, were detected in coincidence with ions that were selected according to their mass and flight time. The coincident velocity distributions of the luminescent products are compared in Fig. 79 with total velocity distributions measured for all CO^+ products. The transverse energy was limited to 80 meV to partially resolve some

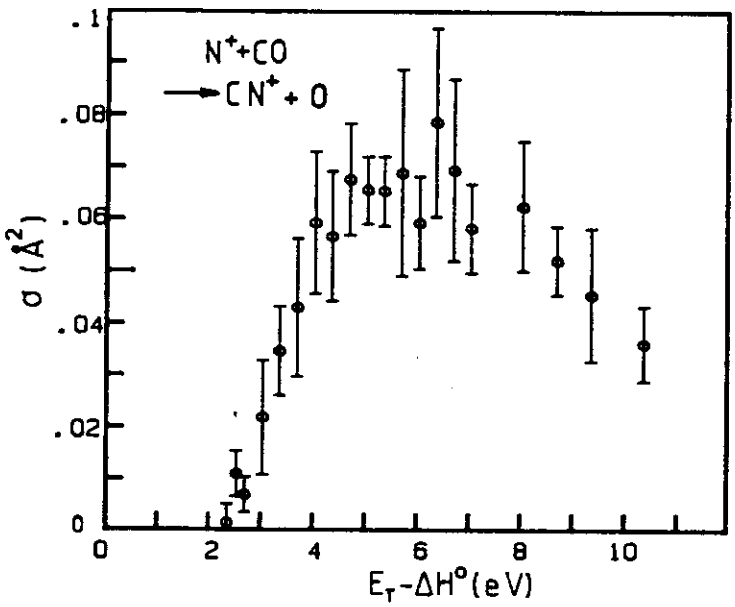

Figure 78. Formation of excited CN^{+*} ions in $N^+ + CO$ collisions. The specific chemiluminescent products are identified by detecting the photons in coincidence with the mass-selected CN^+ ions. The integral cross section is plotted as a function of the total available energy ($\Delta H^0 = 2.97$ eV).

structure, similar to Fig. 73. These axial product velocity distributions show a preference for formation of backward-scattered products. The areas of the luminescent and total intensity correspond to the partial integral cross sections. The double peak at laboratory energies below $E'_{1p} = 0.1$ eV is due to an experimental artifact; however, the structure at higher energies is real. Comparison of this structure with the ΔE_T scale reveals that at the collision energy of 2.66 eV, a significant fraction of products is formed with internal energies above 2 eV. At 7.3 eV (upper panel), a product group with a preference for converting more than 4 eV into internal energy can be identified. Comparison with the luminescent distributions reveals that at 2.66 eV collision energy, the dominant product channel is $CO^+(X\,^2\Sigma) + N(^2D) - 1.86$ eV, while at 7.3 eV, the luminescent distribution indicates excitation of both products, that is, formation of $CO^+(A\,^2\Pi) + N(^2D) - 4.39$ eV.

2. *Laser Preparation of Reactants*

Following the pioneering work of Chupka and Russell (1968), the endothermic reaction $H_2^+(v) + He \rightarrow HeH^+ + H$ has been extensively investigated using state-selective preparation by photoionization. Integral cross sections obtained with a guided-ion-beam apparatus were reported by Turner et al. (1984). We have used this reaction to test our multiphoton ionization source, described in Section III B 3. H_2^+ ions were created using 3 + 1 resonance-enhanced multiphoton ionization at 318.9 nm via the $B\,^1\Sigma_u^+(v' = 3, j')$ intermediate. At this wavelength the energy of the four photons does not

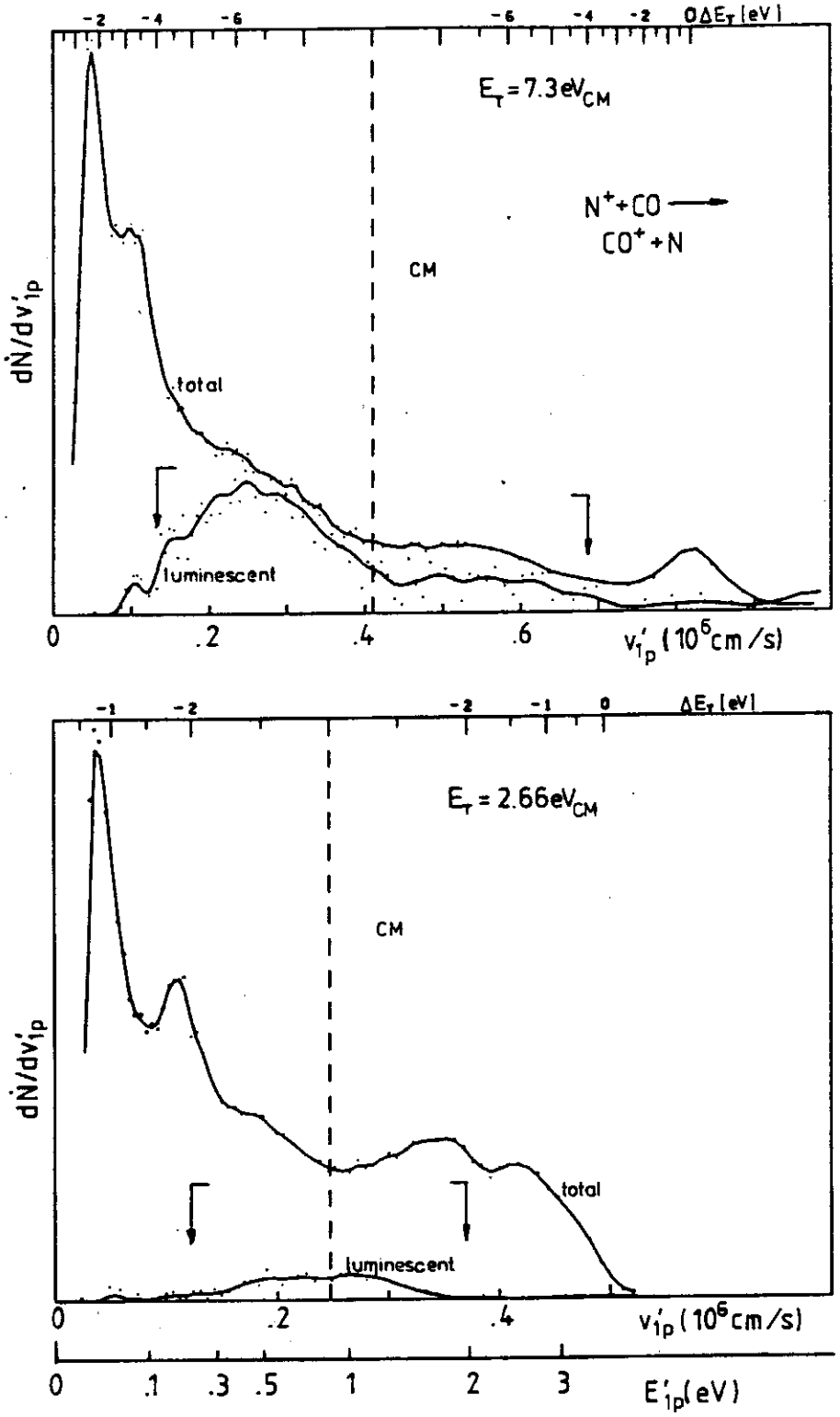

Figure 79. Axial product velocity distributions dN/dv'_{1p} of CO^+ charge-transfer products formed in $N^+ + CO$ collisions at two energies. In this experiment the transverse energy was limited to 80 meV using a low octopole guiding field. The dashed line marks the center-of-mass velocity. The upper scale refers to the translational exoergicity ΔE_T. Compared are the distributions of all CO^+ products (total) with those from luminescent CO^+ ions, distinguished by photon–ion coincidence.

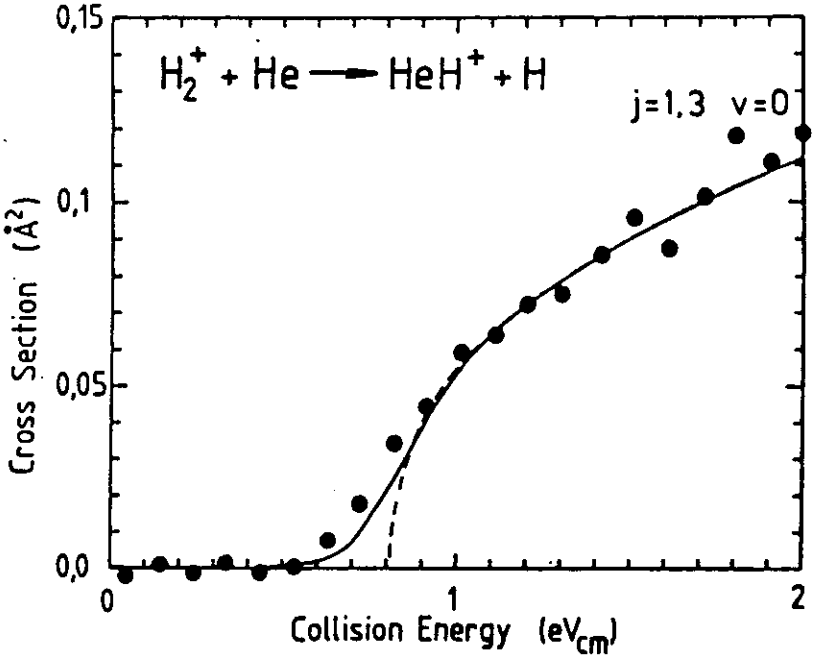

Figure 80. Integral cross section of the endothermic reation $H_2^+(v=0) + He \rightarrow HeH^+ + H$ in the threshold region. State-selective preparation of H_2^+ ions was achieved by multiphoton ionization using the quadrupole photoionization source in the guided-ion-beam apparatus. The data points are in reasonable agreement with the effective cross section (heavy line) calculated from an assumed threshold onset (dashed line) [Eq. (91)].

allow one to reach the first vibrational state of the H_2^+ ion. Thus the H_2^+ ions are all produced in their vibrational ground state. To test experimentally whether absorption of additional photons leads to higher excitation, the cross section for HeH^+ formation has been measured in the threshold region; see Fig. 80. The onset of the integral cross section below 0.8 eV is predominantly due to thermal broadening, as can be seen from a comparison of an assumed cross section (dashed line) and the convoluted result (solid line).

Another method for preparing ions in specific states is to excite them with a laser to a long-lived state. We have used this method to prepare CO^+ ions in the excited $CO^+(A)$ state in order to induce charge transfer with Ar, which for the ground-state $CO^+(X)$ ion is 1.66 eV endothermic. The optical laser excitation spectrum, shown in the upper part of Fig. 81, was recorded by detecting Ar^+ charge-transfer products from $CO^+ + Ar$ in the universal guided-ion-beam apparatus at a collision energy of 0.3 eV. The depicted wavelength range shows a rotational progression of $CO^+(X\,^2\Sigma^+(v=0) \rightarrow A\,^2\Pi(v=2))$ transitions. In this experiment CO^+ ground-state ions were prepared by electron bombardment, thermalized to the temperature of the trapping source, and injected into the octopole system. In the interaction region, the ion beam was crossed (see Fig. 46) with an intense, nonskimmed pulsed beam of Ar gas, creating a momentary and local target density above $10^{13}\,cm^{-1}$. Synchronously, the ions were excited with a pulsed laser (energy

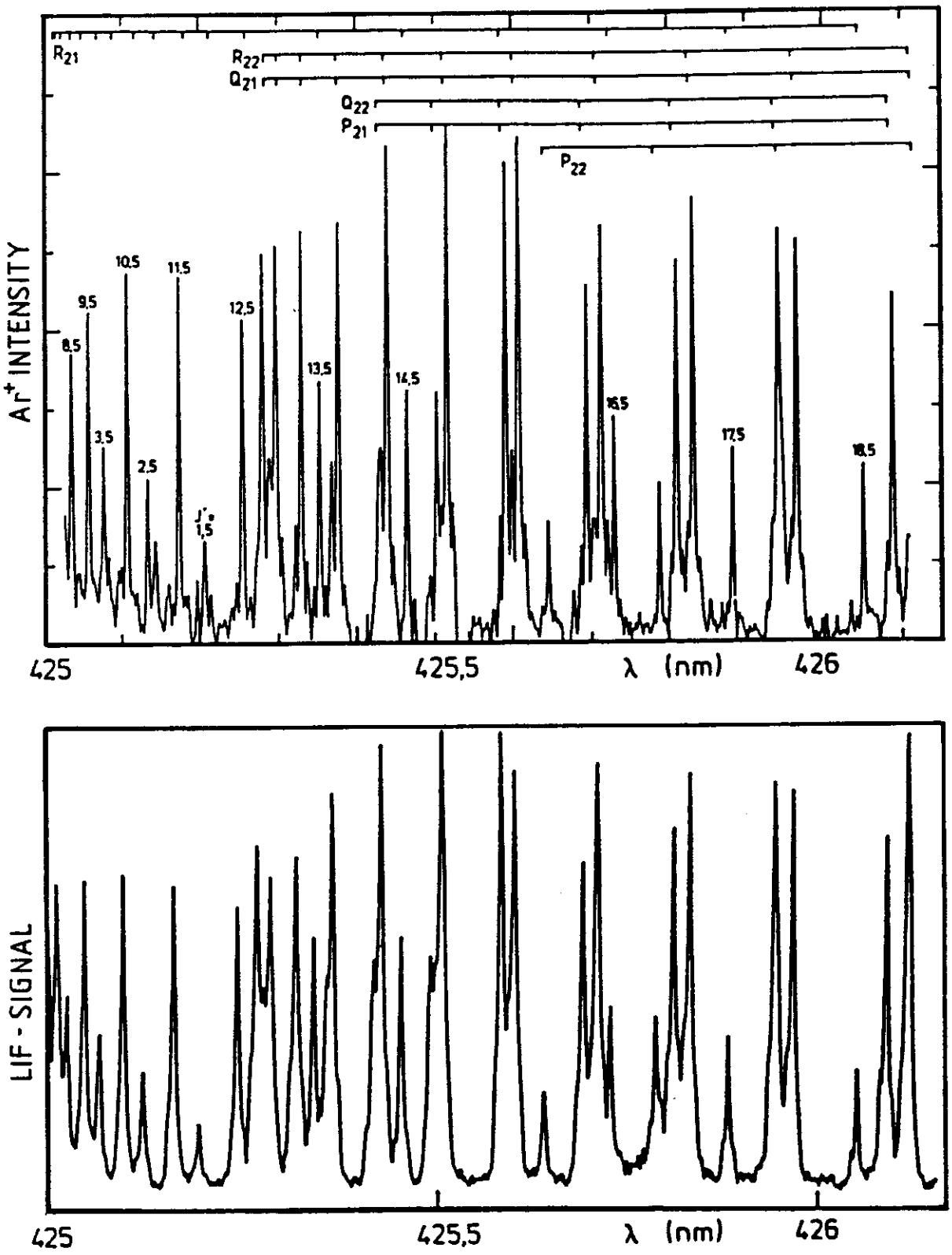

Figure 81. Laser excitation of CO^+ ions in an octopole. In both experiments the CO^+ ions were formed by electron bombardment in the rf storage ion source of the guided-ion-beam apparatus. The upper panel shows the wavelength dependence of Ar^+ charge-transfer products formed in low-energy collisions between laser excited $CO^+(A\,^2\Pi)$ and Ar in the scattering cell. The lower panel depicts, in the same wavelength range, the laser-induced fluorescence signal from CO^+ ions trapped in the scattering cell between two potential barriers.

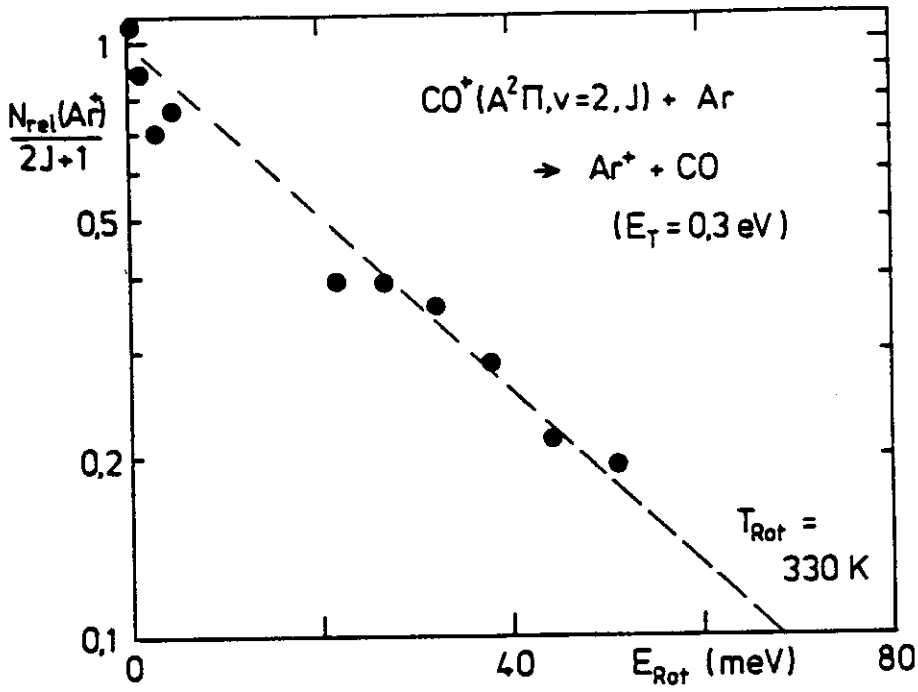

Figure 82. Relative Ar^+ product intensity as a function of the CO^+ rotational states, derived from the upper spectrum in Fig. 81 using $2J + 1$ weighting coefficients. The slope mirrors the 330 K thermal rotational distribution of the $CO^+(X)$ primary ions, that is, there is no significant rotational dependence of the charge transfer cross section at the collision energy of 0.3 eV.

4 mJ, beam diameter of 1 mm). Saturation of the transition and the rather long lifetime of the $CO^+(A)$ (3 μs) led to a significant fraction of excited ions. At a typical primary intensity of 5×10^4 CO^+ ions per laser shot, a product rate of 180 Ar^+ ions was detected.

The product signal is proportional to the thermal population of the rovibrational ground-state CO^+ ions and to the charge-transfer cross section. An evaluation of intensities measured for different rotational states is plotted in Fig. 82. Within the accuracy of our experiment, the relative Ar^+ product intensity can be fitted with a 330 K thermal rotational distribution of the $CO^+(X)$ primary ions. This is so close to the ion source temperature that one can exclude a significant rotational dependence of the charge-transfer cross section at our collision energy of 0.3 eV. This example illustrates that the combination of laser excitation with guided ion beams can be used to study reactions with state-prepared reactants. Of course, this method is also well suited for spectroscopical studies. A similar method, using charge-exchange detection in an ion flow tube, has been reported by Kuo et al. (1986).

3. *Laser Analysis of Products*

CO^+ product-state distributions in the reverse charge-transfer reaction, $Ar^+ + CO \rightarrow CO^+ + Ar$, were examined using laser-induced fluorescence by

the group of Leone (Hamilton et al., 1985; Lin et al., 1985). We have tried to apply this method in combination with the guided-ion-beam apparatus. As explained in Section IV B 4, however, the sensitivity of our arrangement is too low to detect the reaction products. Only when we use primary CO^+ ions and accumulate a sufficient number in the region seen by the photomultiplier (see Fig. 46), can we observe the induced fluorescence signal. A corresponding spectrum, recorded in the same wavelength range as in the case of the laser-induced charge transfer, is depicted in the lower half of Fig. 81. In both spectra, the intensities of the individual lines reveal the rotational temperature of the CO^+ ions.

A significantly more sensitive laser-based technique for product analysis is based on selective photofragmentation of the product ions. As described in Section IV B 4, this method has several advantages including a large laser–ion interaction volume, efficient collection and detection of the fragment ions, and the possibility of saturating the fragmentation process.

We have used selective photofragmentation to study in detail the formation of metastable $O_2^+(a\,^4\Pi_u)$ formed in $Ar^+ + O_2$ collisions (Scherbarth and Gerlich, 1989). The integral cross section, depicted in Fig. 63, shows the threshold onset of this endothermic channel. State-selective analysis of the metastable $O_2^+(a\,^4\Pi_u)$ state has been performed by fragmentation via the $b\,^4\Sigma_g$ state. A small section of the experimental $\Delta v = 3$ photofragment spectrum of the $O_2^+(a\,^4\Pi_u)$ products is plotted in the lowest panel of Fig. 83. Using a set of molecular constants (Hansen et al., 1983), and assuming a microcanonical rovibrational population of the O_2^+ products, we have simulated the O_2^+ fragmentation spectra. Comparison of these results, shown for $v'' = 0$–3 in the upper panels of Fig. 83, with the measured spectrum reveals that most of the experimental lines are due to the $v'' = 0$ products. An analysis of all measured spectra (Scherbarth and Gerlich, 1989) corroborates this nonstatistical preference of the $v'' = 0$ state (more than 90% at $E_T = 0.55$ meV). In contrast to specific excitation of the vibrational ground state, a wide range of rotational states is excited. The population of these $(v'' = 0, j'')$ states is in accordance with a statistical distribution. This can be seen from Fig. 84 where two populations measured at collision energies of 0.53 eV and 1.05 eV are compared with the microcanonical equilibrium distribution. As described briefly in Section IV B 4, we are presently exploring the possibilities of extending the versatility of this method by using a two-photon fragmentation scheme.

D. Radiative Association and Fragmentation

Radiative association of positive ions with molecules is considered to be an important process in the synthesis of complex molecules in low-density interstellar clouds. One of the first applications of an ion trapping method

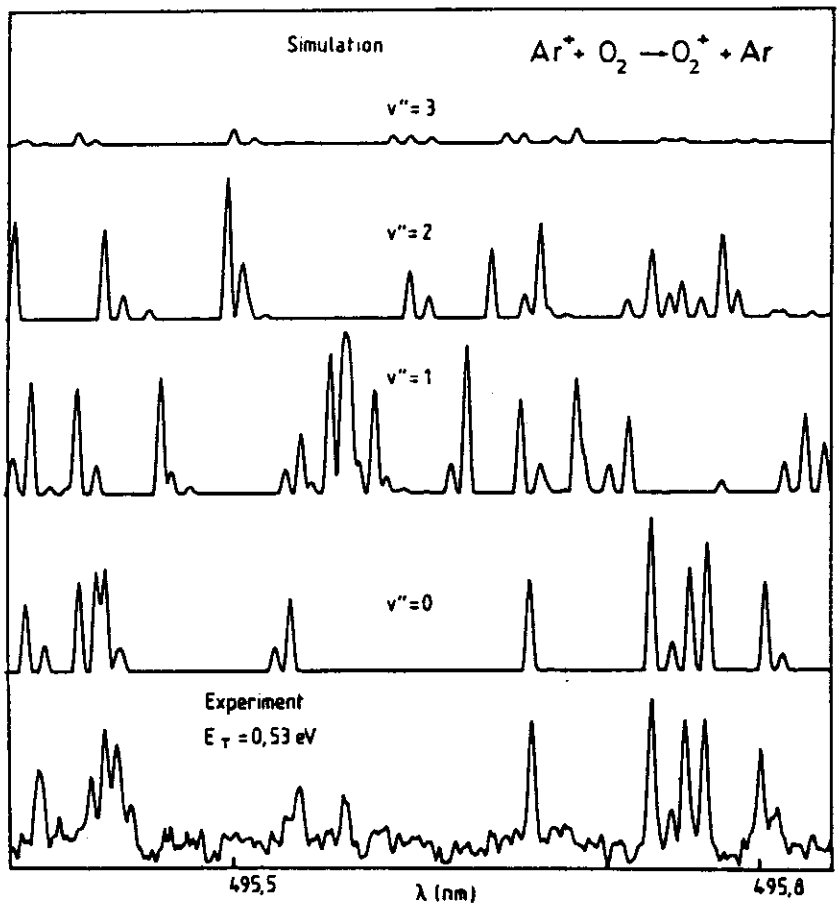

Figure 83. Laser-induced fragmentation of O_2^+ products recorded using the guided-ion-beam apparatus shown in Fig. 46. The lowest panel shows a small section of the experimental $\Delta v = 3$ photofragment spectrum of $O_2^+(a\,^4\Pi_u)$ products populated in the $Ar^+ + O_2$ charge-transfer reaction. The upper curves are simulated spectra calculated separately for the accessible product vibrational states $v'' = 0$–3. For the rovibrational states a statistical population was assumed.

at very low temperatures (11–20 K) for studying radiative association was reported by the group of Dunn (Barlow et al., 1986; Luine and Dunn, 1985). They determined a radiative association rate coefficient of $k_I = 1.1 \times 10^{-13}\,cm^3/s$ for $CH_3^+ \cdot H_2$; however, for the astrophysically important $C^+ \cdot H_2$ radiative stabilization they could only measure an upper limit of $k_I = 1.5 \times 10^{-15}\,cm^3/s$. The higher sensitivity of our temperature variable ring electrode trap has extended the range for determining radiative association rate coefficients from $10^{-15}\,cm^3/s$ to $10^{-17}\,cm^3/s$. Results for the stabilization of the $CH_3^+ \cdot H_2$ complex were reported recently (Gerlich and Kaefer, 1989). In this section, we present similar results for the prototype system $H^+ \cdot H_2$ and for $C^+ \cdot H_2$. Another very recent application of the rf ring electrode trap is the determination of the radiative decay rate of highly excited molecules using photofragmentation with a CO_2 laser. This method will be illustrated using H_3^+ and CH_5^+ as examples.

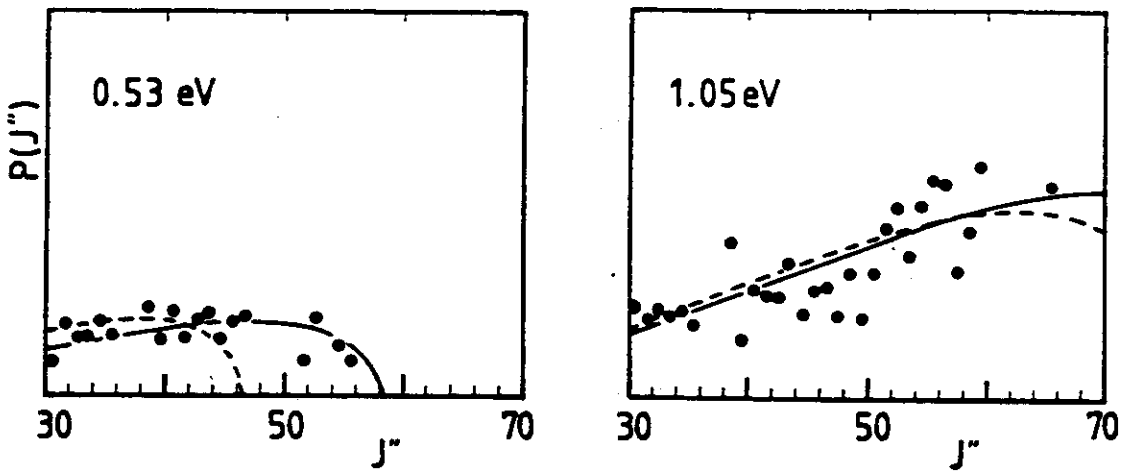

Figure 84. Relative populations of rotational levels for $O_2^+(a\,^4\Pi_u, v=0)$ product ions formed in $Ar^+ + O_2$ collisions at 0.53 eV and 1.05 eV. The depicted probabilities were extracted from photofragmentation spectra [see, for example, Fig. 83 and Scherbarth and Gerlich (1989)]. The lines are the microcanonical equilibrium distributions for the two $Ar^+(^2P_J)$ states.

1. *Association of $H^+ \cdot H_2$ and $C^+ \cdot H_2$*

The prototype reaction $H^+ + H_2$ has been mentioned in several of the preceding examples. It is well known that the reaction proceeds via formation of a long-lived complex. The lifetime of this complex, which is on the order of several 10^{-10} s, has been studied using classical trajectory calculations (Schlier and Vix, 1985). Such a highly excited H_3^+ molecule can emit infrared photons and corresponding calculated radiation spectra, based also on classical trajectories, have been reported (Berblinger and Schlier, 1988). The radiative and three-body stabilization of $H^+ \cdot H_2$ and $D^+ \cdot D_2$ has been studied in the ring electrode trap at 350 K and 80 K. A typical result is shown in Fig. 85 for formation of D_3^+. The procedure used to determine the apparent binary rate coefficient $k^* = k_r + n_2 k_3$ has been described in Section IV E. For $D^+ + D_2$, the slope of the line in Fig. 85 yields a three-body rate coefficient $k_3(80\,\mathrm{K}) = 7.6 \pm 1 \times 10^{-29}\,\mathrm{cm^6/s}$ and the intersection at $n_2 = 0$ can be taken as an estimate for the radiative stabilization rate coefficient $k_r(80\,\mathrm{K}) = 1 \times 10^{-16}\,\mathrm{cm^3/s}$. Similar results have been obtained for $H^+ + H_2$ [$k_3(80\,\mathrm{K}) = 5.4 \pm 1 \times 10^{-29}\,\mathrm{cm^6/s}$ and $k_r(80\,\mathrm{K}) = 1.3 \times 10^{-16}\,\mathrm{cm^3/s}$].

Based on assumptions that have been discussed in Gerlich and Kaefer (1989), one can obtain from the two values k_r and k_3 an estimate of the complex and the radiative lifetimes. An uncertain parameter in this estimation is the stabilization factor f_s, that is, the efficiency of deactivating the intermediate complex via collision with a third body. Assuming $f_s = 0.17$ for $H^+ \cdot H_2$ in a pure H_2 environment, one obtains a complex lifetime of 0.65×10^{-10} s and a radiative lifetime of 1.2×10^{-3} s. These values deviate from those determined from classical trajectory calculations that estimate a

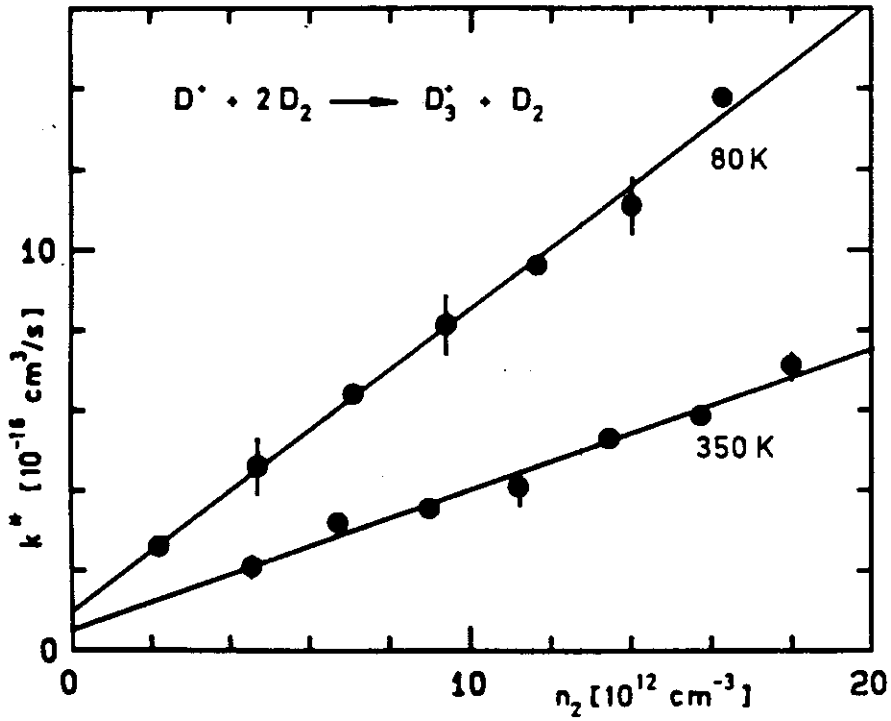

Figure 85. Effective rate coefficient $k^* = n_2 k_3 + k_r$ for D_3^+ formation via ternary and radiative association of $D^+ \cdot D_2$ complexes measured at 80 K and 350 K in the ring electrode trap. Extrapolation of the target density to zero results in an upper limit for the radiative association rate coefficient k_r.

complex lifetime of 6.8×10^{-10} s (Schlier and Vix, 1985) and a radiative lifetime of 0.14×10^{-3} s (Berblinger and Schlier, 1988). This comparison indicates that, even for this simple prototype system, more detailed experiments and theoretical studies are required.

An interesting extension of the $H^+ \cdot H_2$ system is to increase the degrees of freedom by adding additional hydrogen molecules. In Sections III and IV, this was used predominantly to illustrate the low-temperature capabilities of the ring electrode trap. Figure 44, for example, gives several ternary rate coefficients for the growth of hydrogen clusters up to H_9^+ at 25 K, while Fig. 59 demonstrates the increase of the ternary rate coefficients for $H_3^+ \cdot H_2$ stabilization as the temperature is lowered from 80 K to 25 K.

The radiative association of $C^+ \cdot H_2$ is the important first step in the interstellar gas-phase formation of hydrocarbons. This process has been studied in the liquid nitrogen cooled ion trap (Kaefer, 1989). The 80 K data are plotted in Fig. 86. The resulting rate coefficients are $k_3(80\,\mathrm{K}) = 5.9 \times 10^{-29}\,\mathrm{cm^3/s}$ and $k_r(80\,\mathrm{K}) = 7 \times 10^{-16}\,\mathrm{cm^3/s}$. Assuming a third-body stabilization efficiency $f_s = 1$, one obtains a radiative lifetime of $2 \times 10^{-5}\,\mathrm{s^{-1}}$, which indicates that stabilization occurs via an optical transition. Very recent measurements with the liquid-helium-cooled trap at a nominal temperature of 25 K are also included in Fig. 86. The resulting radiative rate coefficient

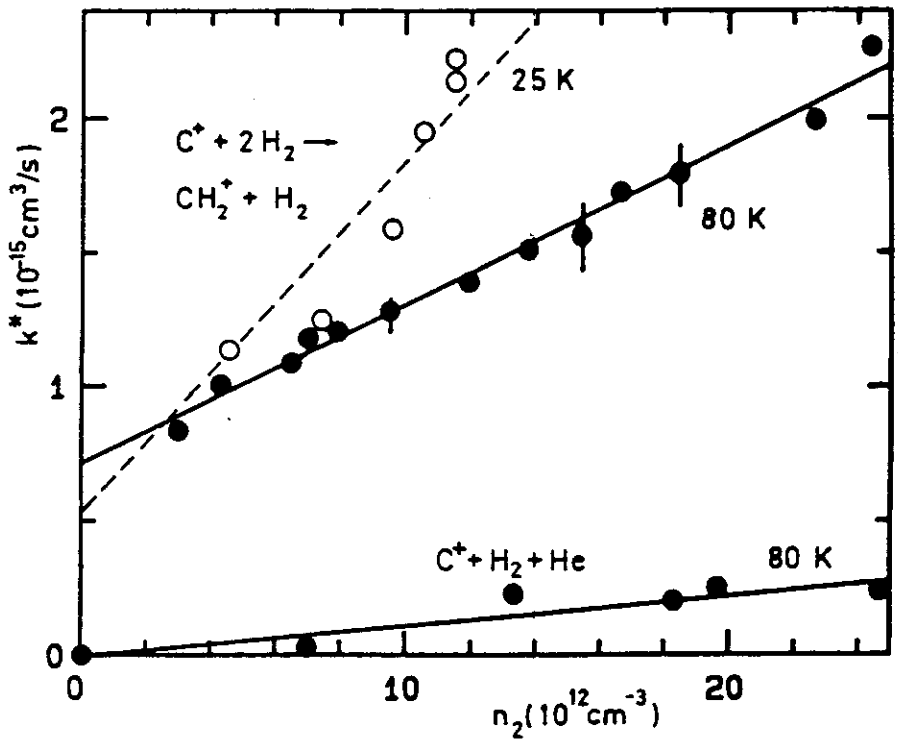

Figure 86. Effective rate coefficients $k^* = n_2 k_3 + k_r$ for associative CH_2^+ formation in the liquid-helium- (25 K) and the liquid-nitrogen-cooled (80 K) ring electrode traps. The two upper curves were recorded using pure hydrogen and include $k_3(H_2)$ and k_r. The data suggest that the radiative association rate coefficients $k_r(25\,K)$ and $k_r(80\,K)$ are smaller than $8 \times 10^{-16}\,cm^3/s$. The lowest curve shows the net influence of additional He acting as the third body.

has the same magnitude, $k_r(25\,K) = 5.5 \times 10^{-16}\,cm^3/s$, but ternary association is two times faster [$k_3(25\,K) = 13 \times 10^{-29}\,cm^6/s$]. The estimated error limits of the two radiative association rates are $\pm 50\%$. The main problem in determining these values arises from reactions with gas impurities, and we have observed variations for data sets obtained under different conditions. Additional complications are due to the fact that the CH_2^+ products, as well as possibly formed CH^+ ions, are not directly observable because they are converted into CH_3^+ by fast secondary reactions with H_2 as has been discussed in Section V A 3.

2. *Radiative Lifetimes of $H^+ \cdot H_2$ and $CH_3^+ \cdot H_2$*

As described previously, intermediate complex and radiative lifetimes can be inferred by measuring the apparent rate coefficient k^* as a function of n_2. In order to obtain more direct insight into the radiative decay of highly exited molecular complexes, we have probed the population of states in the vicinity (0.1 eV) of the dissociation limit via photofragmentation with a CO_2 laser. Owing to a low laser intensity of a few watts, multiphoton transitions can be ruled out. Therefore, only those ions whose internal energy deviates

at most by $h\nu$ from the dissociation limit can be affected by a single CO_2 laser photon.

Highly exited H_3^+ and CH_5^+ ions have been prepared in the storage source, but with high-energy electrons and short storage times to avoid quenching collisions. Under such conditions, a sufficiently large number of excited ions could be created. These ions were injected into the trap, this time under ultrahigh vacuum conditions ($< 10^{-9}$ mbar). After a variable storage time of several ms, a typically 100-μs-short CO_2 laser pulse was sent through the trap leading to the formation of fragment ions. With increasing storage time, the number of ions that could be fragmented decreased, while the total number of trapped ions remained unchanged. The net signal is plotted in Fig. 87. It can be seen that the number of excited ions decreases exponentially. Since under our vacuum conditions collision rates are on the order of $1\,s^{-1}$, this decay must be due to radiative relaxation.

The radiative lifetime determined for H_3^+, 0.37×10^{-3} s, is larger than the calculated value of 0.14×10^{-3} s, but smaller than that deduced from the association measurement, 1.2×10^{-3} s. The deviation of our two experimental values is most probably due to differences in the angular momentum distributions of the two prepared H_3^+ ions, that is, the collision complex $H^+ \cdot H_2$ and the highly excited molecule $(H_3^+)^{**}$. The lifetime ratio,

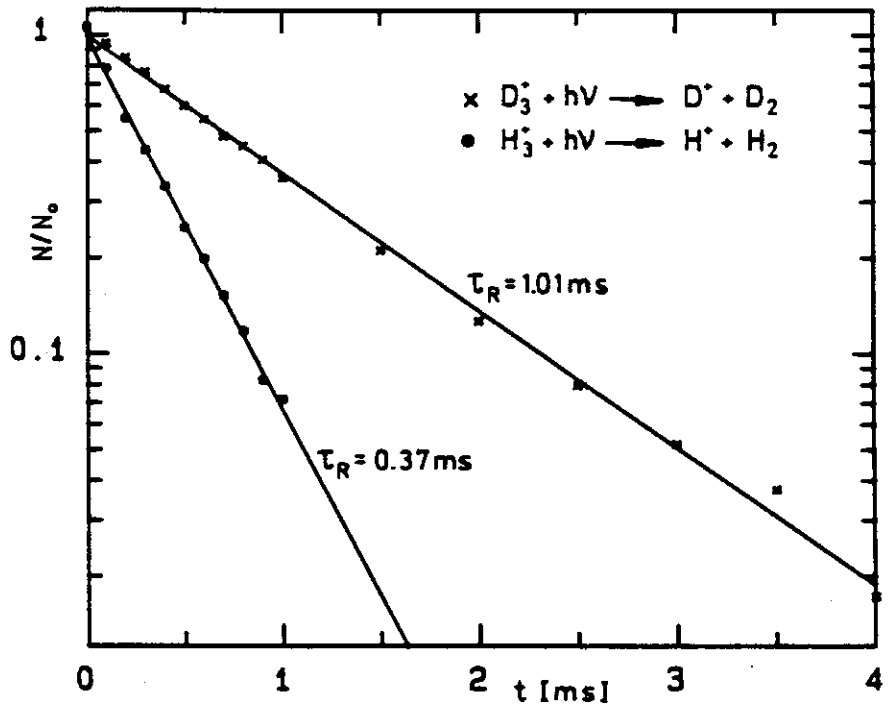

Figure 87. Direct determination of radiative lifetimes of highly exited H_3^+ and D_3^+ ions. Externally created ions were injected into the ring electrode trap, and their spontaneous radiative decay was probed by delayed CO_2 laser-induced fragmentation. Loss by processes other than radiative decay is excluded on the depicted time scale and at the low pressure ($< 10^{-9}$ mbar).

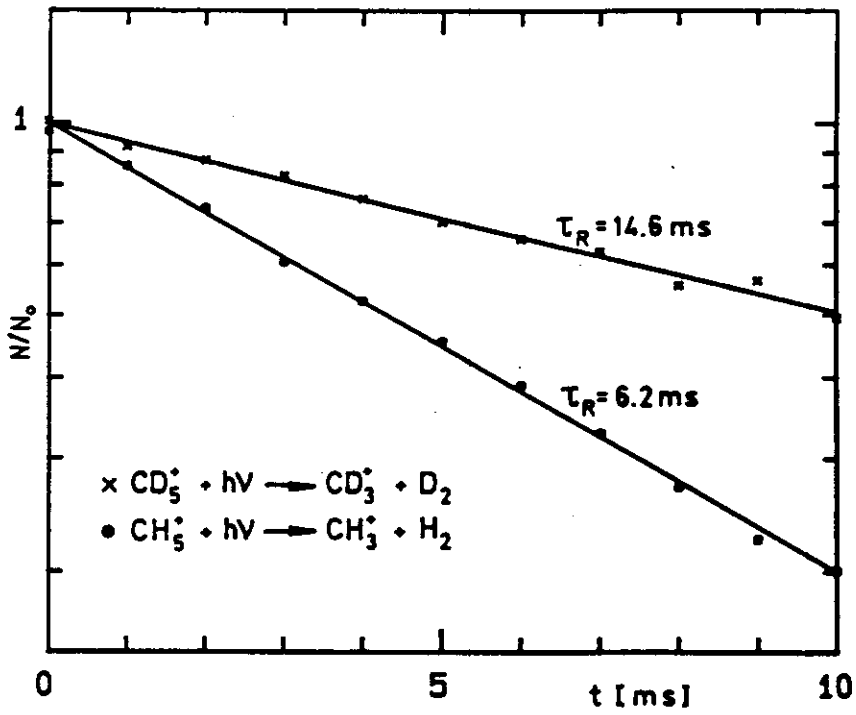

Figure 88. Determination of the radiative lifetimes of highly exited CH_5^+ and CD_5^+ ions using CO_2 laser fragmentation. The lifetimes are significantly longer than for H_3^+ and D_3^+, shown in Fig. 87.

$\tau(D_3^+)/\tau(H_3^+) = 2.4$ is in good agreement with the mass ratio, $(m(D_3^+)/m(H_3^+))^{3/2} = 2.8$.

Similar results for CH_5^+ and CD_5^+ are depicted in Fig. 88. The lifetimes of 6.2 ms and 14.6 ms support the recently published results on ternary and radiative association of the $CH_3^+ \cdot H_2$ complex (Gerlich and Kaefer, 1989). These examples show that combinations of laser methods with the ring electrode trap can also provide interesting spectroscopic and dynamic information.

VI. CONCLUSIONS AND FUTURE DEVELOPMENTS

This chapter has reviewed the theory of the motion of charged particles in fast oscillatory fields and presented several applications of electric rf fields for the study of processes involving slow ions. The major aim of the theoretical part, Section II, was to provide some basic knowledge for understanding the experimental features of the rf devices presented in Section III. Several complete apparatuses were described in Section IV, and Section V gave an overview of typical results obtained using these instruments. In this final section we make a few remarks to the state of the theory and their developmental possibilities, we discuss several improvements of the presented instruments, and add a few speculations.

Our theoretical treatment was dominated by the adiabatic approximation, since conservation of the mean kinetic energy of the ion is required for most experimental application and the adiabatic constants of the motion simplify the determination of conditions for safe confinement of ions in any rf field. Adiabatic theories are well established in theoretical physics and mathematics, the only blemish of the presented theory is the empirical determination of the border line between "safe" and "unsafe" regions, based on $\eta_m(\mathbf{r}) = 0.3$. Here, additional theoretical work is needed for a rigorous justification. More generally, it would be desirable to find a mathematical procedure to completely map out regions of stability and their adiabatic subregions for any rf field. This would also allow one to find out whether there is any suitable rf device, besides the quadrupole, in which one could take experimental advantage of sharp transitions from stability to instability, for example, for mass or phase-space selection. It is suspected that the available modern mathematical methods developed for characterizing nonlinear dynamical systems, provide the framework for a fundamental description of the motion of charged particles in inhomogeneous rf fields.

The presented variety of rf devices has illustrated that there are almost no geometrical restrictions to create two- or three-dimensional potential minima. The applicability of these devices can be further extended by superimposing additional temporal or spatial varying fields (auxiliary low-frequency field, pulsed electrodes, field penetration from correction electrodes, etc.). For example, a series of ring electrodes surrounding a multipole could be used to create an axial, near harmonic dc potential and a weak resonant excitation of the axial motion could result in a mass-selective ejection. Other extensions can be imagined by adding a magnetostatic field in which the cyclotron motion of specific ions may be resonantly excited. Beyond all these discussed quasielectrostatic fields also the nodal points or lines of standing or traveling electromagnetic waves could be used to store ions. A possible application is the making of a well-defined lattice of laser-cooled ions in a microwave guide, for example, for studying collective effects.

The versatility of instruments based on rf devices has been illustrated through a variety of applications, and it can be imagined that these developments will stimulate the invention of new apparatuses or other rf devices. However, many possibilities still remain for improving the existing instruments. Significant progress can be expected from combination of ion guiding or trapping with various optical methods. Especially, laser based methods such as multiphoton ionization, one- or two-color fragment spectroscopy, laser-induced fluroescence, laser cooling, infrared excitation of ions or neutrals, and so on, will lead to many new applications in spectroscopy, reaction dynamics, analytical chemistry, and other fields.

The capability of the new merged-beam arrangement for the study of ion reaction dynamics at very low energies can be further enhanced, for example, by adding a temperature variable ion trap for thermalization of the ionic reactants or by using supersonic beams with various expansion conditions. Other extensions of this instrument could make use of an atomic beam, of a beam of free radicals, or of a second slow ion beam. A more speculative extension of the merged-beam method is the superposition of an electron and an ion beam used to study dielectronic recombination, whereby the beam of slow electrons could be confined in a microwave guide.

Similar improvements can also be imagined for ion-trapping devices. Pulsed gas valves would allow one to utilize different gases for thermalization and reaction. The advantage of time-of-flight mass selection for simultaneous analysis of the entire trap contents is clearly evident. Progress can also be made by mass-selective extraction or mass-selective ejection of product ions without perturbing the thermalized ensemble of primary ions. Finally, laser cooling of stored molecular ions may even be feasible by using stimulated-emission pumping or infrared transitions, and in combination with cold trapped neutrals, could lead to μeV collision energies.

It can be expected that the described methods of trapping and guiding charged particles are not only limited to those applications mentioned in this chapter. Therefore, it is obvious that there is much space for inventiveness and that we can look forward to a much broader application of inhomogeneous rf fields.

Acknowledgements

This work involved the cooperation and assistance of many people. I am indebted especially to Professor Ch. Schlier, who rendered possible a large fraction of this research by providing the scientific environment in his group and by financial support, and who contributed by many stimulating and fruitful discussions and by his continuous interest. I am particularly grateful to Dr. E. Teloy who introduced me into the fundamentals of the theory and applications of inhomogeneous rf fields and with whom I frequently discussed various technical and scientific questions. A large fraction of the recent experiments has been performed by two former students, Dr G. Kaefer and Dr. S. Scherbarth, and in cooperation with several Diplom–students whom I want to thank for their efforts. It is also a pleasure to acknowledge the help and assistance of the technical staff from the Fakultät für Physik, Freiburg, and especially the skills of Dipl. Ing. U. Person. I am especially indebted to Dr. S. Horning for his careful reading of the manuscript and for many suggestions and very helpful hints. Various aspects of this research were supported by the Deutsche Forschungsgemeinschaft (Schwerpunktprogramm "Dynamik zustandsselektierter chemischer Primärprozesse").

References

M. Abramowitz and I. Stegun (1964), *Handbook of Mathematical Functions*, National Bureau of Standards, Washington, DC.

S. L. Anderson, F. A. Houle, D. Gerlich, and Y. T. Lee (1981), *J. Chem. Phys.* **75**, 2153.

V. I. Arnold (Ed.) (1988), *Dynamical Systems III*, Springer-Verlag, Berlin.

P. Ausloos (Ed.) (1979), *Kinetics of Ion–Molecule Reactions*, Plenum Press, New York.

P. Ausloos and S. G. Lias (Eds.) (1987), *Structure/Reactivity and Thermochemistry of Ions*, Reidel, Dordrecht.

R. Bahr (1969), Diplom Thesis, Univ. Freiburg.

R. Bahr, D. Gerlich, and E. Teloy (1970), *Verhandl. DPG (VI)* **5**, 131.

R. Bahr, D. Gerlich, and E. Teloy (1969), *Verhandl. DPG (VI)* **4**, 343.

L. S. Bartell, H. B. Thomson, and R. R. Roskos (1965), *Phys. Rev. Letters* **14**, 851.

S. E. Barlow, J. A. Luine, and G. H. Dunn (1986), *Int. J. Mass Spectrom. Ion Processes* **74**, 97.

S. E. Barlow and G. H. Dunn (1987), *Int. J. Mass Spectrom. Ion Processes* **80**, 227.

E. C. Beaty (1987), *J. Appl. Phys.* **61**, 2118.

K. Berkling, R. Helbing, K. Kramer, H. Pauly, Ch. Schlier, and P. Toschek (1962), *Z. Physik* **166**, 406.

M. Berblinger and Ch. Schlier (1988), *Mol. Phys.* **63**, 779.

W. Beyer (1976), Diplom Thesis, Univ. Freiburg.

G. Bischof and F. Linder (1986), *Z. Phys.* **D1**, 303.

L. A. Bloomfield (1990), *J. Opt. Soc. Am.* **B7**, 472.

R. Blümel, C. Kappler, W. Quint, and H. Walther (1989), *Phys. Rev. A* **40**, 808.

H. Böhringer (1985), *Chem. Phys. Lett.* **122**, 185.

H. Böhringer, W. Glebe, and F. Arnold (1983), *J. Phys. B, At. Mol. Phys.* **16**, 2619.

M. T. Bowers (Ed.) (1979), *Gas Phase Ion Chemistry*, Academic Press, New York, Vols. 1 and 2.

M. T. Bowers (Ed.) (1984), *Gas Phase Ion Chemistry*, Academic Press, New York, Vol. 3.

J. P. Braga, D. B. Knowles, and J. N. Murrell (1986), *Mol. Phys.* **57**, 665.

P. H. Bucksbaum, M. Bashkansky, and T. J. McIlrath (1987), *Phys. Rev. Lett.* **58**, 349.

P. H. Bucksbaum, D. W. Schumacher, and M. Bashkansky (1988), *Phys. Rev. Lett.* **10**, 1182.

F. v. Busch and W. Paul (1961a), *Z. Phys.* **164**, 581.

F. v. Busch and W. Paul (1961b), *Z. Phys.* **164**, 588.

S. W. Bustamente, M. Okumura, D. Gerlich, H. S. Kwok, L. R. Carlson, and Y. T. Lee (1987), *J. Chem. Phys.* **86**, 508.

P. J. Chantry (1971), *J. Chem. Phys.* **55**, 2746.

W. A. Chupka and M. E. Russell (1968), *J. Chem. Phys.* **49**, 5426.

D. A. Church (1969), *J. Appl. Phys.* **40**, 3127.

W. E. Conaway, T. Ebata, and R. N. Zare (1987), *J. Chem. Phys.* **87**, 3447.

R. J. Cook, D. G. Shankland, and A. L. Wells (1985), *Phys. Rev.* **A31**, 564.

E. D. Courant (1952), *Phys. Rev.* **88**, 1190.

J. B. Cross and J. J. Valentini (1982), *Rev. Sci. Instr.* **53**, 38.

P. H. Dawson (1976), *Quadrupole Mass Spectrometry*, Elsevier Scientific Publishing, Amsterdam.

P. H. Dawson and N. R. Whetten (1971), in *Dynamic Mass Spectrometry*, editted by D. Price, Heyden & Son, London, Vol. 2.

I. E. Dayton, F. C. Shoemake, and R. F. Moseley (1954), *Rev. Sci. Instr.* **25**, 485.

H. G. Dehmelt (1967), *Advan. At. Mol. Phys.* **3**, 53.

H. G. Dehmelt (1969), *Advan. At. Mol. Phys.* **5**, 109.

D. R. Dension (1971), *J. Vac. Sci. Technol.* **8**, 266.

F. Diedrich, J. C. Bergquist, W. M. Itano, and D. J. Wineland (1989), *Phys. Rev. Lett.* **62**, 403.

R. Disch, S. Scherbarth, and D. Gerlich, in *Conference on the dynamics of Molecular Collisions*, Snowbird, Utah, edited by D. G. Truhlar and P. J. Dagdigian.

G. G. Dolnikowski, M. J. Kristo, C. G. Enke, and J. T. Watson (1988), *Int. J. Mass Spectrom. Ion Processes* **82**, 1.

C. H. Dougless, G. Ringer, and W. R. Gentry (1982), *J. Chem. Phys.* **76**, 2423.

J. H. Eberly (1969), in *Progress in Optics*, edited by E. Wolf, North-Holland, Amsterdam, Vol. VII, p. 382.

K. M. Ervin and P. B. Armentrout (1985), *J. Chem. Phys.* **83**, 166.

K. M. Ervin and P. Armentrout (1987), *J. Chem. Phys.* **86**, 2659.

K. M. Ervin, S. K. Loh, N. Aristow, and P. B. Armentrout (1983), *J. Phys. Chem.* **87**, 3593.

J. M. Farrar (1988), in *Techniques for the Study of Ion–Molecule Reactions*, edited by J. M. Farrar and W. H. Saunders, Jr., Wiley, New York.

F. C. Fehsenfeld, D. L. Albritton, Y. A. Bush, P. G. Fournier, T. R. Govers, and J. Fournier (1974), *J. Chem. Phys.* **61**, 2150.

E. Fischer (1959), *Z. Phys.* **156**, 26.

G. D. Flesch, S. Nourbakhsh, and C. Y. Ng (1990), *J. Chem. Phys.* **92**, 3590.

J. C. Franklin (Ed.) (1979), *Ion and Molecule Reactions, Kinetics and Dynamics*, Dowden, Hutchinson, & Ross, Stroudsburg, PA.

B. Friedrich, S. Pick, L. Hladek, Z. Herman, E. E. Nikitin, A. I. Reznikov, and S. Ya. Umanskii (1986), *J. Chem. Phys.* **84**, 807.

B. Friedrich, W. Trafton, R. Rockwood, S. Howard, and J. H. Futrell (1984), *J. Chem. Phys.* **80**, 2537.

M. H. Friedman, A. L. Yergey, and J. E. Campana (1982), *J. Phys. E Sci. Instrum.* **15**, 53.

W. Frobin, Ch. Schlier, K. Strein, and E. Teloy (1977), *J. Chem. Phys.* **67**, 5505.

J. H. Futrell (Ed.) (1986), *Gaseous Ion Chemistry and Mass Spectrometry*, Wiley, New York.

H. Gaber (1987), Diplom Thesis, Univ. Freiburg.

A. V. Gaponov and M. A. Miller (1958), *Soviet Phys. JETP* **7**, 168.

W. R. Gentry (1979), in *Gas Phase Ion Chemistry*, edited by M. T. Bowers, Academic Press, New York, Vol. 2.

W. R. Gentry, D. J. McClure, and C. H. Douglas (1975), *Rev. Sci. Instr.* **46**, 367.

D. Gerlich (1971), Diplom Thesis, Univ. Freiburg.

D. Gerlich (1977), PhD Thesis, Univ. Freiburg.

D. Gerlich (1982), in *Symposium on Atomic and Surface Physics*, edited by W. Lindinger et al., Univ. Innsbruck, Salzburg, p. 304.

D. Gerlich (1984), in *Symposium on Atomic and Surface Physics*, edited by F. Howorka et al., Univ. Innsbruck, Salzburg, p. 116.

D. Gerlich (1986), in *Electronic and Atomic Collisions*, edited by D. C. Lorents et al., Elsevier, Amsterdam, p. 541.

D. Gerlich (1989a), *J. Chem. Phys.* **90**, 127.

D. Gerlich (1989b), *J. Chem. Phys.* **90**, 3574.

D. Gerlich (1989c), in *XII International Symposium on Molecular Beams*, edited by V. Aquilanti, Perugia, p. 37.

D. Gerlich (1990), *J. Chem. Phys.* **92**, 2377.

D. Gerlich and H. Bohli (1981), in *European Conference on Atomic Physics*, edited by J. Kowalski, G. zu Putlitz, and H. G. Weber, Heidelberg.

D. Gerlich, R. Disch, and S. Scherbarth (1987), *J. Chem. Phys.* **87**, 350.

D. Gerlich and G. Kaefer (1985), in *Second European Conference on Atomic and Molecular Physics*, edited by A. E. Vries et al., Amsterdam.

D. Gerlich and G. Kaefer (1987), in *5th Int. Swarm Seminar, Proceedings*, edited by N. G. Adams and D. Smith, Birmingham University, 133.

D. Gerlich and G. Kaefer (1988), in *Symposium on Atomic and Surface Physics*, edited by A. Penelle et al., La Plagne, France, 115.

D. Gerlich and G. Kaefer (1989), *Ap. J.* **347**, 849.

D. Gerlich, G. Kaefer, and W. Paul (1990), in *Symposium on Atomic and Surface Physics*, edited by T. D. Märk and F. Howorka, Obertraun.

D. Gerlich, G. Jerke, U. Mück, and U. Person (1991) (unpublished).

D. Gerlich, U. Nowotny, Ch. Schlier, and E. Teloy (1980), *Chem. Phys.* **47**, 245.

D. Gerlich and S. Scherbarth (1987), in *Electronic and Atomic Collisions*, edited by J. Geddes et al., Contributed papers, p. 809.

D. Gerlich and M. Wirth (1986), in *Symposium on Atomic and Surface Physics*, edited by F. Howorka et al., Univ. Innsbruck, Obertraun, p. 366.

P. M. Guyon, G. Bellec, O. Dutuit, D. Gerlich, E. A. Gislason, and J. B. Ozenne (1989), *Bull. Soc. Roy. des Sciences de Liege*, 58e annee 3–4, pp. 187–198.

C. Hägg and I. Szabo (1986a), *Int. J. Mass Spectrom. Ion Processes* **73**, 237.

C. Hägg and I. Szabo (1986b), *Int. J. Mass Spectrom. Ion Processes* **73**, 277.

C. Hägg and I. Szabo (1986c), *Int. J. Mass Spectrom. Ion Processes* **73**, 295.

C. E. Hamilton, V. M. Bierbaum and S. R. Leone (1985), *J. Chem. Phys.* **83**, 601.

J. C. Hansen, J. T. Moseley, and P. C. Cosby (1983), *J. Mol. Spectrosc.* **98**, 48.

L. Hanley and S. L. Anderson (1985), *Chem. Phys. Lett.* **122**, 410.

L. Hanley, S. A. Ruatta, and S. L. Anderson (1987), *J. Chem. Phys.* **87**, 260.

L. Hanley, J. L. Whitten, and S. L. Anderson (1988), *J. Phys. Chem.* **92**, 5803.

C. Hayashi (1985), *Nonlinear Oscillations in Physical Systems*, Princeton University Press, Princeton, NJ.

M. Henchman (1972), in *Ion Molecule Reactions*, edited by J. L. Franklin, Butterworth, London.

M. J. Henchman, N. G. Adams, and D. Smith (1981), *J. Chem. Phys.* **75**, 1201.

K. Hiraoka (1987), *J. Chem. Phys.* **87**, 4048.

F. A. Houle, S. L. Anderson, D. Gerlich, T. Turner, and Y. T. Lee (1982), *J. Chem. Phys.* **77**, 748.

Y. Ikezoe, S. Matsuoka, M. Takebe, and A. Viggiano (1986), *Gas Phase Ion–Molecule Reaction Rate Constants Through 1986*, published by Ion Reaction Research Group of The Mass Spectroscopy Society of Japan, Tokyo.

J. D. Jackson (1962), *Classical Electrodynamics*, Wiley, New York.

G. Kaefer (1984), Diplom Thesis, Univ. Freiburg.

G. Kaefer (1989), PhD Thesis, Univ. Freiburg.

H. Kalmbach (1989), Diplom Thesis, Univ. Freiburg.

P. L. Kapitza (1951), *Zn. Eksperim. i. Teor. Fiz.* **21**, 588.

P. L. Kapitza and P. A. M. Dirac (1933), *Proc. Cambridge Phil. Soc.* **29**, 297.

R. Kohls (1974), Zulassungsarbeit, Univ. Freiburg.

G. Kotowski (1943), *Z. angew. Math. Mech.* **23**, 213.

M. D. Kruskal (1962), *J. Math. Phys.* **3**, 806.

C. H. Kuo, I. W. Milkman, T. C. Steimle, and J. T. Moseley (1986), *J. Chem. Phys.* **85**, 4269.

H. Lagadec, C. Meis, and M. Jardino (1988), *Int. J. Mass Spectrom. Ion Processes* **85**, 287.

L. D. Landau and E. M. Lifschitz (1960), *Theoretical Physics*, Pergamon, Oxford, Vol. 1, p. 93.

R. F. Lever (1966), *IBM J. Res. Develop.* **10**, 26.

R. D. Levine and R. B. Bernstein (1974), *Molecular Reaction Dynamics*, Oxford University Press, Oxford.

R. D. Levine and R. B. Bernstein (1987), *Molecular Reaction Dynamics and Chemical Reactivity*, Oxford University Press, NY.

C. L. Liao, C. X. Liao, and C. Y. Ng (1984), *J. Chem. Phys.* **81**, 5672.

C. L. Liao, C. X. Liao, and C. Y. Ng (1985), *J. Chem. Phys.* **82**, 5489.

C. L. Liao, J. D. Shao, R. Xu, G. D. Flesch, Y. G. Li, and C. Y. Ng (1986), *J. Chem. Phys.* **85**, 3874.

C. L. Liao, R. Xu, G. D. Flesch, m. Baer, and C. Y. Ng (1990), *J. Chem. Phys.* **93**, 4818.

A. J. Lichtenberg and M. A. Lieberman (1983), *Regular and Stochastic Motion*, Springer, NY.

J. G. Linhard (1960), *Plasma Physics*, North Holland, Amsterdam.

G. H. Lin, J. Maier, and S. R. Leone (1985), *J. Chem. Phys.* **82**, 5527.

R. G. Littlejohn (1979), *J. Math. Phys.* **20**, 2445.

S. K. Loh, D. A. Hales, L. Lian, and P. B. Armentrout (1989), *J. Chem. Phys.* **90**, 5466.

J. Luine and G. Dunn (1985), *Ap. J.* **299**, L67.

L. M. Magid (1972), *Electromagnetic Fields, Energy and Waves*, Wiley, NY.

J. Marquette, C. Rebrion, and B. Rowe (1988), *J. Chem. Phys.* **89**, 2041.

R. E. March and R. J. Hughes (1989), *Quadrupole Storage Mass Spectrometry*, Wiley, NY.

H. Matsuda and T. Matsuo (1977), *Int. J. Mass Spectrom. Ion Processes* **24**, 107.

G. Mauclaire, R. Derai, S. Fenistein, and R. Marx (1979), *J. Chem. Phys.* **70**, 4017.

D. C. McGilvery and J. D. Morrison (1978), *Int. J. Mass Spectrom. Ion Processes* **28**, 81.

J. Meixner and F. W. Schäfke (1954), *Mathieusche Funktionen und Sphäroidfunktionen*, Springer, Berlin.

M. A. Miller (1958a), *Soviet. Phys. JETP* **8**, 206.

M. A. Miller (1958b), *Radiofizika* **1**, 110.

M. A. Miller (1959), *Soviet. Phys. JETP* **36**, 1358.

G. Miller (1963), *J. Phys. Chem.* **67**, 1359.

P. E. Miller and M. B. Denton (1986), *Int. J. Mass Spectrom. Ion Processes* **72**, 223.

P. E. Miller and M. B. Denton (1990), *Int. J. Mass Spectrom. Ion Processes* **96**, 17.

R. J. S. Morrison, W. E. Conaway, and R. N. Zare (1985), *Chem. Phys. Lett.* **113**, 435.

H. Motz and C. F. Watson (1967), *Advan. Electron. Electron. Phys.* **23**, 153.

D. Müller (1983), Diplom Thesis, Univ. Freiburg.

W. Neuhauser, M. Hohenstatt, P. Toschek, and H. Dehmelt (1978), *Appl. Phys.* **17**, 123.

W. Neuhauser, M. Hohenstatt, and P. E. Toschek (1980), *Phys. Rev.* **A22**, 1137.

D. Neuschäfer, Ch. Ottinger, and S. Zimmermann (1981), *Chem. Phys.* **55**, 313.

D. Neuschäfer, Ch. Ottinger, S. Zimmermann, W. Lindinger, F. Howorka, and H. Störi (1979), *Int. J. Mass Spectrom. Ion Processes* **31**, 345.

C. Y. Ng (1988), in *Techniques for the Study of Ion–Molecule Reactions*, edited by J. M. Farrar and W. H. Saunders, Wiley, New York.

K. Okuno (1986), *J. Phys. Soc. Japan* **55**, 1504.

K. Okuno and Y. Kaneko (1983), in *Electronic and Atomic Collisions*, edited by J. Eichler, I. V. Hertel, and N. Stolterfoth, Verlag, Berlin, p. 543.

G. Ochs and E. Teloy (1974), *J. Chem. Phys.* **61**, 4930

M. Okumura, L. Yeh, and Y. T. Lee (1988), *J. Chem. Phys.* **88**, 79.

T. M. Orlando, B. Yang, and S. L. Anderson (1989), *J. Chem. Phys.* **90**, 1577.

T. G. Owe Berg and T. A. Gaukler (1959), *Am. J. Phys.* **37**, 1013.

W. Paul (1989), Nobel Lecture, Stockholm.

W. Paul (1990), Diplom Thesis, Univ. Freiburg.

W. Paul and M. Raether (1955), *Z. Phys.* **140**, 262.

W. Paul, H. P. Reinhard, and U. von Zahn (1958), *Z. Phys.* **152**, 143.

W. Paul and H. Steinwedel (1953), Z. Naturforsch. **8a**, 448.

G. Piepke (1980), Diplom Thesis, Univ. Freiburg.

L. A. Posey, R. D. Guettler, N. J. Kirchner, B. A. Keller, and R. N. Zare (1991), *to be published.*

S. Scherbarth (1984), Diplom Thesis, Univ. Freiburg.

S. Scherbarth (1988), PhD Thesis, Univ. Freiburg.

S. Scherbarth and D. Gerlich (1989), *J. Chem. Phys.* **90**, 1610.

Ch. Schlier (1988), *Chem. Phys.* **126**, 73.

Ch. Schlier and U. Vix (1985), *Chem. Phys.* **95**, 401.

M. Schweizer (1988), Diplom Thesis, Univ. Freiburg.

A. Sen and J. B. A. Mitchell (1986), *Rev. Sci. Instrum.* **57**, 754.

K. Simonyi (1963), *Foundations of Electrical Engineering*, Pergamon Press.

A. Sommerfeld (1964), *Elektrodynamik*, Akademische Verlagsgesellschaft, Leipzig.

L. S. Sunderlin and P. B. Armentrout (1990), *Chem. Phys. Lett.* **167**, 188.

I. Szabo (1986), *Int. J. Mass Spectrom. Ion Processes* **73**, 197.

H. Tatarczyk and U. von Zahn (1965), *Z. Naturforsch.* **20**, 1708.

E. Teloy (1978), in *Electronic and Atomic Collisions*, edited by G. Watel, North Holland, Amsterdam, p. 591.

E. Teloy (1980), *Verhandl. DPG (VI)* **15**, 567.

E. Teloy and D. Gerlich (1974), *Chem. Phys.* **4**, 417.

J. F. J. Todd, R. M. Waldren, D. A. Freer, and R. F. Bonner (1980), *Int. J. Mass Spectrom. Ion Processes* **34**, 17.

P. Tosi, F. Baldo, F. Eccher, M. Filippi, and D. Bassi (1989a), *Chem. Phys. Lett.* **164**, 471.

P. Tosi, G. Fontana, S. Longano, and D. Bassi (1989b), *Int. J. Mass Spectrom. Ion Processes* **93**, 95.

S. M. Trujillo, R. H. Neynaber, and E. W. Rothe (1966), *Rev. Sci. Instr.* **37**, 1655.

T. Turner, O. Dutuit, and Y. T. Lee (1984), *J. Chem. Phys.* **81**, 3475.

F. Vedel (1991), *Int. J. Mass Spectrum. Ion Processes* **106**, 33.

M. L. Vestal and J. H. Futrell (1974), *Chem. Phys. Lett.* **28**, 55.

H. Villinger, J. M. Henchman, and W. Lindinger (1982), *J. Chem. Phys.* **76**, 1590.

J. T. Watson, D. Jaouen, H. Mestdagh and C. Rolando (1989), *Int. J. Mass Spectrom. Ion Processes* **93**, 225.

E. S. Weibel (1959), *Phys. Rev.* **114**, 18.

E. S. Weibel and G. L. Clark (1961), *J. Nucl. Energy, Part C, Plasma Physics* **2**, 112.

R. Werner (1968), Diplom Thesis, Univ. Freiburg.

D. J. Wineland, J. C. Bergquist, W. M. Itano, J. J. Bollinger, and C. H. Manney (1987), *Phys. Rev. Lett.* **59**, 2935.

D. J. Wineland and H. G. Dehmelt (1975), *Bull. Am. Phys. Soc.* **20**, 637.

M. Wirth (1984), Diplom Thesis, Univ. Freiburg.

R. F. Wuerker, H. M. Goldenberg, and R. V. Langmuir (1959a), *J. Appl. Phys.* **30**, 342.

R. F. Wuerker, H. M. Goldenberg, and R. V. Langmuir (1959b), *J. Appl. Phys.* **30**, 441.

L. I. Yeh, M. Okumura, J. D. Myers, J. M. Price, and Y. T. Lee (1989), *J. Chem. Phys.* **91**, 7319.

U. von Zahn (1963), *Rev. Sci. Instr.* **34**, 1.

U. von Zahn and H. Tatarczyk (1964), *Phys. Lett.* **12**, 190.